Validation of Ion and Electron Scale Gyrokinetic Simulations in an NSTX H-mode and Comparisons with a Synthetic Diagnostic for High-k Scattering

by

Juan Ruiz Ruiz

B.S. and M.S., Ecole Polytechnique (2015),
S.M., Massachusetts Institute of Technology (2015)

Submitted to the Department of Nuclear Science and Engineering
in partial fulfillment of the requirements for the degree of

Doctor of Philosophy

at the

MASSACHUSETTS INSTITUTE OF TECHNOLOGY

June 2019

Author . . . . . .
Department of Nuclear Science and Engineering
May 22, 2019

Certified by . . . . . .
Anne E. White
Cecil and Ida Green Associate Professor in Nuclear Engineering
Thesis Supervisor

Certified by . . . . . .
Walter Guttenfelder
Research Physicist, Princeton Plasma Physics Laboratory
Thesis Reader

Certified by . . . . . .
Nuno F. Loureiro
Associate Professor of Nuclear Science and Engineering and Associate Professor of Physics
Thesis Committee Member

Accepted by . . . . . .
Ju Li
Battelle Energy Alliance Professor of Nuclear Science and Engineering
Chairman, Department Committee on Graduate Theses

Validation of Ion and Electron Scale Gyrokinetic Simulations in an NSTX H-mode and Comparisons with a Synthetic Diagnostic for High-k Scattering

by

Juan Ruiz Ruiz

Submitted to the Department of Nuclear Science and Engineering
on May 22, 2019, in partial fulfillment of the
requirements for the degree of
Doctor of Philosophy

Abstract

In this thesis I perform an extensive validation study in an NSTX NBI-heated H-mode discharge, predicting that electron thermal transport can be entirely explained by short-wavelength electron-scale turbulence fluctuations driven by the electron temperature gradient mode (ETG), both in conditions of strong and weak ETG turbulence drive. For the first time, local, nonlinear gyrokinetic simulation carried out with the GYRO code [98] reproduce the experimental levels of electron thermal transport, the frequency spectrum of electron-scale turbulence, the shape of the wavenumber spectrum and the ratio of fluctuation levels between strongly driven and weakly driven ETG turbulence conditions. Ion thermal transport is very close to neoclassical levels predicted by NEO [215], consistent with stable ion-scale turbulence predicted by GYRO. Quantitative comparisons between high-k fluctuation measurements [65] and simulations are enabled via a novel synthetic high-k diagnostic implemented for GYRO in real-space. A new type of simulation resolving the full ETG spectrum in an unusually large domain $(L_r, L_\theta) \sim (20, 20)\rho_s$ is required to quantitatively compare with the measured frequency spectra of the high-k density fluctuations. Simulations that best match all experimental observables predict that the measured high-k turbulence is closer to the streamer peak of the density fluctuation spectrum than was previously believed. The frequency spectra characteristics of electron-scale turbulence (spectral peak and width) can be consistently reproduced by the synthetic spectra, but these reveal not to be critical constraints on the simulations. The shape of the high-k wavenumber spectrum and the fluctuation level ratio between the strong and weak ETG conditions can also be simultaneously matched by electron-scale simulations within sensitivity scans about the experimental profile values, and result to be great discriminators of the simulations analyzed. Validation metrics are used to discriminate between simulations, are were able to isolate the effect of safety factor and magnetic shear to match the shape of the measured fluctuation wavenumber spectrum. Together, electron thermal transport comparisons and quantitative agreement of electron-scale turbulence spectra give the strongest experimental evidence to date supporting ETG-driven turbulence fluctuations as the main mechanism driving anomalous electron thermal transport

in the outer-core of modest β NSTX NBI-heated H-modes.

Thesis Supervisor: Anne E. White
Title: Cecil and Ida Green Associate Professor in Nuclear Engineering

Thesis Reader: Walter Guttenfelder
Title: Research Physicist, Princeton Plasma Physics Laboratory

Thesis Committee Member: Nuno F. Loureiro
Title: Associate Professor of Nuclear Science and Engineering and Associate Professor of Physics

Acknowledgments

This PhD would never have been possible without the great help and support from many individuals who directly, or indirectly, have made these six years at MIT an outstanding academic, professional and personal experience. I will carry all of these moments as lessons for the rest of my life.

Before starting the PhD at MIT I was visiting student at the Space Propulsion Laboratory (SPL), in the department of Aeronautics and Astronautics (Aero-Astro). I am deeply grateful to Prof. Manuel Martinez-Sanchez, now Prof. Emeritus, for having given me a first chance to come to MIT as a visiting student to work closely with Carmen Guerra, then a PhD student and now Assistant Professor in Aero-Astro. Without this chance given to me by Prof. Martinez-Sanchez I would very likely not have been able to come to MIT in the first place.

During my time as a visiting student in the Space Propulsion Laboratory, Prof. Anne White, then Assistant Professor in the department of Nuclear Science and Engineering (NSE), gave me the chance to further stay in MIT to work in her group while a masters student in Aero-Astro, and ultimately as a PhD student in NSE. I am incredibly thankful for the faith that Anne put in me at that time, without which none of this would have happened. Reflecting on my PhD in NSE I can only start to realize how much Anne has supported me all along this journey. Anne has taught me a great deal about turbulence and turbulence measurements in plasmas, and I have learned what are the most important questions to tackle and to answer in a research endeavor, why we care about certain things and not others. Most importantly, thanks to Anne I have a vision of what a good research advisor and faculty should be.

I have to thank all the effort dedicated by Dr. Yang Ren at the Princeton Plasma Physics Laboratory, who taught me almost everything I know about high-k scattering at NSTX. Dr. Walter Guttenfelder has also been an incredible guide and mentor throughout my PhD. From Walter I have learned everything I know about transport in the core of NSTX and gyrokinetic simulation. Walter has also taught me what are the most important questions to ask at each step, why things are relevant, why would one care. Additionally, Walter has taught me how important it is to have an intuitive understanding of the physics

phenomena, however complicated they may be. Walter has been a great advisor as well, and I will deeply miss our conversations about turbulence and transport.

I also have to thank Prof. Nuno Loureiro, who has welcomed me to his Theory Group meetings every Friday morning. Nuno has treated me like an integral member of his research group, and has given me great options to practice talks and present my research to his group, an audience that I am not generally exposed to. With Nuno I have also learned a great deal about fundamental plasma physics concepts. It has been invaluable to interact with Nuno and his research group throughout these years.

I would like to thank Dr. Nathan Howard, from whom I have learned a great deal about gyrokinetic simulation and transport, as well as multiscale simulation. Nathan has been an incredible support for the gyrokinetic simulations presented in this thesis.

Outside of my thesis committee I have really enjoyed conversations with Dr. Chris Holland and Dr. Jeff Candy, who have been of great help in the development of the synthetic diagnostic for high-k scattering using GYRO. I really appreciate the time dedicated by Dr. Candy to have conversations and discuss very detailed topics of critical importance to this thesis, despite the limited time he has available. I also thank Dr. Candy for carrying out some linear and nonlinear simulations with CGYRO of interest in this thesis.

I have to thank the company and support from colleagues at the PSFC, specially Alex Creely, Pablo Rodriguez, Norman, Alex Tinguely, Adam Kuang, Lucio Milanese and Francesco Sciortino. I have to thank Adam Kuang for having taken the lead to publish the 'ARC divertor' journal publication, and for all of Adam's support during the last months of writing this thesis and preparing the defense presentation. Within NSE I have to specially thank Marina, who has been an incredible support with the PHinisheD group throughout the last months of my PhD, composed of Cody, Pablo, Carolyne, Karen, Jayson, Etienne and Alex. Marina has created a sense of group and belonging to something that I never thought I would have enjoyed this much. There are too many things to think about and prepare in order to close a PhD, and without the help of Marina through the PHinisheD group my graduation would have been delayed for months. I also have to specially thank Pablo Rodriguez, Cody and Alex Creely, who have been of great help in the preparation of the thesis defense. With Pablo we have lived incredible moments together, and I will miss sharing the hotel room in conferences.

Although time has gone by since 2015, I still remember the great moments I have lived with my former office mate Daniel Kwak at the PSFC, during my time as a masters student in Aero-Astro. Daniel was the best possible office mate I could've had. I will always remember the epic trip we did to Acadia: with Abdulla, Ben, Brandon, Daniel and myself. Abdulla has always been there throughout all my time in MIT, and we have done too many and too insane trips: California, Hamptons, Rayleigh to Boston, Spain, Dubai ... these have been great highlights of my time at MIT.

I am incredibly thankful to all the flatmates with which I have shared apartment in Boston and Cambridge. Anass Afilal during my first year in 119 Bay State Road, the '7 $**$' in 13 Haviland St. with Alejandro, Pierre and Rami. In 'Toscanini Alto' at 891 Main St. Cambridge with Alejandro, Rami and Giulia, and in 'Toscanini Este' at 119 Sciarappa St. with Rami, Giulia and the last months with David. All of these people have made my MIT experience a very sweet one, and I will remember them forever. From Alejandro I will always remember the tunadilla. Among my roommates I have to specially thank my closest friends Giulia and Rami for their great support and friendship. With them we have lived some of the happiest periods in my PhD while at Toscanini Alto, along with Giancarlo, Paolo, Giacomo, Elena, Davide and Reza. I remember this period in Toscanini Alto as a very very special one with them. Elena has been an incredible friend and she has opened the doors of her house to all of us, reminding me how friendship has no age. Toscanini Alto was probably the sweetest period in my PhD, and I could not have shared this moment with better company.

Giulia has been a very special roommate and friend. Giulia has been an incredible support throughout all of these years, in the good but also in the most difficult moments. With Giulia I have learned to appreciate many of the things in life that I would never have thought about. Sharing the small things in life are sometimes the most special moments. Plus, Giulia is an incredible cook, and I will take many Italian recipes that I learned from Giulia, with me wherever I go.

Rami has been my closest friend, the closest to a brother that I have ever had. I have never gotten along so well with anyone in my life. I have lived the best moments in my PhD with Rami: traveling to Hyderabad, Santiago, Bangkok, Grenoble, Dubai, ... Rami has also been there for the good moments and the difficult ones, the small ones and the

big ones: no questions asked. But one of the most important things I take from Rami are the potential that a person has in this world, where the limits are set by oneself and not by the outside, and the unconditional care and love for others. I cannot express in words my appreciation and love to Rami. A best friend forever. Rami has introduced me to great friends outside of MIT, such as Lydia and Capucine. From Lydia I take the constant support to push towards the last moments in my PhD. From Capucine, the great energy to create a community of friends in Boston.

Student clubs at MIT have been a central part of my campus life at MIT. Before MIT I never really participated in student clubs before. During my first year at MIT, my great friend David Colino saw something in me and invited me to participate in Spain@MIT. This moment was a turning point that would mark the rest of my stay in MIT. Colino was an outstanding President at Spain@MIT, a great person and friend. With Colino I discovered what student clubs are like, and opened the doors to the fabulous Spanish community at MIT. I want to remember all of the members in the committee of Spain@MIT during my time: Colino, Maite, Pablo Dueñas, Enrique Fernandez, Enrique Lizarraga, Elisa, Alba, Javier Iglesias de Ussel, Iñigo, Pablo Fernandez, Carlos, Adrià, Andrea, Ramón, Rafa, Ester, Mikel, Ricardo, Pablo Rodriguez y Alex. Spain@MIT has also given me the opportunity to play soccer in the IntraMural League, which has given me many happy moments.

In Spain@MIT I have met some of the most special people in my life, such as Maite and Noel, Ferran, Meryem and Enrique Lizarraga. From Maite and Noel I take their welcoming, both in my early days as well as in my last moments in MIT, with the Game of Thrones viewing crew with Meryem. From Ferran I take his deep sense of friendship. From Enrique I take all the moments in the gym, soccer, Saturday nights in Brahmin and his control of Albany St. from the top of NW12. Enrique also introduced me to incredible people such as the pitbull Alex Guion and Remi Techet, the malakas of my time. The energy of Guion motivated and inspired me to pursue projects such as the Global Startup Workshop, which was a central part in my life at MIT for several years. But maybe the biggest malaka is Aristeidis. Besides being a great promoter of the Hellenic Student Association (HSA) at MIT, Aristeidis has an incredible heart. I have deeply enjoyed working with Aristeidis in organizing events together, such as Mixers between HSA and

Spain@MIT, and in soccer. Aristeidis has also opened the doors of his house in the Boston Common to me in several occasions and I keep some of the most memorable moments in Boston in the company of Aristeidis.

The MIT Global Startup Workshop (GSW) has probably been the student club that has made the most professional impact in me. I have learned what leadership is truly about. I thank Alex Guion for having helped me be a part of GSW. Although I was probably not aware at the time, the potential impact of GSW is really immense, but the lessons taken from such experiences really transforms the students that engage with GSW. I need to specially thank Georgie, Megan, Travis, Reinaldo and SJ for their great support of GSW and their great help in the moments that we most needed it, but also by defending this valuable student club for MIT and its students. GSW teaches you, in a protected academic setting, how real-life problems are solved in the business world, teaches you how to motivate others, how to build a team, how to deal with failure, with conflict, how to compromise and how to understand the psychology of each individual to make the most out of each situation. I say GSW is, truly, an entrepreneurial experience: a one-year experience that culminates in a conference, which we have to reinvent every year depending on the partner and the geographic region. Throughout this journey one has to design the product, analyze the market, look for partners and investors for fundraising, select, build and guide a team, negotiate, perform and execute ... a complete package that has truly transformed me as a person. Thank you GSW. GSW has also been the gathering place where great friendships are forged: Mili, Alex, Felipe, Shikhar, Shaurya, Paula, Maria, Irene, Kiran, Tom, Gabi, Kam, Paolo, Vamsi, Aditi, and of course my beloved Diana and David, we are DDJ! With Diana and David we dedicated incredible amounts of work to make a great conference in Bangkok. Diana and David have also become incredibly close friends, from which I have learned to better know myself, as well as very useful lessons in life.

The MIT Judo Club has been an incredible group of people with which I have practiced one of my favorite sports. I would like to appreciate specially Fil Twarowski and Tarek Fadel for their great dedication to this club. They have created a great sense of belonging, love for a sport, and are also great people. I also really appreciate having done Judo with Pablo and Ted. The late evenings in my MIT life were also gym time, from which I

recognize Theo "La Roca", Faysal "La Bestia" and Juuuuuude. Few are the times when I did not see any of them in the Z Center.

Soccer has also been an important part of my life in MIT, specially with the Equipo and MIT FC. My close friend Toni was able to make a great team of players, but also assemble a great squad of behind-the-scenes counselors, with Cesar, Fran, Jon, Dario and Hasi. Although Toni was only present for some year and a half at MIT, he left a big mark in the people that he met. With Toni I have discovered the joy and the essence of soccer. Soccer has been the greatest excuse for this close group of friends to get together. Toni has also become part of my closest friends, from whom I have learned to appreciate a passion for soccer, but also about academia and academic career. The Equipo has been one of the best highlights in my PhD, and I have to thank Toni for all of his determination and dedication to a project that he truly believed in.

An integral part of the Equipo was Cesar, who was also very involved since the very beginning with Toni and leading the team. Cesar has also a very big heart for his friends, and I appreciate how much he appreciates the Equipo. Dario is the wise man of the Equipo, the one with most experience, suuper fun but also a very reasonable and sensible person. From Dario I have learned a lot of lessons in life. Jon is the young guy in the Equipo, in MIT for his Masters project. With Jon we did one of the most memorable trips during my time in MIT, the "Vegas Madness" trip with Fran and Enrique. Jon is an incredibly appreciative member of the Equipo, and has an incredible sense of sharing and belonging to the group that has only made it stronger. Hasi is the CEO, the calm and composed CEO that has also shown a lot of love and belonging to the Equipo, and has also opened the doors of his house with Adriana in multiple occasions - something that has made me appreciate my life at MIT and also the people that care about me in Cambridge. Ivan is our goalie, our loving goalie. Fran has been a very special friend in the Equipo. With Fran I have shared the most time and most special moments with the equipo. We have lived together so many moments and learned so many lessons in life that it is even difficult to remember them all. But I keep them all with me. With Fran we have been able to interact during the good but also the bad times, the small and the big things, like true friends forever. Fran was always there ready to help a friend on anything, or simply to spend some quality time with a friend. From Fran I also take his sense of

appreciation of life, his hability to put things in perspective and help us truly appreciate the things that happen to us, even in the most difficult moments. The equipo, all of them, have a very special part in my heart and have become family, my Cambridge family, that will last forever.

Besides making some of the best friends in my life, with the Equipo we were the leadership of the wider MIT FC team. Besides living great moments together through soccer trainings and competition, I have also made some great friends. MIT FC has been, and continues to be, a great gathering umbrella not only for soccer enthusiasts, but also great friends and that is part of its great recent success. I will remember Shervin, Nick, Arnaud, Ari, George, Marco, Ahmed, Kris, Markus, Dan, Lucas, Wes, Jack, Sean, Ricooo, Nate, Jeremy. The love for the game and the sense of belonging to MIT FC has been very unique and very, very beautiful, and I thank MIT FC for giving me the chance of have a taste of this sweet moments together.

I also have to give special thanks to the Nuclear Science and Engineering department (NSE) and the Plasma Science and Fusion Center (PSFC) for making me believe in things that go well beyond individual people. It has been incredibly inspiring to see PSFC merge like a phoenix from the darkest places to become the frontrunner in the fusion community worldwide, only within a couple of years. I look up to the leadership of PSFC by Dennis, with the pursuit of the things that are truly important to make fusion a reality, no matter how difficult they are. This is probably one simple example that I have had the great chance to experience in MIT: the transformation of the PSFC. This is probably part of what MIT forges in everyone's mind if they spend enough time in this place. Nothing is impossible. And if it is possible, then it has to happen here. I have not experienced this magic anywhere that I have been. The creativity and impact of MIT transforms people, and gives one the sense of empowerment to take this attitude and transform the world around us. Thank you MIT for caring about your students, for making such an impact in us, and for caring about the biggest problems that humanity faces. Thank you for this time.

Lastly I have to thank my whole family, for all the unconditional support and love throughout this journey: Tia Tere, Isiki, Sebas, Tate, Luis, Martin, Tio Pedro, Maria, Silvia, Tio Francisco, Mari Carmen, Raul, Raquel, and my grandparents Juan, Encarna,

Juan and Pilar. And of course, specially my parents Juan and Juana. I could not have completed this endeavor without them. I am truly thankful for all the support from my four grandparents, who are all still alive. All of my grandparents have been extremely supportive from of me, at all times. They have always been there for me, and have taught me some of the most important lessons in life. Those that you can only teach when you have lived long enough in this world. The unconditional love of my whole family has no limits. My parents have fought very hard in life to give me the best they could, from education and to the values the have instilled in me. I have to thank my parents for having done all of these efforts in life for me. Gracias papá y mamá.

Contents

1 Introduction to Controlled Thermonuclear Fusion, Tokamaks 49

1.1 Role of fusion in the energy scene. 49

1.2 Principles of fusion energy. 50

1.3 Tokamaks and the spherical tokamak (ST) 53

1.3.1 High bootstrap fraction: towards steady-state operation 55

1.3.2 The National Spherical Tokamak eXperiment (NSTX) 55

1.3.3 Spherical tokamak confinement 57

1.3.4 Validation of transport models 58

1.4 Brief summary of this thesis 61

2 Plasma Turbulence and Transport Background 65

2.1 Transport as a diffusive process 65

2.2 The drift wave mechanism 67

2.3 Drift-wave instabilities. 69

2.4 The gyrokinetic model 71

2.5 Core transport in conventional aspect ratio tokamaks. 74

2.6 Anomalous electron thermal transport in spherical tokamaks 75

2.7 The electron temperature gradient mode (ETG) 77

3 Introduction to validation and past validation work of turbulent transport in STs 83

3.1 Introduction to validation in magnetic confinement fusion research 84

3.1.1 Gaining predictive capability 84

3.1.2 Basic concepts 85

3.1.3 Importance of validating turbulent transport models 87
3.2 Review of past validation work of core transport turbulent models in STs 91
3.2.1 Validation efforts in NSTX 92
3.2.2 Validation efforts in MAST 102
3.2.3 Discussion of past validation work on the spherical tokamak and the context of this thesis 110

4 Analysis tools **115**
4.1 Experimental analysis 115
4.1.1 Setting up a PPPL account 115
4.1.2 Accessing NSTX diagnostic data 116
4.1.3 The high-k scattering diagnostic at NSTX 119
4.1.4 Ray tracing 122
4.1.5 Determination of experimental uncertainties 124
4.2 The GYRO code 130
4.2.1 Right-handed system of toroidal coordinates in GYRO (and CGYRO) 131
4.2.2 Linear GYRO simulation 132
4.2.3 Nonlinear GYRO simulation 134
4.2.4 GYRO simulation uncertainties 136
4.2.5 Accessing GYRO and accounts 136

5 Synthetic diagnostic for coherent scattering of density fluctuations **139**
5.1 Scattering as a diagnostic technique 140
5.1.1 Coherent vs. Incoherent scattering 141
5.1.2 Matching conditions and the Bragg condition 142
5.2 Theoretical considerations on density fluctuation measurements based on coherent scattering 144
5.3 Some geometry definitions 146
5.3.1 Wavenumber components in cylindrical coordinates 148
5.3.2 Flux Surface Shape 149
5.3.3 The scattering volume shape U 149
5.3.4 GYRO wavenumber mapping 151

5.4 Computation of the synthetic signal for coherent scattering turbulence measurements . . . 153
5.4.1 General 3D implementation . . . 154
5.4.2 2D, outboard midplane approximation . . . 156
5.5 Application to high-k scattering at NSTX . . . 159
5.5.1 Numerical resolution of nonlinear e- scale GYRO simulations . . 159
5.5.2 Radial and poloidal wavenumber resolution . . . 161
5.5.3 Mapping high-k wavenumbers to GYRO . . . 163
5.5.4 Raw electron-scale simulation spectra . . . 167
5.5.5 Synthetic frequency spectra . . . 170
5.5.6 Equivalence between the real-space and k-space synthetic spectra computed by GYRO . . . 172
5.5.7 Effect of Doppler shift . . . 172
5.5.8 Influence of the diagnostic resolution on the frequency spectrum . 177
5.6 Lessons learned from this chapter . . . 177

6 Validation of gyrokinetic simulations of NSTX H-mode plasma via multi-level hierarchy comparisons 181

6.1 Description of plasma conditions and linear stability . . . 182
6.2 Nonlinear gyrokinetic simulation setup . . . 187
6.3 Validation metrics . . . 188
6.4 Local transport comparisons via gyrokinetic simulation . . . 190
6.4.1 Strong ETG drive conditions . . . 191
6.4.2 Weak ETG drive conditions . . . 192
6.5 Synthetic diagnostic comparisons of high-k fluctuation spectra . . . 197
6.5.1 Frequency spectra comparisons . . . 197
6.5.2 Wavenumber spectra comparisons . . . 202
6.5.3 Validation metrics to quantify overall simulation fidelity . . . 205
6.5.4 Discussion on the metrics employed . . . 207
6.6 Summary of findings . . . 212

7 Discussion, conclusions and future work **215**

7.1 Summary of the main contributions of this thesis 215

7.1.1 Physics contributions 216

7.1.2 Synthetic diagnostic for high-k scattering 218

7.2 Discussion on the approximations performed 220

7.3 Next steps 223

A Basics of coherent scattering theory for density fluctuation measurements **227**

A.1 Scattered electric field from an ensemble of electrons 227

A.2 Computation of synthetic signal without the specification of geometry . . 231

A.3 Scattered power and spectral density 235

B Derivation of the wavenumber mapping to field-aligned geometry **243**

C Derivation of the scattering signal $\&$ comments on toroidal effects **249**

D List of Matlab routines used in this thesis **257**

D.1 Main Matlab routines used in this thesis 257

D.2 Figures generated in this thesis 260

D.2.1 Chapter 1 260

D.2.2 Chapter 4 260

D.2.3 Chapter 5 261

D.2.4 Chapter 6 263

E Experimental plasma parameters input in GYRO **265**

F Electron-scale and 'big-box' electron scale nonlinear simulation resolution tests. **267**

G Effect of ion-ion collisions on low-k turbulence at the weak ETG condition **273**

H Linear effect of β on ion-scale modes **279**

I Deployment of the synthetic diagnostic for Cyclone Base Case turbulence simulations **283**

I.0.1 Simulation setup 285
I.0.2 Numerical implementation of the synthetic diagnostic to circular filters with variable beam width a_0 285
I.0.3 Synthetic diagnostic with non-circular microwave beam widths . 291

List of Figures

1-1 Deuterium-Tritium fusion reaction. P and N stand for $proton$ and $neutron$ respectively. 50

1-2 a) Fusion reaction cross sections. b) Fusion reaction rates, averaged over a Maxwellian distribution function [2]. 51

1-3 Debye shielding effect in a plasma. Beyond the Debye length λ_D a test particle is shielded out. The Debye sphere denotes the volume of particles in the plasma that are sensitive to interact with a test particle. 52

1-4 **a)** Tokamak design concept, courtesy of [4]. **b)** Schematic representation of the geometry in a tokamak device. R_0 is the major radius and a is the minor radius. t denotes the toroidal direction and p the poloidal direction. 53

1-5 Comparison of conventional tokamak and spherical tokamak configurations (from [5]). B is the magnetic field direction and I_p the plasma current. By minimizing the time particles spend on the unstable part of the plasma (the outboard or low-field side), STs can stabilize magnetohydrodynamic instabilities as well as microinstabilities responsible for transport and confinement degradation. 54

1-6 **a)** NSTX device. **b)** Poloidal flux surfaces in a typical NSTX plasma: last closed flux surface (LCFS) in solid red, open flux surfaces in dashed blue lines, closed flux surfaces in dashed red lines. These are also contours of constant pressure. The magnetic axis is a green dot. Courtesy of [5]. . . . 56

1-7 Original NSTX device capabilities as a first of a kind, ultra-low aspect ratio spherical torus (from [15]). Note the magnetic field has since then been increased to $B = 0.55$ T for NSTX, and will achieve 1 T for NSTX-U. The plasma current I_p is expecting a upgrade to 2 MA for NSTX-U. . . 57

2-1 Simple physical mechanism for the propagation of a stable drift wave. The toroidal direction is out of the board in this description. The poloidal direction corresponds to the y-axis, and the radial direction corresponds to the x-axis. 68

2-2 Simple picture of drift-wave instability mechanism in the presence of a background temperature gradient ∇T in an inhomogeneous magnetic field. The instability feedback mechanism takes place on the outboard side of tokamaks, where the temperature gradient ∇T is in the same direction as the gradient of the background magnetic field ∇B. On the inboard side, ∇T and ∇B have opposite signs and the instability mechanism is shut off. 70

2-3 Transformation from guiding-center R_s to gyro-center coordinates used in gyrokinetics to reduce the problem for a 6-dimensional one to a 5-dimensional one. Image taken from [96]. 73

2-4 Electron density fluctuation field at the outboard midplane, at a fixed toroidal location, and at a fixed time slice $t = t_0$ where ETG turbulence fluctuations were highly unstable $\delta n_e(R, Z, \varphi = 0, t = t_0)$. The electron density fluctuations exhibit poloidally thin and radially elongated structures, so-called streamers, that are responsible for the dominant transport losses of electron heat flux from ETG turbulence. 80

3-1 Figure illustrating the concepts of validation, verification and qualification of a physical model with respect to experiments. Image courtesy of [100]. 85

3-2 Figure illustrating the primacy hierarchy for particle transport, highly equivalent for thermal transport. Combination of the lowest level quantities ($\tilde{n}, \tilde{\phi}, ...$) combine to produce higher level quantities such as the wavenumber spectrum, transport fluxes and ultimately predicted profiles. Image courtesy of [99]. 89

3-3 Table highlighting some of the recent validation efforts carried out for the spherical tokamak, both in NSTX and MAST. References are categorized depending on the instability under study (ETG, MT, KBM, ITG/TEM, GAE/CAE/KAW) and also depending on the nature of the work performed: predictions, linear stability comparisons, nonlinear transport comparisons and synthetic comparisons. The scope of this thesis is indicated by the reference **Ruiz-Ruiz MIT 2019**. 111

3-4 Diagrams showing main instabilities present for outer-core ($r/a \sim 0.6$-0.7) of NSTX H-modes for different local parameters β_e, ν^{ei}, $\beta_e \cdot a/L_{Te}$, $\alpha_{\text{MHD, unit}}$, a/L_{Te}-$a/L_{Te,\text{crit}}$, γ_E. The proper definitions of each local value are defined in [136]. Image is courtesy of [136], it has been modified with the blue and green stars from NSTX shot 141767, analyzed in this thesis. 114

4-1 **a)** View from the top of the old high-k scattering diagnostic at NSTX. **b)**. 3D view of the propagation trajectory of the incident probe and scattered rays corresponding to channel 1. The black dot denotes the scattering location. Trajectories are computed by ray tracing calculations, section 4.1.4. 121

4-2 $a)$ Spectrogram of high-k density fluctuations from channels 1, 2 and 3 of shot 141767 of the high-k scattering system at NSTX. $b)$ Frequency spectrum of fluctuations corresponding to times as shown on $a)$ by vertical color lines from channel 1. Note $b)$ are simply time slices of channel 1 at the vertical color lines. Each channel is sensitive to a different wavenumber $k_\perp \rho_s$ as is indicated in $a)$. 123

4-3 **a)** Ensemble of fits to the electron density profile from Thomson scattering $\{n_e\}_N$ generated via a Monte Carlo approach to compute the uncertainty in ∇n_e. The raw profile data is shown by the thick black line with associated error bars. Were generated a total of $N = 100$ fits. The average value of all fits is given by the thick blue line. **b)** Ensemble of electron density gradient fits, computed from a) via the radial derivative of each fit. The average value of all fits is given by the thick blue line. The standard deviation of all fits at a specific radial location r_i provides the experimental uncertainty $\sigma(\nabla n_e)$. 127

4-4 **a)** Real frequency of instability from linear GYRO simulations spanning ion and electron scales. **b)** Growth rate associated to the dominant instability. The linear spectra are computed for a highly unstable ETG regime of NSTX shot 141767 ($cf.$ chapter 6 for details). Ion-scale simulations model electrons by the drift-kinetic equation (DKe-) while electron-scale simulations have to model electron gyrokinetically (GKe-). All simulations model a deuterium main ion species and a carbon impurity gyrokinetically. 132

4-5 Schematic of the range of poloidal wavenumbers k_θ resolved by nonlinear GYRO simulations presented in this thesis: by ion-scale simulations $k_\theta \rho_s \lesssim 1$, standard electron-scale simualtions $k_\theta \rho_s \gtrsim 1$, and 'big-box' electron scale simulation $k_\theta \rho_s \gtrsim 0.3$-$0.4$. The measurement range of the high-k diagnostic is indicated in gray at $k_\theta \rho_s \sim [3\text{-}6]$. 135

4-6 Schematic of the radial profile of the electron thermal power P_e solved by nonlinear GYRO simulation, indicating the domain range covered by the different types nonlinear GYRO simulations performed in this thesis: ion-scale simulation (red), standard electron-scale simulation (blue), and 'big-box' e- scale simulation in magenta. The red peripheral regions denote the radial buffer regions for ion-scale simulation, with width $\Delta_b \sim 8\rho_s$. Buffer regions for electron-scale and big-box e- scale simulations are not shown. The high values of P_e from the ion-scale simulation are merely related to the highly unstable turbulence regime simulated. 135

4-7 Time evolution of the total electron thermal power P_e from a GYRO nonlinear gyrokinetic simulation resolving only electron-scale turbulence. The blue line denotes the average value of P_e, while the red line indicates the uncertainty associated to P_e computed by the standard deviation of the time series $P_e(t)$. 137

5-1 **a)** View from the top of the old NSTX high-k scattering diagnostic. **b)** Schematic of the incident $\vec{k}_i$, scattered $\vec{k}_s$ and plasma wave-vector $\vec{k}_+$, corresponding to a conservation law of type $\vec{k}_+ = \vec{k}_s - \vec{k}_i$. The incident beam of radiation has a $1/e^2$ radius of a_0. The intersecting volume between the incident and the scattered beams is called the scattering volume V_s. 143

5-2 **a)** Cylindrical coordinates (R, Z, φ) used to express density fluctuations amplitudes $\delta n(\vec{r}, t)$ for deployment of synthetic diagnostic in real space. **b)** Definitions of wavenumber $\vec{k}_+$ components in cartesian coordinates $(k_x, k_y, k_z)_+$ and in cylindrical coordinates $(k_R, k_Z, \varphi_k)_+$. Due to axisymmetry I assume a scattering location at $\varphi_0 = 0$. 146

5-3 **a)** Circular wavenumber filter shape in $(k_x, k_z)_+$ corresponding to a circularly shaped scattering volume U in (R, Z), for a fixed toroidal slice $\varphi_0 = 0$. This shape is characteristic of the old tangential scattering diagnostic at NSTX [65]. The dot indicates the dominant measurement wavenumber $(k_x, k_z) = (500, 1)$ m^{-1}. The circles indicate the $1/e$, $1/e^2$ and $1/e^3$ amplitude of the filter k-space filter I in (k_x, k_z) ($cf.$ equation 5.4). **b)** Colored dots are mapped wavenumbers in $(k_r\rho_s, k_\theta\rho_s)$ corresponding to a measurement of $(k_x, k_z)_+ = (500, 1)$ m^{-1} for different poloidal locations along the flux surface. The ellipses surrounding each mapped wavenumber denote the $1/e$ amplitude of the scattering matrix U_{np} corresponding to the different poloidal locations along the flux surface. **c)** Poloidal locations θ_0 along the flux surface used to compute the mapped wavenumbers and $1/e$ filter amplitudes of b). The yellow star corresponds to the experimental location of scattering analyzed in this article with poloidal angle $\theta_0 \approx$ -4^o. The flux-surface geometry is taken from a NSTX H-mode plasma shot. 153

5-4 (k_r, k_θ) grid for a standard electron-scale simulation having a conventional simulation domain $(L_r, L_\theta) = (4.5, 4)\rho_s$ (left) and an electron-scale simulation with increased numerical domain $(L_r, L_\theta) = (20, 20.6)\rho_s$ (right) along with the measurement range of channel 1, 2 and 3 of the old NSTX high-k scattering system [65]. The ellipses denote the $1/e$ amplitude of the wavenumber filters in k-space, essentially the wavenumber resolution from each diagnostic channel. Simulation wavenumbers inside the ellipses will effectively contribute to the synthetic signal. **a)** Electron-scale simulation with standard simulation domain does not well resolve the measurement wavenumbers from the high-k diagnostic due to a coarse (k_r, k_θ)-grid. **b)** Electron-scale simulation with increased simulation domain is needed to accurately resolve the measurement wavenumbers from the old high-k scattering diagnostic. By resolving more (k_r, k_θ)-modes than a standard electron-scale simulation, a bigger domain results in improved resolution in k-space down to ion-scale modes (note the k_θ simulation resolution is d$k_\theta \rho_s^{sim} \sim 0.3$). 162

5-5 **a)** Radial wavenumber filter corresponding to a measurement wavenumber component $k_{r+} \approx -2.57$. **b)** Poloidal wavenumber filter corresponding to a measurement wavenumber component $k_{\theta+} \approx -5.34$. The $(k_r, k_\theta)_+$ components correspond to scattering measurement from channel 1 of the high-k scattering system, from NSTX H-mode 141767. The gaussian shape of Ψ_{kr} and Ψ_{k_θ} stems from the gaussian shape of the scattering volume U in (R, Z) as in the past section ($cf.$ equation 5.9). In red are shown the filters using the numerical grids from a standard e- scale simulation domain $(L_r, L_\theta) = (4.5, 4)\rho_s$, and in blue from an e- scale simulation with a bigger simulation domain $(L_r, L_\theta) = (20, 20.6)\rho_s$. Notice the lack of resolution from using a standard simulation domain (red), especially in k_r, and the improved resolution when using a bigger simulation domain (blue), due to the finer k-grid resolution. The 'virtual' dashed line shows the theoretical gaussian expression of the filter. Note I chose $\Delta Z = 3$ cm (the experimental value) and $\Delta R = 1$ cm (reduced from the experimental ΔR = 3 cm due to the reduced simulation domain, even for the increased box size). The reduced ΔR in a local simulation only scales the fluctuation amplitude by a constant value of irrelevance in the current work. 164

5-6 **a)** and **b)** 2D raw electron density field δn mapped to cylindrical coordinates $(R, Z, \varphi_0 = 0)$, corresponding to an e- scale simulation with standard domain $(L_r, L_\theta) = (4.5, 4)\rho_s$ in $a)$, and increased simulation domain $(L_r, L_\theta) = (20, 20.6)\rho_s$ in $b)$. In **c)** and **d)** the 2D density field δn has been multiplied by the 2D real space filter $U(R\text{-}R_0, Z\text{-}Z_0)$, corresponding to an e- scale simulation with domain $(L_r, L_\theta) = (4.5, 4)\rho_s$ in $c)$, and an electron-scale simulation with increased numerical domain $(L_r, L_\theta) = (20, 20.6)\rho_s$ in $d)$. Since simulations are run in the local approximation, profile parameters are constant within the radial domain and the radial filter is chosen to be constant $= 1$. The poloidal filter shape is gaussian in θ and mapped to (R, Z), having maximum amplitude at the thick black line passing through $Z_0 \approx -0.06$ cm. The additional black dashed lines denote the $1/e, 1/e^2$ and $1/e^3$ amplitude of the filter in the poloidal direction. The filtered density fluctuations in $c)$ and $d)$ are intended to show the amplitude of the selected wavenumbers contributing to the high-k signal. All figures are shown at a fixed toroidal slice at φ_0. . 166

5-7 2D (k_r, k_θ)-spectrum of the electron density normalized per radial and poloidal wavenumber step d$k_r\rho_s$ and d$k_\theta\rho_s$, corresponding to a standard e- scale simulation in $a)(L_r, L_\theta) = (4.5, 4)\rho_s$ and to an e- scale simulation with increased simulation domain in $b)$ $(L_r, L_\theta) = (20, 20.6)\rho_s$. Black dots and ellipses correspond to the measurement k and k-resolution from 3 channels of the high-k diagnostic, also shown in figure 5-4. The improved resolution in k-space due to the increased box size makes a bigger domain more suitable for attempting quantitative comparisons between synthetic and experimental frequency spectra ($cf.$ chapter 7). Initially designed to be a high-k_r scattering system, the measurement wavenumbers detected by the high-k diagnostic are mapped to the internal flux-surface wavenumber definitions (k_r, k_θ) with a much smaller k_r than intuitively expected. This makes the old high-k diagnostic more relevant to ETG transport than initially thought. 167

5-8 **a)** Radial wavenumber spectrum of electron density fluctuations per radial wavenumber step d$k_r\rho_s$, computed by adding all $k_\theta < 0$ contributions from $S(k_r, k_\theta)$. Since k_r changes sign, the $k_r > 0$ and $k_r < 0$ branches are plotted, as indicated. Since the detected k_θ by the high-k scattering system is negative ($cf.$ figure 5-7), adding only $k_\theta < 0$ contributions exalts the difference between measuring in the higher and lower k_r part of the spectrum (here the detected k is also $k_r < 0$). **b)** Poloidal wavenumber spectrum of electron density fluctuations per poloidal wavenumber step d$k_\theta\rho_s$, computed by adding all k_r contributions from $S(k_r, k_\theta)$ (both $k_r > 0$ and $k_r < 0$). Due to the logarithmic scale and the symmetry property in δn_{np}, k_θ should be interpreted as having a negative sign $k_\theta < 0$. The measurement k_θ from channels 1, 2 and 3 are plotted as vertical lines in each figure. An e- scale simulation with a standard domain (red) shows very similar spectra as the simulation with an increased domain $(L_r, L_\theta) = (20, 20.6)\rho_s$ (blue), providing confidence that the resolved physics are very similar between the two simulations models. . . 169

5-9 Synthetic frequency power spectrum of fluctuations $S(\vec{k}_+, \omega)$ corresponding to a filtered wavenumber $\vec{k}_+$ from channel 1 of the high-k scattering system. In red the synthetic spectrum corresponds to an e- scale simulation with standard domain, and in blue to a big-box e- scale simulation with a increased domain necessary for accurate deployment of synthetic diagnostic. Both spectra look qualitatively similar, however a standard e- scale simulation exhibits a 'double-peak' structure, not present when using the increased simulation domain. This can be explained by the reduced number of sampled modes by the synthetic diagnostic when applied to a small simulation domain ($cf.$ figure 5-4.a)): the two peaks in the red curve are shown to correspond to the two dominant toroidal mode numbers within the measurement k-range ($n_+ =$ -270, -360 where n_+ is the sampled mode number). Each mode has its own propagation frequency in the lab-frame and is Doppler-shifted by a different amount ($\omega_{Dop} = \vec{k}_+ \cdot \vec{v} \sim n_+\omega_0$, where ω_0 is the plasma toroidal rotation frequency), which results in a separation of spectral peaks in the frequency spectrum. This phenomenon is not present when using an increased simulation domain (blue curve) due to the increased number of sampled modes. This last point also contributes to a widening of the spectrum with respect to the reduced simulation domain. The differences between both spectra is quantified in table 5.2. 171

5-10 Synthetic frequency power spectrum of fluctuations $S(\vec{k}_+, \omega)$ corresponding to a filtered wavenumber $\vec{k}_+$ from channel 1 of the high-k scattering system. Simulations use a big numerical domain $(L_r, L_\theta) = (20, 20.6)\rho_s$. The real-space filtering method (dashed line) is compared to the k-space filtering method (continuous line). Great agreement is obtained between the two methods of implementing a synthetic high-k diagnostic, within 15% agreement in the total power P_{tot}, and an even improved agreement in the spectral peak $< \omega >$ and spectral width σ_ω. This agreement is not coincidental but is generally observed, and validates the implementation of both synthetic diagnostic methods in the context of realistic flux-surface geometries. 173

5-11 Synthetic frequency power spectrum of fluctuations $S(\vec{k}_+, \omega)$ corresponding to a filtered wavenumber $\vec{k}_+$ from channel 1 of the high-k scattering system. Simulations use a big numerical domain $(L_r, L_\theta) = (20, 20.6)\rho_s$. In gray is shown the frequency spectrum in the plasma-frame, to which no Doppler shift has been added. In blue is shown the frequency spectrum in the lab-frame, to which the experimental value of Doppler shift has been added. The Doppler shift frequency is at least $\times 10$ the plasma-frame frequency of fluctuations and completely dominates the frequency spectrum. The difference between the two spectra is quantified in table 5.3. 174

5-12 Synthetic frequency power spectrum of fluctuations $S_{k_{r+}}(k_\theta, \omega)$ in a)-b) and $S_{k_{\theta+}}(k_r, \omega)$ in c)-d), all computed from a big-box e- scale simulation $(L_r, L_\theta) = (20, 20.6)\rho_s$. Spectra in a) and b) have been filtered in k_r around the radial component k_{r+} corresponding to channel 1 of the high-k scattering system, where no Doppler shift is applied in a) and the experimental Doppler shift value applied in b). These (ω, k_θ)-plots show the impact of Doppler shift for different k_θ is primarily a shift in frequency ω for the different k_θ, namely $\omega \propto k_\theta \omega_0$ as expected. The black vertical band shows the measurement range in k_θ from channel 1 of the high-k system. In c) and d) the spectra $S_{k_{\theta+}}(k_r, \omega)$ have been filtered in k_θ around the poloidal-k component $k_{\theta+}$ corresponding to channel 1 of the high-k scattering system. Differently to the (ω, k_θ) spectra, the (ω, k_r)-spectra show that Doppler shift essentially produces a similar frequency shift for all k_r, also as expected for the present conditions. The black vertical band in c) and d) shows the measurement range in k_r from channel 1 of the high-k system, while the white dashed line denotes the $k_r = 0$ line. 176

5-13 Influence of the diagnostic resolution Δk_Z on the spectral width W_f, in the absence a) and presence of Doppler shift b). These figures show the spectral width W_f can be strongly affected by the wavenumber resolution of the diagnostic in combination to Doppler shift. 178

6-1 **a)** Plasma current time trace for NSTX shot 141767. The **Strong ETG drive time** (blue, t=398 ms) takes place during the flat-top phase right before the start of the controlled current ramp-down. The **Weak ETG drive time** (green, t=565ms) takes place after the current ramp-down during a different flat-top period. **b**) Radial profiles of electron temperature T_e and electron density n_e corresponding to the strong and weak ETG drive times. High-k scattering fluctuation data is available at the gray shaded region ($R \approx 135$ cm, $r/a \approx 0.7$). 183

6-2 **a)** Spectral density $S(f)$, or equivalently the frequency power spectrum of electron-scale turbulence fluctuations detected by channel 1 of the high-k scattering system. **b)** Wavenumber spectrum of fluctuations indicative of the total spectral power $S(k)$ from each high-k diagnostic channel. Here $k_\perp$ is defined as the perpendicular component of $\vec{k}_+$ with respect to the background magnetic field. The strong ETG condition is shown in blue while the weak ETG condition is shown in green. Since the high-k diagnostic is not absolutely calibrated, spectra are shown in arbitrary units. . . 184

6-3 GYRO linear simulation output at strong ETG conditions. **a)**. Real frequency ω_r of instability propagates marginally in the ion direction at low-k ($k_\theta \rho_s \lesssim 1$), and electron directed for $k_\theta \rho_s \gtrsim 1$. **b)** Linear growth rate γ of instability. Zooming on the low-k part of the spectrum shows that the maximum linear growth rate is smaller than the $E \times B$ shearing rate, suggesting the ion-scale instability might be suppressed in this condition (Waltz' rule [184]). 185

6-4 GYRO linear simulation output at weak ETG conditions for the base case (using experimental profile parameters as input). **a)**. Real frequency ω_r of instability propagates in the electron direction at low-k and electron-directed at high-k ($k_\theta \rho_s \gtrsim 10 - 30$). Note the ion directed mode for $1 \lesssim k_\theta \rho_s \lesssim 30$ transitions to the electron direction for $k_\theta \rho_s \gtrsim 30$. **b)** Linear growth rate γ of instability and the $E \times B$ shearing rate γ_E according to the Waltz definition [184]. Note how the linear growth rate at ion-scales is greater than γ_E for the most unstable modes, suggesting ion-scaled turbulence might not be fully suppressed in this condition. 186

6-5 **a)** Total thermal transport budget from experiment (TRANSP, black) along with GYRO simulations that use experimental value of ∇n as input, corresponding to the strong ETG drive condition. The magenta dot corresponds to the 'big-box' electron-scale simulation run for base experimental parameters. The purple square corresponds to 'big-box' electron-scale simulation with scaled (∇T) within 1-σ uncertainty in addition to -10% q and $+20\%\hat{s}$. **b)** GYRO simulations have scaled ∇n by 1-σ to maximize turbulence drive ($-\sigma(\nabla n)$). Black dot corresponds to 'big-box' electron-scale scale simulation scanning $(\nabla T, \nabla n)$ within uncertainty. Green diamond scans (∇n) within uncertainty, -10% q and $+20\%\hat{s}$. Dark green cross scans $(\nabla T, \nabla n)$ within uncertainty, -$10\%q$ and $+20\%\hat{s}$. These simulations show that ion-scale turbulence is stabilized by $E \times B$ shear and electron scale turbulence can explain the experimental electron thermal transport levels within small variations in the input drive terms. 193

6-6 **a)** Total thermal transport budget from experiment (TRANSP, black) along with GYRO simulations that use the experimental value of ∇n as input, corresponding to the weak ETG drive condition. **b)** GYRO simulations with scaled ∇n by 1-σ to maximize turbulence drive ($-\sigma(\nabla n)$). Note the significant increase in stiffness predicted from electron-scale turbulence (blue) and especially ion-scale turbulence (red) when ∇n is scaled by 1-σ. 194

6-7 Total thermal power on the electron and ion channel (P_e and P_i respectively) as a function of driving mechanism a/L_{Te} for the weak ETG drive condition. The density gradient scale length value a/L_{ne} in the simulations presented in this figure has been scaled by 1-σ of the experimental uncertainty. Note the great increase in predicted P_e and P_i for $a/L_{Te} \sim 5$, displaying large stiffness from a highly unstable TEM branch. 196

6-8 Frequency spectrum of high-k fluctuations from channels 1, 2 and 3 and synthetic frequency spectrum corresponding to flux-matched (P_e) simulations. Synthetic spectra includes Doppler shift. For the strong ETG case spectra are computed from the $\sigma(\nabla n), q, \hat{s}$-scan simulation (purple square in figure 6-5.a)), while the weak ETG spectra use the $\sigma(\nabla T, \nabla n)$-scan simulation (magenta dot in figure 6-6.b)). Experiment and simulation are plotted with the same color code, blue for the strong ETG condition and green for the weak ETG condition. 198

6-9 Synthetic frequency spectrum of high-k fluctuations from channel 1, respectively for 5 strong ETG 'big-box' electron-scale simulations in a) and 2 simulations for the weak ETG condition in b). The synthetic spectra was computed in the absence of Doppler shift ($\omega_0 = 0$), showing that the average plasma-frame propagation frequency of fluctuations $< f >_{\omega_0=0}$ is ~ 10 smaller than the experimentally measured value, suggesting the Doppler shift completely dominates the frequency spectrum. Surprisingly, the spectral width W_f exhibits very similar values for all 7 simulations, in spite of the fact that simulations span 5 orders of magnitude in spectral power. This suggests that the spectral width is not sensitive to the plasma turbulence conditions, but is mainly determined by the specific characteristics of the measurement (detected wavenumber $\vec{k}_+$ and diagnostic resolution Δk, implemented here via the synthetic diagnostic) and not by the intrinsic plasma-frame turbulence conditions. This figure shows how neither the spectral peak $< f >$ nor the spectral width W_f provide reliable metrics to discriminate against the different turbulent models with varying drive terms. 201

6-10 Wavenumber spectra shape comparisons for the strong ETG condition. Experimentally detected high-k fluctuations by the high-k system are shown by blue circles. Synthetic turbulence fluctuations correspond to the 5 'big-box' electron-scale-scale simulations in figures 6-5.a) and b). The total synthetic fluctuation power is scaled (only in this plot) to minimize distance with respect to experimental fluctuation levels, allowing accurate comparisons of the wavenumber spectra shape. **a)** 'big-box' electron-scale simulation run for experimental base values of electron temperature and density gradient. **b)** Scaled 'big-box' electron-scale simulation by temperature and density gradient within 1-σ uncertainty. **c)** Flux-matched 'big-box' electron-scale simulation run with scaled temperature gradient within 1-σ uncertainty and an additional -10% in safety factor q and $+20\%$ in magnetic shear $\hat{s}$. **d)** Flux-matched 'big-box' electron-scale simulation run with scaled density gradient within 1-σ uncertainty and an additional -10% in safety factor q and $+20\%$ in magnetic shear $\hat{s}$. **e)** Scaled 'big-box' electron-scale simulation by temperature and density gradient within 1-σ uncertainty and an additional -10% in safety factor q and $+20\%$ in magnetic shear $\hat{s}$. 203

6-11 **a)** Absolute fluctuation power $S(k)^{\text{syn}}$ (wavenumber spectrum) from 'big-box' electron-scale-scale simulation carried for the strong ETG condition. Combinations of input drive terms correspond to the same simulations in figure 6-10 (here the synthetic k-spectrum has not been scaled but has absolute units). **b)** Synthetic fluctuation level ratio between strong ETG and weak ETG conditions. In computing the synthetic fluctuation level ratio $[\langle S\rangle^{\text{strong ETG}}/\langle S\rangle^{\text{weak ETG}}]^{\text{syn}}$, the strong ETG fluctuation power levels correspond to 'big-box' electron-scale simulations from a), while the weak ETG fluctuation power levels are computed from the same simulation for all comparisons in b), corresponding to the flux-matching weak ETG 'big-box' electron-scale simulation (magenta dot in figure 6-6). The gray band denotes the experimental fluctuation power level ratio between the strong and weak ETG conditions, with value of $\sim 14.7 \pm 80\%$. Simulations with scaled $(\nabla T, \nabla n)$ and $(\nabla T), q, \hat{s}$ lie within the 1-σ experimental range of the fluctuation level ratio. 204

6-12 Wavenumber spectra comparisons between experimental spectra and synthetically generated spectra from flux-matched (P_e) simulations, both for the strong and weak ETG conditions. The strong ETG synthetic spectra are generated from the $\sigma(\nabla n), q, \hat{s}$-scan simulation that predicts $P_e^{sim} \approx 95\%\ P_e^{exp}$, and correspond to the frequency spectra in figure 6-8, also producing a best match in the validation metric comparisons (table 6.5). The experimental strong ETG k-spectrum is scaled in order to minimize the 'distance' with the synthetic k-spectra. The weak ETG experimental k-spectra are scaled by the same constant in order to preserve the fluctuation level ratio. The weak ETG simulation spectrum corresponds to a 'big-box' electron-scale simulation that matches P_e within experimental uncertainty ($P_e^{sim} \approx 80\%\ P_e^{exp}$). These results give strong evidence suggesting ETG fluctuations alone may be the main mechanism driving electron thermal transport in both the strong and weak ETG conditions. . 207

6-13 Metric $\mathbf{R_X} \epsilon [0,1]$ as a function of the validation distance $\mathbf{d_X}$ corresponding to the parameters $d_0 = 1.5$ and $\lambda = 0.5$. In this plot the experimental and simulation uncertainties are given the same value σ. 209

6-14 Validation metrics $R_{\text{Pe}}, R_{\text{ratio}}, R_{\text{shape}} \epsilon[0,1]$ as a function of the distance $d_{\text{Pe}}, d_{\text{ratio}}, d_{\text{shape}}$ for the five 'big-box' electron-scale simulations for the strong ETG of interest in this thesis. 210

A-1 Scattering geometry 229

A-2 Schematic of incident $\mathbf{k}_i$, scattered $\mathbf{k}_s$ and plasma wave-vector $\mathbf{k}_+$, corresponding to a conservation law of type $\mathbf{k}_+ = \mathbf{k}_s - \mathbf{k}_i$. The incident beam of radiation has a $1/e^2$ radius of a_0. The intersecting volume between the incident and the scattered beams is called the scattering volume V_s. 230

A-3 Schematic of incident beam propagating in the $\hat{i}$ direction (z'). The x' and y' directions are perpendicular to the incident microwave beam. The incident beam of radiation has a $1/e^2$ radius of a_0. 237

A-4 Time axis showing schematic of time average during detection of scattered power from plasma density fluctuations. Fast time scales associated to EM wave propagation at ω_i are averaged out during detection, while slow time scales associated to plasma turbulence fluctuations δn_{u} are well preserved during measurement. 239

B-1 **a)** Cylindrical coordinates (R, Z, φ) used to express density fluctuations amplitudes $\delta n(\vec{r}, t)$ for deployment of synthetic diagnostic in real space. **b)** Definitions of wavenumber $\vec{k}_+$ components in cartesian coordinates $(k_x, k_y, k_z)_+$ and in cylindrical coordinates $(k_R, k_Z, \varphi_k)_+$. Due to axisymmetry we assume a scattering location at $\varphi_0 = 0$. 244

C-1 **a)** Shape of toroidal mode number filter Ψ_{n^φ} for different toroidal length values $R_0\Delta\varphi$ of the scattering volume. **b)** Comparison of toroidal mode number filters Ψ_{n^φ} and Ψ_{n^θ}. **c)** Comparison of the total effect of a varying toroidal length of the scattering volume $R_0\Delta\varphi$ on the total product toroidal mode number dependence of the scattering matrix U_{np}, given by the product $\Psi_{n^\varphi} \times \Psi_{n^\theta}$. 255

F-1 Radial and poloidal box-size convergence tests carried out for three different radial and poloidal box-size domains, corresponding to electron and hybrid simulations for the strong ETG condition (experimental profile parameters were used as input). **a)** Radial box-size convergence tests: electron thermal power P_e is plotted versus normalized minor radius r/a for standard electron-scale simulations ($L_r = 4.5, 7\rho_s$) and hybrid scale simulation ($L_r = 20\rho_s$). Similar electron thermal power is predicted for simulations with $L_r = 4.5\rho_s$ and $7\rho_s$, and a slight decrease of $\sim 10-15\%$ is observed when the radial box size is increased to $L_r = 20\rho_s$. Although this small decrease might be related to the impact of ion-scale modes associated to the larger box-size, or the shorter simulation time in the larger box-size due to limited computational resources ($T \sim 20$ a/c$_s$), we note however that this small difference lies well inside the simulation standard deviation, indicating convergence in radial box-size (note the error bars in the nearby blue and magenta dots of figure 6-5.a) corresponding to the black and red curves in this plot). The GYRO buffer regions are not included in the calculation of the radial box-size. **b)** Poloidal box-size convergence tests: the fractional electron heat flux ΔQ_e per poloidal wavenumber increment $\Delta k_\theta \rho_s$ is plotted versus normalized poloidal wavenumber $k_\theta \rho_s$ for standard electron-scale simulations ($L_\theta = 4, 6.6\rho_s$) and hybrid scale simulation ($L_\theta = 20.6\rho_s$). A larger box-size is inversely proportional to the poloidal wavenumber increment $\Delta k_\theta \rho_s$. All simulations resolve up to $k_\theta \rho_s^{max} \sim 65$. A very similar k_θ spectrum is obtained for all simulations, in addition to similar predicted electron thermal power ($10 - 15\%$ agreement lying within the numerical standard deviation). We conclude convergence in poloidal box-size. The blue and magenta curves correspond to the nearby blue and magenta simulation points in figure 6-5.a). The hybrid scale simulation with the larger box-size consumed over $1M$ CPU h for completion NERSC's Edison supercomputer. 269

F-2 Radial resolution tests for 5 different radial grid steps $\Delta r/\rho_e$ of electron scale simulations for the strong ETG condition (experimental profile parameters were used as input). **a)** P_e[MW] is shown over the full radial domain, showing very close P_e agreement between all simulation predictions. **b)** Radial wavenumber power spectrum associated to potential fluctuations $|\delta\phi|^2$. The field $\delta\phi$ exhibits the largest amplitude among all electromagnetic field components ($\delta\phi, \delta A_{||}, \delta B_{||}$), and is responsible for the dominant contribution to electron heat transport P_e by some ~ 2 orders of magnitude over contributions from shear $\delta A_{||}$ and compressional perturbations $\delta B_{||}$. All simulation resolution scans presented here are carried out on standard electron scale simulations with box-sizes $(L_r, L_\theta) = (4.5, 4)\rho_s$. 270

F-3 Poloidal resolution tests for 3 different values of the maximum $k_\theta\rho_s$ resolved in electron scale simulations for the strong ETG condition (experimental profile parameters were used as input). Simulation resolving a maximum $\max(k_\theta\rho_s) = 43$ exhibits reduced total electron thermal power (up to 30% reduction) and noticeably different spectral slope at high-k with respect to simulations with $\max(k_\theta\rho_s) = 65, 87$. Note however how negligible differences can be observed between simulations resolving $\max(k_\theta\rho_s) = 65$ $vs.$ $\max(k_\theta\rho_s) = 87$. This last point gives us confidence that simulation is converged for $\max(k_\theta\rho_s) = 65$. Consequently hybrid scale simulations for the strong ETG case will resolve a maximum poloidal wavenumber of 65. 271

G-1 **a)** Electron thermal power from ion-scale simulation run with scaled density gradient value within 1σ uncertainty, for different values of electron temperature gradient a/L_{Te}. In red is shown simulation output when the value of ion-ion collision frequency ν_{ii} was set to 0. In magenta is shown simulation output when the value of ion-ion collision frequency was set to the experimental value $\nu_{ii} = \nu_{ii}^{exp}$ was set to 0. **b**) Same as a) but showing the ion thermal power P_i instead of the electron thermal power P_e. 274

G-2 Time traces of the electromagnetic field r.m.s. fluctuation amplitudes $(\phi, A_{||}, B_{||})$ for the turbulence $(\sum n > 0)$ and zonal flow $(n = 0)$, corresponding to simulations **A**, **B**, **C**, **D**, **E** and **F** in figure G-1. All simulations were run with a scaled value of a/L_{ne} within 1-σ uncertainty. **a)** Simulation was run using $a/L_{Te} = 4.5$. **b)** Simulation was run using $a/L_{Te} = 4.8$. **c)** Simulation was using $a/L_{Te} = 5.4$. 276

G-3 Time traces of electromagnetic field r.m.s. fluctuation amplitudes $(\phi, A_{||}, B_{||})$, similar to figure G-2, but this time carried out for the nominal, experimental profile values (in particular, experimental a/L_{ne} and a/L_{Te}). **a)** The simulation is started at $t = 0$ a/c$_s$ using ion-ion collision frequency set to 0 ($\nu_{ii,ZF} = 0$). **b)** The simulation is started at $t = 0$ a/c$_s$ using ion-ion collision frequency set to the experimental value ($\nu_{ii,ZF} = \nu_{ii}^{exp}$). 277

H-1 **a)** Real frequency from a linear beta scan for $k_\theta \rho_s = 0.48$ for the strong ETG condition. **b**) Corresponding linear growth rate from a linear beta scan for $k_\theta \rho_s = 0.48$. 280

H-2 **a)** Real frequency from a linear beta scan for $k_\theta \rho_s = 0.48$ for the weak ETG condition. **b**) Corresponding linear growth rate from a linear beta scan for $k_\theta \rho_s = 0.48$. 281

I-1 Density fluctuation amplitude plotted in real space for the same numerical simulation, using three distinct beam widths. **a)** $a_0 = 5$ cm, beam width fits fully within the simulation domain. **b)** $a_0 = 10$ cm, beam width up to $1/e^2$ amplitude fits within the simulation domain. **c)** $a_0 = 20$ cm, beam width has significant portion outside the simulation domain. We are interested in applying a synthetic diagnostic to the last case to understand validity of using future synthetic diagnostics with reduced simulation domain, in views of saving computing time by reducing simulation domain. 286

I-2 **a), b), c)** show the wavenumber simulation grid along with the $1/e, 1/e^2$ and $1/e^3$ wavenumber filter amplitudes for $a_0 = 5, 10$ and 20 cm. **d), e), f)** show the wavenumber filters plotted along with the $1/e, 1/e^2$ and $1/e^3$ wavenumber filter amplitudes for $a_0 = 5, 10$ and 20 cm. Note how the $1/e$ amplitude shape of the wavenumber filters in (k_r, k_θ) preserves the circular nature of the filter in real space (Fig. I-1), due to the simplified circular, non-shifted flux surface geometry of the CBC. 287

I-3 1D filters in wavenumber space. **a)**, **b)**, **c)** show the k_r-filter Ψ_{k_r} corresponding to the beam widths $a_0 = 5, 10, 20$ cm. **d)**, **e)**, **f)** show the k_θ-filter Ψ_{k_θ} for beam widths $a_0 = 5, 10, 20$ cm. Note how the radial and poloidal wavenumber filters lose resolution for wider beam widths a_0. The $a_0 = 20$ cm case (**c**, **f**), although laking spectral resolution, will be proven good enough to obtain a quantitative comparison with the synthetic diagnostic. 288

I-4 Spectral measurement range in the GYRO (k_r, k_θ) space. Probed wavenumber $(k_r, k_\theta)_+$ lies close to the spectral peak of ion-scale fluctuations in k-space (electron scale turbulence was not simulated in this case). 289

I-5 Spectral measurement range in k_θ. The spectral density in k_θ is obtained by integration (sum) of $S(k_r, k_\theta, t_0)$ along the k_r component $S(k_\theta, t_0) = \sum_{k_r} S(k_r, k_\theta, t_0)$. 290

I-6 Synthetic power spectra applying both synthetic diagnostic methods to Cyclone Base Case, for different circular beam width parameters $a_0 = 5, 10, 20$ cm. The total fluctuation power from the real and wavenumber space filter lies within 15% for cases $a_0 = 5, 10$ cm. The case $a_0 = 20$ cm shows a factor of 3 discrepancy in total fluctuation power between the real space and wavenumber filters. This last case shows a circular beam that is bigger than the simulation domain. 291

I-7 Poloidal cross section of the density fluctuation amplitude $\delta n/n_0$, plotted along with the $1/e$ amplitude shape of the real space filters. **a)** shows a scan in the radial dimension of the beam $\Delta R = \{2.5, 5, 10, 20, 40\}$ cm), keeping the vertical dimension fixed to $\Delta Z = 5$ cm. **b)** shows a scan in the vertical dimension $\Delta Z = \{2.5, 5, 10, 20, 40\}$ cm, keeping $\Delta R = 5$ cm fixed. 292

I-8 Radial wavenumber filters Ψ_{k_r} corresponding to the different radial extent of the scattering volume $\Delta R = 2.5, 5, 10, 20, 40$ cm), for a fixed $\Delta Z = 5$ cm, as depicted in Figure I-7.**a)**. Note how the resolution is best at lowest value of dR (corresponding to highest value of Δk_r), and decreases as ΔR increases. Recall the relation $\Delta k_r = 2/\Delta R$ applicable to circular non-shifted flux-surface geometry. 294

I-9 Poloidal wavenumber filters Ψ_{k_θ} corresponding to the different radial extent of the scattering volume $\Delta Z = 2.5, 5, 10, 20, 40$ cm), for a fixed $\Delta R = 5$ cm, as depicted in Figure I-7.**b)**. Note how the resolution is best at lowest value of dZ (corresponding to highest value of Δk_θ), and decreases as ΔZ increases. Recall the relation $\Delta k_\theta = 2/\Delta Z$ applicable to circular non-shifted flux-surface geometry. 294

I-10 Total synthetic fluctuation power resulting from application of both synthetic diagnostic methods (real space vs. k-space) to the Cyclone Base Case. **a)** shows the result of a scan in the radial dimension ΔR, showing a quadratic dependency of P_{tot} with ΔR. **b)** shows the result of a scan in the vertical dimension ΔZ. The dashed lines show a quadratic fit $P_{tot} \propto (\Delta R)^2, (\Delta Z)^2$. For values $\Delta R, \Delta Z = 20, 40$ cm, the real space filter ceases to follow the quadratic dependence since it exceeds the simulation domain. For these cases, we rescale P_{tot} by the total beam area missing in the simulation domain (red squares) brings it to agreement with respect to the k-space filter. 296

List of Tables

5.1 Numerical resolution parameters typical of a standard electron-scale simulation and with an increased simulation box: dr radial resolution (ρ_s, ρ_e are respectively the ion and electron sound gyro-radius using electron temperature T_e), $L_r[p_s]$ radial box size, n_r number of radial modes, max$(k_r\rho_s)$ maximum resolved radial wavenumber, $L_\theta[\rho_s]$ poloidal box size, d$k_\theta\rho_s$ poloidal wavenumber resolution, max$(k_\theta\rho_s)$ maximum resolved poloidal wavenumber, n_n number of toroidal modes, T simulation run time, dt simulation time step. Both simulation models resolve purely electron-scale modes. Although a 'big-box' e- scale simulation does simulate ion modes ($k_\theta\rho_s < 1$ due to a diagnostic requirement, $cf.$ figure 5-4), the ion-scale turbulence spectrum is not adequately resolved, neither spatially (would need $L_r \gtrsim 70\rho_s$, $dk_\theta\rho_s \sim 0.05$-$0.1$ as in ion-scale simulation) nor temporally (would need $T^{sim} \gtrsim 200$ a/c$_s$ for ion-scale turbulence to reach a fully saturated state). Accurately simulating both ion and electron-scale turbulence would require multiscale simulation such as shown in [72–74, 74, 76], which is out of the scope of this work. 160

5.2 Values for the total scattered power P_{tot}, spectral peak $< \omega > [c_s/a]$ and spectral width $\sigma_\omega[c_s/a]$ corresponding to synthetic frequency spectra from figure 5-9. Similar values of the total power P_{tot} and spectral peak $< \omega >$ are obtained between the two simulation models (standard e- scale simulation domain $vs.$ big-box e- scale simulation domain). The spectral width is wider for the simulation using a larger simulation domain, due to the increased number of sampled modes contributing to the synthetic signal ($cf.$ figure 5-4), contributing to a widening of the spectrum. The values of P_{tot}, $< \omega >$ and σ_ω are computed by fitting a gaussian profile to the turbulence spectrum and extracting the characteristic gaussian parameters (more details in appendix). 171

5.3 Values for the total scattered power P_{tot}, spectral peak $< \omega > [c_s/a]$ and spectral width $\sigma_\omega[c_s/a]$ corresponding to synthetic frequency spectra from figure 5-11, showing the impact of Doppler shift on the frequency spectrum (M here is Mach number). Similar values of the total power P_{tot} and spectral peak σ_ω are obtained between the two simulation models, but the spectral peak is completely different: fluctuations propagate in the e-diamagnetic direction in the plasma frame ($\omega > 0$ for GYRO), but are shifted to the ion diamagnetic drift direction by Doppler shift. This is an important assessment towards the understanding of the measurement spectra from high-k scattering. 174

6.1 Same as table 5.1, but this time including resolution parameters from ion-scale simulation. 188

6.2 Table summarizing the sensitivity scans performed using 'big-box' electron-scale simulation for the strong ETG case, including the value of the drive terms scanned ($a/L_{Te}, a/L_{ne}, q, \hat{s}$) used in the input, as well as the predicted value of the electron thermal power with respect to the experimental level P_e^{sim}/P_e^{exp}. 192

6.3 Frequency spectra comparisons for the strong ETG condition corresponding to the frequency spectra in figure 6-8 (blue curves). The spectral peak $< f >$ and spectral width W_f are compared between experimental high-k measurements and synthetic predictions, shown for the three operating channels of the high-k diagnostic (in [MHz]). Remarkable agreement is obtained in the spectral peak $< f >$ for all channels, a confirmation of the Doppler shift dependence of the synthetic signal and of the correct wavenumber sampled by the high-k diagnostic (recall the Doppler shift frequency f_D is proportional to the measurement k). Good agreement is also found for the spectral width in this condition, lying within $\sim 20\%$ of the experimentally detected value for all channels. 198

6.4 Frequency spectra comparisons for the weak ETG condition corresponding to the frequency spectra in figure 6-8 (green curves). The spectral peak $< f >$ and spectral width W_f are compared between experimental high-k measurements and synthetic predictions, shown for the three operating channels of the high-k diagnostic (in [MHz]). The uncertainty in $< f >$ and W_f is estimated to be $\sim$ 20-25% computed by varying the prescribed frequency window size. Remarkable agreement is obtained in the spectral peak $< f >$ for all channels. However the spectral width tends to be slightly underpredicted by the synthetic diagnostic (up to 40-50%). This could be due to the reduced signal to noise ratio in this condition, possibly providing an unreliable measure of the spectral width. Alternatively it could be that the discreteness in the simulated turbulence or a missing physics process not being modeled are resulting in a reduced spectral width prediction. 199

6.5 Validation table with the most relevant metrics allowing accurate discrimination between models: the electron thermal power $\mathbf{P_e}$, the electron-scale fluctuation level ratio and the k-spectrum shape. Comparisons are only made for the 5 'big-box' electron-scale-scale simulations in the strong ETG case in figure 6-5. To compute the fluctuation level ratio between the strong and weak ETG conditions, I used the flux-matching 'big-box' electron-scale-scale simulation for the weak ETG case (magenta dot in figure 6-6). The parameters $\mathbf{d_X}$ denote a validation 'distance' for the comparison of each observable $\mathbf{X}$, while $\mathbf{R_X}$ denotes the corresponding bounded error metric between 0 and 1 and computed from $\mathbf{d_X}$. The composite metric $\mathbf{M_1}$ quantifies the overall model agreement, with 0 indicating perfect agreement and 1 indicating complete disagreement. Definitions for $\mathbf{d_X}$, $\mathbf{R_X}$ and $\mathbf{M_1}$ are taken from [101, 103]. 206

6.6 Validation table comparing the five simulations of interest in this chapter using different definitions of validation metrics. $\mathbf{M_0} = \sum_i R_i/3$ where the sum is over the number of comparisons (=3). $\mathbf{M_1} = \sum_i h_i R_i/h_i$ with $h_i = 0.5$ for $\mathbf{P_e}$ and $h_i = 1$ for $\mathbf{ratio}$ and $\mathbf{shape}$. $\mathbf{M_2} = \sum_i h_i S_i R_i/h_i S_i$ where $S_i = \exp(-\sigma(\mathbf{X^{exp}})/\mathbf{X^{exp}})$. Overall very similar conclusions are taken from all three metrics: the best agreement is found for simulations with scaled $\sigma(\nabla T), q, \hat{s}$ and $\sigma(\nabla n), q, \hat{s}$, while the worst is for $\sigma(\nabla T, \nabla n), q, \hat{s}$ closely followed by the Base simulation. 211

E.1 Plasma parameters input in GYRO simulations presented in this work. . . 266

Chapter 1

Introduction to Controlled Thermonuclear Fusion, Tokamaks

1.1 Role of fusion in the energy scene.

The ultimate goal of controlled thermonuclear fusion is the production of energy. In a world with a continuously increasing population and electricity demands, and in the midst of a global warming era, magnetic confinement fusion energy is probably the most promising solution able to realistically tackle the problems of future of world electricity supply and climate change.

The main advantages of fusion are the fuel reserves, the impact on the environment and safety. The basic fuel for a fusion reaction are light elements, such as hydrogen (H) and its isotopes deuterium (D) and tritium (T). The earth's oceans are natural reservoirs of hydrogen and deuterium, containing infinite amounts from a practical viewpoint. Tritium is not naturally present on earth and can be obtained by breeding reactions with the Li^6 isotope. Geological estimates indicate that the natural abundance of the lithium-6 isotope on earth is sufficient for fusion energy to provide the base-load electricity supply for an order of a thousand years [1]. The environmental impact of fusion is practically inexistent since fusion reactions produce no greenhouse emissions. Fusion energy is also a safe nuclear energy source and will not give rise to a radioactive meltdown.

Fusion also faces disadvantages with respect to existing energy sources. Numerous

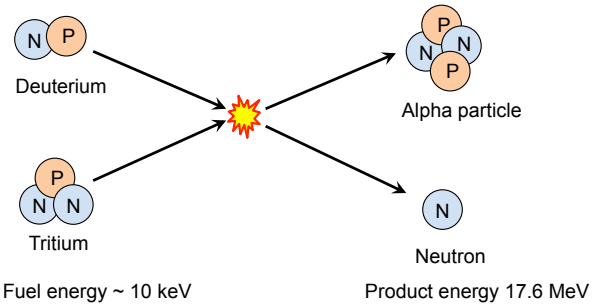

Figure 1-1: Deuterium-Tritium fusion reaction. P and N stand for $proton$ and $neutron$ respectively.

scientific challenges involving the physics of fusion plasmas have yet to find a solution, such as the control of a self-heated plasma, steady state operation, and the confinement of thermal particles and alpha particles. There are also technological challenges such as the plasma interaction with the materials and the problem of heat exhaust. Recent breakthroughs in the development of high-field superconducting magnets and structural materials able to sustain high mechanical strains in extreme temperature and radiation conditions could accelerate the development of fusion allowing for smaller, more cost-effective, compact reactors.

1.2 Principles of fusion energy.

Fusion is a form of nuclear energy and is the source of energy that powers the sun. In a fusion reaction, light elements (nuclei) merge together to form heavier nuclei. Through Einstein's formula, the mass difference between products and reactants provides an excess energy known as reaction yield $E_{reactants} - E_{products} = \Delta mc^2$. The main reaction considered for first generation fusion reactors is the deuterium-tritium (D-T) reaction, which produces an alpha particle (helium nucleus) and a high-energy neutron. In order for fusion reactions to occur, nuclei need to have sufficient energy to overcome the mutual repulsion from the Coulomb potential barrier. The minimum temperature for a D-T fusion reaction to occur is typically on the order of 10^8 K ($\sim$ 10 keV). In plasma physics and in this manuscript I use energy units for temperature ($k_B T \rightarrow T$). As a comparison, the D-T fusion reaction produces 17.6 MeV of energy, as shown in figure 1-1.

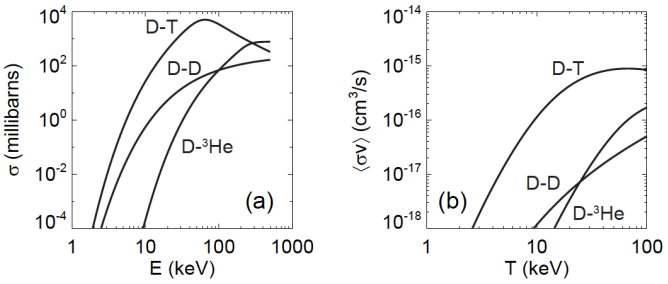

Figure 1-2: a) Fusion reaction cross sections. b) Fusion reaction rates, averaged over a Maxwellian distribution function [2].

Other fusion reactions such as deuterium-deuterium (D-D) and deuterium-helium 3 (D-He^3) could be considered for future generation fusion reactors. On figure 1-2 are compared to the fusion reaction rates and fusion cross sections of the D-T, D-D and D-He^3 reactions, which describe the quality or performance of a fusion reaction based on the probability of occurrance. For values of energy below about 100 keV ($\sim$ 1 billion degrees), the D-T reaction has the largest cross section and reaction rate, making it the primary candidate for first generation fusion reactors. However, as lithium reserves will become scarce on earth in the coming thousand years, alternate fusion reactions such as D-D or D-He^3 could become more interesting in the far future.

At fusion temperatures matter is in the state of plasma. Electrons are completely or partially disassociated from atomic nuclei, resulting in a soup of charged particles made of electrons and ions that we call *plasma*. Charged particles in the plasma respond to electric forces from nearby particles, giving rise to collective behavior and shielding. For distances greater than the Debye length λ_D, particles are essentially shielded from each other ($\lambda_D = \left(\epsilon_0 T_e / n_e e^2\right)^{1/2}$, where T_e is the electron temperature and n_e is the electron density). This process is schematically shown on figure 1-3. In this thesis the Debye length is foundational to the understanding of the coherent scattering process off of density fluctuations, described in chapter 5.

Plasma physicists define the plasma parameter Λ by $\Lambda = \frac{4\pi}{3} n_e \lambda_D^3$ as the number of particles that live inside a sphere centered on the test particle with radius λ_D, called the Debye sphere. If $\Lambda >> 1$ a large number of particles are susceptible of interacting with a test particle and a statistical treatment of the plasma is adequate. Λ can be expressed

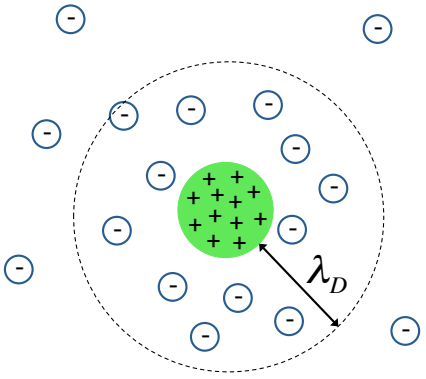

Figure 1-3: Debye shielding effect in a plasma. Beyond the Debye length λ_D a test particle is shielded out. The Debye sphere denotes the volume of particles in the plasma that are sensitive to interact with a test particle.

as the ratio of a characteristic kinetic energy of particles (E_{th}, given by the temperature T_e) to the characteristic energy of Coulomb interactions between particles distant $\sim \lambda_D$ (Fig. 1-3). In a plasma ($\Lambda >> 1$) the kinetic energy of particles is much higher than the Coulomb interaction energy, and collective effects within the plasma dominate over Coulomb collisions.

$$\Lambda = \frac{4\pi}{3} n_e \lambda_D^3 \propto \left(\frac{T_e}{e^2/4\pi\epsilon_0 \lambda_D} \right)^{3/2} = \left(\frac{E_{th}}{E_{Coul}} \right)^{3/2} = 5.4 \times 10^6 \frac{T^{3/2}}{n^{1/2}} \tag{1.1}$$

In equation 1.1, T is measured in keV (1 keV $\sim 10^7 K$) and n is measured in units of $10^{20} m^{-3}$. For typical fusion plasma of $T = 15\ keV$ and $n = 2 \times 10^{20}\ m^{-3}$, $\Lambda \sim 10^8$. The condition of collective effects to dominate over Coulomb interactions is largely satisfied by a fusion plasma. The definition of the Debye length is central in plasma physics as well as to this thesis, and I will make use of the Debye length to define coherent $vs.$ incoherent scattering of waves in the plasma. In this thesis, coherent scattering of micro-waves is used to diagnose turbulence in the plasma through measurement of electron density fluctuations.

In order for fusion energy gain to occur, a plasma has to be confined for a sufficiently long time and be sufficiently dense in order for sufficient fusion reactions to occur. This can be summarized in the triple product condition

$$nT\tau_E > 3 \times 10^{21} m^{-3} keV s \tag{1.2}$$

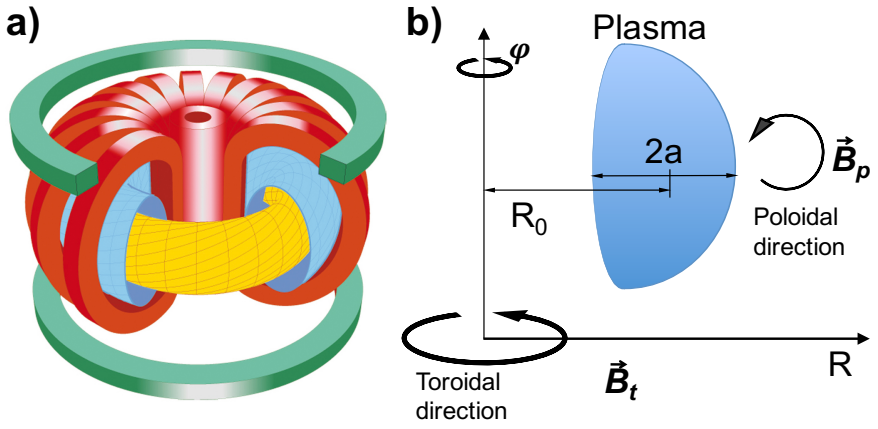

Figure 1-4: **a)** Tokamak design concept, courtesy of [4]. **b)** Schematic representation of the geometry in a tokamak device. R_0 is the major radius and a is the minor radius. t denotes the toroidal direction and p the poloidal direction.

where τ_E is the energy confinement time, defined as the ratio between the total energy in the plasma by the total power losses. Originally introduced by Lawson [3], τ_E is a measure of the confinement quality of the plasma: large τ_E indicate plasma is well confined. The most successful fusion device to date is the tokamak, a 'donut-shaped' device using magnetic fields to produce confinement, as shown in figure 1-4. Achieving good confinement is necessary for the successful development of fusion. This thesis seeks to understand the confinement properties of a specific type of tokamak, called the spherical tokamak ($cf.$ figure 1-5).

1.3 Tokamaks and the spherical tokamak (ST)

The tokamak uses magnetic fields to produce confinement. When subject to a uniform magnetic field charged particles gyrate in circular motion around magnetic field lines and move at constant velocity parallel to the magnetic field line. By bending the magnetic field lines in a closed shape particles should remain confined. This is the principle behind magnetic confinement fusion, as implemented today in tokamaks and stellarators.

Tokamaks are axisymmetric by design (Fig. 1-4 c)). The main component of the magnetic field is in the toroidal direction $\vec{B}_t$, produced by toroidal field magnets (in red in figure 1-4). A smaller component in the poloidal direction $\vec{B}_p$ can be achieved by poloidal

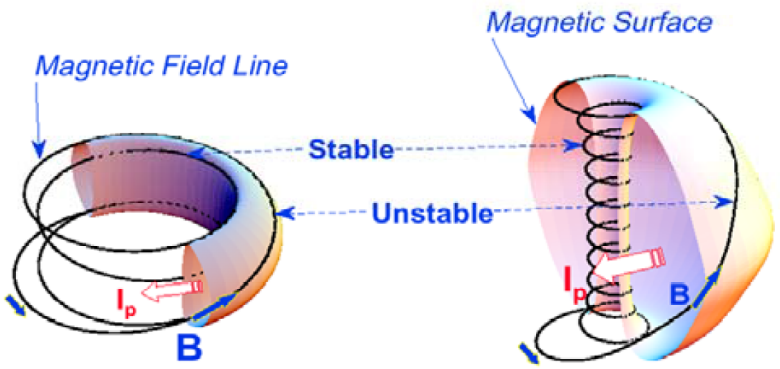

Figure 1-5: Comparison of conventional tokamak and spherical tokamak configurations (from [5]). B is the magnetic field direction and I_p the plasma current. By minimizing the time particles spend on the unstable part of the plasma (the outboard or low-field side), STs can stabilize magnetohydrodynamic instabilities as well as microinstabilities responsible for transport and confinement degradation.

field magnets (green in figure 1-4), as well as through an electric current driven through the plasma along the toroidal direction. The poloidal magnetic field $\vec{B}_p$ in a tokamak curves magnetic field lines in the poloidal direction and produces the confinement.

With respect to the standard tokamak, the spherical tokamak (ST) has a more compact shape and smaller aspect ratio A, defined as $A = R_0/a$. R_0 is called the major radius, while a is called the minor radius ($cf.$ figure 1-4). We also call $\epsilon = 1/A$ the inverse aspect ratio. Standard tokamaks typically have large aspect ratio $A \gtrsim 3$ while STs have $A \sim$ 1-2 (Fig. 1-5). This difference results in new plasma regimes capable of achieving higher plasma beta β. Plasma beta β is defined as the ratio between the plasma pressure p and the magnetic field pressure $B^2/2\mu_0$, namely $\beta = p/(B^2/2\mu_0)$. Achieving high-β is also favorable for future fusion reactors, since the fusion power yield P_{fus} scales as $P_{\text{fus}} \propto \langle\sigma v\rangle p^2 \propto \langle\sigma v\rangle \beta^2 B^4$, where $\langle\sigma v\rangle$ is the fusion reaction rate ($cf.$ figure 1-2).

The toroidal magnetic field in a tokamak plasma (as well as in STs) varies roughly as follows $B_t \sim 1/R$, where R is the major radius location within the plasma. The low-field side region (outboard) of a tokamak plasma is subject to an effective acceleration due to the curvature of the field lines that can destabilize a certain number of instabilities (ballooning instabilities, $cf.$ [6]). For this reason the low-field side region of the plasma is also known as bad-curvature region. On the other hand the high-field side region (inboard) is generally stable. Ballooning instabilities tend to accumulate on the low-field side. The

geometry of STs is optimized to minimize these low-field side instabilities, as can be seen on Fig. 1-5. On a standard tokamak, magnetic field lines wander long distances in the low-field side, bad-curvature region of the plasma. In an ST the curvature introduced in the magnetic field lines shortens the distance that field lines spend on the low-field side region, leading to suppression of bad-curvature instabilities [7].

1.3.1 High bootstrap fraction: towards steady-state operation

In order to produce a magnetic field in the poloidal direction tokamaks rely on a current flowing in the toroidal direction. The traditional way for tokamaks to drive such a current has relied on transformer action via induction, having the plasma as the secondary circuit. We call this Ohmic current j_{OH}. Although successful, this method does not scale for steady state operation in a reactor.

One of the advantages of spherical tokamaks is the high levels of bootstrap current j_{BS} obtained with respect to standard tokamaks. Bootstrap current is a self-produced current in the plasma by the pressure gradients between the hot core and the cold edge region. It is thought that the bootstrap current fractions of future fusion reactors should be on the order of 80%. Due to their aspect ratio and ability to sustain high-β, spherical tokamaks exhibit a favorable dependency on bootstrap current

$$j_{BS}/j_{OH} \sim \epsilon^{1/2}\beta_p \tag{1.3}$$

where $\beta_p = 2\mu_0 P/B_p^2$ is the poloidal beta. STs are well suited for achieving high bootstrap current fraction and non-inductive operation (not relying on inductive transformer action) since it relaxes the constraints for auxiliary current drive systems.

1.3.2 The National Spherical Tokamak eXperiment (NSTX)

The National Spherical Tokamak eXperiment (NSTX) is one example of the spherical tokamak concept (NSTX [15, 16]), situated in the Princeton Plasma Physics Laboratory (PPPL) in Princeton, NJ. PPPL is a U.S. Department of Energy national laboratory 'devoted to creating new knowledge about the physics of plasmas − ultra-hot, charged gases − and to developing practical solutions for the creation of fusion energy' [17]. Figure

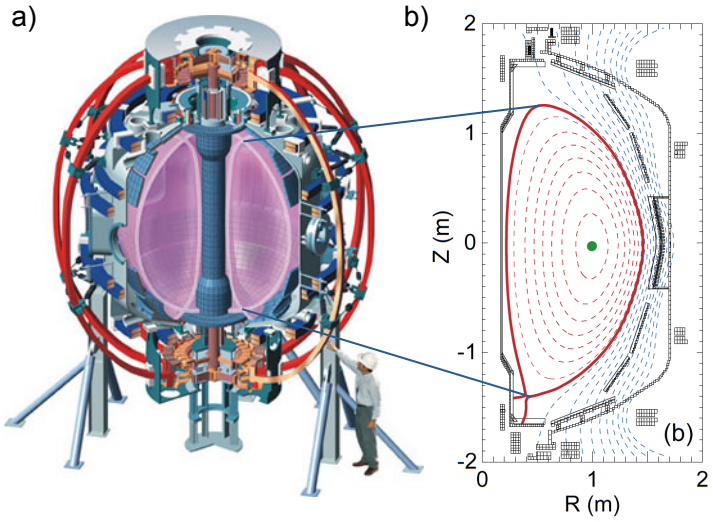

Figure 1-6: **a)** NSTX device. **b)** Poloidal flux surfaces in a typical NSTX plasma: last closed flux surface (LCFS) in solid red, open flux surfaces in dashed blue lines, closed flux surfaces in dashed red lines. These are also contours of constant pressure. The magnetic axis is a green dot. Courtesy of [5].

1-6 shows a schematic of the NSTX device. Other prominent experiments are the Mega Ampere Spherical Tokamak (MAST [18, 19]) at Culham, Oxfordshire, and more recently ST40 from the company Tokamak Energy [20], Oxfordshire. Both NSTX and MAST are currently undergoing major upgrades (NSTX-U [24] and MAST-U [25]), and have the mission of establishing the physics baseline to test the viability of the ST as a practical fusion power source such as ST-FNSF (Spherical Torus Fusion Nuclear Science Facility [21–23]).

The original NSTX device capabilities are shown in figure 1-7 [15]. Since then, NSTX parameters were improved to a major radius $R_0 \approx 0.87$ m, minor radius $a \approx 0.65$ m, toroidal magnetic field $B_t = 0.3\text{-}0.6$ T and plasma current $I_p \leq 1.5$ MA. It is expected NSTX-U will achieve toroidal magnetic field of ~ 1 T and plasma current of ~ 2 MA. Operating at high-β, NSTX experiments have achieved $\beta \lesssim 40\%$, a value over a factor of $\times 4$ higher than in conventional tokamaks. As was previously discussed, NSTX operated at high bootstrap current, exhibiting up to 70% bootstrap current fraction [26].

NSTX complements bootstrap current drive by using a coaxial helicity injection (CHI [27]) system, neutral beam injection (NBI) and a high-harmonic fast wave (HHFW [28]) system. CHI is used at NSTX for plasma non-inductive current initiation and has de-

R	0.85 m
a	0.68 m
I_p	1 MA
B_T	0.3 T
κ	2.0
R/a	1.25
Startup	OH, electron cyclotron heating (CHI)
Wall stabilization	Close-fitting conducting plates
Auxiliary heating and current drive	CHI, HHFW (6 MW), NBI (5 MW)
Profile control	HHFW, CHI, NBI
Maximum pulse length	5 s (> current relaxation time)
Divertor	Single- and double-null, IWL
Profile diagnostics	

Figure 1-7: Original NSTX device capabilities as a first of a kind, ultra-low aspect ratio spherical torus (from [15]). Note the magnetic field has since then been increased to $B = 0.55$ T for NSTX, and will achieve 1 T for NSTX-U. The plasma current I_p is expecting a upgrade to 2 MA for NSTX-U.

livered 160 kA of current. NBI and HHFW act both as auxiliary plasma heating and current drive systems. NBI relies on the injection of fast-neutrals that become ionized as they enter the plasma. The fast-ion population originating from NBI fast neutrals carry a current that eventually slows down on the plasma. With respect to heating systems, the overdense plasma condition of NSTX plasmas ($\omega_{pe}/\Omega_e > 1$) precludes the use of conventional electron cyclotron heating (ECH) and electron cyclotron current drive (ECCD). A HHFW system has proven successful to heat and drive current in NSTX plasmas. The NSTX HHFW system uses 30 MHz waves injected in the plasma, and is able to couple up to 6 MW of power. Core electron temperatures of over 5 keV have been achieved in HHFW heated plasmas at NSTX [29].

1.3.3 Spherical tokamak confinement

The confinement properties of an ST can be substantially different to those in a standard tokamak. Both NSTX and MAST have observed an H-mode global energy confinement exhibiting a very strong dependence on collisionality $B\tau_E \sim 1/\nu_e^*$ [8–13]. This scaling substantially differs from the ITER98y$_2$ scaling $B\tau_E \sim$ independent of ν_e^* [104] (the electron collisionality $\nu_e^* \propto n_e/T_e^2$ measures the importance of Coulomb collisions in the plasma). The ST energy confinement scaling with collisionality is favorable to operation in low-collisionality regimes needed for future reactors.

The physics mechanisms behind the favorable energy confinement scaling in STs are still to be uncovered, but should be directly linked to the different confinement properties with respect to standard tokamaks. Standard tokamaks typically exhibit thermal losses from the hot core to the cold edge region that are dominated by ion thermal transport. However STs routinely exhibit ion thermal transport close to the irreducible collisional minimum (neoclassical), while the dominant thermal losses are through the electron thermal transport channel. Understanding electron thermal transport has become a main research thrust in the spherical tokamak community. Chapter 2 gives an overview of electron thermal transport in spherical tokamaks. This thesis makes a contribution towards understanding electron thermal transport losses in an NSTX H-mode plasma heated by neutral beam injection (NBI), combining experimental measurements, state-of-the-art numerical simulation, and advanced modeling.

1.3.4 Validation of transport models

The ultimate goal of validating transport models in the ST is to be able to predict electron thermal transport and consequently the equilibrium plasma profiles of future high performance plasmas and fusion reactors. Validation of transport models is done through a combination of experimental observations and very sophisticated models. First-principles models (e.g. the gyrokinetic model) are usually too expensive to provide profile predictions. Reduced transport models are, by nature, much less computationally intensive, and can be used for profile prediction and performance optimization of future reactors. Validating first principles nonlinear gyrokinetic simulations is a pre-requisite to generate/calibrate reduced models (such as TGLF) to make new, testable predictions. This thesis will focus on the validation of first-principles nonlinear gyrokinetic simulation. Together, these efforts would drive the prediction and optimization of the performance of future fusion reactors.

In the context of turbulence and transport, comparisons between experimental observations and models have historically focused on the ion and electron heat flux losses. Experimentally, one can estimate the electron and ion heat losses through calculations based on power balance: by knowing how much heating is put in the plasma (via neutral

beams, radio frequency heating, etc.), one can compute what the 'experimental' transport fluxes are (more details on chapter 3). On the other hand, using very sophisticated models of the turbulence (such as the gyrokinetic model) one can run large-scale supercomputer simulations to 'predict' transport fluxes due to turbulence fluctuations. Comparison of the 'experimental' vs. the 'predicted' transport fluxes from simulation can inform about the validity of the models employed, and whether additional physics processes are not modeled that are relevant for transport.

Unfortunately, flux comparisons have proven not completely satisfactory. Experience has shown that turbulence existing in the core of fusion devices exhibits a critical threshold behavior, meaning the gradients of the background plasma profiles (which are responsible for driving the turbulence) are right on the verge of instability. Tiny changes in the background plasma profiles can give rise to extremely different transport flux predictions, from fully stabilized to highly unstable turbulence regimes (within experimental uncertainty in the simulation inputs), producing great uncertainty. This means that agreement between experiment and model is unconstrained. Agreement may not happen because the correct physics is represented. In these situations, additional constraints have to be added to test the turbulence models.

In the context of turbulence and transport, additional experimental observations come in the form of fluctuation measurements such as density and potential fluctuations. These are indicative of the turbulence state of the plasma and provide strict constraints to satisfy by the models. By probing some of the most fundamental properties of the turbulence, experiment/model comparisons of fluctuation quantities lie at a different level than flux comparisons in the validation 'hierarchy' [99, 100]. The validation hierarchy ranks how meaningful each comparison is with respect to others by placing it at a specific level in the hierarchy. The lowest level is generally reserved to the most fundamental quantities such as fluctuation spectra, while at the highest level reside comparisons of the plasma profiles and/or associated fluxes (more details can be found in chapter 3 and [99, 100]). The goodness of the comparisons at the different hierarchy levels can be quantified via validation metrics, which provide a measure of the agreement between an experimental observation and the model prediction. By combining experiment/model comparisons at different levels in the validation hierarchy via the use of validation metrics, one is able

to discriminate between models, with the ultimate goal of finding those that are the best representation of reality.

Comparisons of detailed turbulence characteristics are challenging. Correct interpretation of the data provided by fluctuation measurement requires great physical understanding of the specific diagnostic measurement. In addition, simulation output does generally not overlap with the measurement of the most fundamental quantities at the lowest level in the hierarchy (such as fluctuation data), yielding possible only qualitative comparisons. This difficulty can be overcome by synthetic diagnostics. Synthetic diagnostics are complex numerical tools that incorporate diagnostic characteristics such as viewing geometry, spatial, temporal and spectral resolution with advanced characterization and modeling of the diagnostic to a high level of fidelity, resulting in a direct map of the numerical solution to the experimental measurement.

Validation efforts of turbulence and transport models in the ST have produced numerous comparisons of transport fluxes between experiment and models, but quantitative comparisons of the underlying turbulence characteristics via synthetic diagnostics have been limited [144, 160, 162, 168, 169, 171–173]. In addition, these efforts focused on ion-scale turbulence and on the subdominant ion thermal transport for the most part, with the exception of [144]. No attempt has been made to explain electron thermal transport by combining flux comparisons with detailed, quantitative turbulence comparisons. Furthermore, ref. [144] is the only attempt, to my knowledge, to establish quantitative comparisons of the small electron-scale turbulence (measured via high-k scattering [65]), which has been shown to be a great source of electron thermal transport in the ST [64, 136]. The comparisons shown in [144] proved not to be fully satisfactory due to the presence of 'systematic errors' present in the computation of the synthetic spectra, and were a great motivation for the work of this thesis.

In this thesis, I have implemented two synthetic diagnostics for high-k scattering, yielding for the first time direct quantitative comparisons and successful agreement of high-k frequency and wavenumber spectra of density fluctuations in a spherical tokamak. More importantly, these quantitative comparisons of the turbulence were combined with transport comparisons of ion and electron thermal power. Together, the thermal transport comparisons combined with the detailed turbulence spectra comparisons in this thesis pro-

vide the strongest evidence to date that electron-scale turbulence fluctuations can dominate anomalous electron thermal transport in the core-gradient region of low-to-modest NSTX NBI-heated H-mode plasmas investigated here (driven by the ETG mode, chapter 2).

1.4 Brief summary of this thesis

Chapter 1 was a brief introduction to controlled nuclear fusion, in which were introduced some of the important concepts such as spherical tokamak and some important properties pertaining the spherical tokamak plasma core, such as high-β and high bootstrap fraction. It was briefly introduced in this chapter how confinement in the ST core is dominated by electron thermal transport, which is the underlying question mark being addressed in the present thesis.

Chapter 2 gives a succinct introduction to plasma turbulence and transport in the core of standard and spherical tokamaks, starting from basic principles of diffusive transport and the most basic drift-wave mechanism that is behind many of the more complex drift-wave instabilities studied in this thesis. I discuss how, for a long time, the ITG/TEM/ETG paradigm has proven successful to explain anomalous transport in the core of standard tokamaks. However a wide range of instabilities have been predicted to produce anomalous electron thermal transport in the ST core, and are briefly discussed in this chapter. An important introduction on the electron temperature gradient mode (ETG), the main instability under study in this thesis, is presented. The gyrokinetic model is the main transport model used to study anomalous electron thermal transport, and is also briefly introduced in this chapter.

Chapter 3 introduces the most important concepts behind validation of transport models in the context of magnetic confinement fusion, and presents a succinct review of past validation work performed in the two main exponents of the ST: NSTX and MAST. This chapter highlights how past work in NSTX has emphasized the importance of understanding electron thermal transport losses in the NSTX core. Special emphasis was placed on the ETG mode, making use of the high-k scattering diagnostic, as well as on the micro-tearing mode. However, successful, quantitative turbulence comparisons were lacking in

past work. Past validation work on MAST has given special importance to understanding the subdominant ion-thermal transport, making use of the beam emission spectroscopy system (BES) installed in MAST. From theoretical grounds great efforts were dedicated to understanding the suppression of ion-scale turbulence by $E \times B$ shear along with comparisons to BES measurements. Overall, one of the conclusions from this chapter is the lack of detailed comparisons and synthetic diagnostic implementation of electron-scale turbulence fluctuations, both in NSTX and MAST. This motivated the development of this thesis. This chapter also highlighted some additional missing gaps which could motivate future work, and will be discussed at the end of this chapter.

Chapter 4 presents the analysis tools used in this thesis, from the basics of accessing NSTX/NSTX-U data, to the experimental analysis (profile analysis, TRANSP, high-k scattering data and determination of experimental uncertainties) to the GYRO code. Some of the main routines of analysis are introduced in this chapter, but also in appendix D.

Chapter 5 intoduces the synthetic diagnostic for high-k scattering, which represents a key outcome of this thesis. This chapter introduces some of the main concepts behind scattering as a diagnostic technique, as well as the foundational distinction between coherent scattering and incoherent Thomson scattering. Focusing on coherent scattering for the measurement of turbulence fluctuations, I introduce the possibility of computing the synthetic signal of fluctuations in real space as well as in k-space. In order to implement a successful synthetic diagnostic for high-k scattering, some of the complexity pertaining to field-aligned flux surface geometry is introduced. Finally the synthetic diagnostic formulation is introduced, both in general 3D and in 2D, real space and in k-space. However, only the 2D implementation was numerically implemented for the high-k scattering system in this work. Some clarifying dependencies of the synthetic power spectrum are also introduced, such as the simulation wavenumber resolution, Doppler shift and the diagnostic wavenumber resolution, contributing to the important characterization and understanding to the measurement spectra from high-k scattering.

Chapter 6 presents the main results of this thesis, combining for the first time experiment/model comparisons in three levels in the validation hierarchy: electron thermal power P_e, electron-scale wavenumber spectra comparisons and frequency spectra comparisons. This chapter has proven successful in reproducing experimental constraints at all

hierarchy levels. This chapter identified transport comparisons (P_e) and high-k k-spectra comparisons as the most relevant for the purpose of model selection, and highlighted how frequency spectra comparisons are not model constraining. This suggests that electron-scale frequency spectra characteristics should be able to reproduce those from experimental spectra, however they cannot be used for model selection. Carefully designed validation metrics are then combined in a global, composite metric assessing the overall fidelity of the comparisons established, allowing to choose the models that, according to those metrics, are the most representative of reality.

Chapter 7 presents a summary of the most relevant results outcome of this thesis. A discussion of some of the caveats and approximations made is also presented, along with future lines of work motivated by this work.

Appendices A-H contain some additional information concerning the derivation of the synthetic diagnostic, the Matlab routines used in this work, resolution and numerical convergence tests of the nonlinear gyrokinetic simulations presented, as well as on some additional interesting topics on ion-scale turbulence outcome from this work are all detailed in .

Chapter 2

Plasma Turbulence and Transport Background

This chapter contains a basic introduction to transport processes in tokamaks, with a special emphasis on spherical tokamaks. The theory of transport studies how particles, heat and momentum are lost, or transported, from the confined plasma to the cold edge region across the confining magnetic field. In tokamaks, radial transport can be described by diffusive collisional processes (neoclassical). However, tokamaks experiments have shown transport processes routinely exceeding neoclassical transport estimates. The current belief is that microinstabilities driven by the free energy of the equilibrium plasma profiles (temperature, density, pressure, ..) result in turbulence and drive large amounts of transport. In this chapter I will mainly focus on the turbulent transport of heat, especially turbulent electron thermal transport.

2.1 Transport as a diffusive process

Transport describes phenomena that are out of equilibrium. Particles, heat and momentum have associated thermodynamic fluxes, generally defined as having a linear relation to thermodynamic forces in situations close to equilibrium. For example, a particle flux Γ_r and heat flux Q_r are related to conjugate thermodynamic forces by $\Gamma_r = -D\partial n/\partial r$ and $Q_r = -n\chi\partial T/\partial r$, where n, T are density and temperature, D is the particle diffusivity and χ is the heat diffusivity. The subscript r denotes the flux is in the radial

direction, perpendicular to the flux surfaces. A process in which fluxes exhibit a linear relationship with thermodynamic fluxes is known as a diffusive process.

The simplest mechanism to produce radial transport of particles, heat and momentum in magnetically confined plasmas is through collisions. When subject to a straight magnetic field, collisions between plasma particles are inherently present and produce transport perpendicular to the background magnetic field through collisional diffusion. In tokamak fusion conditions, the effect of collisions is enhanced by effect of the toroidal, inhomogeneous magnetic field, called neoclassical transport. Neoclassical transport is based on robust, first principles physics foundation [30, 31], and many aspects of neoclassical transport theory have been verified experimentally, including the transport of impurities and bootstrap current generation [32–35]. However, neoclassical transport is not able to predict experimental levels of cross-field (perpendicular) heat transport observed in tokamak plasmas.

Tokamak experiments around the world have shown transport processes routinely exceeding neoclassical transport estimates. Situations may arise in which fluxes cannot be simply expressed as a function of its conjugate thermodynamic force, leading to non-diffusive transport. A simple but realistic example of a non-diffusive process is $\Gamma_r = -D\partial n/\partial r + Vn$. In this case, the term Vn is known as the convective term (or pinch) and V is the convective velocity. This form has been applied to tokamak plasmas and experimentally verified in certain conditions [36]. However, in situations far from equilibrium dominated by nonlinear turbulent phenomena, more complex transport processes may arise. In particular, the electron heat flux in the core of tokamak plasmas has been shown to exhibit a critical gradient behavior, namely $Q_e = n_e\chi_e(\nabla T_e - (\nabla T_e)_c)$. Here the electron heat diffusivity χ_e, is equal to $= 0$ for values of $\nabla T_e < (\nabla T_e)_c$, ie. no transport is expected. Such critical gradient behavior is generally observed associated to specific a microinstability, which will produce transport when become unstable. The specific dependencies of this critical gradient behavior generally depend on the specific plasma condition and main instability drive. Ample experimental observations have observed critical gradient behavior in several devices [37, 38, 40]. Next section discusses some of the most important microinstabilities driving turbulent transport in tokamaks.

2.2 The drift wave mechanism

The excess transport observed in tokamak experiments with respect to neoclassical transport estimates is widely referred to as *anomalous* transport, which can exceed neoclassical predictions by up to three orders of magnitude. Current theories are still far from being able to explain anomalous transport in tokamaks, but enormous progress has been made and the gap is closing in [41]. Nowadays anomalous transport is widely attributed to small-scale micro instabilities driving turbulence in the plasma, known as drift-waves [42, 43].

I present here a simplified description of the basic drift-wave mechanism in slab geometry that follows closely [44]. The basic requisite for the existence of drift waves is the presence of a density or temperature gradient. Assume an electron density gradient ∇n_e is directed in the $\hat{x}$-direction, a background magnetic field B_0 coming out of the board in the $\hat{z}$-direction and a constant electron temperature T_e. In the presence of a density gradient, electrons (and ions) are subject to a diamagnetic drift velocity $v_{\star e} = -\frac{\nabla n_e}{n_e}\frac{T_e}{eB_0}$.

Drift waves have small but finite parallel wavenumber $k_\parallel$ to the background magnetic field ($cf.$ [43]), which allows electrons to flow along B_0 and establish a thermodynamic equilibrium. Electrons then satisfy the Boltzmann relation $\frac{\delta n_e}{n_e} = \frac{e\phi}{T_e}$.

Assume a small sinusoidal density perturbation in the $\hat{y}$-direction. The perturbation will generate space charge accumulation zones ($cf.$ 2-1). The radially varying background electron-density produces charge perturbations, which in turn give rise to an electric field in the y-direction. The electric field created translates to an $E \times B$ drift $v_{E\times B}$ in the $\hat{x}$-direction. The $E \times B$ drift created moves the density perturbations in such a way that a wave propagates in the y-direction. Such a perturbation will propagate in the y-direction at the electron diamagnetic drift velocity $v_{\star e}$, and we have $\omega = k_y v_{\star e}$.

Note how this simple mechanism, although able to describe the propagation of perturbations in the y-direction (poloidally in the tokamak context), is unable to capture a net radial flow of particles (in the $\hat{x}$-direction in figure 2-1). In the present discussion, a small parallel wavenumber $k_\parallel$ allows electrons to move freely along B_0 and the Boltzmann relation is fulfilled. In this relation, density δn_e and electric potential ϕ are in phase and drift waves are stable. However, there exist a certain number of mechanisms not presented

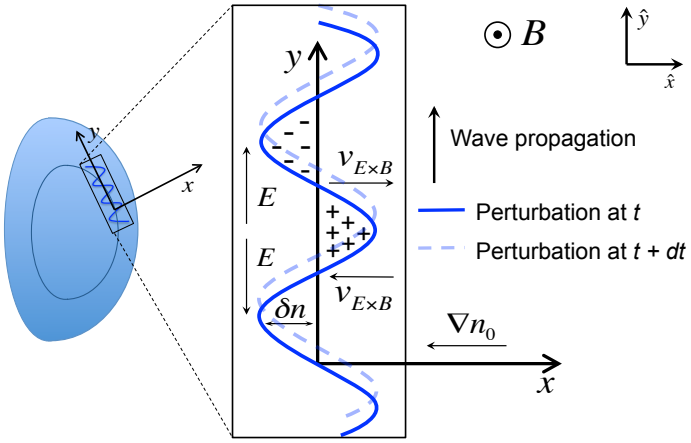

Figure 2-1: Simple physical mechanism for the propagation of a stable drift wave. The toroidal direction is out of the board in this description. The poloidal direction corresponds to the y-axis, and the radial direction corresponds to the x-axis.

here that can limit the parallel electron motion and render drift waves unstable (such as electron-ion collisions, Landau damping, electron inertia, inductance, etc.). If electrons are not able to move freely along the magnetic field, a lag between the electron density and the electric potential will set in and a phase shift δ, assumed small in this description. The Boltzmann relation will then be modified $\frac{\delta n_e}{n_e} = \frac{e\phi}{T_e}(1 - i\delta)$. This small modification due to δ with respect to the Boltzmann relation leads to a modification of the dispersion relation $\omega \approx k_y v_{\star e}(1 + i\delta)$.

Assuming a time variation of $\exp(-i\omega t)$ and $\delta > 0$ means that the potential perturbation has acquired an additional phase with respect to the density perturbation. In this situation the drift wave is unstable, and the linear growth rate is given by $\gamma = k_y v_{\star e}\delta$ in this simple description.

A particle flux Γ is associated to an unstable drift wave and is obtained as the time average of the electron density perturbation δn_e times the $E \times B$ velocity produced by the electric potential perturbation ϕ, as follows $\langle \delta n_e \vec{v}_{E\times B} \rangle_T = k_y \phi \delta n_e / 2B_0 \sin(\delta)\vec{\hat{x}}$. If $\delta = 0$ fluctuations are adiabatic and no particle transport occurs. In the unstable situation where $\delta > 0$ a radial particle flux in the positive $\vec{\hat{x}}$-direction will occur (down the density gradient). Similar considerations will apply to heat flux Q if we consider temperature perturbations and a temperature gradient.

We have considered here a simple slab geometry that is usually not applicable to stan-

dard nor spherical tokamaks. Important effects due to the toroidal geometry, additional gradient dependencies and velocity-space kinetic effects are shown to play a very big role in enhancing/stabilizing this drift wave mechanism. However, the essential physical picture is the one presented here. By including additional effects the drift wave mechanism can explain microinstabilities that are routinely found unstable in current tokamak experiments, such as the ion temperature gradient mode (ITG), the trapped electron mode (TEM) and the electron temperature gradient mode (ETG). Next section describes a similar physical picture of the drift-wave instability mechanism in the presence of a temperature gradient and inhomogeneity in the magnetic field. The interested reader will refer to more complete review papers and manuscripts [43–45] for more detailed explanations and physical insight.

2.3 Drift-wave instabilities.

The previous mechanism described the propagation of drift waves in a straight magnetic field (slab geometry). However, when subject to inhomogeneous, toroidal geometry, a class of drift-wave *instabilities* appear. These are thought to be responsible for the dominant transport losses observed in experiments. We consider here the basic drift-wave instability mechanism in the presence of an inhomogeneous magnetic field and a temperature gradient.

When subject to an inhomogeneous magnetic field, electrons and ions are subject to the ∇B and curvature κ drifts in the poloidal direction ($\hat{y}$ in figure 2-1). For low-β equilibria, these are combined into a magnetic drift with velocity

$$\vec{v_d} = \frac{v_{||}^2 + v_{\perp}^2/2}{\omega_c B} \vec{B} \times \vec{\nabla} B \tag{2.1}$$

which has opposite sign for electrons and ions. We are interested here in the ion drift wave instability. Since we are interested in perturbations such that $(k_\perp \lambda_D)^2 << 1$, quasi-neutrality holds and the ion density follows the electron density $\delta n_i \sim \delta n_e$. For these perturbations, the fast streaming electron motion along the magnetic field produces an adiabatic electron response $\delta n_e / n_0 \sim e\phi / T_e$. A density bunching is associated to an

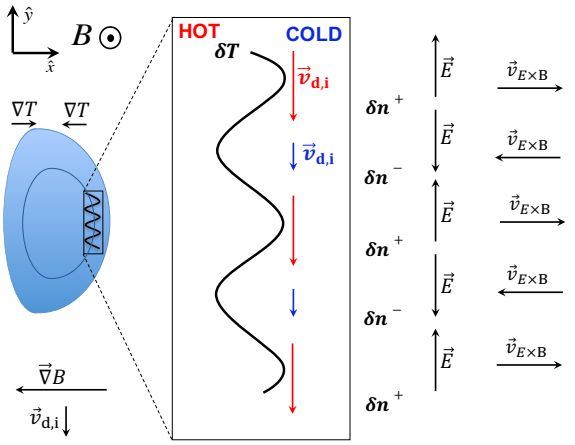

Figure 2-2: Simple picture of drift-wave instability mechanism in the presence of a background temperature gradient ∇T in an inhomogeneous magnetic field. The instability feedback mechanism takes place on the outboard side of tokamaks, where the temperature gradient ∇T is in the same direction as the gradient of the background magnetic field ∇B. On the inboard side, ∇T and ∇B have opposite signs and the instability mechanism is shut off.

electric potential.

Consider a sinusoidal temperature perturbation δT in the presence of a background temperature gradient ∇T on the outer midplane of a tokamak, as shown in figure 2-2. Since the magnetic drifts $\vec{v}_d$ depend on the velocity $\propto v_{||}^2, v_\perp^2 \propto T_{||}, T_\perp$, these cause a density build-up below the hot and above the cold spots. The density build-up produces an electric field $\vec{E}$, which tends to enhance the perturbation through the $E \times B$ drift $\vec{v}_{E\times B}$. Note this enhancement takes place at the outboard side of the tokamak, where the temperature gradient ∇T is directed in the same direction as the magnetic field inhomogeneity ∇B. On the inboard side, ∇T and ∇B have opposite signs and the instability feedback mechanism is suppressed.

This simple physical mechanism can explain the most basic two-fluid version of instabilities such as the toroidal ion temperature gradient mode (toroidal ITG) and toroidal electron temperature gradient mode (ETG), a main focus of this thesis. The reader is referred to [43–45] for additional insight in drift-wave instabilities. Although this physical picture provides intuition behind a drift-wave instability mechanism, additional physical processes having to do with geometry and kinetic effects are required to quantitatively model transport in the core of tokamak plasmas. One has to go beyond the two-fluid model to the gyrokinetic model for a more accurate description of transport.

2.4 The gyrokinetic model

The gyrokinetic model is a widely-used theoretical framework to study turbulence in magnetized plasmas. Simple fluid theories are generally not able to explain the levels of particle and heat transport observed in tokamak experiments and advanced kinetic treatments are needed. The gyrokinetic model is currently believed to capture the main physical mechanisms underlying turbulent transport processes in current tokamak experiments. I will present here a very succinct introduction to the gyrokinetic model. The reader is referred to more advanced treatments for additional details [92–97].

As we saw in chapter 1 fusion plasmas are characterized by being weakly coupled ($n_e\lambda_D^3 \gg 1$) which justifies a kinetic description of the plasma based on one-particle distribution functions f_s. The one-particle distribution f_s for species s is such that $f_s(\vec{r},\vec{v},t)d^3\vec{r}d^3\vec{v}$ is the number of species in a volume $d^3\vec{r}$ located at position $\vec{r}$ and having a velocity $\vec{v}$ within a $d^3\vec{v}$ velocity differential. f_s satisfies the Boltzmann equation in 6D phase-space $(\vec{r},\vec{v})$

$$\frac{\partial f_s}{\partial t} + \vec{v}\cdot\nabla f_s + \vec{a}\cdot\frac{\partial f_s}{\partial \vec{v}} = C(f_s) \tag{2.2}$$

also known as the Fokker-Planck equation depending on the form of the collision operator C, which takes into account the effect of collisions between plasma particles. The reader is referred to [31] for a complete description of the collision operator. The quantity $\vec{a}$ is the acceleration given here by the Lorentz force acting on particles subject to electric and magnetic fields $\vec{a} = \frac{e_s}{m_s}[\vec{E} + \frac{\vec{v}\times\vec{B}}{c}]$, where m_s and e_s are the mass and charge of species s and $\vec{E} = \vec{E}(\vec{r},t)$ and $\vec{B} = \vec{B}(\vec{r},t)$ are the electric and magnetic fields felt by a particle. They satisfy Maxwell's equations

$$\begin{aligned}
\nabla\cdot\vec{E} &= 4\pi\rho_c \\
\nabla\times\vec{B} &= \tfrac{4\pi}{c}\vec{j} + \tfrac{1}{c}\tfrac{\partial\vec{E}}{\partial t} \\
\nabla\times\vec{E} &= -\tfrac{1}{c}\tfrac{\partial\vec{B}}{\partial t} \\
\nabla\cdot\vec{B} &= 0
\end{aligned} \tag{2.3}$$

Equations 2.2 and 2.3 are coupled through the plasma charge density ρ_c and current $\vec{j}$, which are the sources for Maxwell's equations and are linked to the distribution function

through $\rho_c = \sum_s e_s \int d^3v f_s$, $\vec{j} = \sum_s e_s \int d^3v \vec{v} f_s$. They constitute the Vlasov-Landau system of equations.

Although this kinetic description of a fusion grade plasma is fundamentally correct, it is not appropriate from a practical point of view. Analytic solutions to the Fokker-Planck-Maxwell equations are rare, and numerical simulations are extremely time consuming due to the 6D nature of the system. Today's most powerful super-computers are only able to numerically solve equations 2.2, 2.3 in extremely simplified conditions. The theory of gyrokinetics is able to reduce the number of relevant variables in the distribution function from 6 to 5, allowing tractable numerical solution.

The current hypothesis is that transport processes in fusion plasmas are dominated by low-frequency turbulent fluctuations slower than the ion cyclotron frequency ($\omega \ll \Omega_i$). The theory of gyrokinetics exploits this by averaging out the fast gyro-motion from the system, decoupling it from the slower gyro-center dynamics. The drift-ordered, or "local" gyrokinetic model [80] assumes strongly magnetized plasmas, characterized by $\rho_i/L = \rho_\star \ll 1$, where L is an equilibrium characteristic length scale (typically minor radius a or major radius R in tokamak plasmas) and ρ_i is the ion gyro radius $\rho_i = v_{th_i}/\Omega_i$. Parallel length scales are elongated along the background magnetic field $k_\parallel L \sim 1$ and perpendicular motion scales as the gyro radius $k_\perp \rho_i \sim 1$.

The transformation from a 6D to a 5D dimensional problem is achieved by applying the gyro-center transform as outlined in [92] and shown schematically in Fig. 2-3. The guiding center coordinates $\vec{R}_s$ are related to the particle position $\vec{r}$ by $\vec{r} = \vec{R}_s - \vec{v} \times \vec{b}/\Omega_s$, with $\vec{v} = v_\parallel \vec{b} + v_\perp(\cos\varphi \vec{\hat{x}} + \sin\varphi \vec{\hat{y}})$. Here $\vec{b}$ is the unit vector along the background magnetic field $\vec{B}$ (subscripted the parallel $\parallel$ direction), φ is the gyro phase and $\vec{\hat{x}}$ and $\vec{\hat{y}}$ are the perpendicular coordinates to the background magnetic field (noted with a $\perp$ subscript sign). Roughly speaking, the gyrokinetic equation is solved using a gyro-center coordinate system in which the fast time scale phenomena associated with gyro motion is eliminated through gyro phase averaging.

The distribution function f_s and the fields $\phi, \vec{A}$ and $\vec{B}$ are expanded between equilibrium and perturbed quantities, noted with a δ. symbol notation ($f_s = F_{0s} + \delta f_{s1} + ...$, and similarly for $\tilde{\phi}, \delta\vec{A}$ and $\delta\vec{B}$). Here F_{0s} is the equilibrium distribution function for species s. Overall, the commonly used drift-ordered, local assumption leads to the following

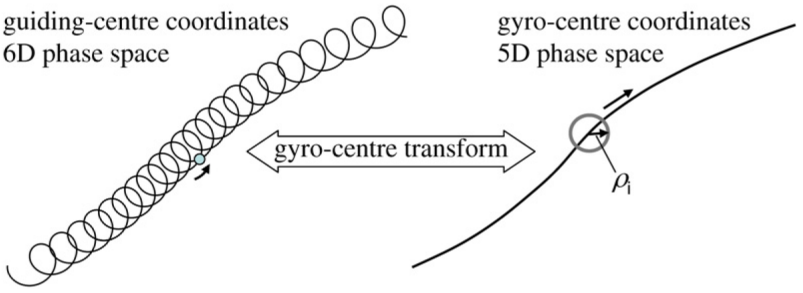

Figure 2-3: Transformation from guiding-center R_s to gyro-center coordinates used in gyrokinetics to reduce the problem for a 6-dimensional one to a 5-dimensional one. Image taken from [96].

orderings

$$\frac{\omega}{\Omega_i} \sim \frac{\rho}{L} \sim \frac{h}{F_0} \sim \frac{e\delta\phi}{T} \sim \frac{\delta A_\parallel}{B\rho} \sim \frac{\delta B_\parallel}{B} \ll 1 \qquad k_\parallel L \sim k_\perp \rho \sim 1 \tag{2.4}$$

where I omitted the subscript s to denote the species. I have already discussed the time and length scale assumptions related to gyro motion. In equation 2.4, h is the non adiabatic part of the first-order perturbed distribution function defined by $h_s = \delta f_{s1} + \frac{e_s \delta\phi}{T_s} F_{0s}$. The condition $\frac{h}{F_0} \ll 1$ simply assumes small perturbations about the background distribution function F_0. The following three assumptions on $\delta\phi, \delta A_\parallel$ and $\delta B_\parallel$ assume small perturbations of the electromagnetic fields to background quantities such as temperature T and background magnetic field B.

Roughly speaking, the gyrokinetic-Maxwell system of equations self-consistently solves for the perturbed distribution function of each species along with the perturbed electromagnetic field components $(h, \delta\phi, \delta A_{||}, \delta B_{||})$. Once the distribution function is calculated, gyrokinetic simulations can calculate particle, energy and momentum fluxes by integrating $\tilde{h}_s$ with the right quantities. However, this last step of calculating transport levels using gyrokinetic simulations is only possible when nonlinear effects are properly taken into account in the numerical solution.

In depth derivations of the gyrokinetic equations can be found in [92–97]. The gyrokinetic system of equations is readily implemented in gyrokinetic codes around the world such as GYR0 [98], which are routinely able to predict numerical solutions of the gyrokinetic-Maxwell system of equation for realistic tokamak conditions. The reader is referred to [98] for a comprehensive understanding of the gyrokinetic equations imple-

mented in GYRO. In the present work I will make extensive use of the gyrokinetic code GYRO, and will apply it to NSTX H-mode plasma conditions. This will predict thermal transport levels by gyrokinetic simulation separately resolving electron and ion scale turbulent fluctuations. GYRO will also be used to predict electron density fluctuation spectra, which will be directly and quantitatively compared to high-k density fluctuations measured by high-k scattering.

2.5 Core transport in conventional aspect ratio tokamaks.

Transport studies in the core of tokamaks can be subdivided between the inner core ($r/a \lesssim 0.3$-0.4), and the core-gradient region $r/a \gtrsim 0.4$-0.5. The inner core generally exhibits the highest densities and temperatures, but nearly flat profile gradients. This will be the fusion generation region of future reactors. Due to the flat profiles, traditional drift wave instabilities such as the one presented here tend to be found stable or marginally stable, unable to produce transport in the inner core. Additional mechanisms may be necessary to explain transport in the inner core region. In this thesis I focus on the core-gradient region, dominated by large profile gradients that provide ample free energy driving drift-wave type microinstabilities.

In the core gradient region of standard tokamaks, the current belief is that most of the turbulence is driven by electrostatic drift wave instabilities. Drift waves can become unstable in a toroidal plasma due to inhomogeneities, profile gradients and due to geometrical and curvature effects, which can further enhance the instability of these modes (as outlined in section 2.3). Depending on the instability drive of drift waves, they are identified as the ion temperature gradient driven instability (ITG [46–49]), the trapped electron mode (TEM [50]) and the electron temperature gradient driven instability (ETG [51]). Drift waves are highly anisotropic. The spatial scale length perpendicular to the magnetic field can be of the order of the ion gyro-radius ρ_i for ITG and TEM, and on the electron gyro-radius ρ_e for ETG. For typical reactor parameters of $T \sim 15$ keV and $B \sim 5$ T, we find $\rho_i \sim 0.5$ cm. As a comparison, the NSTX plasmas presented here have $T \sim 0.4$ keV and $B \sim 0.5$ T, leading to $\rho_i \sim 0.7$ cm. The electron gyro radius is $\sim \times 60$ smaller in a deuterium plasma, since $\rho_e \sim (m_e/m_i)^{1/2}\rho_i$. In the plasma turbulence and trans-

port context, the perpendicular wavenumber component $k_\perp$ associated to the ITG and TEM instabilities are characterized by $k_\perp \rho_i \sim 1$, whereas the ETG instability is characterized by $k_\perp \rho_e \sim 1$. Along the magnetic field, these waves tend to form elongated structures along the magnetic field, having parallel wavelengths of the order of the device size, $k_{||} \sim 1/qR$. We have then a clear separation of length scales between $k_{||}$ and $k_\perp$ ($k_{||} \ll k_\perp$), a fundamental property of drift waves in magnetically confined toroidal plasmas. This property will be fully exploited in the scattering experiments and modeling presented in this thesis. Concerning the time scales, these are low frequency modes and their characteristic frequency is smaller than the ion gyro-frequency (a fundamental assumption in the derivation). Drift waves span a wide variety of modes which, when driven unstable by some mechanism, can result in high transport levels.

Of particular importance is the transport of electron energy in the tokamak core, which has for decades remained elusive. In a thermonuclear fusion reactor, high energy alpha particles will transfer most of their energy to the electrons. Electrons play a key role in the sustainment of plasma energy in a reactor, hence the importance of the electron thermal transport problem. In current fusion experiments such as NSTX, electron thermal transport is regularly found at anomalous levels. As was previously mentioned, this thesis contributes to the understanding of electron thermal transport by focusing on a particular micro instability called the electron temperature gradient instability (ETG). The ETG instability is also found to play a very important role in conventional aspect ratio tokamaks, as will be discussed in the next section.

2.6 Anomalous electron thermal transport in spherical tokamaks

The spherical tokamak is able to operate in different plasma regimes than those accessible to standard aspect ratio tokamaks. STs are characterized by a small aspect ratio A, high elongation κ and high magnetic field line curvature, which allows access to different operational space (higher β, toroidal rotation). Under these conditions, transport processes in spherical tokamaks can be of different nature than in standard tokamaks.

Spherical tokamak plasmas exhibit high levels of toroidal flow induced by Neutral Beam Injection (NBI). Toroidal plasma rotation gives rise to shear in the $E \times B$ flow, perpendicular to the background magnetic field. This leads to high values in the $E \times B$ shearing rate, which is believed to be responsible for the suppression of long-wavelength, ion-scale turbulence ($k_\perp \rho_i \sim 1$). In addition, high beta has also been shown to stabilize the electrostatic ITG mode [52–56]. The suppression of ion-scale turbulence has been routinely observed in NSTX H-mode plasmas [10], and is supported by theory and modeling [57, 58]. This allows to isolate turbulence and transport studies to the electron thermal channel, which is consistently observed to be the dominant power loss channel in the spherical tokamaks. On the other hand, standard tokamaks tend to observe thermal transport dominated by the ion channel.

Several mechanisms have been recently identified as possible candidates for explaining electron thermal transport in the core of spherical tokamaks. The high beta and high collisionality levels attained in NSTX can destabilize electromagnetic modes such as micro-tearing modes (MT) as discussed in [59, 136]. The kinetic-ballooning mode (KBM), driven by beta and the MHD alpha parameter $\alpha_{\text{MHD}} \sim q^2 \nabla p / B^2$ is also found unstable in many NSTX plasmas [136]. Macro-instabilities such as high frequency Alfvén eigenmodes (AE) driven unstable by NBI fast-ion populations have also been shown to produce experimentally relevant values of electron thermal transport [63, 139]. The electron temperature gradient driven mode (ETG) have also been observed to produce experimentally relevant electron thermal transport levels [64, 136]. This thesis will focus on the ETG mode, through experimental measurements (high-k scattering [65]), numerical simulation (nonlinear gyrokinetic simulation) and a synthetic diagnostic for high-k scattering. A more complete discussion on the plasma operating regimes expected unstable for each mode and the specific parametric dependencies can be found in [64, 136].

It is possible that the local assumption of the drift-ordered gyrokinetic model described in 2.4 breaks down in the core of spherical tokamak plasmas. Previous work [81, 82] has shown that the local approximation neglecting variation in the radial profile can reproduce the more general global results when the normalized gyro-radius $\rho_\star = \rho_s / a < 1/300$. The current plasmas under investigation in this thesis have a characteristic value of $\rho_\star \approx 1/100$. This suggests that global effects including profile variation in the equi-

librium might be an important ingredient to include in nonlinear gyrokinetic simulations of the spherical tokamak core. However, due to the importance of the smaller scale ETG-driven turbulence under investigation in this thesis (for which $\rho_e/a << 1/300$), the global approximation could only break down in ion-scale simulations, but not in electron-scale simulation. However, investigation of global effects was out of the scope of this work.

Multiple instabilities may be present simultaneously in NSTX plasmas, and isolating the effects of individual instabilities can be difficult. The higher magnetic field and current in NSTX-U and MAST-U will provide access to much lower collisionality allowing suppression of micro-tearing modes [61, 136]. Higher magnetic field will also provide access to reduced fast-ion instability drive and enable the reduction (possibly suppression) of GAE modes [61]. Elucidating what mechanisms might be responsible for the dominant electron thermal losses and under what conditions is essential for understanding and predicting core performance of future fusion devices, and is part of the scope of this work.

2.7 The electron temperature gradient mode (ETG)

The electron temperature gradient instability is a major candidate for explaining anomalous levels of electron thermal transport experimentally observed in some operating regimes. Ion thermal transport however, is routinely observed at neoclassical levels in most NSTX H-mode plasmas, consistent with low-k (ion-scale) turbulence suppression from large $E \times B$ shear driven by neutral beam (NBI) driven plasmas ([8–10]).

Radial transport of electron thermal heat flux is often modeled with a linear dependence on the electron temperature gradient. In order to account for possible non diagonal transport terms in the electron thermal heat flux, the linear dependence on the electron temperature gradient can be offset by a quantity, which defines a critical gradient $(\nabla T_e)_{crit}$ [37–39], and the expression for the modeled heat flux can be expressed as

$$q_e = n_e \chi_e (\nabla T_e - (\nabla T_e)_{crit}) \tag{2.5}$$

where $\chi_e = 0$ for values of $\nabla T_e < (\nabla T_e)_{crit}$. This formula deserves two important comments: 1) When $\nabla T_e < (\nabla T_e)_{crit}$, the radial electron heat flux predicted by this

model is zero. Experimental observations support this conclusion [37,38]. 2) As its name indicates, the ETG instability is driven by the electron temperature gradient. The critical electron temperature gradient can be also regarded as a threshold for ETG instability.

An analytical expression for the critical gradient was derived in [70] by carrying out many linear gyrokinetic simulations. We refer to this expression by the *Jenko critical gradient*. It is given by

$$(R_0/L_{T_e})_{crit} = \texttt{max} \left\{ \begin{array}{c} 0.8R_0/L_{n_e} \\ (1+\tau)(1.33+1.99\hat{s}/q)(1-1.5\epsilon)(1+0.3\epsilon d\kappa/d\epsilon) \end{array} \right\} \quad (2.6)$$

where $\tau = Z_{eff}T_e/T_i$. In this expression, quantities L_X are defined as $L_X = -\mathrm{d}lnX/\mathrm{d}r$ correspond to typical scale lengths of a quantity X. R_0/L_X are normalized gradients of the quantity X, such as R_0/L_{T_e} and R_0/L_{n_e}, and R_0 is the corresponding flux surface center. Z_{eff} is the effective ion charge, T_e is the electron temperature, T_i is the ion temperature, $\hat{s}$ and q are the magnetic shear and safety factor. ϵ is the inverse aspect ratio. The two components of this formula represent linear instability thresholds for the slab version of the ETG mode ($0.8R_0/L_{n_e}$) and the toroidal version of ETG, which includes the magnetic field inhomogeneity and geometry. It is important to mention the regime of validity of this formula. The electron temperature critical gradient in equation 2.6 was derived under the assumptions of positive magnetic shear ($\hat{s} \geq 0.2$), low-β and large aspect ratio A. These conditions preclude the use of 2.6 in typical NSTX plasmas, characterized by high-β and small aspect ratio. However, the linear critical gradient formula for ETG has been shown to work remarkably well when used in realistic NSTX plasmas [127, 130, 212].

The Jenko critical gradient formula 2.6 results very useful in practice, as it allows to characterize some of the parametric dependencies of the ETG instability. One direct and obvious dependency is the normalized electron density gradient R_0/L_{n_e} of the slab version of ETG. According to expression 2.6, the electron density gradient is predicted to have a stabilizing effect on the ETG instability. High values of the electron density gradient will make the $0.8R_0/L_{n_e}$ term dominant in expression 2.6, thus it will determine the value of the critical gradient. As we have seen, variations in R_0/L_{n_e} or $\hat{s}$ will give rise to different values of $(R_0/L_{T_e})_{crit}$, thus having an effect on transport, as predicted by 2.5.

High enough values of R_0/L_{n_e} will even be able to set the critical ETG to values above the local temperature gradient value. This is thought to be the responsible mechanism behind the stabilization of ETG by density gradient that has been previously reported [127, 130, 212].

The ETG mode was long hypothesized to produce negligible transport in tokamak-scale experiments due to their small characteristic spatial scale $\sim \rho_e$, on the order of 0.1 mm for reactor scale parameters ($T = 15$ keV, $B = 5$ T). Gyro-Bohm estimates indicate that the electron thermal diffusivity $\chi_e^{gB} \sim \rho_e^2 v_{te}/L_{Te}$ is a factor of $\sqrt{m_i/m_e}$ smaller than the ion thermal diffusivity $\chi_i^{gB} \sim \rho_i^2 v_{ti}/L_{Ti}$, such that $\chi_e^{gB} \sim \chi_i^{gB}/60$ in deuterium plasmas. This estimate suggests that transport of electron energy is not a significant fraction of the total transport in the tokamak and should not be relevant in a reactor. Similar conclusions can be reached by applying mixing-length arguments for the transport coefficients $D, \chi \sim \gamma/k_y^2$ [66].

The discovery and prediction of ETG streamers using-state-of-the-art nonlinear gyrokinetic simulations [67–69] supposed a major breakthrough in the understanding of the ETG mode. Streamers are poloidally thin and radially elongated structures capable of very efficiently transporting heat radially out from the hot core region to the cold edge of the plasma ($cf.$ figure 2-4). This seminal work predicted experimentally relevant electron thermal transport dominated by ETG streamers 2-4. Nonlinear gyrokinetic simulation of ETG predicts streamer-dominated transport exceeding up to 10 times the Gyro-Bohm estimates of $\chi_e^{gB} \sim \rho_e^2 v_{te}/L_{Te}$, both in circular model equilibria [67–69, 71] and more recently in realistic NSTX tokamak equilibria [128]. However, electron thermal transport predictions by ETG modes have generally been shown to underpredict experimental transport levels.

More recent work by N. Howard [72–75] has further confirmed the importance of ETG through integrated simulation of ion and electron scale turbulence. Multiscale gyrokinetic simulation able of simultaneously resolving ion and electron scales has allowed the study of complex, non-intuitive cross-scale coupling processes between ion-scales ($k_\theta \rho_s < 1$) and electron scales ($k_\theta \rho_s > 1$). This work highlighted the importance of ETG turbulence in conditions where ion-scale turbulence is close to marginal and electron-scale turbulence is strongly driven. In such conditions, electron-scale turbulence and the ETG mode were

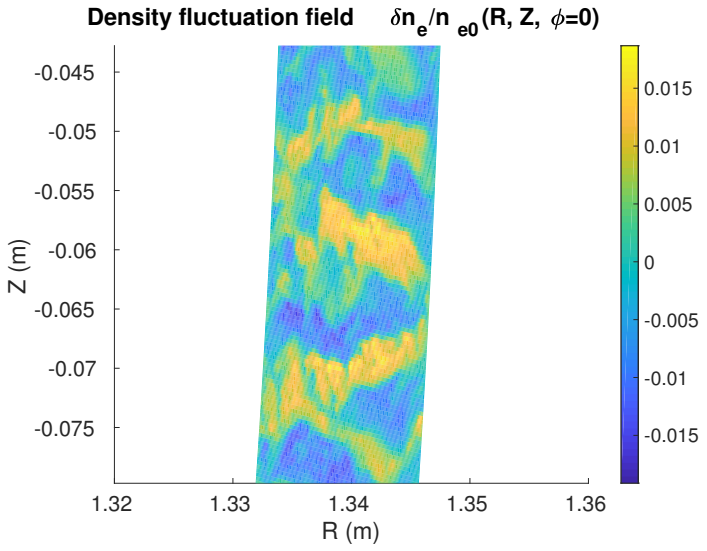

Figure 2-4: Electron density fluctuation field at the outboard midplane, at a fixed toroidal location, and at a fixed time slice $t = t_0$ where ETG turbulence fluctuations were highly unstable $\delta n_e(R, Z, \varphi = 0, t = t_0)$. The electron density fluctuations exhibit poloidally thin and radially elongated structures, so-called streamers, that are responsible for the dominant transport losses of electron heat flux from ETG turbulence.

shown to dominate the electron thermal transport, producing $\sim 70\%$ of the total electron heat flux [74]. However, the transport predicted from multi-scale simulation could not be simply reproduced by summing single-scale ion and electron simulations, due to the important effects of cross-scale coupling. Due to the computational demands, only a handful of multiscale simulations have been carried to date [74, 76, 223]. Determining the conditions in which cross-scale coupling interactions are important is critical for reactors, since electron thermal transport is expected to dominate in burning plasma conditions.

There are many indications in the literature that ETG-driven turbulence may play a role in anomalous electron thermal transport in NSTX, depending on the parametric regime of operation [78, 136]. Nonlinear gyrokinetic simulations of the ETG mode have been shown to match the electron heat flux in some high-beta NSTX NBI-heated H-mode plasmas, exhibiting dominant transport contributions by streamer-like fluctuations. Recent work in a MAST NBI-heated H-mode discharge [79] found a remarkable correlation between the ETG-driven electron heat flux and electron collisionality, through the interaction of ETG turbulence and the long-time saturation of zonal flows. This work suggested the spherical tokamak collisionality scaling $B\tau_E \sim 1/\nu_e^*$ [8] be related to the collisional damping of electron-scale zonal flows. However, this work was performed with adiabatic ions, electrostatic fluctuations and no impurities, and more dedicated simulations would be required to confirm these results with additional physics. Although remarkable, these simulations were shown to be far from reproducing the experimental electron heat flux levels, leaving an important question mark to understanding the full picture of electron thermal transport and the spherical tokamak collisionality scaling through the ETG mode.

Chapter 3

Introduction to validation and past validation work of turbulent transport in STs

This thesis presents systematic and rigorous experiment/model comparisons of turbulence and transport processes in the context of spherical tokamak H-mode plasmas. In the broader scheme of things, this thesis is a 'validation' effort that combines experiment/model comparisons at different levels of hierarchy. In this chapter I introduce some of the fundamental concepts in validation of turbulence and transport models for magnetic confinement fusion, which will serve as a basic guideline for the experiment/model comparisons presented in this thesis. Many of the validation concepts I introduce here are taken from seminal references in the validation community to magnetic confinement fusion [99–103]. The reader is referred to those references for more complete description of the concepts and examples. In the second part of this chapter I also present a short, non-exhaustive review of previous validation work of turbulence and transport models carried out in the context of spherical tokamak plasmas. This discussion will help put in context some of the novelties of this thesis, such as multi-level hierarchy comparisons and the first successful quantitative comparison of frequency and wavenumber spectra of high-k turbulence in spherical tokamak plasmas.

3.1 Introduction to validation in magnetic confinement fusion research

3.1.1 Gaining predictive capability

In the world of magnetic confinement fusion, gaining predictive capability has become a major priority. Current high performance fusion experiments such as tokamaks and stellarators operate ever closer to fusion conditions, but future fusion reactors still represent a notable extrapolation in terms of physics parameters and physics processes with respect to current experiments. As an example, the population of fusion alpha particles in ITER [104] will greatly exceed those of any past fusion experiment: how well will those particles be confined? what will be their effect on destabilizing Alfven eigenmodes? how will that impact transport processes of the background plasma, especially electron thermal transport? how well will they transfer their energy to electrons in the presence of turbulence? In this context, extrapolating to new physics regimes in fusion naturally opens up currently unanswered questions that we can only start tackling by combining advanced physical models with current experimental measurements. We wish to gain confidence in our predictions using the currently available physical models.

Other related fields to fusion have in fact already gained great confidence in their physical models, such as the field of aerodynamics and computational fluid dynamics (CFD). Nowadays CFD codes are routinely used for the design of commercial airplanes, and they have been shown to produce great reliability. This signifies maturity in the understanding of the physical processes taking place, allowing confidence in their predictions. Unfortunately, the field of fusion has still not reached that level of confidence. Confidence in the physical models is only gained through a thorough validation process.

Validation of physical models in fusion is specifically important due to the wide range of spatial and temporal scales involved. As is described in [100], there is currently not one single (useful) model able to describe all physical scales in a fusion plasma: the largest scales, typically on the device size $\sim a$ (minor radius) are usually described by the field of magneto-hydrodynamics (MHD or related models); smaller scales on the ion-gyroradius scale ρ_i are usually described by the gyrokinetic model (or reduced deriva-

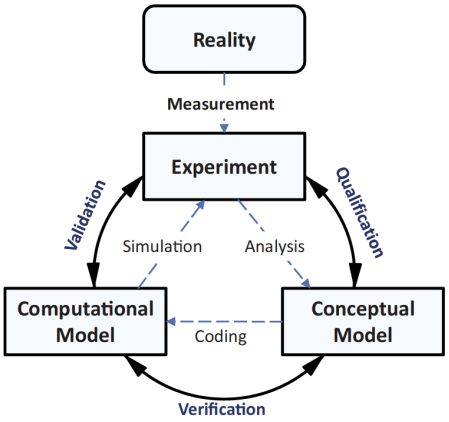

Figure 3-1: Figure illustrating the concepts of validation, verification and qualification of a physical model with respect to experiments. Image courtesy of [100].

tions such as fluid models); even smaller scales such as the Debye length can be described by radiofrequency (RF) models. Similar categorizations can be made for the temporal scales, as well as for the different physical domains in the plasma: the plasma core, the pedestal, the scrape-off layer ... we find a wide range of physical models describing very specific physical conditions in fusion plasmas. Additionally, plasmas routinely exhibit highly nonlinear behavior, and they exist in complex geometries that are dictated by the structure of the magnetic field. All of these factors have resulted in highly sophisticated numerical codes, each describing very specific physical phenomena. This has naturally increased the difficulty of comparisons with experimental measurements, which have very limited diagnostic capability in fusion conditions. The field of validation tries to overcome these difficulties by presenting systematic methodologies for establishing experiment/model comparisons to "improve the confidence in predictions derived from complex simulations" [100].

3.1.2 Basic concepts

I start by briefly introducing the concepts of validation, verification and qualification. As is described in [100], the concept of ***validation*** is "the process of determining the degree to which a model is an accurate representation of the real world from the perspective of the intended uses of the model; an exercise in physics". Validation of a physical model

requires meaningful comparisons between a computational model and experiment, as is illustrated by figure 3-1 taken from [100]. A model is said to be validated if it is able to consistently reproduce experimental measurements over a wide range of physics parameters and operating regimes for which it is designed to be applicable (qualified). The process of ***verification*** "assesses the degree to which simulations correctly implement a physical (conceptual) model" [100]. The exercise of verification tries to answer the question: does a computational model correctly implement a conceptual model? In a verification activity one tries to understand whether the conceptual model equations are correctly implemented in the computational model, and whether the numerical algorithms implemented provide reliable numerical solutions: a problem naturally pertaining to the field of applied mathematics. The concept behind ***qualification*** can be defined as "the theoretical specification for the expected domain of applicability for a model" [100], ie. a conceptual model is qualified to explain a certain experimental measurement if experiment lies within the realm of applicability of the conceptual model. For example, Newton's theory of gravity would not be qualified to explain the physics behind black holes (for which one would need the model of general relativity or more advanced treatments), but Newton's theory of gravity is generally well qualified to explain the dynamics of planets around the solar system. The three concepts of validation, verification and qualification are all illustrated in figure 3-1. The present thesis will mainly focus on validation. Extensive verification work has already been performed for the gyrokinetic code GYRO used in this thesis [98]. However, as will be shown in appendix F, numerical resolution and convergence tests performed in this thesis can be seen as part of the verification effort. With respect to verification, current fusion experiments routinely lie in the regime of applicability of the gyrokinetic model: the gyrokinetic model is generally well qualified to explain small scale microinstabilities and turbulent processes in magnetic confinement fusion plasmas (although situations exist in which it may not, such as in the pedestal region or scrape-off layer in tokamaks).

In order to perform a quantitative validation analysis of a specific model, care must be taken to compute **uncertainties**, both in experimental measurements and in the models. Only by comparison of experiment and model with uncertainty one is able to assess the fidelity of the model. Experimental uncertainty is inherent to any successful measurement

of any physical quantity, due to lack of knowledge of relevant control parameters, and can result in randomness of the measurement. Numerical models also have uncertainties. When treating chaotic, turbulence predictions such as in this thesis, one common way to treat uncertainties is by using statistical methods (e.g. standard deviation), as will be done in this thesis. **Validation metrics** try to quantify the agreement in a specific experiment/model comparison. As explained in [100], if we denote by y_i a set of n simulated values, and Y_i a set of n experimental measurements associated to a specific observable (heat flux, for example), a simple validation metric might be $V = 1 - \frac{1}{n}\sum_{i=1,n}\tanh|\frac{y_i - Y_i}{Y_i}|$. In this simple expression, the value 1 would signify perfect agreement, while the value 0 would mean complete disagreement. The specific mathematical definition of a validation metric can be variable, but they could (and probably should!) take into account experimental and simulation values and uncertainties, as well as the meaningfulness of the comparison (hierarchy level, see below) to provide a quantitative assessment of the experiment/model comparisons. References [99–103] all provide different examples of validation metrics at different levels of sophistication. In the present work I will closely follow definitions of a validation distance and metric introduced in [101–103]. In order to quantify the overall assessment of a specific model, one can design a **composite metric** taking into account values of the different metrics associated to each specific observable. In the present work, I will use metrics quantifying the predictions of turbulence spectra as well as the thermal transport predictions from nonlinear gyrokinetic simulation. These will ultimately combine to a composite metric providing the overall assessment of each numerical model.

3.1.3 Importance of validating turbulent transport models

In [103] it is argued how validation is specifically important for the field of turbulence and transport. The ultimate goal of the field of turbulence and transport is the prediction of equilibrium density and temperature profiles of future fusion devices. Equilibrium profiles are set by transport processes. However as we saw in chapter 2, very sophisticated models such as the gyrokinetic model need to be used to explain the anomalous electron thermal transport losses in current tokamak experiments. To date, experimental measure-

ments, theory and modeling efforts have provided strong evidence supporting the premise that turbulent processes are the main driving factors of the cross-field particle and energy fluxes that end up ultimately determining the plasma profiles. However, current plasma experiments cannot directly measure cross-field fluxes: no probe or physical device would survive the harsh environments of fusion plasmas. The field has recently relied on establishing comparisons of experimental transport estimates (via power-balance calculations such as in TRANSP [105]) with transport model predictions, and in the best of cases, coupled with simultaneous comparisons between limited measured and predicted turbulence fluctuation characteristics.

Years of research in the field of transport have taught us that transport processes exhibit great sensitivity to plasma control parameters and turbulence drive terms, resulting in equilibrium profiles lying very close to criticality. This means that tiny changes in turbulence drive terms (generally lying well within the experimental uncertainty) can result in wildly different transport scenarios and predictions. This problematic reality results in highly unconstrained transport models, and could naturally open the door to fortuitous agreement between model and experiment. It is then of great interest to improve the quality of experiment/model comparisons via the implementation of additional constraints on the turbulence model.

Validation hierarchy

In order to quantify and improve the experiment/model comparisons, the concept of validation hierarchy was introduced in [99] to combine meaningful comparisons at differing levels of significance: "The primacy hierarchy tracks how measured quantities integrate or combine to produce other measured quantities. A quantity is assigned a lower primacy level if its measurement integrates fewer quantities" [99]. To illustrate this, in figure 3-2 is shown the primacy hierarchy for turbulent transport, taken from [100]. At the lowest level lie the rapidly fluctuating quantities such as density and potential fluctuations $\tilde{n}, \tilde{\phi}$. Recall from section 2.2 using the simplest drift wave mechanism in a slab how radial transport needs a phase shift between the potential and density fluctuations. At a higher level in the hierarchy of turbulent transport would be the wavenumber spectrum and related quantities computed by use of primary quantities, such as the coherency,

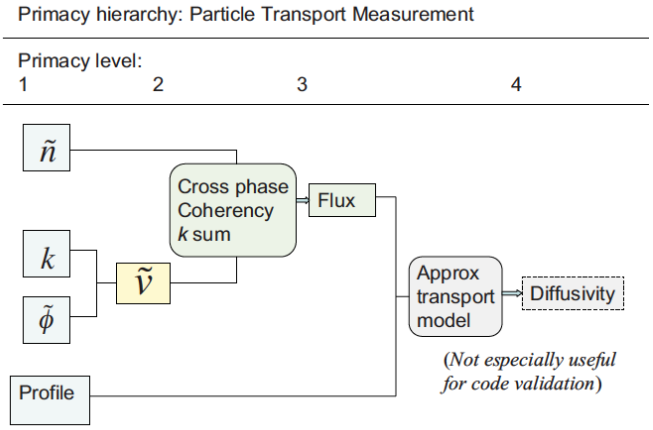

Figure 3-2: Figure illustrating the primacy hierarchy for particle transport, highly equivalent for thermal transport. Combination of the lowest level quantities ($\tilde{n}, \tilde{\phi}, ...$) combine to produce higher level quantities such as the wavenumber spectrum, transport fluxes and ultimately predicted profiles. Image courtesy of [99].

cross-phase, etc. At en even higher level one would find the transport fluxes, which are computed by integration of the wavenumber spectra quantities. At the highest level would be the predicted profiles from the model, computed by transport analysis of the predicted fluxes. Achieving meaningful equilibrium profile predictions is the ultimate goal of the turbulence and transport community. Quantitative validation of the models used for profile prediction requires comparisons at all levels in the validation hierarchy.

Synthetic diagnostics

Nowadays there exist high quality diagnostics able to measure plasma quantities at the lowest level in the validation hierarchy, such as density fluctuations. High quality diagnostics are of great importance to model validation, since they provide strict constraints that models should satisfy. As it is argued in [100], "comparison of time series data provide some of the most fundamental validation tests", meaning they are the most constraining, ultimate test that a transport model should pass to be fully validated. Although significant progress has been made in the development of advanced high quality diagnostics, they still suffer from limited resolution (temporal, spatial, and spectral) and they generally require advanced modeling and a-priori knowledge for the interpretation of the measurement as a meaningful plasma quantity. With respect to numerical model simulations, most of them have been designed to provide meaningful predictions and comparisons of the highest

level quantities in the hierarchy, such as fluxes in a gradient-driven simulation or profiles in a flux-driven simulation. Direct numerical simulation provide more turbulence fluctuation "data" than could ever be measured, but can generally not be directly compared to measurements of the most fundamental quantities (lowest level in the hierarchy such as fluctuation data). This is due to specific information of the diagnostic e.g. frequency and wavenumber resolution, yielding possible only qualitative comparisons. This difficulty can be overcome by the more recent development of synthetic diagnostics.

Synthetic diagnostics are complex numerical tools that incorporate diagnostic characteristics such as viewing geometry, spatial, temporal and spectral resolution with advanced characterization and modeling of the diagnostic to a high level of fidelity, resulting in a direct map of the numerical solution to the experimental measurement. Synthetic diagnostics naturally yield direct, quantitative comparisons of plasma quantities lying at the lowest level in the validation hierarchy. However, as complex numerical tools they require a careful and thorough verification and numerical testing procedure themselves. In the context of the present thesis, I have implemented two synthetic diagnostics for high-k scattering, yielding for the first time direct quantitative comparisons (and agreement) of high-k frequency and wavenumber spectra of density fluctuations in a spherical tokamak. Careful verification and testing of the synthetic diagnostic was performed with reduced model cases such as in 1D, 2D circular geometry, the exclusion of plasma rotation (no Doppler shift), etc. but ultimately the most stringent verification test for the synthetic diagnostics presented in this thesis is the accurate quantitative agreement between both synthetic diagnostic implementations, in real space $vs.$ k-space. The equivalent formulation and implementation of synthetic diagnostics in real space and in k-space, applied to coherent scattering fluctuation measurements is a novel contribution to the field and provides great confidence in the accuracy of the synthetic spectra presented in this thesis.

Validation efforts of this thesis

In the context of the present thesis I will make extensive use of the high-k scattering diagnostic, sensitive to high-k electron density fluctuations. Lying at the lowest level of the hierarchy will be the measurement of the frequency spectrum of high-k fluctuations, that will be compared with synthetically generated frequency spectra from a gyrokinetic

simulation. Analysis of the frequency spectrum will yield the wavenumber spectrum of density fluctuations, naturally lying at a higher level in the hierarchy. Transport fluxes will be internally computed from simulated wavenumber spectra, and will lie at the highest level in the hierarchy for the present work. In this thesis I will not make profile predictions with the present models, as they are out of the scope of the present work. I will focus on establishing meaningful, quantitative comparisons at the most fundamental levels in the validation hierarchy, to validate local, nonlinear gyrokinetic simulation of electron scale turbulence in spherical tokamak H-mode plasmas.

3.2 Review of past validation work of core transport turbulent models in STs

In this section I introduce some of the most recent validation efforts of turbulence and transport models in spherical tokamaks, focusing attention to NSTX and MAST. I first introduce validation efforts in the NSTX device, which has focused a lot of attention to the study of the ETG mode and the micro-tearing mode, both from linear and nonlinear experiment/model comparisons, as well as some early work to establish quantitative comparisons of electron-scale density fluctuations. I then introduce a summary of past modeling and gyrokinetic simulation validation work performed in the MAST device, from linear gyrokinetic comparisons to nonlinear and even more recent efforts of establishing direct quantitative comparisons of low-k turbulence using a beam emission spectroscopy diagnostic (BES).

As discussed in chapter 2, electron thermal transport is routinely observed to be the dominant heat loss mechanism in spherical tokamak H-mode plasmas such as NSTX [8] and MAST [13] while ion thermal transport lies close to neoclassical estimates. However, although commonly observed, ion thermal transport is not always neoclassical and understanding the underlying causes is important for achieving a complete picture of the ST confinement properties. Likely for different motivating reasons, recent validation efforts in NSTX appear to have mainly focused on understanding anomalous electron thermal transport, while MAST's efforts appear to have mainly focused attention, especially in

most recent times, to ion thermal transport.

The work highlighted in the following sections will be shown in increasing order in the validation hierarchy comparisons: I have included some more fundamental work focusing on instability and transport predictions for NSTX (section 3.2.1.1) and MAST (section 3.2.2.1), work focusing on preliminary qualitative comparisons between experiment and models (NSTX in section 3.2.1.2 and MAST 3.2.2.2), quantitative comparisons of transport fluxes (NSTX in sections 3.2.1.3, 3.2.1.4, and MAST 3.2.2.2), and finally some initial efforts on direct turbulence comparisons that have only very recently started to appear with the high-k scattering diagnostic in NSTX (section 3.2.1.5) and with the BES system in MAST (sections 3.2.2.3, 3.2.2.4).

3.2.1 Validation efforts in NSTX

3.2.1.1 Initial linear instability and transport projections

Some of the early microstability calculations in NSTX carried out by M. Redi already projected unstable tearing parity micro-tearing modes in an NSTX H-mode [106], using the gyrokinetic code GS2 in fully electromagnetic mode. In this work the micro-tearing mode was projected as a potential candidate for explaining anomalous electron heat diffusivities χ_e experimentally inferred. The following year, Redi reported on progress in nonlinearly simulating the micro-tearing mode in NSTX [107], highlighting the high computational requirements, some 2 orders of magnitude higher with respect to standard nonlinear ITG simulations at the time. Further progress on NSTX microstability analyses was reported yet one year after by the same author in [108], additionally reporting on NSTX L-mode discharges sitting very close to the kinetic-ballooning mode threshold.

Motivated by previous microstability studies and projections for spherical tokamak equilibria, C. Bourdelle [109] carried out detailed microstability analyses of spherical tokamak equilibria that highlighted the stabilizing impact of β' on conventional electrostatic instabilities such as the ITG, TEM and ETG. The high β' values reachable in spherical tokamaks with respect to conventional tokamaks should stabilize ITG, TEM and ETGs, and was proposed as a control stabilizing parameter of microturbulence in addition to the already known background $E \times B$ shear. In addition, β' stabilization could possibly

form a positive feedback loop, in which high β' stabilization of electrostatic instabilities would further enable increased β'. It was also highlighted in this work that the kinetic ballooning mode remained unstable at high β', possibly limiting the pressure gradient in these conditions.

With respect to transport calculations, early work by W. Horton *et al.* [110] showed that electron heat fluxes and heat diffusivities χ_e could be entirely explained via a reduced model for the ETG mode, providing some of the first evidence supporting turbulent transport associated to the electron temperature gradient mode in NSTX. Analysis was performed on an NSTX HHFW-heated L-mode, and used a reduced FLR-modified fluid code solving reduced transport fluid equations relevant for the ETG in slab geometry. Later calculations by S. M. Kaye [8] also reported on the relevance of ETG electron thermal transport in NSTX H-modes via reduced fluid model nonlinear calculations, GYRO nonlinear calculations and theoretical scalings of the electron heat diffusivity due to the ETG mode compared with inferred power balance heat diffusivities. These works are some of the first modeling evidence supporting the ETG mode as a potential candidate responsible for anomalous electron thermal transport in NSTX, and consequently motivated further experimental developments and modeling efforts on the ETG mode.

Later work by Stutman *et al*. [111] predicted micro-tearing modes to be unstable in the inner core of a low density NSTX NBI-heated L-mode plasma, in conditions in which ETG and ITG instabilities were stable due to the lack of instability drive. These linear electromagnetic calculations were carried out with the gyrokinetic code GS2, and were consistent with anomalous electron thermal transport at the inner core. This work also reported electrostatic instabilities such as ETG and ITG to be unstable at outer radii due to the increased instability drive, emphasizing the importance of the microtearing instability in the inner core of NSTX. Similar calculations by S. M. Kaye [8] and Levinton [112] also pointed out unstable micro-tearing modes in the core of NSTX by use of linear gyrokinetic calculations with GS2 [113], GYRO [114] and GTC [115]. Subsequent efforts by K. L. Wong *et al.* [116, 117] observed the electron thermal diffusivity χ_e in an NSTX NBI-heated H-mode discharge could be explained by electromagnetic fluctuations from the microtearing mode. Wong's works used a quasi-linear theoretical estimate for the saturation amplitude for the microtearing mode proposed by Drake [118], coupled with

electron thermal conductivity estimates derived from the Rechester-Rosenbluth stochastic model [119]. Although these calculations provided values of the electron heat diffusivity that were consistent with experimental estimates, it is important to note that they were based on slab theory calculations in [118] and cylindrical geometry in [119].

These initial efforts presented here have focused on the ETG mode on the one hand, and on the microtearing mode on the other. They combined linear stability calculations of realistic NSTX plasmas for both modes, and were coupled with preliminary assessments of electron thermal transport. Although not quantitative and often based on reduced model simplifications such as slab geometry and in 2D, these works already provided some of the first motivations for more detailed experimental, theoretical and model validation efforts of the ETG and microtearing modes that would follow on NSTX.

3.2.1.2 Qualitative experiment/linear comparisons

The implementation of the old high-k scattering diagnostic in NSTX by D. R. Smith, E. Mazzucato *et al.* [65, 120] (the same diagnostic used in the present thesis) triggered much of the validation work that would consequently follow on NSTX. These efforts at NSTX were an important breakthrough in the understanding electron thermal transport in STs, resulting in a series of papers [121–124] revealing the first direct measurements of high-k electron density fluctuations in a spherical tokamak plasma. The fluctuation spectra was subsequently correlated to some of the linear properties of the ETG mode. As a consequence early validation efforts mainly focused on establishing qualitative comparisons between measured fluctuations and linear gyrokinetic simulation, mostly for the purpose of identification of the ETG mode and some of its parametric dependencies.

Consequent efforts by E. Mazzucato [121, 122] revealed electron-scale density fluctuations in NSTX L-mode plasmas that were heated by high-harmonic fast wave heating. The amplitude of the detected fluctuations was shown to be correlated to the background electron temperature gradient and exhibited a propagation frequency in the electron diamagnetic drift direction, as suggested by linear gyrokinetic simulations of the ETG mode. Fluctuations were detected in linearly-unstable ETG regimes. In addition, electron-scale fluctuations were not observed in internal transport barrier conditions developed due to negative magnetic shear, where negligible transport is expected. These correlation prop-

erties provided increased evidence supporting the ETG mode as a potential candidate for explaining electron thermal transport in NSTX, based on the detection of electron-scale fluctuations and linear correlation properties to the ETG mode.

Subsequent work by Smith *et al*. [123, 124] performed in an NSTX NBI-heated H-mode plasma showed that electron-scale density fluctuations detected by the high-k scattering system were anti-correlated to the background level of the $E \times B$ shearing rate, suggesting ETG turbulent fluctuations can be stabilized by strong $E \times B$ shear, just as the ITG mode counterpart. Work by H. Yuh *et al* [125, 126] reported that detected electron-scale density fluctuations can be fully suppressed by strong negative magnetic shear in an internal transport barrier. Subsequent comparisons with linear gyrokinetic calculations showed that the so-claimed ETG turbulence suppression could not be explained by the linear physics, since suppressed density fluctuations were observed in highly linearly unstable ETG regimes, suggesting negative magnetic shear must be nonlinearly suppressing ETG turbulence.

Y. Ren *et al*. [127] made an important contribution by analysis of high-k scattering data via the "first clear experimental evidence of density gradient stabilization of electron-gyro scale turbulence in a fusion plasma". The analysis was performed in an NSTX H-mode plasma, where a local change in the background density gradient at the scattering measurement location (following an ELM event) was shown to be the main responsible mechanism behind the stabilization of e- scale turbulent fluctuations detected by the high-k scattering system. This observation was coupled with linear gyro-kinetic calculations of the ETG mode carried out with the gyrokinetic code GS2, which further supported the experimental observations and led to to the identification of the observed turbulent fluctuations as toroidal electron temperature gradient (ETG) modes.

These works supposed the first experiment/model comparisons of the ETG mode in a spherical tokamak plasma, although they were restricted to comparisons of the linear properties of the ETG mode and were unable to assess any transport contributions to electron thermal transport. However these efforts motivated subsequent nonlinear gyrokinetic calculations of NSTX plasmas.

3.2.1.3 Experiment/nonlinear comparisons of the ETG mode

Much of the work described in this section focuses on comparisons between experimentally detected electron-scale fluctuation spectra from the NSTX high-k scattering system with thermal transport predictions from ETG-turbulence using nonlinear gyrokinetic simulation.

Work by W. Guttenfelder [128] reported on successful nonlinear gyrokinetic calculations of ETG turbulence in NSTX plasma using the gyrokinetic code GYRO. This work was an important contribution to the understanding of ETG transport and was foundational for the realistic high fidelity characteristics of the simulations, based on the first-principles gyrokinetic model. Although these nonlinear gyrokinetic simulations were electrostatic and collisionless, they modeled both electrons and ions gyrokinetically, included background flow and flow shear, and demonstrated convergence on numerical grid resolution, physical domain size and boundary conditions. Importantly, the predicted electron thermal transport via nonlinear gyrokinetic simulation was consistent with experimental transport observations in NSTX and MAST, a clear first step towards the validation of electron-scale gyrokinetic simulations in NSTX. This work was also part of the basis for the electron-scale nonlinear simulations presented in this thesis.

Consequent efforts by J. L. Peterson *et al.* [129] built upon Guttenfelder's nonlinear simulation work and H. Yuh's work on internal transport barriers in NSTX [125, 126], and carried the first nonlinear gyrokinetic ETG simulations of NSTX internal transport barriers. In such conditions ETG was predicted to be highly unstable. Local nonlinear simulations showed that the local magnetic shear value was a critical parameter for triggering the formation of the barrier and determining the nonlinear critical gradient for turbulent transport. Global nonlinear gyrokinetic simulations including profile variation of the barrier showed that the predicted ETG-driven flux was comparable to the experimentally inferred value in the outer part of the barrier (where magnetic shear was mildly negative). However, in the inner part of the barrier where magnetic shear was strongly negative, nonlinear simulation showed that ETG-driven turbulent transport was fully suppressed, and unable to account for the residual transport levels observed experimentally. This work had strong implications for the ETG mode, emphasizing how the control of

the plasma current profile is able to stabilize and even fully suppress ETG-driven electron thermal transport via negative magnetic shear, without having to recourse to background flow-shear as a stabilizing mechanism of ETG turbulence.

Y. Ren *et al*. extended previous work on density gradient stabilization of ETG to include nonlinear gyrokinetic simulation transport estimates in [130]. For the same experimental discharge as in [127], nonlinear gyrokinetic simulations using the GYRO code predicted electron heat flux values consistent with the reported density gradient stabilization of ETG. This contribution suggested that density profile control may be used to control microturbulence in STs via the suppression of ETG, while keeping lower-k ITG and TEM modes quiet. [130] also performed a parametric study of electron-scale turbulence with electron collisionality. This former study was motivated by the strong collisionality scaling of the energy confinement $B\tau_E \propto 1/\nu_*$ observed both in NSTX [8] and MAST [13]. In this work, the authors observed that experimentally detected spectral power from electron-scale fluctuations increased as collisionality decreased, contrary to what one might expect from the collisionality scaling. Linear and nonlinear gyrokinetic simulations using GS2 and GYRO showed almost no dependence of the ETG linear growth rate and electron heat flux with electron collisionality, suggesting other mechanism than ETG might be necessary to explain the ST collisionality scaling (nonlinear GYRO simulations included experimental profiles, gyrokinetic kinetic electrons and ions, collisions, fully electromagnetic fluctuations, toroidal flow and flow shear). The authors also reported that ETG turbulence alone was not able to explain the experimental electron thermal transport in those conditions. However, this work was a confirmation of the suppression of ETG turbulence by density gradient using nonlinear gyrokinetic simulation, and motivated further detailed parametric studies of turbulence and transport to understand the ST collisionality scaling.

Later work by Ren *et al*. [131] reported on the "first observation of the change in electron-scale turbulence wavenumber spectrum and thermal transport responding to continuous $E \times B$ shear ramp-up in an NSTX centre-stack limited and NBI-heated L-mode plasma". Analysis of high-k scattering spectra coupled to nonlinear GYRO simulation confirmed the stabilizing effect of $E \times B$ shear in both ion and electron-scale turbulence. The authors also included comparisons of both electron and ion heat fluxes, since ion

heat flux was observed to be above neoclassical levels. From the validation perspective, this work showed a clear step forward by combining electron and ion-scale gyrokinetic simulation comparisons of both ion and electron-scale turbulence in an NSTX L-mode plasma. Nonlinear GYRO simulations included experimental profiles, gyrokinetic electrons and ions, collisions, fully electromagnetic fluctuations, toroidal flow and flow shear

In [132] Ren reported on the "first observation of the fast response of electron-scale turbulence to auxiliary heating cessation in National Spherical Torus eXperiment RF-heated L-mode plasmas". In this work electron-scale fluctuation spectra was shown to decrease following the RF cessation. Power balance analysis showed the electron thermal diffusivity decreased by about a factor of 2 after the RF cessation, consistent with the observation of decreased fluctuation spectral power. However, neither linear GS2 calculations nor nonlinear, global gyrokinetic simulations with GTS were able to explain the experimental observation of decreased electron-scale fluctuation spectra. I note the GTS simulations were probably electrostatic (not clear in the publication).

The outcome of these works claimed for future work on improved quantitative comparisons of electron-scale turbulence, via a synthetic diagnostic, as well as multi-scale gyrokinetic simulation in NSTX plasma. This thesis supposes a step forward for the establishment of quantitative comparisons of electron-scale turbulence with a synthetic diagnostic for high-k scattering.

3.2.1.4 Experiment/nonlinear comparisons of micro-tearing turbulence

Previous work on the micro-tearing mode at NSTX included initial predictions of unstable micro-tearing instability in NSTX plasmas [8, 112], as well as subsequent transport studies in [116, 117] claiming the electron thermal diffusivity χ_e in an NSTX H-mode discharge could be explained by electromagnetic fluctuations from the micro-tearing mode. Building upon those works, an important breakthrough was accomplished via nonlinear gyrokinetic simulation of the micro-tearing mode in NSTX plasma conditions by W. Guttenfelder [133–136].

References [133, 134] by W. Guttenfelder reported on the "first-of-a-kind nonlinear gyrokinetic microtearing mode simulations which predict transport comparable to experimental results in the National Spherical Torus Experiment (NSTX)". The analysis was

performed in an NSTX NBI-heated H-mode discharge in which only the micro-tearing mode was found unstable. These nonlinear GYRO simulations predicted an electron heat diffusivity within experimental uncertainty of the experimental value, and dominated by magnetic flutter fluctuations (shear magnetic field perturbations $\delta A_{||}$). The GYRO simulations included two kinetic species, collisions and electromagnetic fluctuations, but not flow shear. Although it was observed how flow shear could in fact stabilize micro-tearing transport, still today it is not fully understood if and how, and how much $E \times B$ shear suppresses micro-tearing fluctuations.

Reference [134] by the same author included a systematic study of the parametric dependencies of the nonlinear turbulent flux, showing the micro-tearing mode was driven by electron temperature gradient, electron beta and collisionality and stabilized by $E \times B$ shear. The scaling of electron heat diffusivity with collisionality $\chi_e/(\rho_s^2 c_s/a) \sim 1/\nu_*$ was particularly important, as it was consistent with the observed ST energy confinement time scaling with collisionality (assuming a direct relationship between global confinement τ_E and local transport χ_e). Although quantitative numerical convergence was not shown, this work was the first serious step to validate nonlinear gyrokinetic simulations of microtearing mode turbulence in NSTX. Subsequent efforts by Smith [137] and Guttenfelder [135] provided further analysis of the linear micro-tearing mode in realistic NSTX plasmas, where they were shown to be unstable across much of the plasma profile. ETG-modes and kinetic-ballooning modes were also found unstable, indicating that multiple instabilities can be simultaneously driven unstable in experimental NSTX plasma scenarios. It is interesting to note that Smith [137] found unstable micro-tearing modes at electron-scales $k_\theta \rho_s \sim$ 3-15, while work by Guttenfelder mainly found micro-tearing unstable at ion-scales $k_\theta \rho_s \lesssim 1$.

Building on previous simulation work on the micro-tearing mode, Kaye *et al*. [138] have more recently reported on a reduced transport model for the prediction of the electron temperature profile in NSTX plasma. Based on a Rebut-Lallia-Watkins (RLW) electron thermal diffusivity model for microtearing-induced transport, the model was shown to predict reasonably well the electron temperature profile in microtearing dominated conditions, but not when microtearing was predicted to be stable or subdominant. The comparisons of the predicted and measured electron temperature profile were quantified via

validation metrics, and showed improved agreement than previous reduced models for microtearing [117]. From the validation perspective, this work was significant for the use of metrics to quantify the goodness of the comparisons found. Although the comparisons and T_e agreements in [138] are meaningful, Kaye concludes with an interesting discussion on the necessity to improve reduced transport models such as RLW, and base future reduced models on first principles, detailed gyrokinetic calculations (such as those performed by Guttenfelder) including much of the relevant fundamental physics processes thought to dominate transport processes in the spherical tokamak. Without that, experiment/model comparisons may suffer from fortuitous agreement, or even from qualification to the applicability in regimes relevant for spherical tokamak parameters.

References [136] by Guttenfelder and [64] by Ren include much of the previous discussions in a review format, summarizing recent understanding and efforts in simulating turbulent electron thermal transport in NSTX. [136] includes a particularly important section on TEM/KBM turbulence (to my knowledge not reported elsewhere in NSTX), in which hybrid TEM/KBM modes are shown to produce experimentally relevant electron heat fluxes at high-β, and are ultimately driven by the α parameter more commonly encountered in MHD calculations $\alpha_{\texttt{MHD}}$. The KBM mode is especially important since it is expected to be unstable in next generation spherical tokamak devices operating at high-β and lower collisionality, where the micro-tearing mode is predicted to be stable ($cf.$ figure 3-4). Particularly interesting is the discussion in [64] on electron thermal transport in the core flat region of NSTX, where traditional drift-wave instabilities are routinely found stable due to the flat profiles and reduced microinstability drive. Recent modeling work has shown that fast ion populations from the neutral beam injection can destabilize a broad range of Alfven eigenmodes (CAE/GAE) and drive electron thermal transport [139, 140], or even couple to kinetic Alfven waves (KAW) and drive electron thermal transport in the inner core via efficient outward energy channeling [141]. Although significant, these later modeling works on fast particle instabilities and transport are still in the exploratory phase and would need further comparisons and thorough validation studies in the inner core of NSTX.

3.2.1.5 Preliminary electron-scale turbulence comparisons with a synthetic diagnostic

Many of the discussions presented until now have focused on qualitative linear comparisons in 3.2.1.2. More comprehensive validation efforts of nonlinear gyrokinetics in NSTX plasmas resolving the electron temperature gradient mode are presented in 3.2.1.3, while efforts focusing on the micro-tearing mode are presented in 3.2.1.4. The nonlinear gyrokinetic simulation work presented so far is significant from the validation perspective since it establishes experiment/model comparisons of some of the highest level quantities in the validation hierarchy such as heat diffusivity, heat flux and profiles. However, as already mentioned in the previous section, a thorough validation study necessitates comprehensive experiment/model comparisons at multiple levels in the validation hierarchy, as well as direct comparisons of fluctuation quantities such as density fluctuations. The latter can be obtained by the use of synthetic diagnostics.

R. Bravenec's work [142] and M. W. Shafer's [143] were foundational to the tokamak turbulence and transport community by the implementation of synthetic diagnostics for beam emission spectroscopy (BES). In NSTX, F. Poli and W. Wang successfully implemented a synthetic diagnostic for high-k scattering [144] using the GTS code. This work consisted on the first attempt to establish direct, quantitative comparisons of high-k turbulence in NSTX. Foundational, this work provided some initial quantitative comparisons of electron-scale turbulence with synthetically generated turbulence. However the authors reported on uncertainties and systematic errors affecting the computation of the synthetic spectra, such as "errors in the measured profiles, in the integration of measured profiles onto magnetic coordinates, or from an imperfect mapping of magnetic topology to laboratory coordinates". Consequently, quantitative agreement between the experimental and synthetic frequency and wavenumber spectra could not be obtained. However, this pioneering work by F. Poli [144] laid down part of the foundations and initial motivation for the present thesis to develop a synthetic diagnostic for high-k scattering and establish quantitative comparisons of electron-scale turbulence in NSTX.

3.2.2 Validation efforts in MAST

3.2.2.1 Initial linear instability and transport projections

The development of the MAST spherical tokamak in the UK [18, 19] came about the same time as NSTX in the early 2000s. Validation work of linear and nonlinear gyrokinetic simulations was motivated by some early microinstability projections of MAST and MAST-like equilibria by Akers [145], Wilson [147] and Applegate [146]. Subsequent efforts followed similar lines as in NSTX via the study the ETG and micro-tearing modes, but the study of ion thermal transport and the stabilizing influence of flow shear on ion-scale instabilities in MAST was later emphasized, especially following the implementation of the BES system [169].

The first linear gyrokinetic simulations for MAST were carried out by R. J. Akers *et al*. [145] using the code GS2. These simulations were carried out both for low-k as well as high-k instabilities, respectively $k_\theta \rho_i \sim 1$ and $k_\theta \rho_e \sim 1$ in a high-β H-mode plasma. Low-k modes were claimed to be ITG, and shown to be destabilized by electromagnetic effects with eigenfunctions exhibiting tearing parity, being largely extended along the field lines and destabilized by collisions. It is likely that the authors simulated micro-tearing modes. Even earlier work by Kotschenreuther *et al.* [148] had already described the presence of unstable micro-tearing modes in low aspect ratio equilibria. For MAST, Akers reported on linear low-k growth rate values similar to the background $E \times B$ shearing rate, suggesting that these modes could be nonlinearly stabilized by background flow shear. At electron scales, ETG modes were shown to exhibit linear growth rates much higher than the $E \times B$ shearing rates and stabilized by electromagnetic effects.

Later work by Wilson *et al*. [147] performed linear microinstability analyses of ST equilibria as part of an integrated modeling study projecting future ST power plants (STPP). As in previous work by Akers, these linear studies carried out with GS2 also predicted the presence of tearing parity micro-instabilities at ion-scales and ETG modes at electron-scales. Similar observations were obtained by Applegate *et al*. [146] in microstability calculations with GS2 carried out for a spherical tokamak equilibrium that closely resembled a MAST H-mode plasma, highlighting the importance of electromagnetic effects.

Although qualitative, these studies were significant as being the first scoping microinstabilty studies motivating further developments on full nonlinear micro-tearing and ETG gyrokinetic simulations of MAST plasmas.

3.2.2.2 Linear and nonlinear gyrokinetic simulation comparisons in MAST

C. M. Roach *et al*. [149] presents a succinct review of microinstability studies performed to L-mode and H-mode MAST equilibria using the gyrokinetic code GS2. This work presented further evidence highlighting the importance of electromagnetic instabilities in the ST. In the L-mode case, low-k instabilities were shown to sit very close to the critical β for the onset of the kinetic ballooning mode, while in the H-mode tearing parity modes where shown to be the dominant instability. Electromagnetic effects were also shown to be important for the high-k ETG mode, behaving especially sensitively to parallel fluctuations in the electromagnetic field $\delta B_{||}$. Nonlinear gyrokinetic simulations carried out resolving the ETG mode exhibited highly elongated streamers structures, producing electron heat diffusivities χ_e much larger than simple mixing length arguments. Although experimentally relevant, the computed χ_e values underpredicted the experimentally inferred χ_e.

N. Joiner *et al.* [150] performed a systematic study of electron heat transport coefficients from ETG turbulence by use of nonlinear gyrokinetic simulation with GS2. The authors paid close attention to radial and poloidal box-size convergence and resolutions. At the inner flux-surface of MAST-like equilibrium at $\rho = 0.4$, the predicted electron heat diffusivities from nonlinear ETG simulation were comparable with the experimentally inferred χ_e values. Nonlinear simulation for outer flux-surface parameters at $\rho = 0.8$ was shown to underpredict the experimental χ_e values by close to an order of magnitude. At both locations, simulations predicted the presence of radially elongated streamers, but they were shown to produce more transport at the inner flux-surfaces. These results were further evidence from nonlinear gyrokinetic simulation pointing to the ETG mode as a major candidate to explain electron heat transport in MAST, especially at the inner flux-surfaces.

D. J. Applegate *et al*. [151] performed a thorough study of the micro-tearing instability characterizing the main linear dependencies in MAST equilibria using the gyrokinetic

code GS2. The authors performed the analysis on a neutral beam heated MAST Elmy H-mode discharge. The characterization of the instability current layer was consistent with linear tearing mode theory originally described by H. P. Furth [154]. In addition, the authors observed the micro-tearing instability was destabilized by magnetic drifts and by the electrostatic potential. As a consequence the authors predicted an enhanced micro-tearing drive at low aspect ratio and higher beta characteristic of STs. Collisionality was shown to exhibit a non-monotonic dependence: destabilizing for low collisionality values, but stabilizing at high collisionality values. Although this work cannot be considered a validation study since no comparisons to experimental measurements were performed, this contribution was highly relevant for the characterization of the micro-tearing instability predicted to be present in MAST H-mode plasmas.

R. J. Akers *et al.* [152] presented "the first non-linear Ion Temperature Gradient (ITG) and Electron Temperature Gradient (ETG) range simulations for MAST using the ORB5 and GYRO models". Global nonlinear simulations with the ORB5 PIC code (particle in cell) found temperature profiles lying close to the instability threshold in the absence of background flow shear, and suggested ITG could play an important role in MAST. For ETG, the authors compared a phenomenological critical gradient transport model for the electron heat diffusivity $\chi_e^{ETG} = F(\hat{s}, T_e/T_i, ...)(\rho_e^2 v_{Te}/L_{Te})[R/L_{Te}\text{-}R/L_{Te}^{crit}]$ to the experimentally inferred χ_e. The reduced ETG model was shown to produce experimentally relevant levels of χ_e, but could not match the experimental profile shape of the heat diffusivity, suggesting additional physics should be included in the reduced ETG χ_e model. This left the authors unable to conclude on the relevance of ETG transport on MAST. Motivated by previous work on the micro-tearing mode from Roach [149], Applegate [151] and Wong NSTX [116, 117], Akers carried out preliminary nonlinear gyrokinetic simulations of the micro-tearing simulations with GS2, using an s-α model fit to MAST equilibrium. These simulations exhibited unphysical rapid growth of highest radial-k_x wavenumber component which limited the nonlinear calculations. The simulations also exhibited the onset of stochastic magnetic field lines giving rise to high magnetic transport. All of these features were consistent with the MT mode, and highlighted the difficulty towards obtaining resolved simulations of the MT mode. This work included an important section comparing multiple reduced transport model predictions with experi-

mentally measured profiles. For a MAST L-mode discharge, the reduced model GLF23 coupled with the ASTRA transport solver predicted high-k dominated transport exhibiting good Te and Ti predictions for $r/a > 0.4$, but overpredicted experimental values at the inner core $r/a < 0.4$. Similar predictions using the TGLF reduced model in a MAST H-mode were able to simultaneously match ion temperature, electron density and temperature for $r/a > 0.2$, but slightly overpredicted T_e at the inner core. This effort by Akers was a significant validation study of transport models in ST relevant regimes via direct comparisons at the highest level in the hierarchy: equilibrium profiles and experimental diffusivity values.

Work by C. M. Roach *et al*. [153] presented a review of the current transport and confinement understanding of the spherical tokamak, by focusing on the influence of flow shear in low-k ITG and high-k ETG modes, which had previously not been thoroughly studied before. Using GS2 with the additional capabilities of including background flow shear (via the $E \times B$ shearing rate γ_E), the authors discuss how the perpendicular background flow shear in typical ST parameters is enhanced with respect to standard tokamak parameters (via the $E \times B$ shearing rate), which favors additional suppression of the low-k modes in the ST. The linear effect of parallel flow shear was shown to destabilize a parallel-velocity-gradient instability that had been previously identified [155], but this effect was unfavored in the ST, concluding that toroidal flow shear should favorably suppress rather than drive ion-scale turbulence in the ST. The authors included improved ETG simulations with respect to previous works [150] by including kinetic ions, flow shear and collisions. These additional physics mechanisms confirmed the conclusion from previous studies [150] that "ETG turbulence can carry significant electron heat transport at mid-radius in MAST". Although no comparisons with experimental measurements were made, this work provided further confidence with improved physics models that low-k instabilities could be suppressed by background $E \times B$ in the ST, while reaffirming the relevance of the ETG mode in driving electron thermal transport.

Finally, it is worth pointing out simulation work by S. Saarelma *et al.* [156] for a MAST L-mode featuring an internal transport barrier. Using ORB5 code [157, 158], linear gyrokinetic analyses emphasized the important role of including kinetic electrons, which raised the linear growth rate values above the background $E \times B$ shearing rate,

but not with the adiabatic electron model. Nonlinearly, global electrostatic simulations showed the turbulent ion heat flux from ion scale turbulence was sensitive to the electron response. Including kinetic electron response and background flow shear on global ORB5 nonlinear gyrokinetic simulations showed ion heat flux can significantly overpredict the neoclassical heat flux value in the outer region of the MAST L-mode plasma under study. Importantly, turbulence was shown to spread from the linearly unstable region in the outer core to the linearly stable region in the inner core, both when using adiabatic electrons and kinetic electrons. This work left the door open to the importance that ion-scale turbulence can have in enhancing ion heat flux levels above the neoclassical value, and motivated consequent comparisons of ion-scale turbulence with the beam emission spectroscopy diagnostic (presented in the next section).

3.2.2.3 Experimental and preliminary synthetic diagnostic work in MAST with BES

The previous modeling and simulation studies and the implementation of the 2D beam emission spectroscopy imaging diagnostic in MAST [169] motivated experimental analysis of the turbulence features and patterns detected by the BES system. Initial efforts were led by Y.-c. Ghim and presented in this section.

Prior to the installation of the 2D BES array on MAST, synthetic work characterizing the point-spread function from the BES system was performed by Y. C. Ghim *et al*. [160], following pioneering experimental and synthetic diagnostic work by the DIII-D group on BES [142, 143, 161]. Consequent work by Ghim [162] further exploited the measured turbulence characteristics using a turbulence cross-correlation time-delay method to extract the velocity of density fluctuations, concluding poloidal motion of the detected BES fluctuations on MAST was dominated by advection of the turbulence patterns by the background toroidal flow, and not due to intrinsic propagation of turbulence in the lab frame. It is interesting to note that similar conclusions will be reached in this thesis when analyzing electron scale turbulence with the high-k scattering diagnostic.

In [163], the same author reported on an argument of critically balanced [164] ion density fluctuations from the MAST BES system, showing experimental evidence of the 3D anisotropy of the turbulence, consistent with the gyrokinetic ordering and previous simu-

lation work [165]. This work also projected the ratio of the zonal to non-zonal potential component of the turbulence to scale as $\varphi^{ZF}/\varphi^{NZ} \sim 1/\nu_{*i}^{-0.8\pm0.1}$, quoting this situation to be qualitatively distinct in far-from-threshold theoretical predictions [165] but qualitatively consistent with ITG-zonal flow theories predicting a scaling $\sim 1/\nu_{*i}^{-0.5}$ [166]. As will be seen in this thesis' appendix, nonlinear gyrokinetic simulation of ion-scale turbulence (dominated by a trapped electron mode/kinetic ballooning mode) in near marginal conditions exhibits zonal-flow components that can be extremely sensitive to ion-ion collisions, which can act as a zonal flow damping mechanism in close to marginal turbulence conditions, but not far from threshold conditions (in general the zonal flow amplitude tends to be dominated by the turbulence drive in far from threshold conditions, and the damping due to ion-ion collisions is shown to have a lesser effect on the zonal flow).

In [167], Y.-c. Ghim analyzed a database of 39 NBI-heated L-mode discharges, showing the local ion temperature gradient value R/L_{T_i} was directly correlated to the background flow shear (consistently with flow-shear stabilization of ion-scale turbulence) and inversely correlated to q/ϵ. Importantly, the amplitude of ion density fluctuations from the MAST BES diagnostic showed an inverse correlation with R/L_{T_i}, which was indicative of turbulence states in close to threshold conditions.

All in all, the relevance of these efforts greatly contributed to the detailed characterization of BES spectra, motivating consequent validation work with synthetic diagnostics on MAST. In addition, these efforts contributed to the understanding of the fundamental properties of detected ion-scale turbulence in MAST, such as critical balance and close-to-threshold turbulence behavior. However, no direct comparisons of ion-scale turbulence characteristics such as correlation times and lengths were made to first-principles nonlinear gyrokinetic simulations and synthetically generated spectra.

3.2.2.4 Detailed experiment/model comparisons and synthetic diagnostic work in MAST

A. R. Field performed pioneering validation work in [168] by completing "the first validation exercise for a MAST plasma comparing the characteristics of ion-scale turbulence measured using a 2D BES turbulence imaging system [169] with synthetic data produced from nonlinear simulations performed using the global particle-in-cell (PIC)

code NEMORB [170]". The analysis was performed in a low density NBI-heated L-mode plasma exhibiting an internal transport barrier, which was previously predicted to be unstable to ITG turbulence. This validation work was significant as it combined experiment/model comparisons with direct nonlinear gyrokinetic simulations at different levels in the validation hierarchy: turbulence amplitudes, radial and poloidal correlation lengths, correlation time, poloidal propagation velocity of the turbulence, and turbulent ion heat fluxes. The conclusion from this work was that higher fidelity simulations including kinetic electrons, background flow shear and collisions exhibit enhanced degree of agreement with experiment. However, considerable discrepancies in the correlation time as well as the fluctuation levels in the peripheral region were observed, pointing possibly to a deficient numerical boundary condition implemented in these global simulations, but also to some missing physics mechanisms in the pedestal and SOL that were not taken into account by the models.

M. J. Fox *et al.* [171] performed a rigorous study measuring the effect of background flow shear on detected density fluctuations by the BES system, and compared them to those from numerically generated turbulence using the gyrokinetic code GS2. In this study background flow shear was shown to break an underlying symmetry of the turbulence and manifested itself as a finite skewness in the distribution of density fluctuations and as a tilt in the correlation function when turbulence was close to the nonlinear threshold, but the symmetry was recovered in far from threshold conditions where flow shear is expected to have a relatively reduced impact. The authors pointed that the tilt of the correlation function was indicative of a measure of the turbulence correlation time, and could be used as a diagnostic measure of the eddy lifetime in future studies. The simulated skewness and tilt in the correlation function were shown to be qualitatively similar to the experimental ones. The significance of this work highlighted and tested some interesting fundamental properties of ion-scale turbulence with flow shear, but pointed to further work on more comprehensive direct validation comparisons, similarly to those carried out in [168]. Many of the details of the statistical analysis of the experimentally detected fluctuations as well as simulated fluctuations can be found in [172].

F. van Wyk *et al.* performed more detailed experiment/model comparisons in [173] using the MAST BES system applied to strongly rotating L-mode plasmas. Nonlinear

simulations using the GS2 code showed that the turbulence is very close to the nonlinear threshold, and subcritical for finite values of the $E \times B$ shearing rate: the system is shown to be in a linearly stable regime allowed by the finite γ_E, but large enough initial perturbations are allowed to grow nonlinearly and ultimately reach a saturated turbulence state. More details about the subcritical turbulence features in MAST are reported in [174]. From the validation perspective, experiment/model comparisons were focused on the ion heat flux (exhibiting a similar value to the electron heat flux but subdominant to it) and ion-scale turbulence comparisons with BES. GS2 simulations were local, resolving main ion species and electrons kinetically and purely electrostatic due to the low value of beta. Quantitative comparisons of simulated density fluctuations with measured fluctuations by the BES system on MAST used previously reported statistical techniques [162, 168], and found good agreements in the poloidal correlation length and correlation time, but not for the radial correlation length. The latter disagreement on the radial correlation length was attributed to a lack of resolution limit reached in the BES system. This work seemed to resolve discrepancies in the correlation time from previous work on MAST using the same BES system [168]. Notably, the authors showed that flux-matching simulations underpredicted the experimental fluctuation levels from BES, while fluctuations that matched the fluctuation level (with increased turbulence drive) were shown to significantly overpredict the experimental transport level. The GS2 simulations were shown to underpredict the BES fluctuation amplitude, possibly related to missing physics processes that could be relevant for the dominant electron heat flux levels, not included in this work. From the validation perspective, this work was a significant validation effort of ion-scale turbulence simulations in MAST L-mode discharges by combining experiment/model comparisons at different levels in the validation hierarchy (ion heat flux, correlation lengths and time).

The detailed characterization and analysis of the BES system allowed the first quantitative comparisons of ion-scale fluctuations in MAST. Consequently most thorough studies have been focused on understanding ion heat transport. However, to my knowledge little work has been recently performed to study the dominant electron thermal transport on MAST. Future validation efforts on MAST should further focus on understanding and characterizing electron thermal transport, both experimentally and from the theoretical/modeling perspective.

3.2.3 Discussion of past validation work on the spherical tokamak and the context of this thesis

The present chapter has highlighted some of the recent turbulence and transport validation studies performed in NSTX and MAST. The objective was not to provide an exhaustive list of the validation work and references that have been performed, but rather to give an overview on where the emphasis has been put both in NSTX and MAST. However, I would like to apologize for the missing pieces of relevant work not included in this chapter, purely due to my lack of knowledge and not to do with the relevance of the missing pice of work.

This chapter has allowed us to have an overview of some of the older and more recent validation efforts for the spherical tokamak. It would appear that validation work on NSTX has mainly focused on understanding electron thermal transport in NSTX L-modes and H-modes. One strong research line focused on understanding electron thermal transport from the ETG mode, via comparisons with the high-k scattering diagnostic installed on NSTX [65, 120], both through linear and nonlinear gyrokinetic simulation work. An important contribution reported on the development of a high-k scattering synthetic diagnostic [144], for which some sources of systematic errors led to disagreements between experiment and simulation that motivated further work. A second strong research line on NSTX focused on understanding electron thermal transport from the micro-tearing mode, also linearly as well as nonlinearly. The latter supposed a recent breakthrough to nonlinearly resolve unstable micro-tearing mode turbulence in a spherical tokamak plasma, predicting experimentally relevant levels of electron heat flux. On MAST, much of the simulation work and flux comparisons have focused on understanding both ion and electron heat transport. More systematic validation efforts comparing direct turbulence measurements with simulation have focused on ion-scale turbulence with the MAST BES system. Consequently, these efforts have initially been preferentially targeted to understanding ion thermal transport and the effect of flow shear on ion-scale turbulence, and have left more rigorous and detailed validation efforts on electron thermal transport for future studies.

The present chapter has also allowed to identify the missing gaps where more research

			Linear/NL predictions	Qualitative linear comparisons	Nonlinear transport comparisons	Synthetic comparisons
NSTX	**Q_e (Guttenfelder NF 2013, Ren NF 2017)**	**ETG**	Horton NF 2005,	Mazzucato PRL 2008, Mazzucato NF 2009, Smith PRL 2009, Smith PoP 2009, Yuh PoP 2009, Yuh PRL 2011, Ren PRL 2011,	Kaye NF 2007, Guttenfelder PoP 2011, Peterson PoP 2012, Ren PoP 2012, Ren NF 2013, Ren PoP 2015, **Ruiz-Ruiz MIT 2019**	Poli PoP 2010, **Ruiz-Ruiz MIT 2019**
		MT	Redi EPS 2003, Redi EPS 2004, Stutman PoP 2006, Levinton PoP 2007,	Guttenfelder PoP 2012a, Smith PPCF 2011,	Wong PRL 2007, Wong PoP 2008, Guttenfelder PRL 2011, Guttenfelder PoP 2012b, Kaye PoP 2014,	
		KBM	Bourdelle PoP 2003, Redi EPS 2005,	Guttenfelder NF 2013, Roach PPCF 2005,	Guttenfelder NF 2013, **Ruiz-Ruiz MIT 2019**	
		GAE/CAE, KAW			Stutman PRL 2009, Gorelenkov NF 2010, Belova PRL 2015	
	Q_i	**ITG/TEM**		Guttenfelder NF 2013	Guttenfelder NF 2013, **Ruiz-Ruiz MIT 2019**	
MAST	**Q_e**	**ETG**	Akers PPCF 2003, Wilson NF 2004,	Akers IAEA 2008,	Roach PPCF 2005, Joiner PPCF 2006, Akers IAEA 2008, Roach PPCF 2009,	
		MT	Kotschenreuther NF 2000, Akers PPCF 2003, Wilson NF 2004, Applegate PoP 2004, Akers IAEA 2008,	Roach PPCF 2005, Applegate PPCF 2007,		
		KBM		Roach PPCF 2005,		
	Q_i	**ITG/TEM**	Akers PPCF 2003, Wilson NF 2004,	Akers IAEA 2008, Roach 2009,	Akers IAEA 2008, Roach PPCF 2009, Saarelma PPCF 2012	Ghim PPCF 2012, Field PPCF 2014, Fox PPCF 2017a-b, Van Wyk PPCF 2017,

Figure 3-3: Table highlighting some of the recent validation efforts carried out for the spherical tokamak, both in NSTX and MAST. References are categorized depending on the instability under study (ETG, MT, KBM, ITG/TEM, GAE/CAE/KAW) and also depending on the nature of the work performed: predictions, linear stability comparisons, nonlinear transport comparisons and synthetic comparisons. The scope of this thesis is indicated by the reference **Ruiz-Ruiz MIT 2019**.

emphasis should be put in future efforts, and has also allowed us to distinctively place the present thesis in context with respect to past work. Table 3-3 highlights recent validation efforts carried out for the spherical tokamak, both in NSTX and MAST. The references are categorized depending on the instability under study (ETG, MT, KBM, ITG/TEM, GAE/CAE/KAW) and also depending on the nature of the work performed: predictions, linear stability comparisons, nonlinear transport comparisons and synthetic comparisons. The scope of the present thesis is indicated by the reference **Ruiz-Ruiz MIT 2019**. A big part of this thesis has been dedicated to establishing quantitative comparisons of electron-scale turbulence, where previous efforts lacked quantitative agreement. In addition, significant efforts have been put to determine the transport from nonlinear ion and electron-scale gyrokinetic simulations.

Table 3-3 can give a general idea of where most of the recent validation efforts of transport models for the spherical tokamak have been put in recent times. As anticipated at the beginning of this chapter, efforts in NSTX have primarily been focused on understanding electron thermal transport (Q_e). On MAST, more efforts have been put, especially recently, on understanding ion thermal transport. Table 3-3 also shows the limited range of synthetic diagnostic comparisons in both machines, with initial comparisons for the high-k diagnostic in NSTX [144] and recent developments with BES on MAST [162, 168, 171–173]. In addition, the difficulty towards establishing direct measurements of internal magnetic field fluctuations have prevented synthetic turbulence comparisons on this end. However, recent diagnostic development of Doppler Backscattering (DBS, [177, 178]) and Cross-Polarization Scattering (CPS, [175, 176]) diagnostics in MAST-U tokamak as well as in NSTX-U will tackle these deficiencies. The DBS diagnostic is sensitive of intermediate-k and high-k electron density fluctuations, while the CPS diagnostic is sensitive to internal magnetic field fluctuations characteristic of the MT and KBM modes. Analysis and validation work based on DBS and CPS measurements should be a priority for the spherical tokamak validation community.

On another note, limited work recently been performed to study global effects on either machine, especially in fully electromagnetic conditions. Initial work in [156] and in [132, 168] using electrostatic simulations should be completed by fully electromagnetic global gyrokinetic simulations, which have up to date been extremely challenging

for global codes to implement. In addition, to my knowledge no effort has been done to perform multiscale simulation of the spherical tokamak, simultaneously resolving ion and electron-scale modes. This is likely due to computational requirements and the complexity of the simulations. I also judge important these two lines for future validation work on the ST.

As we have seen in the course of this chapter, experimental, modeling and theoretical validation work on turbulence and transport carried out in the last 2 decades for the spherical tokamak has highlighted a sea of instabilities and transport processes able to drive ion and electron thermal transport in the ST: the electron-scale ETG modes at $k_\theta \rho_s \gtrsim 1$, tearing-parity micro-tearing modes, kinetic ballooning modes, fast particle/MHD GAE/CAE/KAW modes, and conventional ITG/TEM modes at $k_\theta \rho_s \lesssim 1$. As it turns out, the whole sea of microinstabilities present in the ST all have different parametric dependencies and physics regimes in which they are expected to be unstable. A useful way to understand the expected regimes of each instability is to map them out with respect to some local driving parameters, as was done in [136]. These parameters were identified to be β_e, ν^{ei}, $\beta_e \cdot a/L_{Te}$, $\alpha_{\text{MHD, unit}}$, a/L_{Te}-$a/L_{Te,\text{crit}}$, γ_E ($cf.$ in [136] for a detailed definition of each parameter). Figure 3-4 shows the result of the dominant instability from linear gyrokinetic simulation carried out for various NSTX H-mode discharges in the outer-core ($r/a \sim 0.6$-0.7).

The result of figure 3-4 is only indicative and highly qualitative, but it does retain the essential driving mechanisms and parameter regimes of some of the instabilities being identified unstable in the outer core of NSTX. As expected, conventional electrostatic ITG/TEM/ETG modes are expected to dominate at low electron beta $\beta_e \lesssim 4\%$. At higher beta, the kinetic ballooning mode KBM and the micro-tearing mode MT are destabilized. However these two modes exhibit different parametric dependency with electron-ion collisionality ν^{ei}, the MT mode being driven at high collisionality while the KBM remains unstable at low collisionality. The MT mode is also highly sensitive to the electron temperature gradient, and that dependency can be condensed in the parameter $\beta_e \cdot a/L_{Te}$, with values $\beta_e \cdot a/L_{Te} \gtrsim 10$ generally indicating unstable micro-tearing modes. The KBM mode itself is also sensitive to β_e and a/L_{Te}, but that dependency can generally be condensed via the α_{MHD} parameter. This is not coincidental since the KBM mode can be

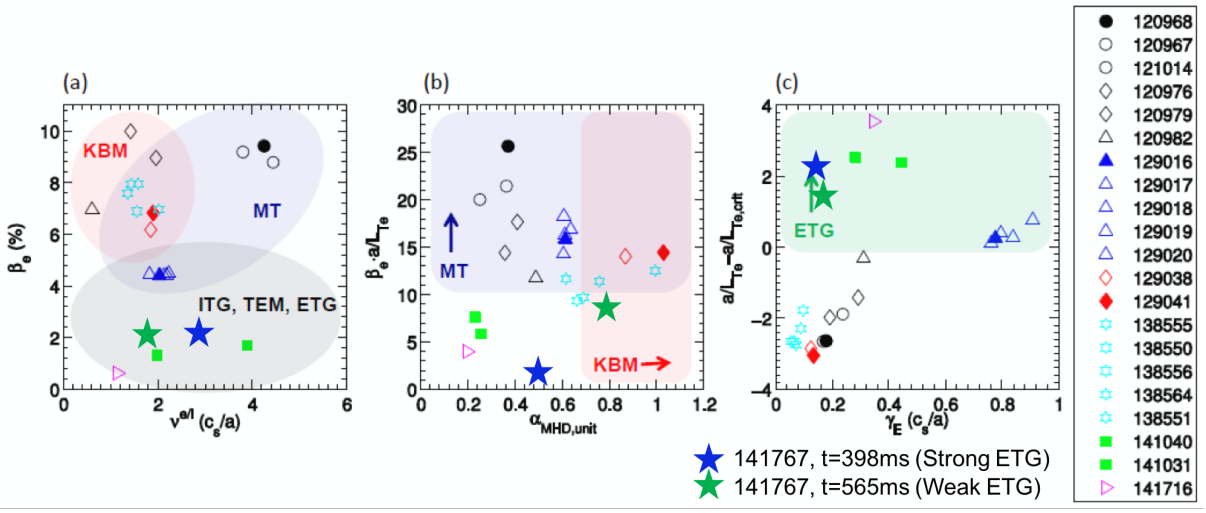

Figure 3-4: Diagrams showing main instabilities present for outer-core ($r/a \sim 0.6$-0.7) of NSTX H-modes for different local parameters β_e, ν^{ei}, $\beta_e \cdot a/L_{Te}$, $\alpha_{\text{MHD, unit}}$, a/L_{Te}-$a/L_{Te,\text{crit}}$, γ_E. The proper definitions of each local value are defined in [136]. Image is courtesy of [136], it has been modified with the blue and green stars from NSTX shot 141767, analyzed in this thesis.

seen as an extension of the traditional MHD ballooning mode [179]. Figure 3-4 shows α_{MHD} values greater than $\alpha_{\text{MHD, unit}} \gtrsim 0.7$ predict unstable KBM modes (the unit subscript references the specific normalization used in [136]). Finally, ETG modes are expected unstable when the background temperature gradient a/L_{Te} exceeds the critical electron temperature gradient $a/L_{Te,\text{crit}}$ (equation 2.6), even for strong values of the background $E \times B$ shearing rate γ_E.

In these regime diagrams, I have overplotted the experimental parameter regimes that will be analyzed in this thesis by the blue and green stars (strong and weak ETG regimes respectively), and specifically labeled at the bottom of the figure. This will be again discussed in the following chapters, but already qualitatively predicts unstable ETG modes in both conditions (Strong and Weak ETG conditions), and possibly an unstable KBM regime at the weak ETG condition.

In this way, the regime diagrams in 3-4 can give rough predictions of the expected instabilities for given ST configurations. Future high performance STs such as NSTX-U and MAST-U will approach expected regimes of future ST reactors at low collisionality and high-β. Following figure 3-4 would point right in the unstable KBM regime expected for future high performance STs.

Chapter 4

Analysis tools

This chapter introduces the main experimental and numerical simulation analysis tools of use in this thesis, excluding the synthetic high-k diagnostic which is the object of the following chapter. Most of the analysis tools are based on servers in the Princeton Plasma Physics Laboratory (PPPL), for which remote connection is needed in order to access the routines and data described in this chapter. The experimental analysis tools of most relevance are described in 4.1, such as data from diagnostics such as Thomson scattering (MPTS), charge-exchange recombination spectroscopy (CHERS), and the equilibrium magnetics, some of which are included in the equilibrium reconstruction by EFIT, or its improved version LRDFIT (constrained by the motional Stark effect diagnostic, MSE). The experimental power balance calculations are carried out with the TRANSP code. From the simulation perspective, the main tool used is the gyrokinetic code GYRO [98], succinctly described in section 4.2.

4.1 Experimental analysis

4.1.1 Setting up a PPPL account

In order to access data from NSTX (and NSTX-U), one of the first things to do for on-site and remote users is to create a PPPL account. In the framework of the present project and contract between MIT and PPPL I was working under the supervision of Dr. Walter Guttenfelder (wgutten@pppl.gov), staff Research Physicist at PPPL. Lena Scimeca

(lscimeca@pppl.gov), former Technical Assistant at PPPL provided me the information necessary for creating a PPPL account and a UNIX account. Following Lena's recent retirement, the interested user could contact Daniel Ascione (dascione@pppl.gov), Systems Administration Team Lead, or should work directly with their advisor. In the case where the user will be running TRANSP, it the main contact person would be Francesca Poli, staff Research Physicist at PPPL, for establishing TRANSP account. More information on TRANSP can be found in the new TRANSP website (`https://transp.pppl.gov/`).

PPPL has recently switched the remote connection procedure over to DUO (`https://guide.duo.com/enrollment`), which is soft method that allows the use of personal cell phone, tablet or other device to make the connection to PPPL through VPN. For that, the given electronic device would need to be enrolled via a link provided by your administrator. The interested user could contact Daniel Ascione, their own advisor/administrator, or directly the PPPL helpdesk (helpdeskstaff@pppl.gov) in order to register the device. Instructions should follow to install DUO in the personal device.

Information for VPN access is detailed at `https://vpn.pppl.gov`. Once VPN is established through DUO, the user has the choice of connecting to the PPPL servers by SSH connection or using NoMachine. For both purposes the contact is Ashwini Borkar, Unix/Linux System Engineer at PPPL (aborkar@pppl.gov). For downloading NoMachine to a Student Workstation at PSFC-MIT or to a personal/work computer, the user should go to the website `https://www.nomachine.com`. Any additional questions concerning setting up PPPL accounts and related can be directed to the Helpdesk Group (helpdeskstaff@pppl.gov, 609-243-2275).

Once all these connections are established, the user is now able to access NSTX data from the tree and proceed with the physics analysis.

4.1.2 Accessing NSTX diagnostic data

In this chapter I refer to 'NSTX data' as data stored in the MDSplus tree from each diagnostic corresponding to past NSTX discharges. Typical data used in this thesis comes from the magnetics (Mirnov coils, Rogowski coil, etc.), profile diagnostics (Thomson

scattering MPTS, charge exchange CHERS etc.), equilibrium reconstruction (EFIT, LRDFIT), high-k scattering, and other such as the D_α signal and interferometer for the line-integrated density.

There are several ways to access data stored from past NSTX experiments, and one could choose either options depending on the purpose. One method is using the Web, namely the Web Tools platform provided by PPPL available at `https://nstx.pppl.gov/nstx/Software/WebTools/`. Web Tools are particularly useful for finding MDSplus signal names as well as for preliminary data visualization and analysis. However the most efficient way to perform detailed analysis of NSTX experiments is to access MDSplus data directly from UNIX clusters or personal computers without the use of the Web. The software Matlab was used in the course of this work as a tool to access and perform analysis of NSTX data. Matlab commands $mdsconnect('lark.pppl.gov:8501')$, $mdsopen('activespec', shot)$, $mdsclose$ and $mdsdisconnect$ need to be included in the beginning and the end of each Matlab script to access MDSplus data. The routine $mdsvalue('signalname')$ is also necessary for accessing a particular signal data. The Matlab routines used to create the work presented here can be found in my personal directories at PPPL `/u/jruizrui/matlab/myroutines` and `/p/gyro/jruizrui/matlab/myroutines`. A short list of some of the main routines is given as follows. A more comprehensive of the routines employed is given in the appendix.

· **Thomson scattering** provides radially and temporally resolved measurements of electron density n_e and electron temperature T_e. Data can be accessed through the routine `get_mpts.m`.

· **Charge exchange recombination spectroscopy** provides radially and temporally resolved measurements of carbon density n_C, temperature T_C, rotation v_C and Z_{eff}. The data can be accessed through the routine `get_chers.m`.

· **The magnetic equilibrium reconstruction** with EFIT or LRDFIT provides information about the equilibrium magnetic field, plasma current and related quantities such as safety factor q and magnetic shear $\hat{s}$ and the magnetic flux surface geometry. The data can be accessed through the routine `get_efit.m` and `get_lrdfit.m`.

· **Power balance calculations** with TRANSP [105, 180] provide estimates of internal ion and electron transport quantities such as particle, heat and momentum diffusivities, fluxes and related quantities. The data can be accessed through the routine `get_transp.m`.

· **The high-k scattering diagnostic** provides frequency and wavenumber spectra of electron density fluctuations δn_e at a specific radial location in the plasma. The data can be accessed with the routine `get_hkdata.m`.

It is worth expanding on the power balance calculations employed in this thesis. The high-k scattering diagnostic description and access to high-k scattering data and routines is described in the following section 4.1.3.

Power balance calculations with TRANSP

With respect to power balance, TRANSP is a time dependent numerical transport code used in tokamak experiments [105,180,181]. As was previously mentioned in the preceding chapter, it is impossible to obtain a direct measurement of plasma transport quantities such as fluxes of particle, heat and momentum, since no material probe would survive the harsh conditions of the core of fusion plasmas. TRANSP calculates transport fluxes based on power balance calculations. TRANSP takes as input experimental profiles (MPTS, CHERS, ...) along with detailed models of unavailable data from experiments (such as NBI deposition profile using Monte Carlo calculations, current diffusion equation, ...) and neoclassical calculations to solve the power balance equation for all species in the plasma, and arrive to an expression for the effective particle, heat and momentum fluxes, from which diffusivities can be calculated (if one assumes a diffusive transport model is relevant). For reference, the volume integrated form of the ion and electron power balance equations solved by TRANSP are:

$$\begin{aligned} P_{condi} &= -\frac{\partial U_e}{\partial t} - P_{convi} + P_{compi} + P_{ei} + P_{aux,i} - P_{cx} + P_{i,source} \\ P_{conde} &= -\frac{\partial U_e}{\partial t} - P_{conve} + P_{compe} - P_{ei} + P_{aux,e} + P_{OH} - P_{rad} - P_{ion} \end{aligned} \tag{4.1}$$

The terms in equation 4.1 are: P_{condi}, P_{conde} are the ion and electron radial thermal

conduction terms (noted P_i, P_e in the rest of this thesis). These are the most important terms of interest to be directly compared to predicted thermal transport estimates from nonlinear gyrokinetic simulations. U_i, U_e are the ion and electron internal energies. P_{convi}, P_{conve} are the ion and electron radial convection terms. P_{compi}, P_{compe} are the ion and electron compression terms. P_{ei} is the electron-ion energy exchange power term. $P_{aux,i}, P_{aux,e}$ are the ion and electron auxiliary heating sources, such as RF or NBI. The plasmas analyzed in this thesis are only subject to NBI heating. P_{cx} is the charge exchange loss term. $P_{i,source}$ is the power gain from an ion particle source. P_{OH} is the Ohmic heating term. P_{rad} is the radiative loss term, and P_{ion} is the ionization term. These equations are analyzed in this thesis and performed error propagation analysis to provide the uncertainties in the conduction terms P_{condi}, P_{conde} ($cf.$ next section). The interested reader is encouraged to turn to references [105, 180–183] for details about TRANSP as well as power balance transport calculations in general, from the physics foundation to the practical matters. The Matlab routine `get_transp.m` is used in this thesis to access TRANSP data from previous TRANSP runs. TRANSP was also of particular use in this thesis to obtain values of the $E \times B$ shearing rate according to the Waltz-Miller definition [184], and provided the basis for the input files of linear and nonlinear gyrokinetic simulations with GYRO.

This thesis made use of NSTX shot 141767, for which I used the following TRANSP IDs: $a11, a21, a23, a24, a27, a28, a29, a30$. Details about these TRANSP IDs can be found in [186]. In the course of this thesis I have not made extensive use of TRANSP and was not responsible for completing the particular TRANSP runs presented here, but I have made considerable use of TRANSP output data for the purposes of calculating transport fluxes, $E \times B$ shearing rates and input files for GYRO simulations.

4.1.3 The high-k scattering diagnostic at NSTX

Of particular importance in this work is the access of data from the high-k scattering diagnostic, and the subsequent frequency analysis. Detection of electron-scale fluctuations associated to the ETG mode has proven to be a daunting task due to the small characteristic scales of the fluctuations. Experimentally, coherent scattering has recently

become a popular diagnostic technique to probe internal density perturbations associated to electron-scale turbulent plasma phenomena. Two diagnostics have proven successful in detecting electron-scale turbulence fluctuations in recent years ($k_\perp \rho_s > 1$, ρ_s is the ion-sound gyroradius): the Doppler Backscattering technique, implemented in different tokamaks around the world [83–88], and the high-k scattering technique. This thesis will analyze experimental spectra from the high-k scattering system in NSTX.

4.1.3.1 NSTX high-k diagnostic description

A high-k scattering diagnostic designed for the measurement of electron density fluctuations on the electron gyro-radius scale ($k_\perp \rho_e \lesssim 1$) was designed, built and operated in NSTX [65, 89]. This high-k scattering system used a 280 GHz microwave beam source of 15 mW, propagating very close to the midplane in a tangential geometry with respect to the flux surfaces, as can be seen on figure 4-1. In this geometry, measured wave vectors are primarily radial k_x, with a smaller vertical component k_z satisfying $k_z/k_x \approx 0.2 - 0.3$ (k_x is the component along the major radius, perpendicular to the flux surface at the outboard midplane, and k_z is the vertical component - more details in the following section). The scattering system consisted of five collection channels that simultaneously measure five different wave numbers in the range $5 \lesssim k_\perp \lesssim 30$ cm^{-1}. Heterodyne receivers installed on each channel allowed to determine the direction of propagation of the observed fluctuations. The wavenumber resolution of the observed electron density fluctuations is $\Delta k \approx \pm 0.7$ cm^{-1} and the radial resolution $\Delta R \approx \pm 3$ cm. The near mid-plane trajectory of the probe beam and the k-response are computed using a ray tracing code ($cf.$ [89], section 4.1.4). In Fig. 4-1.a) is shown the trajectory of 4 channels of the high-k scattering system for NSTX shot 141767. In the experiment I present here, the scattering system is sensitive to fluctuations taking place at $R \approx 135$ cm (major radius of NSTX is 0.85 m, minor radius 0.68 m, r/a ~ 0.7). Channel 1 measures $k_x \rho_s \sim$ 13-17 and $k_z \rho_s \sim$ 3-4, which in physical units typically corresponds to $k_x \sim$ 18-25 cm^{-1} and $k_z \sim$ 5-6 cm^{-1} (ρ_s is computed using local values of electron temperature T_e and magnetic field from LRDFIT equilibrium reconstruction). The electron and ion gyro-radii typically have values $\rho_e \approx 0.1$ mm and $\rho_i \approx \rho_s \approx 0.7$ cm in these NSTX plasmas. For additional details on the high-k scattering system, the reader is referred to [65, 89].

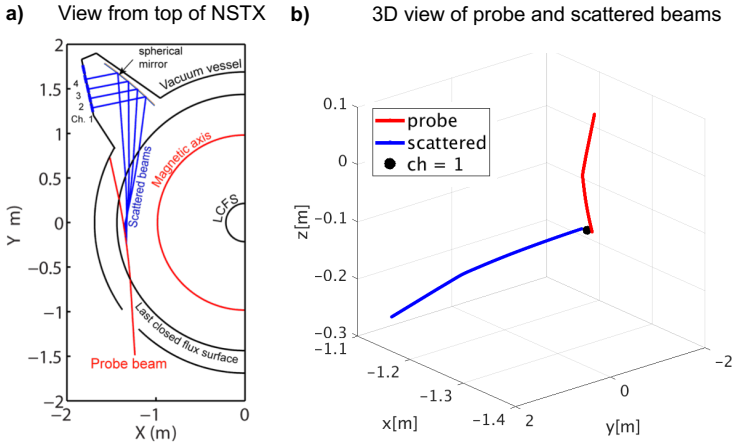

Figure 4-1: **a)** View from the top of the old high-k scattering diagnostic at NSTX. **b)**. 3D view of the propagation trajectory of the incident probe and scattered rays corresponding to channel 1. The black dot denotes the scattering location. Trajectories are computed by ray tracing calculations, section 4.1.4.

In spite of its tangential geometry, the old high-k scattering system was able to produce spatially localized measurements. As outlined in [90] and [91], the principle of spatial localization is relies on the high curvature of the magnetic field lines at NSTX. The strong magnetic field line curvature in NSTX constrains the size of the scattering volume, producing a localized measurement. A small angle between the incident beam and the magnetic field is a crucial requirement for obtaining well-localized measurements. Oblique propagation of the incident beam (out of midplane) modifies the angle it makes with respect to the magnetic field, hence it allows for a better localized measurement than for midplane beam propagation. Thus the importance of launching the probe beam slightly off midplane.

A newly designed high-k scattering diagnostic is planned to be installed in NSTX-U. Projected to be sensitive to smaller k_x and higher k_z, it is expected that this diagnostic will be able to detect streamer fluctuations.

4.1.3.2 Accessing high-k scattering data

The routine `get_hkdata.m` provides two arrays of time and raw signal from the high-k scattering system, for each channel. Measurements presented in this thesis were performed using 7.5 MS/s. The time history of the high-k data was subdivided in Hann

windows of 546 μs. Fast Fourier Transforms (FFTs) were calculated within each Hann window using 8192 time samples. The frequency resolution is 1.83 kHz. For each time window with $N = 8192$ time points, the time averaged signal power is

$$P = \frac{1}{N}\sum_{j=1}^{N}|V(t_j)|^2 = \sum_{k=1}^{N}|\hat{V}(f_k)|^2 \tag{4.2}$$

where $\hat{V}$ is the Fourier Transform of V over the time interval of the Hann window

$$\hat{V}(f_k) = \frac{1}{N}\sum_{j=1}^{N}V(t_j)\text{exp}(-2i\pi f_k t_j) \tag{4.3}$$

Using this technique of frequency analysis with Hann windows on raw high-k data one is able to reconstruct figure 4-2. Figure 4-2.a) shows the spectrogram of measured fluctuations channels 1, 2 and 3 of the high-k scattering diagnostic, along with time slices of channel 1 in 4-2.b) as reconstructed using the Matlab routine `plot_highk_spec.m`. Fig. 4-2 is plotted in log scale and units are in dB (details about power calibration and dB definition are given in [89]). Note that the high central peak at $f = 0$ is due to stray radiation (possibly reflections of the incident microwave beam within the chamber). The high-k features of electron density fluctuations I focus on are at negative frequencies around ~ -1-2 MHz.

As can be seen from figure 4-1, each channel of the high-k scattering system is oriented at a given angle with respect to the incident beam of radiation, which selects a different wavenumber of fluctuations for each channel. The wavenumbers $k_\perp\rho_s$ that each channel is sensitive to are explicit in Fig. 4-2.a).

4.1.4 Ray tracing

In multichannel scattering experiments it is of paramount importance to determine the correct value of the wavenumber $\vec{k}$ that is detected by each channel of the scattering diagnostic. As will be explained more in detail in the following chapter and appendix, the mode frequency ω and wavenumber $\vec{k}$ detected by the high-k system follow the $(\omega, \vec{k})$ matching conditions: $\vec{k} = \vec{k}_s - \vec{k}_i$ and $\omega = \omega_s - \omega_i$, where $(\omega_i, \vec{k}_i), (\omega_s, \vec{k}_s)$ are the frequency and wavenumbers of incident i and scattered rays s respectively. One then

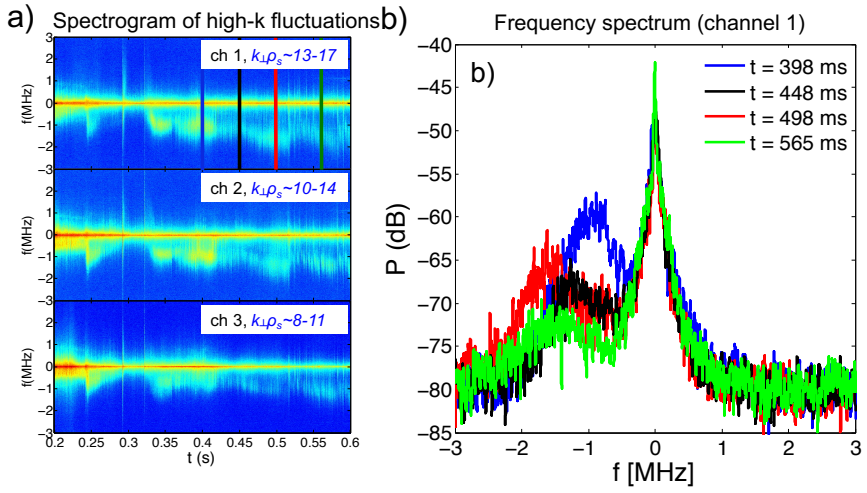

Figure 4-2: $a)$ Spectrogram of high-k density fluctuations from channels 1, 2 and 3 of shot 141767 of the high-k scattering system at NSTX. $b)$ Frequency spectrum of fluctuations corresponding to times as shown on $a)$ by vertical color lines from channel 1. Note $b)$ are simply time slices of channel 1 at the vertical color lines. Each channel is sensitive to a different wavenumber $k_\perp\rho_s$ as is indicated in $a)$.

needs a reliable method to determine $\vec{k}_i, \vec{k}_s, \omega_i$ and ω_s. These values of $\vec{k}_i$ and $\vec{k}_s$ can be computed by ray tracing calculations (ω_i is set by the diagnostic and ω_s is measured at the detector).

Ray tracing calculations of the incident and scattered rays are based on the cold plasma model or small variants of it. The cold plasma model is valid in conditions where the propagation frequency of the beam ω_i is much higher than any characteristic frequency in the plasma $(\omega_{ce}, \omega_{pe}, ...)$. The electromagnetic waves associated to the incoming microwave beam propagate far from resonances and cut-offs, and the trajectory of the incident beam is then well described by the cold-plasma dispersion relation due to Appleton-Hartree ($cf.$ [89]).

In the NSTX plasma conditions under study in this thesis, typical time scales of the plasma are the electron plasma frequency $f_{pe} = \omega_{pe}/2\pi = 1/2\pi(n_e e^2/m_e\epsilon_0) \approx 60$ GHz ($n_e \sim 5.10^{19}\text{m}^{-3}$), the electron cyclotron frequency $f_{ce} = \omega_{ce}/2\pi = 1/2\pi(eB_0/m_e) \approx 14$ GHz ($B_0 \sim 0.5$T). The electron thermal speed $v_{te} = \sqrt{2T_e/m_e}$ takes the value $\approx 10^7$ m/s ($T_e \sim 0.5$ keV). In comparison, the probe frequency of the incident beam is 280 GHz. At this frequency we're in the high frequency regime, far from cutoffs and resonances ($\omega \gg \omega_{pe}, \omega_{ce}$). The cold plasma model is a valid description and ray tracing of the

incident and scattered rays is appropriate.

The ray tracing equations compute the trajectory of the incident and scattered rays by evolving the position $\boldsymbol{r}$ and wave-vector $\boldsymbol{k}$ of the rays

$$\frac{d\boldsymbol{r}}{d\tau} = \frac{\partial \mathcal{D}}{\partial \boldsymbol{k}}\bigg|_{\mathcal{D}=0} \qquad \frac{d\boldsymbol{k}}{d\tau} = -\frac{\partial \mathcal{D}}{\partial \boldsymbol{r}}\bigg|_{\mathcal{D}=0} \tag{4.4}$$

where $\boldsymbol{k} = \vec{k}_i$ or $\vec{k}_s$ and $\mathcal{D} = \mathcal{D}(\omega, \boldsymbol{k}, \boldsymbol{r})$ is the determinant of the cold plasma dispersion tensor, and $\mathcal{D} = 0$ constitutes the cold plasma dispersion relation [187]. The ray tracing equations take into account the effect of inhomogeneities present in the plasma such as density gradients that can refract the propagating rays and result in bending the ray trajectories.

In figure 4-1 are shown a view from the top of the trajectories of the incident ray (red) and scattered rays (blue) output from a ray calculation, as well as the 3D view for channel 1 in 4-1.b). The black dot in 4-1.b) denotes the scattering location. Since ray tracing propagates the probe and scattered rays independently (set by geometric directions of viewing angles and launching angles), the probe and incident rays rarely exactly intersect at one exact point in the simulation domain, due to experimental uncertainty errors etc., but rather the incident and scattered beams cross trajectories that very closely pass by each other with a typical minimum distance of ~ 1 mm. The scattering location in this thesis is defined to be the midpoint between the two minimum distance points in the incident and scattered beams respectively.

The ray-tracing code used during the course of this work was implemented by Dr. Y. Ren, research scientist at the Princeton Plasma Physics Laboratory, and Dr. D. R. Smith, associate scientist at University of Wisconsin-Madison. The matlab routines used in this thesis are all noted in appendix D. For more details about the ray tracing code used in this work, the reader is referred to D. R. Smith's PhD thesis [89].

4.1.5 Determination of experimental uncertainties

All experimental measurements have associated errors and uncertainties. As was discussed in chapter 3, these experimental uncertainties have to be properly quantified and taken into account in any validation study, such as the one presented in this thesis. I will

first discuss profile gradient uncertainties via error propagation, followed by uncertainties in the computed fluxes via TRANSP. Uncertainties are also present in the simulation outputs, and are also discussed in this section. Here I will simply sketch some of the essential elements concerning uncertainty quantification and propagation, without recursing to rigor in notation. The reader is referred to Dr. M. Chileski's website [193], a former recent graduate student at MIT, and references therein about uncertainty quantification via advanced statistical treatments.

As is described in "Introduction to uncertainty in measurement" in [193], 'aleatory uncertainties can usually be modeled as random variables that obey a probability distribution that can be determined from your measurements and other knowledge of experiment'. As such, this allows the use of the standard deviation associated to the probability distribution function as a measure of the uncertainty. This is the basis of essentially all of the uncertainty calculations described in this thesis.

In some situations the experimental uncertainty is directly provided by preliminary analysis of the measurement. Such is the case for example of uncertainties in some of the main profile quantities such as electron density n_e and temperature T_e provided by the `get_mpts.m` routine. This routine provides raw measurement data of n_e and T_e (`nef, tef` respectively), as well as their associated experimental uncertainties `dne, dte`. A similar situation is encountered with CHERS data. In these instances the experimental uncertainty is calculated via specific knowledge of the measurement and diagnostic and directly provided to the user. However, in most situations one is faced with the need of computing the uncertainty of a given quantity x for which no information is provided via a specific measurement, but depends on other quantities $u, v, ...$ etc. for which the user has specific knowledge of the uncertainty. Such is the case for the uncertainty in the the fluxes computed by TRANSP Q_e, Q_i (which directly depend of profile quantities such as $n_e, T_e, T_i, ...$), gradients of the plasma profiles $\nabla n_e, \nabla T_e, ...$, the $E \times B$ shearing rate γ_E, etc. Computing the uncertainties associated to such quantities is the starting point for uncertainty propagation.

The **uncertainty propagation equation** relates the uncertainty σ_x associated to a quantity x to the uncertainties $\sigma_u, \sigma_v, ...$ associated to the quantities $u, v, ...$ by

$$\sigma_x^2 = \sigma_u^2 \left(\frac{\partial x}{\partial u}\right)^2 + \sigma_v^2 \left(\frac{\partial x}{\partial v}\right)^2 + ... + 2\sigma_{uv} \left(\frac{\partial x}{\partial u}\right)\left(\frac{\partial x}{\partial v}\right) + ... \tag{4.5}$$

In the case of independent errors ($\sigma_{uv} = 0$), some commonly encountered cases of interest are

$$\begin{aligned} x = au + bv \qquad &\rightarrow \qquad \sigma_x^2 = a^2\sigma_u^2 + b^2\sigma_v^2 \\ x = auv \qquad &\rightarrow \qquad \frac{\sigma_x^2}{x^2} = \frac{\sigma_u^2}{u^2} + \frac{\sigma_v^2}{v^2} \end{aligned} \tag{4.6}$$

where a, b are simply constants. These are the main equations used in the course of this thesis to quantify uncertainties in radial profile gradients (such as $\partial n_e/\partial r$, etc.) as well as electron and ion thermal fluxes Q_e and Q_i computed by TRANSP. These are implemented in the matlab routine `get_sigmagrad.m` in my PPPL directory. The methods used here are relatively standard to the validation community. The reader is referred to [103] for additional methods.

Profile gradient error bars

Linear and nonlinear gyrokinetic simulations use information about the equilibrium profiles in the inputs. As we learned in chapters 2 and 3, instabilities and turbulence associated to a particular mode are driven unstable by gradients in the equilibrium profiles, which are a source of free energy that feeds the instabilities. As a result, it is especially important to quantify the uncertainty in the main profile gradient quantities that are input in the gyrokinetic simulations. In a thorough validation activity, sensitivity scans should be performed in gyrokinetic simulations about the main instability drives, as is performed in this thesis.

Imagine we desire to compute the uncertainty in ∇n_e at radial location r_i, noted $\sigma(\nabla n_e)$, while we only have knowledge of n_e and $\sigma(n_e)$. One common procedure employed in this thesis is to calculate $\sigma(\nabla n_e)$ via the construction of probability distribution functions and spline fits. By knowledge of the electron density n_e and uncertainty $\sigma(\nabla n_e)$ at a specific radial location r_i, one can construct an ensemble of N equilibrium profiles $\{\hat{n}_e\}_N$. These can be computed via a Monte Carlo approach by generating random data points $\hat{n}_e$ about a mean value given by $n_e(r_i)$, and deviated from $n_e(r_i)$ according to the

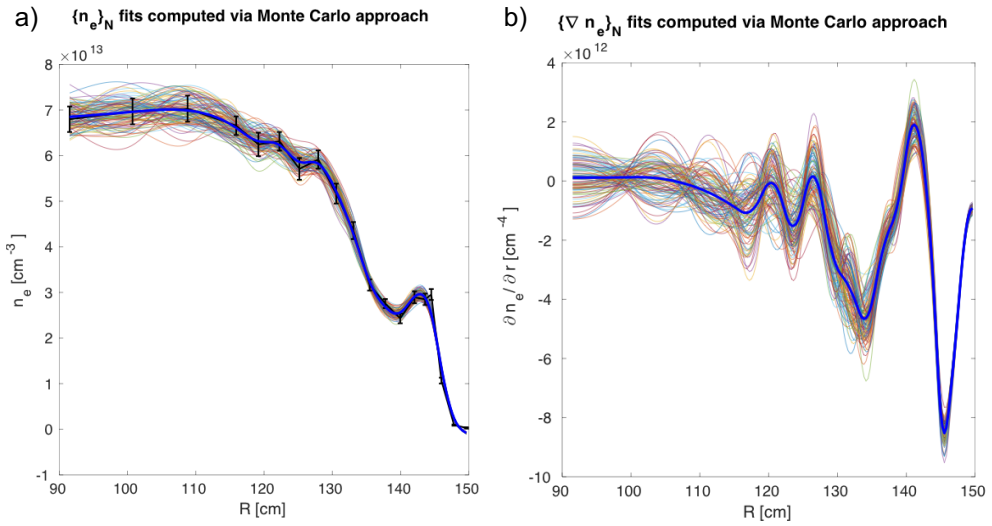

Figure 4-3: **a)** Ensemble of fits to the electron density profile from Thomson scattering $\{n_e\}_N$ generated via a Monte Carlo approach to compute the uncertainty in ∇n_e. The raw profile data is shown by the thick black line with associated error bars. Were generated a total of $N = 100$ fits. The average value of all fits is given by the thick blue line. **b)** Ensemble of electron density gradient fits, computed from a) via the radial derivative of each fit. The average value of all fits is given by the thick blue line. The standard deviation of all fits at a specific radial location r_i provides the experimental uncertainty $\sigma(\nabla n_e)$.

uncertainty $\sigma(n_e(r_i))$. Performing this procedure for all data points r_i one can obtain an ensemble $\{\hat{n}_e\}_N$ of N different profiles for the electron density n_e. One can then compute the radial gradient of each of the N generated profiles $\hat{n}_e$. This will yield a set of N gradient profiles $\{\nabla\hat{n}_e\}_N$. The quoted uncertainty in the electron density gradient $\sigma(\nabla n_e(r_i))$ at location r_i can then be directly computed via the standard deviation of the profile gradient ensemble $\{\nabla\hat{n}_e(r_i)\}_N$ at r_i. This is the common way uncertainties in the background profile gradients are computed in the context of this thesis. An example of this procedure is shown on figure 4-3.

Uncertainty in the $E \times B$ shearing rate γ_E

Here I sketch the procedure employed in this thesis to compute the uncertainty in the background $E \times B$ shearing rate, given by the Waltz-Miller definition [184]: $\gamma_E = \frac{r}{q}\frac{d}{dr}\left(\frac{E_r}{RB_p}\right)$. This definition for γ_E is input in the GYRO input files.

In order to compute γ_E, the radial electric field E_r must be calculated, via the momentum conservation equation (for the carbon impurity $i = C$ in our case), given by

$$E_r = \frac{\nabla p_i}{Z_i e n_i} - v_p B_t + v_t B_p \tag{4.7}$$

In this expression, the following terms are: p_i, n_i are the carbon pressure and density from CHERS measurements (and the use of quasineutrality and Z_{eff}); v_p is the poloidal component of the carbon velocity, which can be well approximated by neoclassical calculations (NCLASS, NEO); v_t is the toroidal component of the carbon velocity, measured by CHERS; B_t, B_p are respectively the toroidal and poloidal components of the equilibrium magnetic field, taken from EFIT/LRDFIT calculations. An estimate of the total electric field value and the three terms in the right hand side of equation 4.7 is given by the TRANSP namelist `ertot, erpress, ervpol, ervtor`. In the highly rotating conditions characteristic of spherical tokamak plasmas such as NSTX, one generally finds that the radial electric field is almost completely dominated by the toroidal rotation term, and $E_r \approx v_t B_p$. In the conditions analyzed in this thesis the toroidal rotation terms make up $\sim 70 - 90\%$ of the total radial electric field.

One can still compute the uncertainty in E_r and the associated uncertainty in γ_E via the standard error propagation techniques described in the previous section ($cf.$ equation 4.6). In a first approximation the uncertainty in B_t and B_p is assumed 0 - which is surely not accurate, but likely not to have a substantial impact due to the dominance of the v_t term. In addition, I note how the profiles under study in this thesis were constrained by internal magnetic field measurements via the Motional Stark Effect diagnostic (MSE), providing high reliability and reducing the associated uncertainties to B_t, B_p. One surprising result is that the uncertainty in γ_E is found to be on the order of $\sim$ 10-20%, a relatively low value. This is the result of the E_r field being dominated by the $v_t B_p$ term, where v_t is known with high accuracy from CHERS, while the term $\propto \nabla(\frac{\nabla p_i}{R B_p e n_i Z_i})$, which should in principle have great uncertainty, has a relatively small contribution to the global uncertainty in γ_E due to its relatively small contribution to the radial electric field equation 4.7. In this thesis will be carried out sensitivity scans of nonlinear gyrokinetic simulations with GYRO within experimental uncertainty values of γ_E.

Thermal power uncertainties from TRANSP

The procedure employed in this thesis to compute the power balance error bars closely

follows the analysis presented by J. M. Schachter in his PhD dissertation completed at MIT [183], to which the reader is referred to for additional details.

We wish to compute the uncertainties in the ion and electron conduction power, noted P_{condi}, P_{conde} in equation 4.1. Using the uncertainty propagation equation 4.6 one can show that the main sources of uncertainty to the conduction P_{condi}, P_{conde} are given by:

$$\begin{aligned}\sigma(P_{condi})^2 &= \sigma(P_{NBI,i})^2 + \sigma(P_{ei})^2 \\ \sigma(P_{conde})^2 &= \sigma(P_{OH})^2 + \sigma(P_{NBI,e})^2 + \sigma(P_{rad})^2 + \sigma(P_{ei})^2\end{aligned} \tag{4.8}$$

The problem is reduced to determining the uncertainties in the individual terms in the right hand side. The NBI heating terms $P_{NBI,i}, P_{NBI,e}$ have generally subdominant contributions to the power balance equations in the outer-core part of the plasma ($r/a \sim 0.7$ in this thesis). However one can obtain a crude estimate of $\sigma(P_{NBI})/P_{NBI}$ based on the beam-electron collision frequency ν_{be}, since $P_{NBI} \propto \nu_{be}$, to find $\sigma(P_{NBI})/P_{NBI} \sim 10\%$. The Ohmic heating term depends on the parallel conductivity and current $P_{OH} = \int \eta_{||} j_{||}^2 \cdot dV$, where V is the enclosed plasma volume. The parallel conductivity is generally well described by neoclassical theory ($cf.$ [183] for details). Assuming negligible uncertainty in the parallel current $j_{||}$ (justified by MSE constrained magnetic equilibria), one finds an uncertainty of $\sigma(P_{OH})/P_{OH} \sim 10-15\%$. The radiative term is negligible in the outer core conditions analyzed here. One important source of uncertainty is the electron-ion collisional exchange term P_{ei}. As is described in detail in [183], the electron-ion exchange power density Q_{ei} [MW/m^3] can be written by

$$Q_{ei} = c_0 \frac{n_e^2}{T_e^{1/2}} \left(1 - \frac{T_i}{T_e}\right) = Q_x(1 - \Theta) \tag{4.9}$$

Note how P_{ei} is related to Q_{ei} via $P_{ei} = \int dV Q_{ei}$, and the quantity $\Theta = T_i/T_e$. Standard error propagation of equation 4.9 leads to

$$\frac{\sigma(Q_{ei})}{Q_{ei}}^2 = 4\frac{\sigma(n_e)^2}{n_e^2} + \frac{1}{4}\frac{\sigma(T_e)^2}{T_e^2} + \frac{Q_x^2}{Q_{ei}^2}\sigma(\Theta)^2 \tag{4.10}$$

where $\sigma(\Theta)$ can be computed from uncertainties in T_i and T_e. We find $\sigma(P_{ei})/P_{ei} \sim 20-30\,\%$. Putting all of the uncertainties together, one ends up finding $\sigma(P_{conde})/P_{conde} \sim 20 - 25\%$, while and $\sigma(P_{condi})/P_{condi} \sim 30 - 40\%$ depending on the plasma conditions

presented in this thesis.

The uncertainty estimates presented here will be used in this thesis and be compared to predicted thermal power predictions from nonlinear gyrokinetic simulations. In the remainder of this thesis I will use the notation $P_e = P_{conde}$ and $P_i = P_{condi}$. The calculations presented here are implemented in the Matlab routine `get_sigmagrad.m` in my PPPL directory.

4.2 The GYRO code

GYRO is a widely used nonlinear gyrokinetic code implemented and maintained at General Atomics, part of the GACODE suite that is available for public use [188]. As a code designed to simulate micro-instabilities in strongly magnetized plasmas, GYRO solves the gyrokinetic-Maxwell system of equations for the perturbed, non-adiabatic part of the distribution function ($cf.$ section 2.4), that is coupled through the perturbed electromagnetic fields via Maxwell's equations. GYRO is capable of computing fully electromagnetic fluctuations of fields, ion and electron collisions, sheared flow in full toroidal, field-aligned geometry and can be run in the local approximation ($\rho_s/a \ll 1$) or in global mode. In this thesis GYRO is run in the linear initial value mode, as well as nonlinearly in simulations separately spanning ion and electron scale turbulence, as will be shown in this section.

GYRO uses a particular definition of the normalizing magnetic field B_{unit}, defined as $B_{\text{unit}} = \frac{q}{r}\frac{d\psi}{dr}$ where ψ is the poloidal flux divided by 2π [189]. Due to the flux-surface shaping such as elongation, B_{unit} is generally found to have a slightly higher value than the local value of B_t at the center of the flux surface. This effect is exaggerated in the spherical tokamak, where one can find B_{unit} up to factors of 3 higher than the local B_t values. In this regard, GYRO uses this internally defined B_{unit} as the normalizing magnetic field in the ion-sound gyroradius ρ_s, which in turn is used to normalize the poloidal wavenumber values k_θ.

4.2.1 Right-handed system of toroidal coordinates in GYRO (and CGYRO)

As is detailed in appendix C and references [98, 189, 190], it is of common use of gyrokinetic codes to expand fluctuations as having slowly varying component along the field line and rapidly varying component perpendicular to the field line. The gyrokinetic code GYRO and its recent evolution CGYRO both operate in a field-aligned flux coordinate system (r, θ, α), that is thoroughly described in reference [189]. In this section I use the symbol f to designate a general fluctuating field f, which could be $\delta n, \delta\phi$, etc. In GYRO and CGYRO the fluctuation fields are expanded in (r, θ, α) as follows

$$\begin{aligned} \mathrm{f}(r,\theta,\alpha,t) &= \sum_n \mathrm{f}_n(r,\theta,t) e^{-in\alpha} e^{in\overline{\omega}_0 t} \\ &= \sum_{n,p} \mathrm{f}_{np}(\theta,t) e^{-in\alpha} e^{i\frac{2\pi p}{L_r}r} e^{in\overline{\omega}_0 t} \end{aligned} \tag{4.11}$$

where the variable $\alpha = \varphi + \nu(r,\theta)$, φ is the toroidal angle coordinate (in the toroidal direction), L_r is the radial domain size and the function $\nu(r,\theta)$ can be interpreted as a poloidally varying safety factor q. A fluctuating field f can be written in the right-handed system of toroidal coordinates (r, θ, φ) and expanded as a function of the toroidal and radial mode number components (n, p) (note however GYRO internally computes $\mathrm{f}_n(r,\theta,t)$ in real space while CGYRO computes $\mathrm{f}_{np}(\theta,t)$ spectrally). The Doppler shift factor given by $e^{in\overline{\omega}_0 t}$ takes into account the frequency shift in the lab-frame with respect to the plasma frame frequency of fluctuations ($\overline{\omega}_0$ is the toroidal rotation frequency of the background plasma). Since microinstabilities are characterized by $n, p \gg 1$, the terms $e^{-in\alpha}e^{i\frac{2\pi p}{L_r}r}$ capture the rapid variation of fluctuations perpendicular to the field line, while the slow variation along the field line (or equivalently, poloidally) is captured in $\mathrm{f}_{np}(\theta,t)$. Note also how the Doppler shift $e^{in\overline{\omega}_0 t}$ can also result in the fastest time scale in the lab frame, depending on the value of $\overline{\omega}_0$ with respect to the time evolution of $\mathrm{f}_n(r,\theta,t)$. In this thesis I will make extensive use of the GYRO expansion of fields 4.11 to compute the synthetic spectra from electron-scale density fluctuations, for which we identify $\mathrm{f} = \delta n_e$.

GYRO operates in real space in the radial direction r, discretizing the radial direction with finite differences [98]. From this one defines the radial wavenumber k_r by $k_r = \frac{2\pi p}{L_r}$,

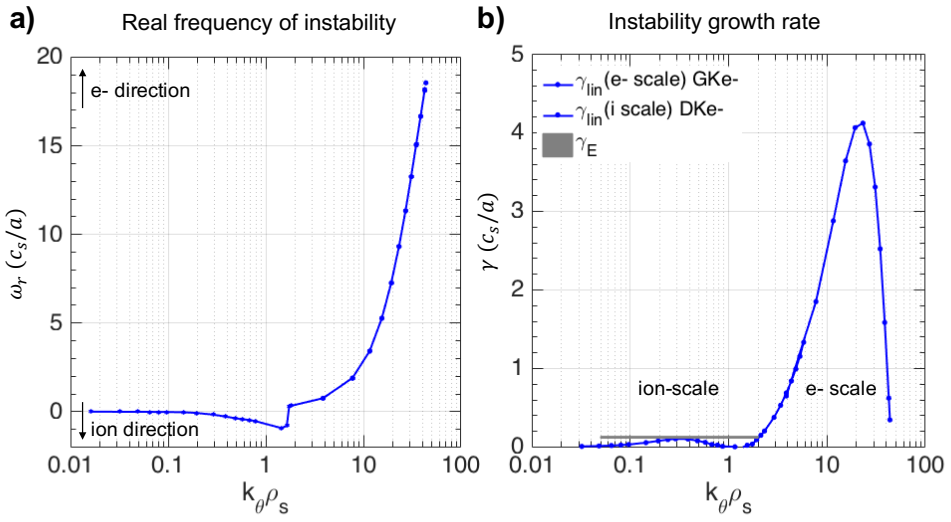

Figure 4-4: **a)** Real frequency of instability from linear GYRO simulations spanning ion and electron scales. **b)** Growth rate associated to the dominant instability. The linear spectra are computed for a highly unstable ETG regime of NSTX shot 141767 ($cf.$ chapter 6 for details). Ion-scale simulations model electrons by the drift-kinetic equation (DKe-) while electron-scale simulations have to model electron gyrokinetically (GKe-). All simulations model a deuterium main ion species and a carbon impurity gyrokinetically.

where p is the radial mode number. The poloidal wavenumber k_θ is directly related to the toroidal mode numbers n via $k_\theta = \frac{nq}{r}$, where q is the safety factor and r is the minor radius. Note this k_θ definition is not local, but is a flux-function. In this thesis I will make extensive use of these wavenumber and mode number definitions to map the measurement wavenumbers by the high-k scattering system, from the standard cylindrical coordinates employed in the experimental measurements into the internal GYRO wavenumber definitions. This will be implemented in the synthetic diagnostic for high-k scattering defined in the next chapter.

4.2.2 Linear GYRO simulation

When run in the linear mode, GYRO provides information about the dominant linear instabilities unstable in the system. The linear gyrokinetic simulations presented in this thesis are computed using an initial value approach, capable of procuring the most unstable mode in the plasma. GYRO has also the capability to compute the subdominant modes using an eigenvalue solver, but this was not performed in the context of this dissertation.

In figure 4-4 is shown an example of the linear spectrum from a GYRO simulation car-

ried out for a highly unstable ETG regime. The real part of the spectrum (ω_r, k_θ) shown in 4-4.a) indicates the propagation direction of the instability. GYRO uses the convention of negative $\omega_r < 0$ being the ion direction (same direction as the ion diamagnetic drift), while $\omega_r > 0$ is the electron direction (electron diamagnetic drift direction). In this particular example the ion-scale instability ($k_\theta \rho_s \lesssim 1$) propagates in the ion direction with a low frequency value, while the electron-scale instability ($k_\theta \rho_s \gtrsim 1$) propagates in the electron direction, characteristic of ETG modes. The imaginary part of the spectrum is the linear growth rate $(\gamma_{\text{lin}}, k_\theta)$, shown in figure 4-4.b). Note the growth rate spectrum exhibits two different peaks at ion scales and at electron scales. The linear growth rate associated to electron-scale modes is generally much higher than the ion-scale one, consistent with mixing length arguments and the isomorphism between ITG and ETG, suggesting that $\gamma_{\text{lin}}(\text{e- scale})/\gamma_{\text{lin}}(\text{ion scale}) \sim (m_i/m_e)^{1/2}$. Although the associated linear growth rate is generally much higher, the modes tend to peak at much higher $k_\theta \rho_s$ values, meaning much smaller structures. It is difficult, and often misleading to use simple mixing length arguments to estimate electron heat transport diffusivities as $\chi_e \sim \gamma_{\text{lin}}(\text{e- scale})/k_\theta^2$. More accurate transport predictions can be obtained through nonlinear gyrokinetic simulation.

In this thesis, the routine `make_gacode_radial_resolution_scan.m` was used to generate and submit the GYRO input files of linear calculations. The routine `plot_gyro_linear_scan_ga.m` was used to analyze the output of the linear calculations, such as the mode structure along the ballooning angle, as well as the real dispersion relation and linear growth rates shown in figure 4-4. Linear simulations are generally not very computationally demanding. In this thesis these were run for individual toroidal modes (n, or equivalently k_θ) in the PPPL Dawson cluster and in the MIT engaging cluster, typically using 32 cores at taking on the order of $\sim 1 - 24$ h for completion. Figure 4-4 is made from the output of ~ 30 linear simulations (one for each toroidal mode number n, or equivalently for each poloidal wavenumber k_θ). More details about the linear simulations performed in this thesis can be found on chapter 6.

4.2.3 Nonlinear GYRO simulation

When run in the nonlinear mode, GYRO simulates the evolution and dynamics of turbulent fluctuations in the plasma, and provides information about the saturated turbulence amplitudes and turbulent radial fluxes of particles, heat and momentum. One important physics ingredient simulated in nonlinear simulations are zonal flows. Zonal flows are toroidally and poloidally symmetric potential perturbations with toroidal mode number $n = 0$. They are self generated by the turbulence, and have been shown capable of stabilizing and self-regulating turbulence saturation.

Nonlinear gyrokinetic simulation is able to predict the electron and ion thermal powers P_i, P_e [MW]. These will be directly compared to TRANSP power balance estimates. Nonlinear gyrokinetic simulation is also able to provide the full fluctuation field of the electron density δn, which will be used to generate synthetic frequency and wavenumber spectra of electron-scale turbulence and will be ultimately compared with measured frequency and wavenumber spectra from the high-k scattering diagnostic.

Traditional nonlinear gyrokinetic simulation has been primarily only capable of performing single-scale simulations: ion-scale simulations resolving ion-scale turbulence $k_\theta \rho_s \lesssim 1$, and electron-scale simulations resolving electron-scale turbulence $k_\theta \rho_s \gtrsim 1$. Recent work has shown capable of performing gigantic multiscale nonlinear simulations, simultaneouly spanning ion and electron scales [72–74, 74, 76] by Howard and Maeyama. This was out of the scope of the thesis I present. In this thesis I have performed 3 different kinds of nonlinear gyrokinetic simulations: ion-scale simulations ($k_\theta \rho_s \lesssim 1$); standard electron-scale gyrokinetic simulation spanning only electron-scale turbulence ($k_\theta \rho_s \gtrsim 1$); 'big-box' electron-scale simulation ($k_\theta \rho_s \gtrsim 0.3$). The latter was run merely for synthetic diagnostic purposes to overlap with the spectral measurement of the high-k diagnostic. A schematic of the k_θ resolution range of each type of nonlinear simulation is shown on figure 4-5. The specific numerical resolution details of these simulations will be provided in sections 5.5.1 and 7. The three simulation types performed in this study (ion-scale, standard electron-scale and 'big-box' e- scale) will be used to compare turbulence fluxes with TRANSP power balance estimates in chapter 7, but only 'big-box' e- scale simulation will prove sufficient for direct high-k turbulence comparisons ($cf.$ chapter 5, 7).

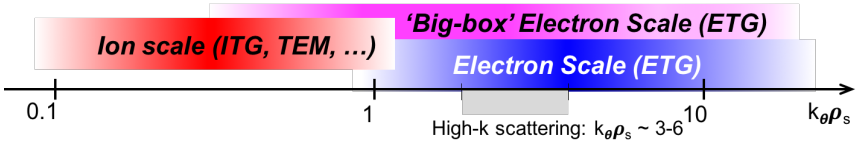

Figure 4-5: Schematic of the range of poloidal wavenumbers k_θ resolved by nonlinear GYRO simulations presented in this thesis: by ion-scale simulations $k_\theta\rho_s \lesssim 1$, standard electron-scale simualtions $k_\theta\rho_s \gtrsim 1$, and 'big-box' electron scale simulation $k_\theta\rho_s \gtrsim 0.3$-$0.4$. The measurement range of the high-k diagnostic is indicated in gray at $k_\theta\rho_s \sim$ [3-6].

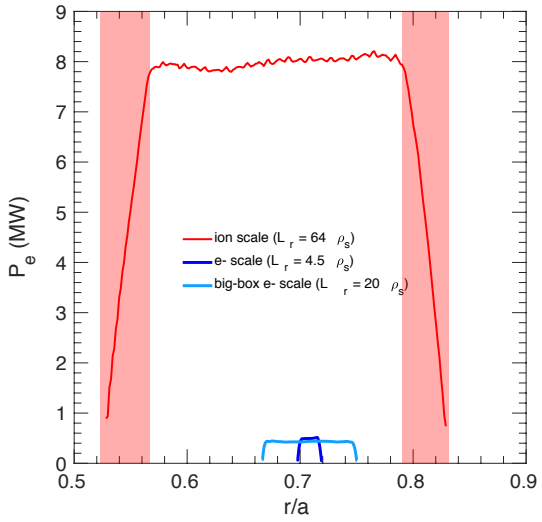

Figure 4-6: Schematic of the radial profile of the electron thermal power P_e solved by nonlinear GYRO simulation, indicating the domain range covered by the different types nonlinear GYRO simulations performed in this thesis: ion-scale simulation (red), standard electron-scale simulation (blue), and 'big-box' e- scale simulation in magenta. The red peripheral regions denote the radial buffer regions for ion-scale simulation, with width $\Delta_b \sim 8\rho_s$. Buffer regions for electron-scale and big-box e- scale simulations are not shown. The high values of P_e from the ion-scale simulation are merely related to the highly unstable turbulence regime simulated.

In this thesis, turbulent fluxes and preliminary flux spectra were analyzed with the routine `plot_gyro_gbflux_ga.m`. I am greatly thankful to Dr. Walter Guttenfelder for providing me with these routines. For more information about the GYRO inputs and output files the reader is referred to the GYRO technical guide [189] and the GYRO git repository [188]. Details about the GYRO input parameters used in this thesis can be found in the appendix E.

4.2.4 GYRO simulation uncertainties

The GYRO output file `out.gyro.gbflux` provides the flux-surface averaged values of the ion and electron heat fluxes $\langle Q_i \rangle_{FS}, \langle Q_e \rangle_{FS}$ [MW/m^2]. In this thesis I choose to present the associated total ion and electron thermal powers P_i, P_e [MW], which are related to $\langle Q_i \rangle_{FS}, \langle Q_e \rangle_{FS}$ via integration along the flux-surface ($P_{i,e}$ [MW] $= \langle Q_{i,e} \rangle$ [MW/m^2] $\cdot \partial V / \partial r$, $cf.$ [189]). The Matlab routine `plot_gyro_gbflux_ga.m` is used for this purpose.

The uncertainties in the predicted ion and electron thermal powers P_i, P_e are given in this thesis by the standard deviation of the corresponding time series (using the Matlab routine `std` $\propto \sigma / \sqrt{(N)}$). As an example, in figure 4-7 is given the time evolution of the total electron thermal power P_e [MW] from a GYRO nonlinear gyrokinetic simulation resolving only electron-scale turbulence. The time period $t \, \epsilon [0, 10]$ [a/c$_s$] corresponds to the linear growth phase in the simulation, in which a small initial seeds exponentially grow due to a particular plasma instability present, the ETG mode in this case. After $t \sim 10$ a/c$_s$ the system reaches a turbulence saturated state. In the particular case shown in figure 4-7 the time average of the simulation is chosen in the turbulence saturated regime $t \, \epsilon$[30-80] a/c$_s$. The blue line denotes the average value of P_e, while the red line indicates the uncertainty associated to P_e computed by the standard deviation of the time series $P_e(t)$.

4.2.5 Accessing GYRO and accounts

In the context of this thesis GYRO was run both at the NERSC supercomputers Edison and Cori for the largest jobs (up to $\sim 10,000 - 20,000$ cores), as well as on the

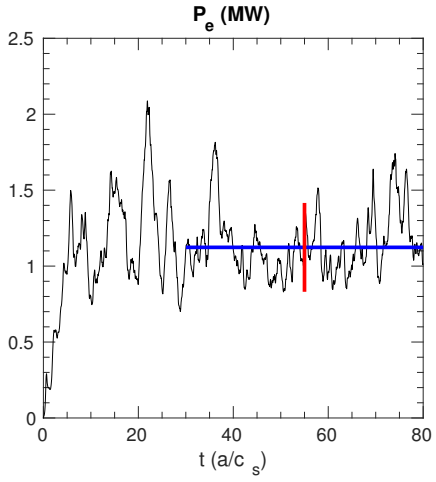

Figure 4-7: Time evolution of the total electron thermal power P_e from a GYRO nonlinear gyrokinetic simulation resolving only electron-scale turbulence. The blue line denotes the average value of P_e, while the red line indicates the uncertainty associated to P_e computed by the standard deviation of the time series $P_e(t)$.

engaging cluster recently set up by MIT, most useful for the midsize jobs (requiring less than $\sim 1,500$ cores). For accessing NERSC's supercomputers, I used the MIT Project Repo m224 "Computational studies in plasma physics and fusion energy", led by Principal Investigator Dr. Abhay Ram (abhay@mit.edu) and PI Proxy Dr. Paul Bonoli (bonoli@psfc.mit.edu). My principal contact for the account usage was Dr. Nathan Howard (nthoward@psfc.mit.edu). These should be the primary contacts for getting a NERSC account and accessing the m224 MIT repo. Additional information is also provided in [191]. With respect to accessing MIT's engaging cluster, the reader is referred to [192] for all the details about the Massachusetts Green High Performance Computer Center, for which MIT and the Plasma Science and Fusion Center (PSFC) have large partitions. The primary contacts for accessing the PSFC partition at MIT are Dr. Jon Wright (jcwright@mit.edu) as well as the admins (engaging-admin@techsquare.com).

Chapter 5

Synthetic diagnostic for coherent scattering of density fluctuations

This chapter focuses on the implementation of the synthetic diagnostic for coherent scattering off of density fluctuations. Section 5.1 is a general introduction to the scattering principles. Section 5.2 discusses some important theoretical considerations of coherent scattering for the measurement of electron density fluctuations, highlighting two alternate ways to interpret the scattering measurement, in real space $vs.$ in k-space. Section 5.3 introduces some important geometry definitions related to the complexity of the field-aligned geometry, that will prove crucial for the implementation of the synthetic diagnostic. Section 5.4 describes a general procedure to implement synthetic diagnostics for coherent scattering density fluctuation measurements in two equivalent ways: in real space $vs.$ in k-space. The principles outlined remain general and applicable to the old high-k scattering system in NSTX [65], but also to the new high-k scattering system to be implemented in NSTX-U [197], and even to Doppler backscattering and reflectometry measurements [198–200]. With respect to synthetic diagnostic, previous efforts have already been reported for the DBS technique [208–211] and for high-k scattering [144]. Building on this knowledge section 5.5 describes the implementation of synthetic diagnostics for the high-k scattering at NSTX.

5.1 Scattering as a diagnostic technique

Scattering of electromagnetic radiation encompass widely used, non-perturbing diagnostic techniques in the fusion plasma community to diagnose internal plasma quantities such as the electron density and temperature, ion density and temperature. In this chapter I will discuss the scattering process of electromagnetic radiation as a diagnostic technique to measure electron density fluctuations, making special emphasis on the old high-k scattering diagnostic at NSTX that I already introduced in the previous chapter. Other sister techniques to high-k scattering are the Doppler backscattering technique and reflectometry [198–200], which have already proven highly successful in determining electron density fluctuations in a series of tokamaks around the world [201–207].

The physical process of scattering of electromagnetic radiation from plasmas may be understood as follows. The fundamental principles of electromagnetic theory establish that when an electric charge is accelerated, it emits electromagnetic radiation as a result of its acceleration. The scattering process takes place when the acceleration on the electric charge is produced by an electromagnetic wave. When the energy associated to the frequency ω of the electromagnetic wave is low compared to the electron rest mass $m_e c^2$, such that $\hbar\omega \ll m_e c^2$, the process is known as Thomson scattering. The scattering processes are primarily dominant for electrons due to their small mass and higher acceleration, giving rise to higher scattered power. Scattering techniques can be categorized between incoherent and coherent scattering. Incoherent scattering is routinely used by diagnostics such as the Thomson scattering (MPTS) diagnostic implemented at NSTX to measure electron density and temperature. These measurements are based on scattering of high power, pulsed lasers (with pulse widths on the order of nanoseconds) off of individual electrons, where it can be shown that the scattered power signal per unit frequency is proportional to the one-particle distribution function of the electrons $dP_s/d\omega \propto f_e$. From this the electron density n_e and temperature T_e can be readily extracted from the height and width of the distribution function f_e. Coherent scattering on the other hand is dominated by the collective motion of electrons, and is thus sensitive to electron density fluctuations $dP_s/d\omega \propto |\delta n_e|^2$, such as used by the high-k scattering diagnostic at NSTX.

5.1.1 Coherent vs. Incoherent scattering

In the introductory chapter of this thesis I discussed the importance of the Debye length λ_D as a fundamental characteristic scale length in a plasma. The effects of a potential-perturbing charge in a plasma are much shorter-range than in the vacuum. Charges in a plasma tend to redistribute themselves so as to shield the plasma from the electric field generated by the perturbing charge. In thermal equilibrium, perturbing effects of a charge will penetrate into the plasma a distance only of the order of the Debye length λ_D. For distances longer than the Debye length, the charge is screened out by a shielding cloud, and practically nonexistent. To each point charge in the plasma we can associate a Debye sphere of radius λ_D centered on the point charge ($cf.$ Fig 1-3). Charges inside that Debye sphere will be of opposite sign of the test charge, and will be able to interact with it.

In a scattering experiment, an incident electromagnetic wave (typically a laser or a microwave beam) interacts with charged particles of the plasma and a scattered wave is radiated. We call $\vec{k}_i$ the wave number of the incident wave, $\vec{k}_s$ the wave number of the scattered wave, and k plasma wavenumber matching $\vec{k}_i$ and $\vec{k}_s$ by $k = |\vec{k}_i - \vec{k}_s|$ (k obeys a conservation law of type $\vec{k} = \vec{k}_s - \vec{k}_i$, $cf.$ Fig. 5-1). The product $k\lambda_D$ measures the correlation between a point charge and its surrounding shielding cloud. The limit $k\lambda_D \gg 1$ corresponds to the limit of incoherent scattering. In this limit, we are probing length scales in the plasma that are much smaller than the Debye length ($\lambda \ll \lambda_D$) in which electrons are not correlated.

The limit $k\lambda_D \leq 1$ corresponds to coherent (or collective) scattering. In this regime, we are probing length scales in the plasma that are bigger than the Debye length ($\lambda \gtrsim 2\pi\lambda_D$). As electrons provide shielding to ions and to other electrons in the plasma, the scattering process reveals information about the collective behavior of particles in the plasma. We are able to observe coherent structures and collective motion of plasma particles. Even though it is the electrons that contribute to the shielding (due to their small mass), the shielding on the ions can provide information about the ion temperature, density and flow. Collective Thomson scattering has been used in tokamaks such as JT60U and Asdex Upgrade for these purposes ([194, 195]). However, collective Thomson scattering can also be designed to probe the macroscopic, coherent structures that can be

indicative of internal turbulent processes. In this thesis, collective Thomson scattering is used to detect electron density fluctuations δn via the high-k scattering diagnostic implemented at NSTX [65].

5.1.2 Matching conditions and the Bragg condition

Consider a scattering process between an incident electromagnetic beam of radiation (subscripted i) and a plasma, giving rise to a scattered beam (subscripted s). In the rest of this chapter we will call $\vec{k}_+ = \vec{k}_s - \vec{k}_i$. In diagnosing density fluctuations by collective scattering measurements, $\vec{k}_+$ corresponds to the wavenumber of the fluctuation that is present in the plasma, that is providing the dominant contribution to the scattering signal. The second matching wave-vector is $\vec{k}_- = \vec{k}_s + \vec{k}_i$, however this has a negligible contribution to the synthetic signal, and can generally be neglected to a high level of accuracy. Typically this fluctuation wave vector is due to some turbulent process in the plasma. At NSTX, the high-k scattering diagnostic is sensitive to wavenumbers that are characteristic of the ETG turbulent mode (such that $k_\perp \rho_s > 1$). We denote by ω_i and ω_s the angular frequencies of the incident and scattered beams, and ω the angular frequency of the fluctuation in the plasma. In a scattering process we have conservation laws between energy and momentum

$$\begin{aligned} \omega &= \omega_s - \omega_i \\ \vec{k}_+ &= \vec{k}_s - \vec{k}_i \end{aligned} \tag{5.1}$$

where $k_i = |\vec{k}_i| = \omega_i/c$ and $k_s = |\vec{k}_s| = \omega_s/c$. Fluctuations probed by the high-k system at NSTX are typically low frequency, such that $\omega \ll \omega_i$, which means $\omega_i \approx \omega_s$ and $k_i \approx k_s$. In this situation, we have $|\vec{k}_s - \vec{k}_i|^2 \approx 2k_i^2 - 2\vec{k}_s \cdot \vec{k}_i$, which leads to the well known Bragg condition

$$k = 2k_i \sin(\theta_s/2) \tag{5.2}$$

where θ_s is the scattering angle between $\vec{k}_i$ and $\vec{k}_s$ ($cf.$ Fig. 5-1) and $k = |\vec{k}_+|$. One of the main advantages of a scattering diagnostic is the ability to produce a frequency and wavenumber spectrum of the turbulent process under study. Equation 5.2 is a very

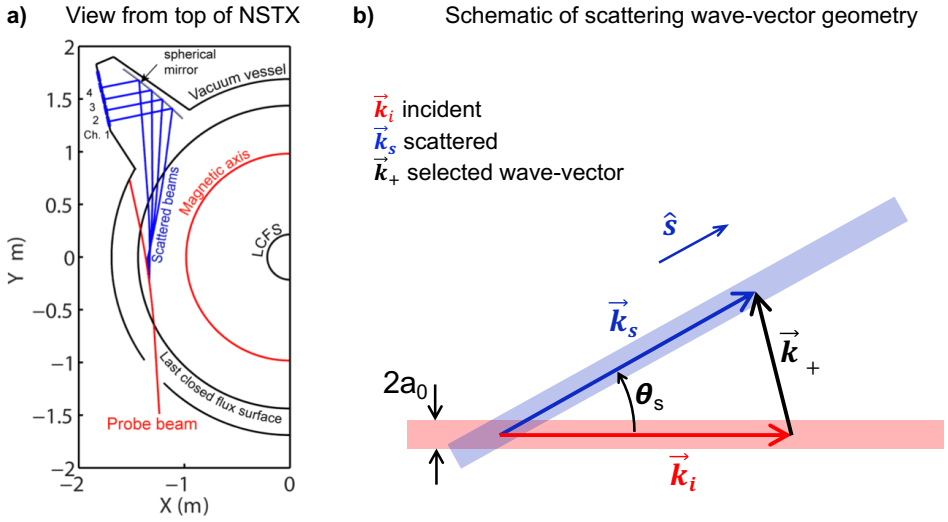

Figure 5-1: **a)** View from the top of the old NSTX high-k scattering diagnostic. **b)** Schematic of the incident $\vec{k}_i$, scattered $\vec{k}_s$ and plasma wave-vector $\vec{k}_+$, corresponding to a conservation law of type $\vec{k}_+ = \vec{k}_s - \vec{k}_i$. The incident beam of radiation has a $1/e^2$ radius of a_0. The intersecting volume between the incident and the scattered beams is called the scattering volume V_s.

useful and important relation keep in mind, as it relates the wavenumber k of the plasma fluctuations that are being probed with the wavenumber of the incident electromagnetic wave k_i and the scattering angle θ_s. k_i is well determined by the wavelength of the incident beam ($k_i = 2\pi/\lambda_i$,) and θ_s is determined by the viewing geometry and the collection optics ($cf.$ figure 5-1). These two quantities alone are well determined beforehand in a scattering experiment, and they alone completely determine the wavenumber of the measured fluctuations. The old high-k scattering diagnostic presented in this thesis uses a 280 GHz incident beam with $\lambda_i \approx 1.07$ mm. Typical scattering angles are $\theta_s \sim 5 - 30^o$, which allows to probe plasma fluctuations with wavenumbers $k \approx k_\perp \lesssim 30$ cm^{-1} (recall $k_\parallel \ll k_\perp$), or $k_\perp \rho_s \lesssim 20$. These values correspond to high-k fluctuations, typical of the ETG mode. Owing to particularly low values of the magnetic field, NSTX is able to diagnose high-k turbulence due to particularly high values of $k_\perp \rho_s$ (typically $k_\perp \rho_s \sim 20$). These values of $k_\perp \rho_s$ are much harder to measure in conventional aspect ratio tokamaks, and makes the high-k scattering system at NSTX a unique measurement, which along with the Doppler backscattering technique are essentially the only diagnostic techniques able to detect electron-scale density fluctuations in tokamak plasmas.

5.2 Theoretical considerations on density fluctuation measurements based on coherent scattering

In this section I show two equivalent ways to implement synthetic diagnostics for turbulence measurements based on coherent scattering of microwaves in tokamak plasmas. Coherent scattering off of turbulence fluctuations inherently takes place in a confined region known as the scattering volume V_s, which is generally determined by the size of the microwave beam input in the plasma, and also by the geometry between the magnetic field and the probe beam. This leads one to interpret the scattering process as an integration of fluctuations in real space within the scattering volume. However, scattering measurements are usually interpreted in wavenumber space, based on the measurement of a specific turbulence wavenumber $\vec{k}_+$ which itself is determined by the launching and receiving geometries of the microwave beam. This leads one to interpret the scattering process as a selection of a specific wavenumber $\vec{k}_+$ from the density fluctuations. In this section I aim to reconcile both views, and show how the scattering process can be interpreted in real space as well as in k-space. I then show two equivalent ways of implementing synthetic diagnostics for turbulence measurements based on coherent scattering.

In the coherent scattering process, the expression for the scattered power per unit frequency and unit solid angle $\frac{d^2P_s}{d\omega d\Omega}$ is related to the frequency signal of density fluctuations $\delta n_{\mathrm{u}}(\vec{k}_+, \omega)$ by the textbook formula ($cf.$ appendix A)

$$\frac{d^2P_s}{d\omega d\Omega} = \frac{P_0}{A_i} r_0^2 |\hat{s} \times (\hat{s} \times \hat{e})|^2 \frac{1}{2\pi T} \left\langle |\delta n_{\mathrm{u}}(\vec{k}_+, \omega)|^2 \right\rangle \tag{5.3}$$

where the subscript u indicates that the density fluctuation signal has been properly filtered in the scattering process by a filter U in real space (and does not directly correspond to the actual density fluctuation). In expression 5.3 $d\Omega$ is the solid angle, P_0 is the incident beam power in W, A_i is the incident beam area $A_i = \pi a_0^2$, $r_0 = \frac{e^2}{m_e c^2}$ is the classical electron radius, T is the collection time, $\hat{s}$ is the direction of scattering, $\hat{e}$ is the direction of the scattered electric field, and $\langle . \rangle$ denotes an ensemble average. Recall the incident and scattered frequencies are typically much higher than any other frequency in the plasma ($\omega_i, \omega_s >> \omega_{pe}, \omega_{ce}, ...$).

The quantity $\delta n_{\mathrm{u}}(\vec{k}_+, \omega)$ in equation 5.3 has been Fourier decomposed from $\delta n_{\mathrm{u}}(\vec{k}_+, t)$, the synthetic time signal of electron density fluctuations for the selected turbulence wavenumber $\vec{k}_+$. This quantity can be computed in real space as well as in wavenumber space as follows

$$\delta n_{\mathrm{u}}(\vec{k}_+, t) = \int_{V_s} d^3\vec{r'}\, \delta n(\vec{r'}, t) U(\vec{r'}) e^{-i\vec{k}_+ \cdot \vec{r'}} = \frac{1}{(2\pi)^3} \int d^3\vec{k}\, \delta n(\vec{k}, t) I(\vec{k} - \vec{k}_+) \quad (5.4)$$

In this expression U is the filter of fluctuations in real space, and is composed by the incident and scattered beam profiles that determine the shape of the scattering volume V_s. The quantity real quantity $\delta n(\vec{r'}, t)$ is the electron density fluctuation field, and $\delta n(\vec{k}, t)$ is the electron density fluctuation spectrum. I is the scattering filter in wavenumber space, and is directly related to the Fourier transform of the scattering volume shape U. For simplicity in notation I will omit the Doppler shift term in the scattering signal in this section, but will be taken into account in section 5.5 and consequent chapters when implementing the synthetic diagnostic to the old high-k scattering system and comparing to experimental high-k turbulence measurements. The reader is referred to the appendix A for additional details.

Equation 5.4 states the equivalence between the computation of the synthetic signal of fluctuations in real space and in wavenumber space. In wavenumber space, one can think of the synthetic signal as a sum over all turbulence wavenumber contributions around the detected wavenumber $\vec{k}_+$, where a filter $I(\vec{k} - \vec{k}_+)$ applied to the wavenumber spectrum of fluctuations $\delta n(\vec{k}, t)$. I tends to peak around the measurement wave-vector $\vec{k}_+$, and down-selects a range of wavenumbers neighboring $\vec{k}_+$ within the range $\Delta\vec{k}^3 \sim 1/V_s$, where V_s is the scattering volume extent. In real space, the synthetic signal can be thought of as the Fourier component $\vec{k}_+$ of $\delta n(\vec{r'}, t) U(\vec{r'})$. As a result of U in the real integration, the scattering signal has not only contributions from one lone $\vec{k}_+$(obtained for $U = 1$) , but also from an array of wavenumbers around $\vec{k}_+$, as dictated by the scattering volume extent in U by $\Delta\vec{k}^3 \sim 1/V_s$. Here the spectral width of the filter $I(\vec{k} - \vec{k}_+)$ is noted as $\Delta\vec{k}^3$. Full information about the detected turbulence wavenumber $\vec{k}_+$ and the spectral width $\Delta\vec{k}^3$ is preserved in both implementations while computing $\delta n_{\mathrm{u}}(\vec{k}_+, t)$. In this chapter I

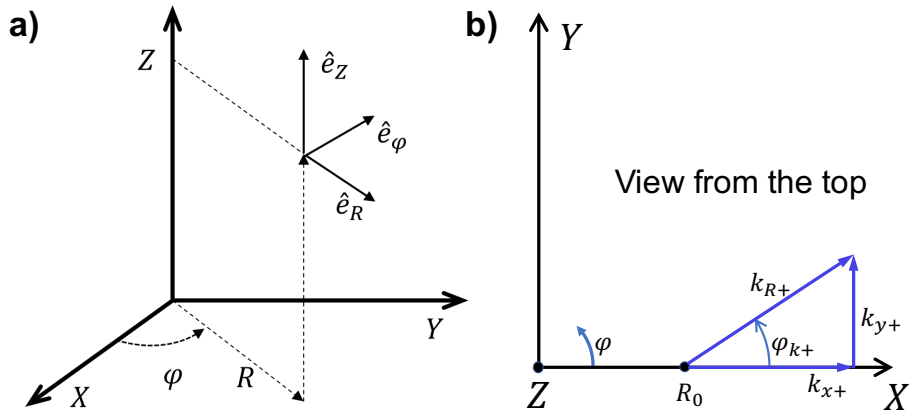

Figure 5-2: **a)** Cylindrical coordinates (R, Z, φ) used to express density fluctuations amplitudes $\delta n(\vec{r}, t)$ for deployment of synthetic diagnostic in real space. **b)** Definitions of wavenumber $\vec{k}_+$ components in cartesian coordinates $(k_x, k_y, k_z)_+$ and in cylindrical coordinates $(k_R, k_Z, \varphi_k)_+$. Due to axisymmetry I assume a scattering location at $\varphi_0 = 0$.

will exploit equation 5.4 and implement two equivalent formulations for computing the synthetic signal in k-space $vs.$ real space. In the meantime, we will have to deal with the complexity of tokamak geometry, as will be outlined next. The implementation of both methods will provide a mean of cross-verification when developing a synthetic diagnostic for the validation of plasma turbulence simulations.

5.3 Some geometry definitions

In this section I specify some details pertaining the toroidal geometry, flux-surface shape and wavenumber definitions in GYRO. I will make extensive use of the cylindrical coordinate system (R, Z, φ), where R is the major radius coordinate, Z is the elevation coordinate, and φ is the toroidal angle coordinate (figure 5-2).

Before proceeding to implement a synthetic diagnostic, one needs information about the scattering location $\vec{r}_0$, the measurement wavenumber $\vec{k}_+$, as well as the scattering volume V_s, which itself is related to the wavenumber resolution of the diagnostic. This information can generally be provided by ray tracing or beam tracing calculations, and was briefly outlined in chapter 4.

In order to compute the synthetic signal of density fluctuations $\delta n_{\mathrm{u}}(\vec{k}_+, t)$ in realistic flux-surface geometry, I start from equation 5.4 in real space written in cylindrical

coordinates (R, Z, φ)

$$\begin{aligned}\delta n_{\mathrm{u}}(\vec{k}_+, t) &= \int_{V_s} d^3\vec{r'}\, \delta n(\vec{r'}, t) U(\vec{r'}) e^{-i\vec{k}_+ \cdot \vec{r'}} \\ &= \int_{V_s} d\varphi R dR dZ \delta n(R, Z, \varphi, t) U(R\text{-}R_0, Z\text{-}Z_0, \varphi\text{-}\varphi_0) e^{-i\vec{k}_+ \cdot \vec{r}}\end{aligned} \tag{5.5}$$

where R is the major radial direction, Z is the vertical direction and φ is the toroidal direction. The filter in real space U is centered around the scattering location $\vec{r}_0 = (R_0, Z_0, \varphi_0)$, and has spatial extent $\sim (\Delta R, \Delta Z, \Delta\varphi)$. Equation 5.5 already shows the implementation of the synthetic diagnostic in real space, where the product $\vec{k}_+ \cdot \vec{r}$ and the real space filter U need to be mapped to cylindrical coordinates. Those are the subject of sections 5.3.1, 5.3.2, C.11.

This implementation in real space, although quite straightforward, lacks the necessary intuition of scattering off of turbulence fluctuations. This real space implementation does not provide information about the measured turbulence wavenumbers in the field-aligned coordinate system (k_r, k_θ), which are wavenumber coordinates in which density fluctuation fields from gyrokinetic codes are generally expressed. Where does the measurement wavenumber $\vec{k}_+$ map to in the density fluctuation field output from GYRO? What is the wavenumber resolution of the diagnostic? For this one needs to implement the synthetic diagnostic in k-space.

The implementation of the synthetic diagnostic in k-space in the context of field-aligned coordinates is slightly more cumbersome than in real space due to the complex geometry and the ballooning transform of fields used in gyrokinetic codes such as GYRO ($cf.$ equation 4.11, references [98, 189]). The turbulence wavenumber $\vec{k}_+$ needs also be expressed as a function of k_r and k_θ that are internal to the specific gyrokinetic code. This wavenumber-mapping is presented in section 5.3.4. I focus specifically on the geometry implementation of the GACODE suite [188] and gyrokinetic codes GYRO [98, 189] and CGYRO [190]. The full wavenumber implementation of the synthetic signal in terms of the scattering matrix formulation is presented in the following section 5.4.

5.3.1 Wavenumber components in cylindrical coordinates

As we saw in equation 5.5, the product $\vec{k}_+ \cdot \vec{r}$ needs to be computed in cylindrical coordinates. First one needs to define the wavenumber components of $\vec{k}_+$ in cylindrical coordinates. Due to the axisymmetry of the system around the toroidal direction, I choose a coordinate system in which I set the toroidal angle of scattering to $\varphi_0 = 0$. As an intermediate step, I define the wavenumber components in cartesian coordinates $\vec{k}_+ = (k_x, k_y, k_z)_+$ as shown in figure 5-2. In the context of this thesis, the turbulence wavenumber $\vec{k}_+$ will be assumed constant in time and space.

I define k_{x+} as the projection of $\vec{k}_+$ along x, i.e. along the major radius direction. k_{y+} is the projection of $\vec{k}_+$ along y, i.e. the toroidal direction. k_{z+} is the projection of $\vec{k}_+$ along z, the vertical direction. In these coordinates, the product $\vec{k}_+ \cdot \vec{r}$ can be expressed as

$$\begin{aligned} &\vec{k}_+ \cdot \vec{r} = Rk_{R+}\cos(\varphi\text{-}\varphi_{k+}) + Zk_{Z+} \\ &\text{where} \\ &k_{x+} = k_{R+}\cos(\varphi_{k+}) \\ &k_{y+} = k_{R+}\sin(\varphi_{k+}) \\ &k_{z+} = k_{Z+} \end{aligned} \tag{5.6}$$

The geometric interpretation of $(k_x, k_y, k_z)_+$ and $(k_R, \varphi_k, k_Z)_+$ are shown in figure 5-2.b). These wavenumber definitions are suitable for the present problem, since the wavenumber components $(k_{R+}, k_{Z+}, \varphi_{k+})$ do not vary in space. Additionally, note how the wavenumber components $(k_{R+}, k_{Z+}, \varphi_{k+})$ are cylindrical in k-space, but NOT in real space, ie. k_{R+} is the norm of $\vec{k}_+$ in the (x, y)-plane, namely $k_{R+} = \sqrt{k_{x+}^2 + k_{y+}^2}$, and does not generally correspond to the wavenumber component along the major radius direction.

One can associate a specific wavelength to each wavenumber component $(\lambda_x, \lambda_y, \lambda_z) = (2\pi/k_{x+}, 2\pi/k_{y+}, 2\pi/k_{z+})$. In the scattering experiments presented here, these wavelengths are much smaller than the corresponding extent of the scattering volume $(\Delta R, \Delta Z, R_0\Delta\varphi)$. In turn, the extent of the scattering volume is much smaller than minor radius a. We have the following inequalities

$$\begin{aligned} \lambda_x &\ll \Delta R \quad \ll a \\ \lambda_y &\ll R_0 \Delta\varphi \ll a \\ \lambda_z &\ll \Delta Z \quad \ll a \end{aligned} \tag{5.7}$$

5.3.2 Flux Surface Shape

To compute the synthetic signal of fluctuations from equation 5.5 one needs to specify the flux surface shape. In this thesis I use model-shape flux surface geometry implemented in GYRO and based on the Miller equilibrium specification [196], in which (R, Z) are parametrized by

$$\begin{cases} R(r,\theta) = R_0(r) + r\cos(\theta + \arcsin(\delta)\sin(\theta)) \\ Z(r,\theta) = Z_0(r) + r\kappa(r)\sin(\theta) \end{cases} \tag{5.8}$$

where I have introduced the elongation κ, triangularity δ, flux-surface center R_0 and flux-surface elevation Z_0. Specification of these quantities allows to perform a complete mapping from flux surface coordinates (r, θ, φ) to real space cylindrical coordinates (R, Z, φ) as in equation 5.5. The the Jacobian from $(r, \theta, \varphi) \rightarrow (R, Z, \varphi)$, defined by $d^3\vec{r} = J_r(r,\theta)drd\theta d\varphi$, is given by $J_r(r,\theta) = R(\frac{\partial R}{\partial r}\frac{\partial Z}{\partial \theta} - \frac{\partial R}{\partial \theta}\frac{\partial Z}{\partial r})$. In this thesis, measurements will mainly focus to the outboard midplane $(\theta_0 \sim 0)$, in which case the Jacobian can be simplified by $J_r \sim \frac{R_0 r_0 \kappa}{|\nabla r|_0}$. The gradient $|\nabla r|_0$ is directly related to the Shafranov shift Δ via $|\nabla r|_0 \approx 1/(1+\Delta)$ $(cf.$ [189]) and κ is the flux-surface elongation in the Miller parametrization [196]. In what follows, the subscripts 0 denote that quantities are evaluated a local position (R_0, Z_0, φ_0), or equivalently $(r_0, \theta_0, \varphi_0)$.

5.3.3 The scattering volume shape U

The specific shape of the scattering volume can vary depending on the specific scattering geometry of particular experiments. In this thesis I assume the scattering volume envelope is separable with gaussian shape centered around $(R_0, Z_0, \varphi_0 = 0)$

$$
\begin{aligned}
U(R,Z,\varphi) \quad &= \Psi_R(R\text{-}R_0)\Psi_Z(Z\text{-}Z_0)\Psi_\varphi(\varphi) \\
&\text{with} \\
\Psi_R(R\text{-}R_0) \quad &= \exp[\text{-}(R\text{-}R_0)^2/\Delta R^2] \\
\Psi_Z(Z\text{-}Z_0) \quad &= \exp[\text{-}(Z\text{-}Z_0)^2/\Delta Z^2] \\
\Psi_\varphi(\varphi) \quad &= \exp[\text{-}\varphi^2/\Delta\varphi^2] \qquad\qquad 3D \\
&= \delta(\varphi/\Delta\varphi) \qquad\qquad 2D
\end{aligned}
\tag{5.9}
$$

where I have made the distinction between a 3D and a 2D implementation in the toroidal filter Ψ_φ, where the function $\delta(\varphi/\Delta\varphi)$ is the Dirac delta function. In the 2D approximation I will neglect any toroidal variation and the fluctuations will be filtered at a fixed toroidal slice. Equations 5.9 are indeed a reasonable approximation and likely applicable to a wide range of coherent scattering experiments. In the context of the old high-k scattering system at NSTX, the near tangential geometry suggests $\Delta R = \Delta Z$, equal to 3 cm which is precisely the beam width ($cf.$ figure 5-1). The gaussian shape of the electric field associated to the probe beam justifies the form of Ψ_R and Ψ_Z ($cf.$ [89]). The specific shape of the toroidal filter Ψ_φ is not specified in this work, since I will mainly work on 2D as I will justify in the next section. However, work by E. Mazzucato [90, 91] showed that the toroidal filter is highly localized, and has a shape that can be approximated by a gaussian. Preliminary results shown on appendix 7.3 suggest a 2D approximation is sufficient to describe the high-k scattering system in NSTX.

Next we seek to write U in (r,θ,φ) coordinates by expanding (R,Z,φ) about $(r_0,\theta_0,\varphi_0 = 0)$. We find

$$
\begin{aligned}
R(r,\theta) \qquad &\approx R(r_0,\theta_0) + (r-r_0)\frac{\partial R}{\partial r}\Big|_0 + (\theta-\theta_0)\frac{\partial R}{\partial \theta}\Big|_0 \\
Z(r,\theta) \qquad &\approx Z(r_0,\theta_0) + (r-r_0)\frac{\partial Z}{\partial r}\Big|_0 + (\theta-\theta_0)\frac{\partial Z}{\partial \theta}\Big|_0 \\
\cos(\varphi-\varphi_{k+}) &\approx (1-\varphi^2/2)\cos(\varphi_{k+}) + \varphi\sin(\varphi_{k+})
\end{aligned}
\tag{5.10}
$$

Where (R,Z) are given by equation 5.8. Now try to express Ψ_R, Ψ_Z in (r,θ). At the outboard midplane $\theta_0 \approx 0$ find

$$\begin{aligned}\exp[(R-R_0)^2/\Delta R^2] &\approx \exp[\text{-}(r-r_0)^2/\Delta r^2] = \Psi_r(r-r_0)\\ \exp[(Z-Z_0)^2/\Delta Z^2] &\approx \exp[\text{-}(\theta-\theta_0)^2/\Delta\theta^2] = \Psi_\theta(\theta-\theta_0)\end{aligned} \tag{5.11}$$

where $\Delta r = |\nabla r|_0 \Delta R$ and $\Delta\theta = \Delta Z/(r_0\kappa)$. This allows us to write $U(R,Z,\varphi) \approx \Psi_r(r\text{-}r_0)\Psi_\theta(\theta\text{-}\theta_0)\Psi_\varphi(\varphi)$. The particular values of r_0 and θ_0 can be computed from the scattering location R_0 and Z_0 by inverting equation 5.8, where R_0 and Z_0 are directly provided by ray-tracing calculations. Note that flux tube simulations that are based on the local approximation allow one to write a constant radial filter $\Psi_r = 1$ due to the fact that all parameter inputs are constant along the full radial domain ($cf.$ section 5.4.1 for a more detailed discussion). The particular shape of the filters in real space $\Psi_r, \Psi_\theta, \Psi_\varphi$ is used in section 5.4 to compute the corresponding filters in wavenumber space and the scattering matrix.

5.3.4 GYRO wavenumber mapping

As we saw in section 4.2, GYRO and CGYRO use the internal wavenumber definitions $(k_r, k_\theta) = (\frac{2\pi p}{L_r}, \frac{nq}{r})$, where (n,p) are the toroidal and radial mode numbers. With these definitions, electron density fluctuations δn are naturally expressed as a function of (n,p) as $\delta n(r,\theta,\varphi) = \sum_{n,p} \delta n_{n,p}(\theta,t) e^{-in\alpha} e^{i\frac{2\pi p}{L_r}r}$ (identify $\mathrm{f} = \delta n$ in equation 4.11).

We wish to map the turbulence wavenumber $\vec{k}_+$ expressed in cylindrical coordinates (or cartesian coordinates, $cf.$ equation 5.6) to k_r and k_θ, or equivalently to n and p. For this one needs to implement a wavenumber mapping to the field-aligned geometry implemented in GYRO/CGYRO. The wavenumber mapping is

$$\begin{cases} \dfrac{2\pi p_+}{L_r} - n_+^\theta \dfrac{\partial\nu}{\partial r}\bigg|_0 = \dfrac{\partial R}{\partial r}\bigg|_0 k_{x+} + \dfrac{\partial Z}{\partial r}\bigg|_0 k_{z+} \\ -\dfrac{n_+^\theta}{r_0}\dfrac{\partial\nu}{\partial\theta}\bigg|_0 = \dfrac{1}{r_0}\dfrac{\partial R}{\partial\theta}\bigg|_0 k_{x+} + \dfrac{1}{r_0}\dfrac{\partial Z}{\partial\theta}\bigg|_0 k_{z+} \\ -\dfrac{n_+^\varphi}{R_0} = k_{y+} \end{cases} \tag{5.12}$$

Recall all quantities computed here are local, given by the subscript 0. The geometry function ν takes into account the poloidal variation of the local field line pitch [189]. In 5.12 I make the distinction between a toroidal mode number n_+^θ associated to the vertical

component k_{z+}, and a different toroidal mode number n_+^φ associated to the toroidal component k_{y+}. These mapped toroidal mode numbers are in principle independent of each other, however we will see how the scattering condition restricts them to have similar value $n_+^\theta \approx n_+^\varphi$. Although GYRO/CGYRO use internal, integer (n, p) values, note how the mapped mode numbers $n_+^\theta, n_+^\varphi, p_+$ are generally not integers.

Note how k_r and k_θ are constant on the flux-surface. The term $\partial\nu/\partial\theta$ captures the poloidal variation of the local field line pitch through the geometry function $\nu = \nu(r, \theta)$. The term $\partial\nu/\partial r$ captures the effect of magnetic shear $\hat{s}$ as one moves poloidally along the flux surface. For unshifted, s-α geometry ($\nu \approx -q\theta$), one has $\frac{2\pi p}{L_r} - n\frac{\partial\nu}{\partial r} = k_r + \hat{s}\theta\, k_\theta$, $-\frac{n}{r}\frac{\partial\nu}{\partial\theta} = k_\theta$. Note how even in s-α geometry, the same k_{x+} and k_{z+} couple will result in a different GYRO (k_r, k_θ) as one moves along the flux-surface due to the influence of magnetic shear $\hat{s}$. Additionally, in s-α geometry and at the midplane n_+^θ would reduce to $n_+^\theta = (r_0/q)k_{z+}$ while $2\pi p_+/L_r = k_{x+}$. In s-α geometry and at the outboard midplane, the wavenumber mapping reduces to $k_{r+} = k_{x+}$ and $k_{\theta+} = k_{z+}$. The reader is referred to appendix B for additional details about the derivation of the wavenumber mapping along with some simplified examples.

For clarity, in figure 5-3 is given an example mapping of equation 5.12, corresponding to a pair $(k_x, k_z)_+ = (500, 1)$ m^{-1} when the mapping is computed at different poloidal locations along the flux surface and at a fixed toroidal slice (2D approximation). Here I have picked a circular scattering volume cross-section in (R, Z) (characteristic of the old high-k scattering system), resulting in a circularly shaped filter when expressed in (k_x, k_z) as in figure 7.3.a). Figure 5-3.b) shows how a circularly-shaped filter in (k_x, k_z)-space is mapped to (k_r, k_θ) (or equivalently (n, p)), depending on the flux-surface location where scattering takes place. Note how even a very small $k_{z+} = 1$ m^{-1} value maps to finite $k_{\theta+}\rho_s$, which can itself be positive or negative depending on the location of scattering along the flux surface. This means that the same measurement of $(k_x, k_z)_+$ at different poloidal locations will actually be sampling very different turbulent wavenumbers when expressed in $(k_r\rho_s, k_\theta\rho_s)$, which are the normalized wavenumber components characterizing microturbulence fluctuations in the field-aligned flux-coordinate system. This will likely result into different scattering amplitudes at each poloidal location. Note also how the circular shape of the filter in (k_x, k_z) coordinates is mapped to an elliptical shape in

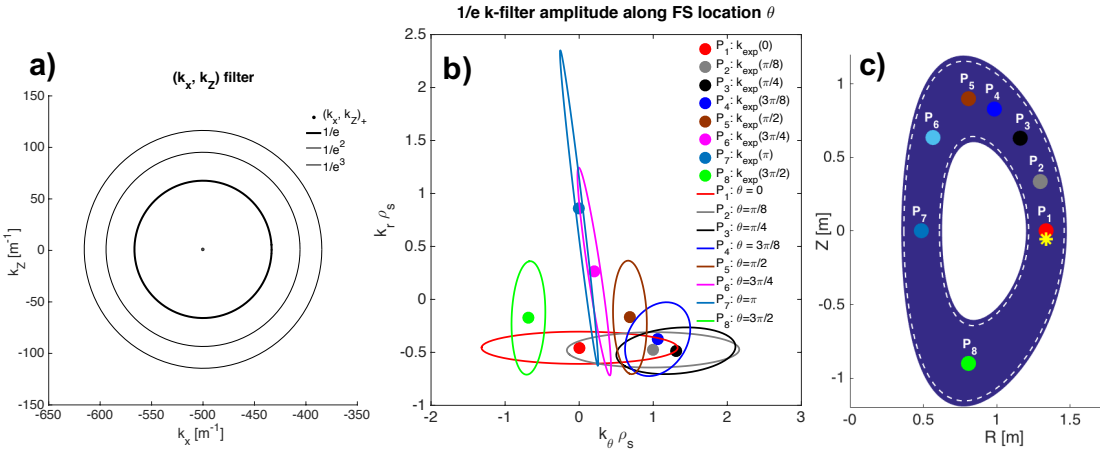

Figure 5-3: **a)** Circular wavenumber filter shape in $(k_x, k_z)_+$ corresponding to a circularly shaped scattering volume U in (R, Z), for a fixed toroidal slice $\varphi_0 = 0$. This shape is characteristic of the old tangential scattering diagnostic at NSTX [65]. The dot indicates the dominant measurement wavenumber $(k_x, k_z) = (500, 1)$ m^{-1}. The circles indicate the $1/e$, $1/e^2$ and $1/e^3$ amplitude of the filter k-space filter I in (k_x, k_z) ($cf.$ equation 5.4). **b)** Colored dots are mapped wavenumbers in $(k_r\rho_s, k_\theta\rho_s)$ corresponding to a measurement of $(k_x, k_z)_+ = (500, 1)$ m^{-1} for different poloidal locations along the flux surface. The ellipses surrounding each mapped wavenumber denote the $1/e$ amplitude of the scattering matrix U_{np} corresponding to the different poloidal locations along the flux surface. **c)** Poloidal locations θ_0 along the flux surface used to compute the mapped wavenumbers and $1/e$ filter amplitudes of b). The yellow star corresponds to the experimental location of scattering analyzed in this article with poloidal angle $\theta_0 \approx$ -4^o. The flux-surface geometry is taken from a NSTX H-mode plasma shot.

(k_r, k_θ), which becomes slanted and elongated for off-midplane locations. The particular case of outboard midplane location is discussed in subsection 5.4.2.

5.4 Computation of the synthetic signal for coherent scattering turbulence measurements

In this section I put together all the previous geometry definitions from the previous section to calculate the synthetic signal $\delta n_u(\vec{k}_+, t)$ in the wavenumber space associated to the GYRO/CGYRO field-aligned coordinates. I start by presenting the general 3D formulation in a formal way in section 5.4.1. I will argue in appendix C how the 2D-approximation is in fact a good approximation for the old high-k scattering system. Owing to the prevalence of most scattering measurements being performed at the outboard midplane, I present the 2D + outboard midplane approximation in section 5.4.2.

5.4.1 General 3D implementation

Using all the previous geometric definitions, we are now ready to calculate the synthetic signal $\delta n_{\mathrm{u}}(\vec{k}_+, t)$ in the wavenumber space associated to the GYRO/CGYRO field-aligned coordinates. Recall expression 5.5, repeated here for reference $\delta n_{\mathrm{u}}(\vec{k}_+, t) = \int_{V_s} d^3\vec{r'}\ \delta n(\vec{r'}, t) U(\vec{r'}) e^{-i\vec{k}_+ \cdot \vec{r'}}$. Plugging in the expression 4.11 for $\delta n(\vec{r}, t)$ into equation 5.5 we find

$$\begin{aligned} &\delta n_{\mathrm{u}}(\vec{k}_+, t) \approx \sum_{n,p} U_{np} \delta n_{np}(\theta_0, t) \\ &\text{where } U_{np} \text{ is defined by} \\ &U_{np} = \int d^3\vec{r} U(\vec{r}) e^{-in\alpha} e^{i2\pi pr/L_r} e^{-i\vec{k}_+ \cdot \vec{r}} \end{aligned} \tag{5.13}$$

where I have assumed slowly varying $\delta n_{np}(\theta_0, t)$ in θ. U_{np} is the scattering matrix. Expressed in (n, p), the scattering matrix is essentially a filter in wavenumber space equivalent to the general k-space filter $I(\vec{k} - \vec{k}_+)$ from equation 5.4. The scattering matrix U_{np} peaks around toroidal and radial mode numbers $n_+^\theta, n_+^\varphi, p_+$, which can be calculated and mapped from a turbulence wavenumber $\vec{k}_+$ by use of equation 5.12. U_{np} can be interpreted as a 'Fourier-like' transform of the scattering volume shape U, similar to the relation between $U(\vec{r})$ and $I(\vec{k}\text{-}\vec{k}_+)$ in equation 5.4. U_{np} can be analytically computed for simple cases such as the outboard midplane and separable $U(R, Z, \varphi)$ as a product of separable functions of R, Z and φ, by use of the expression for U (Eqs. 5.9, 5.11), the wavenumber mapping (Eq. 5.12) and the product $\vec{k}_+ \cdot \vec{r}$ (Eq. 5.6).

A particular example illustrating the shape of U_{np} can also be schematically seen on figure 5-3, corresponding to a circularly shaped scattering volume U in the R and Z directions and neglecting the toroidal extent of the scattering volume (2D approximation for a fixed toroidal slice). The flux-surface geometry is taken from a NSTX H-mode plasma shot 141767 at $r/a \sim 0.7$. As is shown in detail in appendix C, under the assumption of separable scattering volume shape (equation 5.9) and at the outboard midplane $\theta_0 \approx 0$, the scattering matrix U_{np} can be decomposed as a product of toroidal and radial mode number filters $\Psi_{n^\varphi}, \Psi_{n^\theta}, \Psi_p$ as follows

$$
\begin{aligned}
U_{np} \quad & = e^{-in\nu_0} e^{ir_0 k_r} \Psi_{n^\varphi}(n\text{-}n_+^\varphi)\Psi_{n^\theta}(n\text{-}n_+^\theta)\Psi_p(p\text{-}p_+) \\
&\text{with} \\
\Psi_{n^\varphi}(n\text{-}n_+^\varphi) &\approx R_0 \left(\frac{4\pi}{(\Delta n^\varphi)^2}\right)^{1/2} e^{-(n\text{-}n_+^\varphi)^2/(\Delta n^\varphi)^2} \qquad \text{3D} \\
&\approx R_0 \Delta\varphi \qquad \text{2D} \\
\Psi_{n^\theta}(n\text{-}n_+^\theta) &\approx \sqrt{\pi}(\Delta Z) e^{-(n\text{-}n_+^\theta)^2/(\Delta n^\theta)^2} \\
\Psi_p(p\text{-}p_+) &\approx \sqrt{\pi}(\Delta R) e^{-(k_r\text{-}k_{r+})^2/\Delta k_r^2} \qquad \text{Global simulation} \\
&\approx \frac{L_r}{|\nabla r|_0} \mathrm{sinc}[(k_r\text{-}k_{r+})L_r/2] \qquad \text{Local simulation}
\end{aligned}
\tag{5.14}
$$

The toroidal and radial mode number filters Ψ_{n^φ}, Ψ_{n^θ} and Ψ_p are respectively centered at $(n_+^\varphi, n_+^\theta, p_+)$, which can be calculated using equation 5.12. Note the different expressions of the toroidal mode number filter Ψ_{n^φ} in the 2D-approximation $vs.$ in full 3D. The 2D approximation relies on a fixed toroidal slice and U has no toroidal dependence, which translates to an infinitely thin toroidal extent $\Delta\varphi \to 0$, or equivalently $\Psi_\varphi = \delta(\varphi/\Delta\varphi)$ ($cf.$ equation 5.9). The resulting toroidal mode number filter Ψ_{n^φ} is simply constant = $R_0\Delta\varphi$. In full 3D, a finite value of $\Delta\varphi$ is retained. In this thesis I will implement the synthetic diagnostic for high-k scattering based on the 2D approximation, which is well justified in detail in appendix C.

Equation 5.14 also shows a different radial mode number filter Ψ_p in a local $vs.$ global simulation. Local simulation has the same profile values along the full radial domain, ie. same turbulence drive in all radial locations. For all intents and purposes the radial filter in real space takes the value $\Psi_r = 1$, resulting in the sinc function (where L_r is the radial extent of the simulation). However a global simulation retains the radial profile variation, and the radial filter in real space Ψ_r has to take the shape dictated from experiment (e.g. gaussian as in equation 5.9) to accurately implement the correct filter weights at each radial location, give by Ψ_r. In this thesis the gyrokinetic code GYRO is run in 'flux-tube' mode, in which the background profiles and profile gradients take the same value along the full radial domain.

In order to implement equation 5.14, one needs detailed information about the toroidal,

poloidal and radial mode number resolutions, which can be shown to be ($cf.$ appendix C)

$$\begin{aligned}(\Delta n^{\varphi})^2 &= 4/\Delta\varphi^2\text{-}2iR_0k_{x+}\\ \Delta n^{\theta} &= \frac{2}{\Delta\theta\frac{\partial\nu}{\partial\theta}|_0}\\ \Delta k_r &= \frac{2}{\Delta r} = \frac{2}{|\nabla r|_0\Delta R}\end{aligned} \tag{5.15}$$

Note how the resolution associated to the toroidal filter Δn^{φ} is complex. $\Psi_{n^{\varphi}}$ is complex in nature and depends on the relative ratio between the toroidal extent of the scattering volume $\Delta\varphi$ and the x component of the sampled wavenumber R_0k_{x+}. The ratio between these two quantities is dependent on the specific scattering experiment and geometry and would have to be analyzed case by case. The ratio between the resolutions Δn^{φ} and Δn^{θ} will determine the importance of 3D effects in the computation of the synthetic signal. As is shown on appendix C, the filter $\Psi_{n^{\varphi}}$ is much wider than the filter $\Psi_{n^{\theta}}$ for the old high-k scattering conditions. As a result, the product $\Psi_{n^{\varphi}}(n\text{-}n_+^{\varphi})\Psi_{n^{\theta}}(n\text{-}n_+^{\theta})$ involved in the definition of the scattering matrix U_{np} turns out to be essentially independent of the toroidal extent of the scattering volume $R_0\Delta\varphi$ for well aligned scattering conditions, and one has $\Psi_{n^{\varphi}}(n\text{-}n_+^{\varphi})\Psi_{n^{\theta}}(n\text{-}n_+^{\theta}) \approx \Psi_{n^{\theta}}(n\text{-}n_+^{\theta})$ to a great degree of approximation. This is the essence behind the validity of the 2D approximation.

Equations 5.5, 5.13 and 5.14 show two equivalent ways of computing the synthetic signal of fluctuations $\delta n_{\mathrm{u}}(\vec{k}_+, t)$, respectively in real space $vs.$ k-space. Both implementations are implemented in the context of the old high-k scattering system with GYRO, and shown to quantitatively agree in the context of realistic flux surface geometry in the 2D approximation (neglecting toroidal variation along the field line). I have not in this work numerically implemented a 3D synthetic diagnostic.

5.4.2 2D, outboard midplane approximation

Most scattering measurements of turbulent fluctuations tend to take place at the outboard midplane, which is also the location in which traditional ballooning drift wave instabilities and consequent microturbulence fluctuations tend to exhibit highest amplitude. For this reason I pay special attention to the outboard midplane location in this section.

At the outboard midplane and in the 2D approximation (no toroidal variation), the

wavenumber mapping 5.12 can be simplified, and the corresponding $(k_r, k_\theta)_+$ values mapped from a $(k_x, k_z)_+$ couple take the following form

$$\begin{cases} (k_{r+}\rho_s)^{\text{sim}} \approx \dfrac{2\pi p_+}{L_r}\rho_s^{\text{sim}} & \approx \dfrac{k_{x+}}{|\nabla r|_0}\rho_s^{\text{sim}} \\ (k_{\theta+}\rho_s)^{\text{sim}} = \dfrac{n_+ q}{r}\Big|_0 \rho_s^{\text{sim}} & \approx -\dfrac{\kappa q}{\frac{\partial \nu}{\partial \theta}}\Big|_0 k_{z+}\rho_s^{\text{sim}} \end{cases} \tag{5.16}$$

where the gradient $|\nabla r|_0$ is directly related to the Shafranov shift Δ via $|\nabla r|_0 \approx 1/(1+\Delta)$ ($cf.$ [189]) and κ is the flux-surface elongation in the Miller parametrization [196]. We see how Shafranov shift $\Delta = \partial R_0/\partial r$ primarily affects k_r due to the compression of flux-surfaces at the outboard midplane, and elongation primarily affects k_θ due to flux-surface 'stretching' poloidally. In unshifted s-α geometry we have $\nu \approx$ -$q\theta$, $\Delta = 0$ and $\kappa = 1$, resulting in $(k_r, k_\theta)_+ = (k_x, k_z)_+$ as expected. However, realistic flux-surface geometries and off-midplane locations can significantly modify the mapping with respect to the s-α approximation. In expression 5.16, the subscript $(.)^{\text{sim}}$ denotes the values of mapped wavenumbers have been properly normalized to be directly compared with numerically simulated wavenumbers. In particular, ρ_s^{sim} uses electron temperature T_e and toroidal magnetic field B_t normalization proper to the specific simulation code, which does not generally correspond to the local T_e and B_t values used. In particular, GYRO uses B_{unit} as the normalizing magnetic field, equivalent to the toroidal field in a circular flux surface with same minor radius and enclosed toroidal flux.

As shown in figure 5-3, at $\theta_0 = 0$ a wavenumber with components $(k_x, k_z)_+ = (500, 1)$ m^{-1} is mapped to $(k_r\rho_s, k_\theta\rho_s) \approx (-0.5, 0)$ where ρ_s value of ~ 1.5 mm was used (red dot). The specific values of $(k_x, k_z)_+$ and ρ_s in this subsection are shown merely for illustration purposes and do not directly correspond to a specific experimental configuration. The negligible k_θ component is consistent with $k_{z+} \sim 0$. With respect to the circular filter shape in (k_x, k_z), it is mapped to a non-slanted ellipse that is stretched in k_θ (due to κ) and compressed in k_r (due to Shafranov shift Δ) as can be seen by the red ellipse in figure 5-3.

As already mentioned, the scattering matrix U_{np} is essentially a filter in (n, p) that primarily selects n and p values from a density fluctuation field $\delta n_{np}(\theta_0, t)$. Within the 2D approximation, at the outboard midplane and assuming a separable scattering volume shape

in (R, Z), the scattering matrix U_{np} can take a simpler form than in 5.14. The scattering volume with gaussian shape centered around (R_0, Z_0) and no toroidal variation can be written as follows $U(R, Z) = \Psi_R(R\text{-}R_0)\Psi_Z(Z\text{-}Z_0) = \exp[\text{-}(R\text{-}R_0)^2/\Delta R^2] \exp[\text{-}(Z\text{-}Z_0)^2/\Delta Z^2]$. In this approximation, the scattering matrix can be expressed as a product of separate filter functions Ψ_{k_r} and Ψ_{k_θ} that are equivalent to the previous Ψ_p, Ψ_{n^θ} respectively

$$
\begin{aligned}
U_{np} \qquad & = (R_0\Delta\varphi)e^{\text{-}in\nu_0}e^{ir_0k_r}\Psi_{k_r}(k_r\text{-}k_{r+})\Psi_{k_\theta}(k_\theta\text{-}k_{\theta_+}) \\
&\text{with} \\
\Psi_{k_\theta}(k_\theta\text{-}k_{\theta+}) &\approx \sqrt{\pi}(\Delta Z)e^{\text{-}(k_\theta\text{-}k_{\theta+})^2/\Delta k_\theta^2} \\
\Psi_{k_r}(k_r\text{-}k_{r+}) &\approx \sqrt{\pi}(\Delta R)e^{\text{-}(k_r\text{-}k_{r+})^2/\Delta k_r^2} \qquad \text{Global simulation} \\
&\approx \frac{L_r}{|\nabla r|_0}\,\mathrm{sinc}[(k_r\text{-}k_{r+})L_r/2] \qquad \text{Local simulation}
\end{aligned}
\tag{5.17}
$$

where I recall $(k_r, k_\theta) = (2\pi p/L_r, nq/r)$ and the radial and poloidal filters Ψ_r, Ψ_θ are in 5.11. Note I have expressed the toroidal and radial mode number filters Ψ_{n^θ} and Ψ_p in 5.14 as poloidal and radial *wavenumber* filters Ψ_{k_θ} and Ψ_{k_r}. Additionally, note the absence of the toroidal mode number filter Ψ_{n^φ} in the 2D approximation. In figure 5-5 are shown two examples of radial and poloidal wavenumber filters corresponding to realistic geometry from the high-k scattering diagnostic at NSTX.

It is useful to say a few words about the extent of the scattering volume U and how it might affect the measurement wavenumbers. A scattering measurement sensitive to a scattering vector with components $(k_r, k_\theta)_+$ and having a scattering volume with a characteristic length along the major radius ΔR and vertical dimension ΔZ. Within the outboard midplane approximation, this will result in a wavenumber resolution $\Delta k_r, \Delta k_\theta$ given by

$$
\begin{cases}
\Delta k_r\rho_s \approx \dfrac{2}{\Delta R|\nabla r|_0}\rho_s \\
\Delta k_\theta\rho_s \approx \dfrac{2\kappa q}{\Delta Z\frac{\partial\nu}{\partial\theta}\Big|_0}\rho_s
\end{cases}
\tag{5.18}
$$

which directly corresponds to the extent of the filters in equation 5.17 in the $\theta_0 = 0$ approximation. Here again as in equation 5.16 one should be careful with the ρ_s normalization used in experiments $vs.$ simulation. Note how $\Delta k_r \propto 1/\Delta R$ and $\Delta k_\theta \propto 1/\Delta Z$.

Equation 5.18 indicates that a wider scattering volume extent will result in more spectrally localized measurements in k-space. A scattering measurement with a very extended scattering volume will result in a very sharp and narrow selection in k-space (however coming from an extended volume and not producing a local measurement). On the other hand, a very narrow scattering volume extent will result in a very spatially localized measurement, having contributions from a wide array of wavenumbers. Said in other words, a well spatially localized measurement is associated to a poorly spectrally localized measurement in k-space, and vice versa. This feature is reminiscent of Heisenberg's uncertainty principle in quantum mechanics.

5.5 Application to high-k scattering at NSTX

In this section I deploy a synthetic diagnostic for collective turbulence scattering measurements discussed in the previous section, and then characterize the implementation based on the high-k scattering system in NSTX. I will restrict to the 2D implementation of the synthetic diagnostic, since we have arguments to believe that no substantial changes will be added by a 3D implementation (appendix C). Before attempting to show the synthetic diagnostic implementation and spectra, I begin by specifying the numerical resolution for the electron scale simulations for which the synthetic diagnostic is deployed. I will then discuss the raw simulation spectra as well as the synthetic spectra, along with some important dependencies such as Doppler shift.

5.5.1 Numerical resolution of nonlinear e- scale GYRO simulations

Two types of nonlinear gyrokinetic simulations spanning electron-scale turbulence and with varying box-size are shown in this section: standard electron-scale gyrokinetic simulation ($k_\theta \rho_s \gtrsim 1$), featuring a typical box size characteristic for the resolution of electron-scale modes $(L_r, L_\theta) = (4.5, 4)\rho_s$; 'big-box' electron-scale simulation with an increased simulation domain $(L_r, L_\theta) = (20, 20.6)\rho_s$, resolving modes down to $k_\theta \rho_s \gtrsim 0.3$ (the radial buffer region implemented in GYRO is not taken into account in the calculation of L_r). The latter simulation domain was employed merely for synthetic diagnostic requirements, and only accurately resolves the electron-scale turbulence spectrum. The increased

	dr	$L_r[\rho_s]$	n_r	max$(k_r\rho_s)$	$L_\theta[\rho_s]$	d$k_\theta\rho_s$	max$(k_\theta\rho_s)$	n_n	$T[a/c_s]$	$dt[a/c_s]$
std. e- scale	$2\rho_e$	4.5	≈ 200	50.5	4	1.5	65	42	30	$10^{-3} - 5.10^{-4}$
'big-box' e- scale	$2.5\rho_e$	20	≈ 500	30	20.6	0.3	65	≈ 200	30	$10^{-3} - 5.10^{-4}$

Table 5.1: Numerical resolution parameters typical of a standard electron-scale simulation and with an increased simulation box: dr radial resolution (ρ_s, ρ_e are respectively the ion and electron sound gyro-radius using electron temperature T_e), $L_r[p_s]$ radial box size, n_r number of radial modes, max$(k_r\rho_s)$ maximum resolved radial wavenumber, $L_\theta[\rho_s]$ poloidal box size, d$k_\theta\rho_s$ poloidal wavenumber resolution, max$(k_\theta\rho_s)$ maximum resolved poloidal wavenumber, n_n number of toroidal modes, T simulation run time, dt simulation time step. Both simulation models resolve purely electron-scale modes. Although a 'big-box' e- scale simulation does simulate ion modes ($k_\theta\rho_s < 1$ due to a diagnostic requirement, $cf.$ figure 5-4), the ion-scale turbulence spectrum is not adequately resolved, neither spatially (would need $L_r \gtrsim 70\rho_s$, $dk_\theta\rho_s \sim 0.05$-0.1 as in ion-scale simulation) nor temporally (would need $T^{sim} \gtrsim 200$ a/c$_s$ for ion-scale turbulence to reach a fully saturated state). Accurately simulating both ion and electron-scale turbulence would require multiscale simulation such as shown in [72–74, 74, 76], which is out of the scope of this work.

simulation domain results in effectively simulating ion-scale modes at $\Delta k_\theta\rho_s \sim 0.3$, however this 'big-box' e- scale simulation does not correctly resolve the full spectrum of ion-scale turbulence (would need $\Delta k_\theta\rho_s \sim 0.05$-0.1). In addition, simulations shown in this section are only run for electron time scales ($T \sim\ 30\ a/c_s$, when ions have not had time to reach a fully saturated state). Consequently, the 'big-box' e- scale simulation should not be considered as multiscale simulation such as the ones documented in [72–74, 76] by Howard and Maeyama.

The same physics parameters are employed in both simulation types presented. Standard electron-scale and 'big-box' electron-scale simulations are local and run at the local scattering location $r/a \sim 0.7$ (for attempting quantitative comparisons with experimental spectra in chapter 6), modelling 3 gyrokinetic species (e-, D^+, C^{+6}), including collisions ($\nu_{ei} \sim 1$), background flow and flow shear ($M \sim 0.2$-0.3, $\gamma_E \sim 0.1$-0.2, $\gamma_p \sim 1$) and fully electromagnetic fluctuations.

With respect to numerical resolution parameters, linear background profiles were simulated employing nonperiodic boundary conditions in the radial direction with typical buffer widths $\Delta_b \sim 1(2.5)\rho_s$ respectively for standard e- scale ('big-box' e- scale) simulation. Parallel resolution employed 14 poloidal grid points ($\times 2$ signs of parallel velocity), 12 energies and 12 pitch-angles (6 passing + 6 trapped). This choice of numerical grids was made according to previous convergence and accuracy tests for the GYRO code simulating microinstabilities in the core of NSTX [136], and was also tested for convergence

for the present conditions ($cf.$ appendix F for additional details).

5.5.2 Radial and poloidal wavenumber resolution

The radial and poloidal wavenumber resolution of the nonlinear simulations presented is of crucial importance in order to overlap and accurately resolve the wavenumbers measured by the high-k system. Standard electron-scale simulation resolves only electron-scale turbulence wavenumbers $k_r\rho_s\epsilon$ $[1, 3050]$ and $k_\theta\rho_s\epsilon$ $[1.5, 65\text{-}85]$ depending on the plasma condition. 'Big-box' electron-scale simulation only accurately resolves electron-scale turbulence, but includes modes characteristic of low-k instabilities, $k_r\rho_s$ $\epsilon[0.3, 40]$ and $k_\theta\rho_s$ $\epsilon[0.3, 65\text{-}88]$ depending on the plasma condition. Figure 5-4 displays the radial and poloidal wavenumber simulation grid from a standard electron-scale simulation (left) and a 'big-box' e- scale simulation (right). In figure 5-4 are also overplotted the typical wavenumbers detected by channels 1, 2 and 3 of the high-k scattering system denoted by the black dots, and the ellipses surrounding them are the $1/e$ amplitude of the effective wavenumber filter indicative of the wavenumber resolution of the diagnostic. Ideally, one would want to simulate several radial and poloidal wavenumbers inside each (k_r, k_θ)-ellipse in figure 5-4 to more accurately replicate the experimental fluctuation measurement. However, due to a coarse wavenumber grid spacing, standard electron-scale simulation can at most resolve one radial and two poloidal wavenumbers inside the effective measurement range delimited by the elliptical shape of the wavenumber filter. This poor resolution due to the diagnostic requirements and numerical resolution requirements will result in inaccurate synthetic frequency spectra computed from electron-scale simulation ($cf.$ figure 5-9). On the other hand, by decreasing the wavenumber grid spacing (dk_r) and (dk_θ) and still resolving the full electron-scale spectrum, a 'big-box' e- scale simulation can effectively filter a handful of poloidal wavenumbers inside the measurement range from each channel, yielding it adequate for attempting quantitative turbulence spectra comparisons as will be seen in the following sections. In turn, this results in very computationally intensive simulations, typically running on 10-20 thousand parallel CPU cores taking $\sim$1-2 M CPU hours to complete on leadership high-performance supercomputers such as NERSC's Edison.

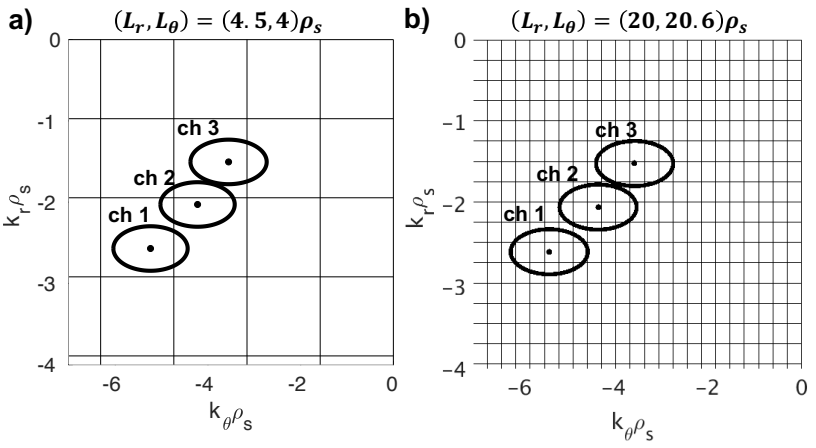

Figure 5-4: (k_r, k_θ) grid for a standard electron-scale simulation having a conventional simulation domain $(L_r, L_\theta) = (4.5, 4)\rho_s$ (left) and an electron-scale simulation with increased numerical domain $(L_r, L_\theta) = (20, 20.6)\rho_s$ (right) along with the measurement range of channel 1, 2 and 3 of the old NSTX high-k scattering system [65]. The ellipses denote the $1/e$ amplitude of the wavenumber filters in k-space, essentially the wavenumber resolution from each diagnostic channel. Simulation wavenumbers inside the ellipses will effectively contribute to the synthetic signal. **a)** Electron-scale simulation with standard simulation domain does not well resolve the measurement wavenumbers from the high-k diagnostic due to a coarse (k_r, k_θ)-grid. **b)** Electron-scale simulation with increased simulation domain is needed to accurately resolve the measurement wavenumbers from the old high-k scattering diagnostic. By resolving more (k_r, k_θ)-modes than a standard electron-scale simulation, a bigger domain results in improved resolution in k-space down to ion-scale modes (note the k_θ simulation resolution is $\mathrm{d}k_\theta\rho_s^{sim} \sim 0.3$).

I want to emphasize that the 'big-box' electron-scale simulations presented here resolve the same physics phenomena as standard electron-scale simulations. The essential difference between the two simulation types resides in the numerics (radial and poloidal wavenumber resolution), and not in the simulated physics phenomena: the ETG mode dynamics and nonlinear physics. I do not claim big-box electron-scale simulations to include additional physics phenomena such as coupling to ion-scale dynamics or more complex interactions with zonal flows. From this point of view, 'big-box' and standard electron-scale simulations are essentially equivalent. However, the numerical resolution is different, and adapted in 'big-box' electron-scale simulation to accurately resolve the measured wavenumbers from the high-k scattering system. The difference resides in the numerics, not in the simulated physics.

5.5.3 Mapping high-k wavenumbers to GYRO

The measurement wavenumber from channel 1 of the high-k system was $\vec{k}_+ = (k_x, k_y, k_z)_+ =$ (-1883.5, 138.3, -347.2) m^{-1}, which is mapped to figure 5-4 by use of equation 5.12. This measurement is local to the outboard midplane with poloidal angle $\theta_0 \sim$ -4^o. We wish to compute the mapped wavenumbers to the GYRO (k_r, k_θ), using the full mapping 5.12 and the outboard midplane approximation 5.16.

I present here the wavenumber mapping using the outboard midplane approximation of equation 5.16. To compute the geometric factors $|\nabla r|_0, \kappa, q, \frac{\partial \nu}{\partial \theta}|_0$ and the GYRO normalizing ρ_s^{unit} I use the flux-surface geometry of NSTX H-mode 1741767, and find $|\nabla r|_0 \approx 1.43$, $\kappa \approx 2.11$, $q \approx$ -3.79 and $\frac{\partial \nu}{\partial \theta}|_0 \approx 1.33$ and $\rho_s^{\text{unit}} \approx 0.2$ cm. Note here how ρ_s^{unit} is some $\sim \times 3$ smaller than the experimental, local value of $\rho_s \sim 0.7$ cm, due mainly to the B_{unit} definition in GYRO ($cf.$ section 4.2). Using equation 5.16 we find $(k_r\rho_s^{\text{unit}}, k_\theta\rho_s^{\text{unit}}) \approx$ (-2.59, -4.11). For reference, had one used the full mapping as in equation 5.12, one would have found $(k_r\rho_s^{\text{unit}}, k_\theta\rho_s^{\text{unit}}) \approx$ (-2.57, -5.34), which is more consistent with the plotted values for channel 1 in figure 5-4. This emphasizes the importance of using the full mapping, even for rather small off-midplane poloidal angles $\theta_0 \sim$ -4^o, due to the larger k_{x+} component of the old high-k scattering system and extreme flux surface shaping of this spherical tokamak plasma. For reference, using the local value of ρ_s as typically used in experimental measurements to normalize the radial and vertical wavenumbers (k_x, k_z), one finds a couple $(k_x\rho_s, k_z\rho_s)_+ \approx$ (-13, -2.4). However the correct wavenumbers needed to compare to nonlinear gyrokinetic simulation are really (k_r, k_θ) as discussed. Originally designed to be a high-k_r scattering system, we find that the corresponding $(k_r\rho_s)_+$ values mapped to field-aligned geometry are not as high-k_r as originally thought. This brings the measurement from the high-k scattering system closer to the spectral peak in the streamer peak in the density fluctuation spectrum.

For the same present example, figure 5-5 shows the shape of the radial and poloidal wavenumber filters Ψ_{kr} and $\Psi_{k\theta}$ in the $\theta_0 \approx 0$ approximation, using a simulation grid from a standard e- scale simulation $(L_r, L_\theta) = (4.5, 4)\rho_s$ (red) and from a 'big-box' e- scale simulation $(L_r, L_\theta) = (20, 20.6)\rho_s$ (blue). The gaussian shape stems from the gaussian shape of the scattering volume U in (R, Z) as in the past section ($cf.$ equation 5.9). Here

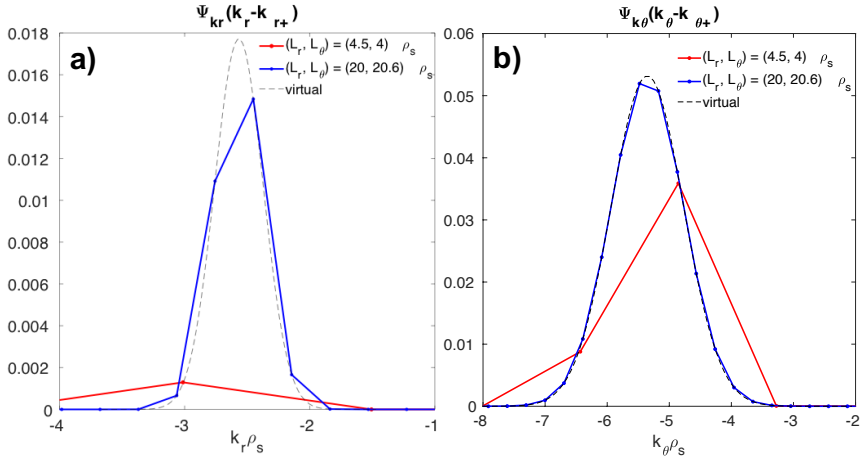

Figure 5-5: **a)** Radial wavenumber filter corresponding to a measurement wavenumber component $k_{r+} \approx -2.57$. **b)** Poloidal wavenumber filter corresponding to a measurement wavenumber component $k_{\theta+} \approx -5.34$. The $(k_r, k_\theta)_+$ components correspond to scattering measurement from channel 1 of the high-k scattering system, from NSTX H-mode 141767. The gaussian shape of Ψ_{kr} and Ψ_{k_θ} stems from the gaussian shape of the scattering volume U in (R, Z) as in the past section ($cf.$ equation 5.9). In red are shown the filters using the numerical grids from a standard e- scale simulation domain $(L_r, L_\theta) = (4.5, 4)\rho_s$, and in blue from an e- scale simulation with a bigger simulation domain $(L_r, L_\theta) = (20, 20.6)\rho_s$. Notice the lack of resolution from using a standard simulation domain (red), especially in k_r, and the improved resolution when using a bigger simulation domain (blue), due to the finer k-grid resolution. The 'virtual' dashed line shows the theoretical gaussian expression of the filter. Note I chose $\Delta Z = 3$ cm (the experimental value) and $\Delta R = 1$ cm (reduced from the experimental ΔR = 3 cm due to the reduced simulation domain, even for the increased box size). The reduced ΔR in a local simulation only scales the fluctuation amplitude by a constant value of irrelevance in the current work.

the wavenumber sensitivity Δk_r and Δk_θ is computed using the $\theta_0 = 0$ approximation (equation 5.18), however the mapped k_{r+} and $k_{\theta+}$ are computed using the full mapping in equation 5.12 as discussed in the previous paragraph. This is justified since the error made in the calculation of $(k_r, k_\theta)_+$ for off-midplane locations is $\propto \theta_0$, however the error in computing the resolution Δk_r and Δk_θ scales quadratically with $\propto \theta_0^2$, which results completely negligible for the present conditions. Notice the lack of resolution from using a standard simulation domain (red in figure 5-5), especially in k_r, and the improved resolution when using a bigger simulation domain (blue), due to the finer k-grid resolution. The 'virtual' dashed line shows the theoretical gaussian expression of the filter. Note I chose $\Delta Z = 3$ cm (the experimental value) and $\Delta R = 1$ cm (reduced from the experimental ΔR = 3 cm due to the reduced simulation domain, even for the increased box size). The reduced radial extent of the scattering volume ΔR in a local simulation only scales the fluctuation amplitude by a constant value of irrelevance in the current work.

Figure 5-6 shows the raw 2D electron density field in $\delta n(R, Z, \varphi_0 = 0)$ for a standard e- scale simulation 5-6.a) and for a 'big-box' e- scale simulation in 5-6.b). Note the elongated streamer structures are tilted by the strong $E \times B$ shear flow present, which is shown to reduce the ETG spectrum but not completely stabilize it. In $c)$ and $d)$ is shown the corresponding electron density field that is filtered by a 2D filter in real space $U(R\text{-}R_0, Z\text{-}Z_0)$ and selecting the $\vec{k}_+$ component in the complex exponential, respectively for a standard $c)$ and big-box e- scale simulation $d)$. Note that volume integration of $\mathrm{Re}[\delta n(R, Z, \varphi_0 = 0) U(R\text{-}R_0, Z\text{-}Z_0) e^{-i\vec{k}_+ \cdot \vec{r}}]$ yields directly the synthetic signal of fluctuations δn_{u} as in equation 5.5, and serves as great illustration for the implementation of the synthetic diagnostic in real space (Re denotes the real part). Figures $c)$ and $d)$ give a spatial representation in real-space of the detected structures by the high-k system. Although they show a finite amplitude, note how the inspected radial and poloidal correlation length does not correspond to the highest amplitude streamers present in figures $a)$ and $b)$. Since simulations are run in the local approximation, profile parameters are constant within the radial domain and the radial filter is chosen to be constant $= 1$ ($cf.$ appendix 5.5.6 for additional details). The poloidal filter shape is gaussian in θ and mapped to (R, Z), having maximum amplitude at the thick black line passing through $Z_0 \approx -0.06$ cm. The additional black dashed lines denote the $1/e, 1/e^2$ and $1/e^3$ amplitude of the filter in the

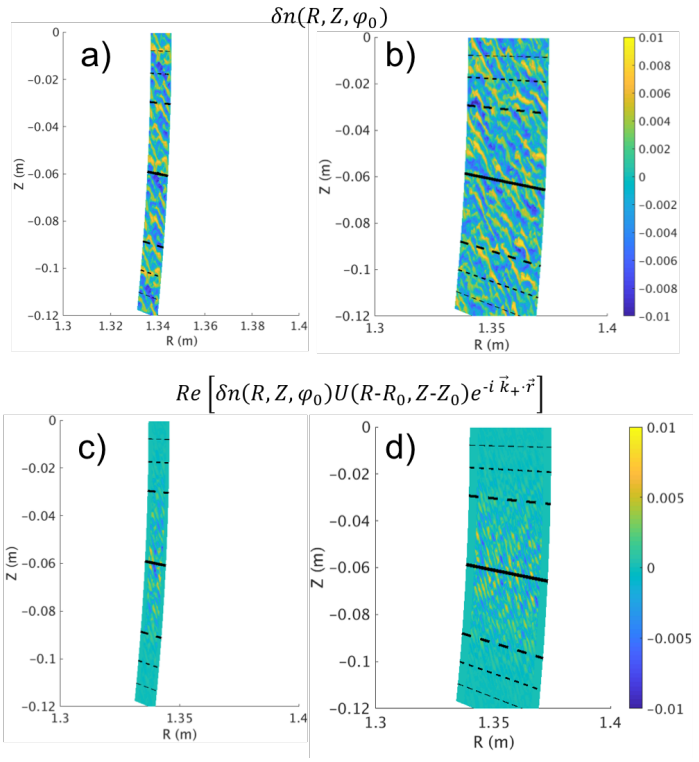

Figure 5-6: **a)** and **b)** 2D raw electron density field δn mapped to cylindrical coordinates $(R, Z, \varphi_0 = 0)$, corresponding to an e- scale simulation with standard domain $(L_r, L_\theta) = (4.5, 4)\rho_s$ in $a)$, and increased simulation domain $(L_r, L_\theta) = (20, 20.6)\rho_s$ in $b)$. In **c)** and **d)** the 2D density field δn has been multiplied by the 2D real space filter $U(R\text{-}R_0, Z\text{-}Z_0)$, corresponding to an e- scale simulation with domain $(L_r, L_\theta) = (4.5, 4)\rho_s$ in $c)$, and an electron-scale simulation with increased numerical domain $(L_r, L_\theta) = (20, 20.6)\rho_s$ in $d)$. Since simulations are run in the local approximation, profile parameters are constant within the radial domain and the radial filter is chosen to be constant $= 1$. The poloidal filter shape is gaussian in θ and mapped to (R, Z), having maximum amplitude at the thick black line passing through $Z_0 \approx -0.06$ cm. The additional black dashed lines denote the $1/e, 1/e^2$ and $1/e^3$ amplitude of the filter in the poloidal direction. The filtered density fluctuations in $c)$ and $d)$ are intended to show the amplitude of the selected wavenumbers contributing to the high-k signal. All figures are shown at a fixed toroidal slice at φ_0.

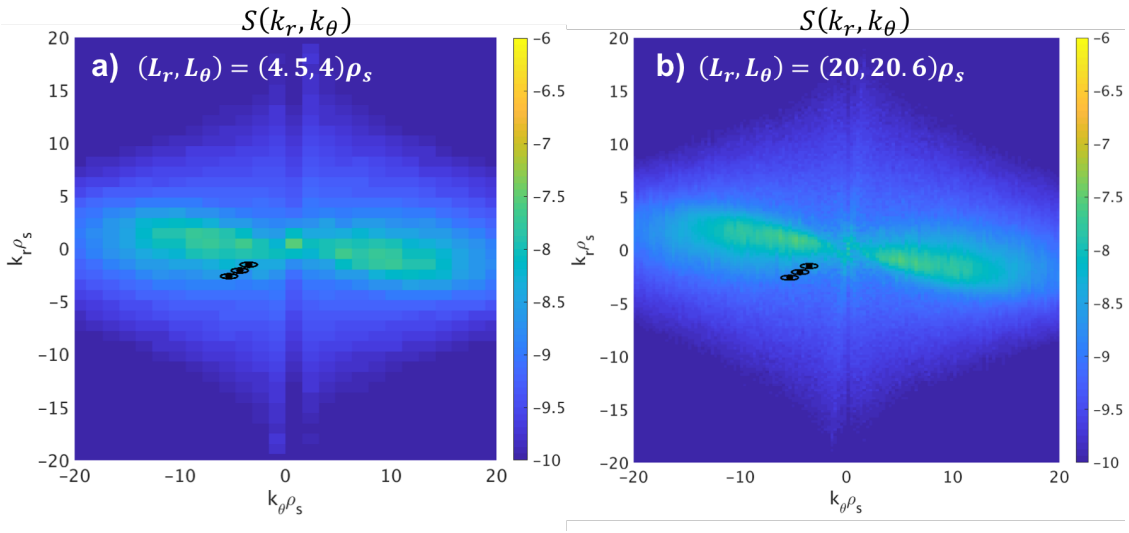

Figure 5-7: 2D (k_r, k_θ)-spectrum of the electron density normalized per radial and poloidal wavenumber step $\mathrm{d}k_r\rho_s$ and $\mathrm{d}k_\theta\rho_s$, corresponding to a standard e- scale simulation in $a)(L_r, L_\theta) = (4.5, 4)\rho_s$ and to an e- scale simulation with increased simulation domain in $b)$ $(L_r, L_\theta) = (20, 20.6)\rho_s$. Black dots and ellipses correspond to the measurement k and k-resolution from 3 channels of the high-k diagnostic, also shown in figure 5-4. The improved resolution in k-space due to the increased box size makes a bigger domain more suitable for attempting quantitative comparisons between synthetic and experimental frequency spectra ($cf.$ chapter 7). Initially designed to be a high-k_r scattering system, the measurement wavenumbers detected by the high-k diagnostic are mapped to the internal flux-surface wavenumber definitions (k_r, k_θ) with a much smaller k_r than intuitively expected. This makes the old high-k diagnostic more relevant to ETG transport than initially thought.

poloidal direction.

5.5.4 Raw electron-scale simulation spectra

In this subsection I show e- scale simulation spectra to gain insight into the measurement range of the high-k diagnostic in k-space, serving as illustration to the implementation of the synthetic diagnostic in k-space. Spectral differences between a standard e- scale simulation and a 'big-box' e- scale simulation will also be discussed.

Figure 5-7 shows the GYRO 2D electron density fluctuation power spectrum from a standard e- scale simulation $a)$ and big-box e- scale simulation $b)$, directly proportional to the spectral density $S(k_r, k_\theta)$. (k_r, k_θ) are the internal field-aligned definitions in GYRO. Here I define $S(k_r, k_\theta) = \frac{\langle|\delta n_{np}|^2\rangle_{\theta,T}}{(dk_r\rho_s)(dk_\theta\rho_s)}$, where $\langle.\rangle_{\theta,T}$ denotes the θ and time averages, and $\mathrm{d}k_r\rho_s$, $\mathrm{d}k_\theta\rho_s$ are the simulation radial and poloidal wavenumber grid resolution. The

black dots surrounded by ellipses correspond to the wavenumber measurement range from channels 1, 2 and 3 of the high-k diagnostic, the same as were shown in figure 5-4. As can be seen, the spectrum is not symmetric in k_θ due to the high $E \times B$ flow shear. The improved resolution in k-space due to the increased box size makes the bigger domain in $b)$ more suitable for attempting quantitative comparisons between synthetic and experimental frequency spectra ($cf.$ section 5.5.5, chapter 7). The highest spectral power given by streamers is characterized by $(k_r > 0, k_\theta < 0)$ and $(k_r < 0, k_\theta > 0)$, consistent with the tilt of streamers in real space shown shown in figures 5-6.$a)$ and $b)$.

I note that filtering in k-space does not correspond to a direct filter of the spectral density S (a power $\propto |\delta_{np}|^2$) as might be wrongly interpreted from figure 5-7. As we saw in section 5.4, scattering is performed as a filter of the *amplitude* δn_{np} that preserves phase information ($cf.$ equations 5.4 and 5.13) and not as a filter of the *power* $\propto S \propto |\delta_{np}|^2$. Consequently, figure 5-7 should only be interpreted qualitatively, providing the necessary guidance towards understanding the measurement wavenumbers with respect to the simulated spectrum, and not as a filtering process of S by k-space filter functions.

Figure 5-8.$a)$ and $b)$ shows the k_r and k_θ electron density fluctuation power spectrum $S(k_r)$ and $S(k_\theta)$ from a standard e- scale simulation (red) and from a big-box e- scale simulation (blue). Specifically, I define

$$\begin{cases} S(k_r) = \mathrm{d}k_\theta \rho_s \sum_{k_\theta < 0} S(k_r, k_\theta) \\ S(k_\theta) = \mathrm{d}k_r \rho_s \sum_{k_r} S(k_r, k_\theta) \end{cases} \tag{5.19}$$

The choice of $k_\theta < 0$ is made due to the symmetry property of the density spectrum $\delta n_{np} = \delta n^*_{\text{-}n\text{-}p}$ (where $.^*$ indicates the complex conjugate, $cf.$ [189]). Inspection of $S(k_r)$ in figure 5-8.$a)$ emphasizes the high-k measurement is not sensitive to the same sign of k_r as that associated with the highest amplitude streamer fluctuations. For a measurement with negative $k_\theta < 0$ ($cf.$ figure 5-7), streamers have positive $k_r > 0$ while the measurement is made for $k_r < 0$. Vertical black lines indicate the measurement wavenumbers by the high-k system. Since $S(k_r)$ is defined for positive and negative k_r, the $k_r > 0$ and $k_r < 0$ branches are plotted, as indicated in figure 5-8.$a)$. Figure 5-8.$a)$ shows that a measurement of streamer fluctuations might have been possible in the present experiment had

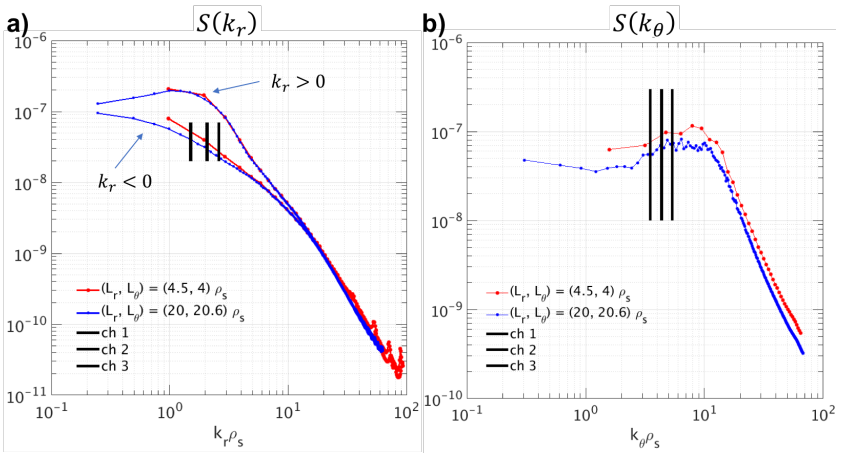

Figure 5-8: **a)** Radial wavenumber spectrum of electron density fluctuations per radial wavenumber step d$k_r\rho_s$, computed by adding all $k_\theta < 0$ contributions from $S(k_r, k_\theta)$. Since k_r changes sign, the $k_r > 0$ and $k_r < 0$ branches are plotted, as indicated. Since the detected k_θ by the high-k scattering system is negative ($cf.$ figure 5-7), adding only $k_\theta < 0$ contributions exalts the difference between measuring in the higher and lower k_r part of the spectrum (here the detected k is also $k_r < 0$). **b)** Poloidal wavenumber spectrum of electron density fluctuations per poloidal wavenumber step d$k_\theta\rho_s$, computed by adding all k_r contributions from $S(k_r, k_\theta)$ (both $k_r > 0$ and $k_r < 0$). Due to the logarithmic scale and the symmetry property in δn_{np}, k_θ should be interpreted as having a negative sign $k_\theta < 0$. The measurement k_θ from channels 1, 2 and 3 are plotted as vertical lines in each figure. An e- scale simulation with a standard domain (red) shows very similar spectra as the simulation with an increased domain $(L_r, L_\theta) = (20, 20.6)\rho_s$ (blue), providing confidence that the resolved physics are very similar between the two simulations models.

the measurement been designed for positive radial wavenumbers. However, the measurement is performed for negative radial wavenumbers and falls in the negative-k_r branch, exhibiting close to an order of magnitude difference in spectral power with respect to the streamer branch ($k_r > 0$) near $k_r\rho_s \sim$ 1-2. The k_r spectra between standard and big-box e- scale simulation exhibit quantitative agreement, from the low-k wavenumber peak of the spectrum to the spectral slope at higher k.

Figure 5-8.b) shows the k_θ density power spectrum of fluctuations from a standard e- scale simulation (red) and from a big-box e- scale simulation (blue). Due to the logarithmic scale and the symmetry property in δn_{np} (translating to $S(k_\theta) = S(-k_\theta)$), is only shown here the $k_\theta < 0$ branch and k_θ should be interpreted as having a negative sign (similarly to the negative k_r branch in a)). Figure 5-8.b) shows that the big-box e- scale simulation exhibits a quantitatively similar spectrum to a standard e- scale simulation, exhibiting very similar wavenumber peaking and spectral slopes. However, the predicted spectral power is about a $\sim 20\%$ lower for the big-box e- scale simulation.

Similarly as was discussed for figure 5-7, figures 5-8.a) and b) should only be interpreted qualitatively, since the scattering process is not based on a filtering of $S(k_r), S(k_\theta)$ but on the filtering on the density fluctuation amplitude δn_{np}. All in all, figures 5-7, 5-8.a) and b) show how the big-box e- scale simulation spectra is very quantitatively similar to that of a standard e- scale simulation, providing ultimate confidence that the resolved ETG physics are very similar between the two simulations models.

5.5.5 Synthetic frequency spectra

Building on the last statement, I set out to deploy a 2D synthetic diagnostic for high-k scattering in k-space. Equivalence between the real space and the k-space implementation of the synthetic diagnostic was essentially identical, as is discussed in the next section 5.5.6. The power spectral density $S(\vec{k}_+, \omega)$ can be easily computed from the synthetic signal $\delta n_{\mathrm{u}}(\vec{k}_+, \omega)$ as shown in appendix A. In figure 5-9 is shown the spectral density $S(\vec{k}_+, \omega)$ predicted from a standard and big-box e- scale simulation, where both simulation models exhibit the same plasma physics parameters but different wavenumber grid-resolution as was previously discussed. In red is shown the frequency power spectrum computed from a standard e- scale simulation and in blue from a big-box e- scale simulation. Both spectra exhibit qualitatively similar features, similar frequency response and very close power levels (within $\sim 20\%$ agreement), which are quantified in table 5.2. However, the spectra exhibit at least two main appreciable differences. The spectrum in red exhibits a 'double-peak' structure in frequency, whereas the blue spectrum from the bigger simulation domain shows only one hump in the spectrum. In addition, the spectrum from the bigger simulation domain is wider than the spectrum from the simulation with the smaller-box.

As was discussed in figures 5-4 and 5-5.b), the reduced wavenumber grid-resolution from a standard e- scale simulation only allows it to sample a maximum of 2 simulation toroidal mode numbers contributing to the high-k signal. The standard electron scale simulation used to compute the red spectrum in figure 5-9 had a toroidal mode number spacing $\Delta n = 90$. The two peaks in the red curve correspond to the two dominant toroidal mode numbers within the measurement k_θ-range, $n = -270$ and $n = -360$ re-

	P_{tot}	$< \omega >$	σ_ω
Std. e- scale	$1.82\ 10^{-11}$	-24.18	3.04
Big-box e- scale	$2.17\ 10^{-11}$	-23.29	5.13

Table 5.2: Values for the total scattered power P_{tot}, spectral peak $< \omega > [c_s/a]$ and spectral width $\sigma_\omega [c_s/a]$ corresponding to synthetic frequency spectra from figure 5-9. Similar values of the total power P_{tot} and spectral peak $< \omega >$ are obtained between the two simulation models (standard e-scale simulation domain $vs.$ big-box e- scale simulation domain). The spectral width is wider for the simulation using a larger simulation domain, due to the increased number of sampled modes contributing to the synthetic signal ($cf.$ figure 5-4), contributing to a widening of the spectrum. The values of P_{tot}, $< \omega >$ and σ_ω are computed by fitting a gaussian profile to the turbulence spectrum and extracting the characteristic gaussian parameters (more details in appendix).

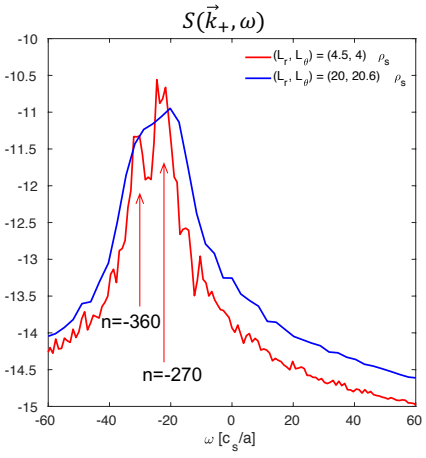

Figure 5-9: Synthetic frequency power spectrum of fluctuations $S(\vec{k}_+, \omega)$ corresponding to a filtered wavenumber $\vec{k}_+$ from channel 1 of the high-k scattering system. In red the synthetic spectrum corresponds to an e- scale simulation with standard domain, and in blue to a big-box e- scale simulation with a increased domain necessary for accurate deployment of synthetic diagnostic. Both spectra look qualitatively similar, however a standard e- scale simulation exhibits a 'double-peak' structure, not present when using the increased simulation domain. This can be explained by the reduced number of sampled modes by the synthetic diagnostic when applied to a small simulation domain ($cf.$ figure 5-4.a)): the two peaks in the red curve are shown to correspond to the two dominant toroidal mode numbers within the measurement k-range ($n_+ =$ -270, -360 where n_+ is the sampled mode number). Each mode has its own propagation frequency in the lab-frame and is Doppler-shifted by a different amount ($\omega_{Dop} = \vec{k}_+ \cdot \vec{v} \sim n_+ \omega_0$, where ω_0 is the plasma toroidal rotation frequency), which results in a separation of spectral peaks in the frequency spectrum. This phenomenon is not present when using an increased simulation domain (blue curve) due to the increased number of sampled modes. This last point also contributes to a widening of the spectrum with respect to the reduced simulation domain. The differences between both spectra is quantified in table 5.2.

spectively. Each simulated toroidal mode has its own propagation frequency and is additionally Doppler-shifted by a different frequency ($\omega_{Dop} = \vec{k}_+ \cdot \vec{v} \sim n_+ \omega_0$, where n_+ is the sampled mode number and ω_0 is the plasma toroidal rotation frequency). This results in

a separation of spectral peaks in the frequency spectrum due to the two dominant modes contributing to the synthetic signal as is shown in figure 5-9. This phenomenon is not present when using an increased simulation domain (blue curve) due to the increased number of sampled modes. Using a bigger simulation domain increases the number of toroidal modes sampled within the measurement k_θ range, which 'fill-in' the frequency spectrum and yield a single frequency feature. This last point also contributes to a widening of the spectrum with respect to the reduced simulation domain, from a value of $\sigma_\omega \sim 3a/c_s$ (red) to a value of $\sim 5a/c_s$ (blue). The differences between both spectra are quantified in table 5.2. As will be shown in chapter 6, the frequency spectra from a big-box e- scale simulation yields a much improved quantitative agreement with respect to the experimentally detected high-k frequency spectra. In what follows I will preferentially focus on synthetic spectra from 'big-box' electron-scale simulations.

5.5.6 Equivalence between the real-space and k-space synthetic spectra computed by GYRO

In this short section I show how the real space and the wavenumber space implementation of the synthetic high-k diagnostic quantitatively agree. In figure 5-10 is shown the frequency power spectrum $S(\vec{k}_+, \omega)$ from big-box electron-scale simulation. The dashed blue line shows the spectra computed using the real space implementation of the synthetic diagnostic (equation 5.5). The thin continuous blue line shows the computed spectra using the wavenumber implementation of the synthetic diagnostic (equation 5.13). Great agreement is obtained between the two methods of implementing a synthetic high-k diagnostic, within 15% agreement in the total power P_{tot}, and an even improved agreement in the spectral peak $< \omega >$ and spectral width σ_ω. This validates the equivalent approaches presented here and provides great confidence on the validity of the computed synthetic spectra.

5.5.7 Effect of Doppler shift

One important aspect of the high-k frequency spectra is the influence of Doppler shift. In the present conditions, the relatively high toroidal rotation levels typical of neutral beam

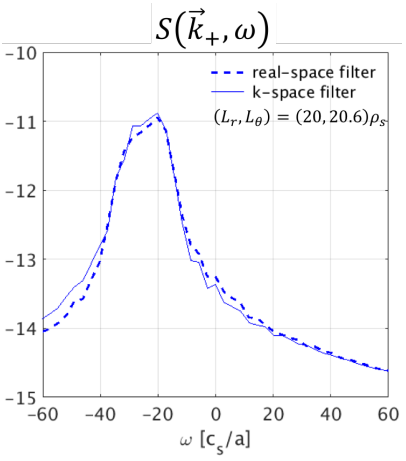

Figure 5-10: Synthetic frequency power spectrum of fluctuations $S(\vec{k}_+, \omega)$ corresponding to a filtered wavenumber $\vec{k}_+$ from channel 1 of the high-k scattering system. Simulations use a big numerical domain $(L_r, L_\theta) = (20, 20.6)\rho_s$. The real-space filtering method (dashed line) is compared to the k-space filtering method (continuous line). Great agreement is obtained between the two methods of implementing a synthetic high-k diagnostic, within 15% agreement in the total power P_{tot}, and an even improved agreement in the spectral peak $< \omega >$ and spectral width σ_ω. This agreement is not coincidental but is generally observed, and validates the implementation of both synthetic diagnostic methods in the context of realistic flux-surface geometries.

heated plasmas (Mach number $M \sim 0.2$ in the present cases) added to the relatively high poloidal wavenumbers sampled ($k_{\theta+}\rho_s \sim$ 3-5) contribute to a Doppler shift frequency ω_{Dop} that can exceed the plasma-frame frequency of fluctuations by factors of $\sim \times 10$ or more (recall the Doppler shift frequency $\omega_{Dop} \sim k_{\theta+}\omega_0 r_0/q_0$). In figure 5-11 is shown the frequency power spectrum from a big-box e- scale simulation in which no Doppler-shift was applied to the fluctuations (gray), and with the experimental Doppler shift value applied (blue). The different frequency response between the two spectra highlights the important effect of Doppler shift in these conditions, shifting the frequency peaking from $< \omega >_{M=0} \sim 1.54\ c_s/a$ with no Doppler shift applied (> 0 is in the e- diamagnetic drift direction) to $< \omega >_{M=M^{exp}} \sim -23.29\ c_s/a$ when Doppler shift is applied. Here Doppler shift is shown to shift the frequency spectrum to the ion diamagnetic drift direction. Other frequency spectra quantities such as the total power P_{tot} and spectral width σ_ω are however quantitatively similar, as is shown in table 5.3. The small differences in the total spectral power P_{tot} might be related to numerical errors, but also to a pure effect of Doppler shift in scattering experiments. Scattering measurements are sensitive to phase information of the sampled modes, and one can show that the total scattered power can

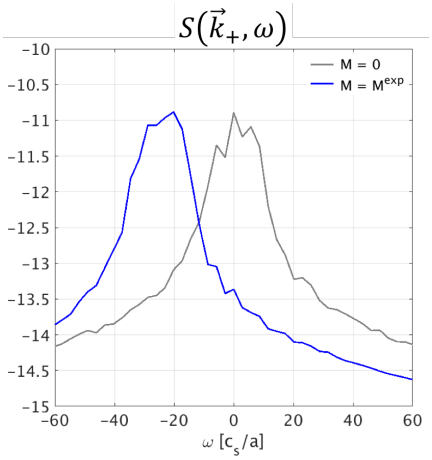

Figure 5-11: Synthetic frequency power spectrum of fluctuations $S(\vec{k}_+, \omega)$ corresponding to a filtered wavenumber $\vec{k}_+$ from channel 1 of the high-k scattering system. Simulations use a big numerical domain $(L_r, L_\theta) = (20, 20.6)\rho_s$. In gray is shown the frequency spectrum in the plasma-frame, to which no Doppler shift has been added. In blue is shown the frequency spectrum in the lab-frame, to which the experimental value of Doppler shift has been added. The Doppler shift frequency is at least $\times 10$ the plasma-frame frequency of fluctuations and completely dominates the frequency spectrum. The difference between the two spectra is quantified in table 5.3.

be written as a function of a correlation function between the different sampled modes. Since Doppler shift is high in this condition, it greatly modifies the phase of the individual toroidal modes selected, modifying the mutual correlation between them and resulting in changes in the total spectral power. Doppler shift can modify the total spectral power by correlating/decorrelating the synthetic signal of fluctuations.

	P_{tot}	$< \omega >$	σ_ω
Plasma frame: $M = 0$	$1.62\ 10^{-11}$	1.54	4.89
Lab frame: $M = M^{exp}$	$2.17\ 10^{-11}$	-23.29	5.13

Table 5.3: Values for the total scattered power P_{tot}, spectral peak $< \omega > [c_s/a]$ and spectral width $\sigma_\omega [c_s/a]$ corresponding to synthetic frequency spectra from figure 5-11, showing the impact of Doppler shift on the frequency spectrum (M here is Mach number). Similar values of the total power P_{tot} and spectral peak σ_ω are obtained between the two simulation models, but the spectral peak is completely different: fluctuations propagate in the e- diamagnetic direction in the plasma frame ($\omega > 0$ for GYRO), but are shifted to the ion diamagnetic drift direction by Doppler shift. This is an important assessment towards the understanding of the measurement spectra from high-k scattering.

One can also observe the effect of Doppler shift in frequency spectra plots (ω, k_θ) and (ω, k_r). In figure 5-12.a) and b) is shown the synthetic frequency power spectrum of fluctuations $S_{k_{r+}}(k_\theta, \omega)$ computed from a big-box e- scale simulation, where spectra have

been filtered in k_r around the radial component k_{r+} corresponding to channel 1 of the high-k scattering system, but not in k_θ. The black vertical band shows the measurement range in k_θ from channel 1. No Doppler shift is applied in $a)$, and the experimental Doppler shift value is applied in $b)$. Comparison between 5-12.$a)$ and $b)$ shows the effect of Doppler shift for the different k_θ (and same k_r) is primarily a shift in frequency ω proportional to $\omega \propto k_\theta \omega_0$ as expected. A smaller effect is a widening of the spectrum σ_ω, which is negligible for the present conditions but becomes more important for higher toroidal rotation values and higher k_θ. The spectrum also shows how the positive $k_\theta > 0$ part of the spectrum exhibits higher spectral power than the negative $k_\theta < 0$ counterpart. This is consistent with the spectrum shape shown in figure 5-7 and 5-8. Spectra in 5-12.$a)$ and $b)$ have been filtered about the $k_r = k_{r+} < 0$ experimental value component, itself having a negative value. As suggested by figures 5-7 and 5-8, negative $k_r < 0$ fluctuations exhibit highest spectral power for positive $k_\theta > 0$ fluctuations (streamers in this case are $(k_r < 0, k_\theta > 0)$). This is consistent with the higher spectral power in figures 5-12.$a)$ and $b)$ for positive $k_\theta > 0$ with respect to negative $k_\theta < 0$ fluctuations.

Figures 5-12.$c)$ and $d)$ show the synthetic frequency power spectrum of fluctuations $S_{k_{\theta+}}(k_r, \omega)$ computed from a big-box e- scale simulation, where spectra have been filtered in k_θ around the radial component $k_{\theta+}$ corresponding to channel 1 of the high-k scattering system, but not in k_r. The black vertical band shows the measurement range in k_r from channel 1 of the high-k system, and the white dashed line denotes the $k_r = 0$ line. Differently to the (ω, k_θ) spectra, the (ω, k_r)-spectra show that Doppler shift essentially produces a similar frequency shift for all k_r (corresponding to the same k_θ since it has been previously filtered in k_θ), as expected for the current conditions. However, it is possible that the (ω, k_r) spectrum will be affected by Doppler shift for far off-midplane fluctuations due to the dependence of k_r on toroidal mode number ($cf.$ equation 5.16). Recall here fluctuations are taken close to the midplane. As was observed for the corresponding (ω, k_θ) plots, here again one can notice the asymmetry in $S_{k_{\theta+}}(k_r, \omega)$ for positive $vs.$ negative k_r: a higher spectral power is observed for positive $k_r > 0$ fluctuations (right of the vertical white dashed line). This is once more consistent with the (k_r, k_θ) spectra shown in figures 5-7 and 5-8. Recall that spectra in 5-12.$c)$ and $d)$ have been filtered about the measurement $k_\theta = k_{\theta+} < 0$ component.

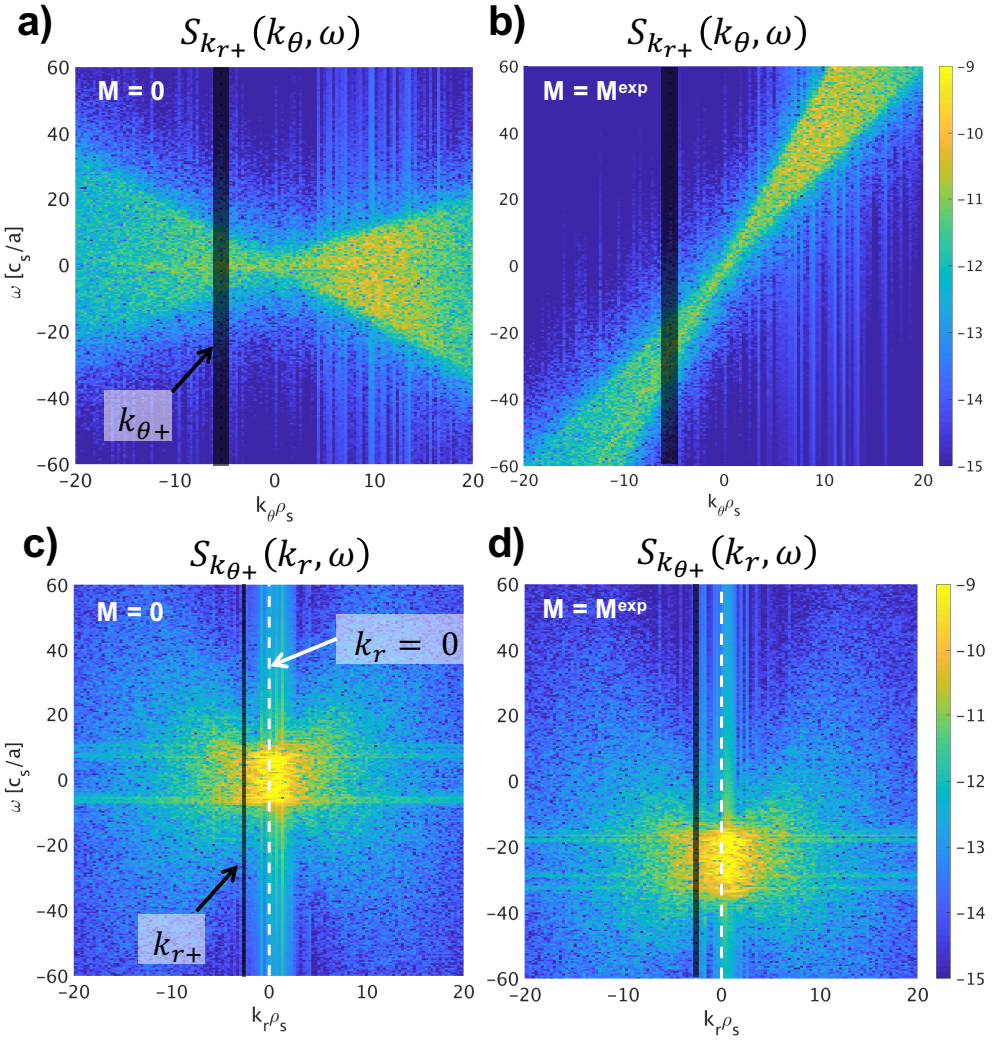

Figure 5-12: Synthetic frequency power spectrum of fluctuations $S_{k_{r+}}(k_\theta, \omega)$ in a)-b) and $S_{k_{\theta+}}(k_r, \omega)$ in c)-d), all computed from a big-box e- scale simulation $(L_r, L_\theta) = (20, 20.6)\rho_s$. Spectra in a) and b) have been filtered in k_r around the radial component k_{r+} corresponding to channel 1 of the high-k scattering system, where no Doppler shift is applied in a) and the experimental Doppler shift value applied in b). These (ω, k_θ)-plots show the impact of Doppler shift for different k_θ is primarily a shift in frequency ω for the different k_θ, namely $\omega \propto k_\theta \omega_0$ as expected. The black vertical band shows the measurement range in k_θ from channel 1 of the high-k system. In c) and d) the spectra $S_{k_{\theta+}}(k_r, \omega)$ have been filtered in k_θ around the poloidal-k component $k_{\theta+}$ corresponding to channel 1 of the high-k scattering system. Differently to the (ω, k_θ) spectra, the (ω, k_r)-spectra show that Doppler shift essentially produces a similar frequency shift for all k_r, also as expected for the present conditions. The black vertical band in c) and d) shows the measurement range in k_r from channel 1 of the high-k system, while the white dashed line denotes the $k_r = 0$ line.

5.5.8 Influence of the diagnostic resolution on the frequency spectrum

As it turns out, the diagnostic wavenumber resolution Δk can have a profound impact on the frequency spectrum characteristics, in particular on the spectral width W_f measured by the high-k system.

Using the exact same simulation, I perform parametric scans of the synthetic diagnostic for varying values of the wavenumber resolution Δk_Z. In the actual experiment, $\Delta k_Z = 2/\Delta Z = 67$ cm^{-1}, where ΔZ is the vertical extent of the microwave beam a_0. In figure 5-13.a) is shown how the plasma-frame spectral width value tends to increase with Δk_Z. This is consistent with our intuition, since lower Δk_Z is implies a smaller wavenumber window contributing to the high-k signal - since nearby modes have similar propagation frequencies, this results in smaller spectral width. The spectral width is shown to be strongly affected by the inclusion of Doppler shift, especially for a large wavenumber resolution in which W_f is increased by a factor of 2. However, note how for lower wavenumber resolutions the spectral width seems to be unaffected by Doppler shift. Figure 5-13 shows how a combination of the wavenumber resolution and Doppler shift can have a very substantial impact on the spectral width W_f.

5.6 Lessons learned from this chapter

It is useful to briefly summarize some of the main takeaways from this chapter.

Equivalence between real-space $vs.$ k-space implementation of synthetic diagnostic

By realizing that the synthetic, filtered signal of density fluctuations δn_{u} can be equivalently written in real space as well as in wavenumber space (equation 5.4), I have proposed here two alternate ways of implementing a synthetic diagnostic for coherent scattering turbulence fluctuation measurements in full tokamak geometry. In real space, the filtering is directly applied to the GYRO density fluctuations via a filter in real space $U(\vec{r})$, which determines the shape of the scattering volume. In wavenumber space, the filter $U(\vec{r})$ is transformed to a scattering matrix U_{np} depending on the toroidal and radial mode num-

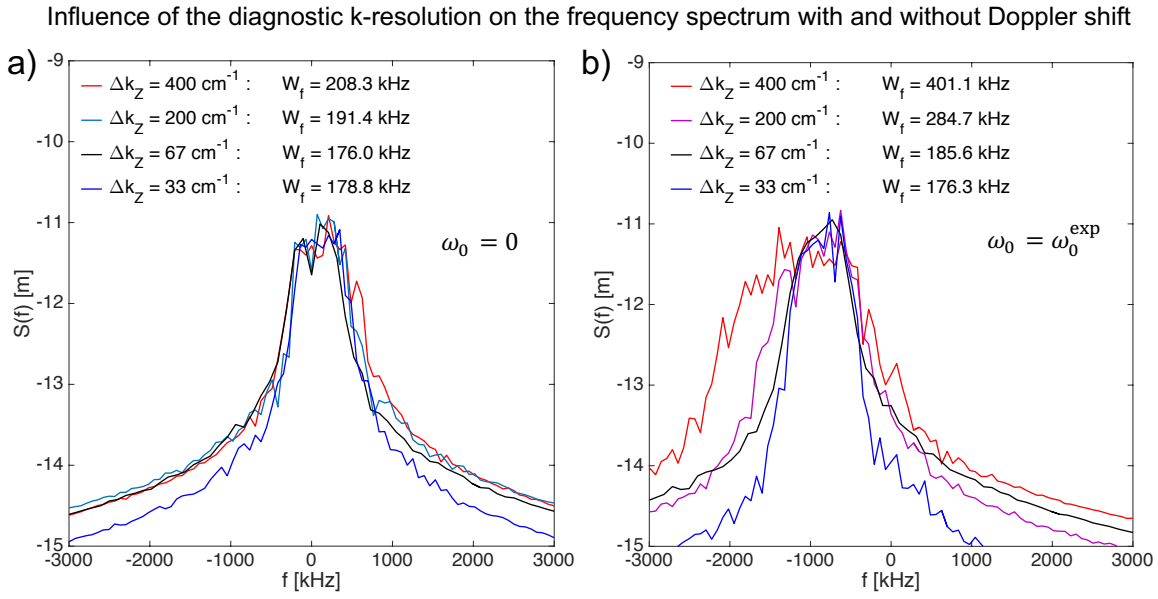

Figure 5-13: Influence of the diagnostic resolution Δk_Z on the spectral width W_f, in the absence $a)$ and presence of Doppler shift $b)$. These figures show the spectral width W_f can be strongly affected by the wavenumber resolution of the diagnostic in combination to Doppler shift.

bers n and p that are used by gyrokinetic codes to expand the density fluctuation field in field-aligned toroidal geometry. I have derived the expression for U_{np} in 2D and in full 3D geometry, assuming localized measurement and separable U. The wavenumber space implementation based on the scattering matrix necessitates a careful wavenumber mapping between the experimentally detected $\vec{k}_+$ in cylindrical coordinates to the field-aligned mode numbers (n, p), or equivalently wavenumbers (k_r, k_θ). The wavenumber mapping of equation 5.12 is also developed as part of this work. Both the real space as well as the wavenumber space formulations presented remain general, and are valid and applicable for the implementation of synthetic diagnostics for coherent scattering density fluctuation turbulence measurements such as Doppler backscattering, reflectometry as well as high-k scattering as presented in this section.

Measurement range of the old high-k scattering system is close to streamer peak of fluctuations

I have applied the real space and the scattering matrix formulation to the old high-k scattering system in NSTX. One of the main results is that the old high-k scattering system is sensitive to fluctuations that are much closer to the spectral peak of fluctuations

given by streamers than previously thought. Originally designed to be sensitive to small k_θ and high-k_r, accurate mapping of the detected $\vec{k}_+$ to the field-aligned wavenumber definitions reveals that $\vec{k}_+$ has a much smaller k_r component than previously predicted (factor $\sim$ $\times$3-6), while k_θ remains relatively unchanged from previous predictions. In addition to using the correct flux-surface averaged definition of ρ_s^{unit} of gyrokinetic codes, equation 5.16 shows that Shafranov shift primarily affects k_r due to the compression of flux-surfaces at the outboard midplane, while flux-surface elongation primarily affects k_θ due to flux-surface 'stretching' poloidally. The geometric effects impacting the wavenumber mapping are exaggerated in the small aspect ratio (impacting B_{unit}), high Shafranov shift and strong flux-surface shaping of spherical tokamaks. In addition, the spectral density $S(k_r, k_\theta)$ is shown to exhibit a tilt in (k_r, k_θ) space (mainly due to the background $E \times B$ shearing rate γ_E), exhibiting a finite k_r peaking at values $k_r\rho_s \sim 1-2$, which are very accessible by the old high-k system. This shows the measurement range of the old high-k system was very close to the streamer fluctuations. This hints at the possibility that the old high-k scattering system may in fact already have been sensitive to streamer fluctuations for other experimental conditions and high-k scattering geometry. This motivates careful analysis of additional NSTX plasma discharges, similar to the one presented here, in order to confirm this speculation.

High-k frequency spectrum dominated by Doppler shift component

In the last section of this chapter I have characterized some of the most important features of the frequency spectra from the old high-k scattering system. This chapter has highlighted the profound impact of Doppler shift on the measured high-k signal, making the frequency spectrum of fluctuations completely dominated by Doppler shift. In particular, figure 5-11 and table 5.3 showed how the spectral peak of fluctuations shifts from a value of $< \omega > \sim 1.5$ c_s/a in the plasma frame, to a value of ~ -23 c_s/a in the lab frame. This suggests the spectral peak of the high-k measurement is completely opaque to the intrinsic plasma frame value. In a validation exercise, the frequency spectral peak of fluctuations from the high-k system would be nearly useless as a quantitative discriminator on the turbulence model. Agreement in the frequency spectral peak will not necessarily imply a close agreement in the propagation frequency of the turbulence in the plasma frame, but

rather that Doppler shift is correctly implemented in the model. In fact I generally observe very close agreement in the spectral peak for essentially all turbulence models, independently of the pertinence to reality, as long as a correct Doppler shift value is applied. This shows one cannot discriminate between turbulence models by direct comparison of the spectral peak $< \omega >$ of fluctuations (specifically for the discrimination between different plasma conditions associated to different turbulence drives). The spectral width W_f will be revisited in chapter 6.

Chapter 6

Validation of gyrokinetic simulations of NSTX H-mode plasma via multi-level hierarchy comparisons

This chapter presents the main results outcome from this thesis. As the title suggests, I combine experiment/model comparisons at different levels in the validation hierarchy: electron thermal transport, followed by quantitative frequency spectra comparisons as well as wavenumber spectra comparisons of electron-scale turbulence. Contributions presented in this thesis are the first simultaneous agreement between simulated and measured frequency and wavenumber spectra of electron-scale turbulence with transport predictions in a spherical tokamak via first-principles gyrokinetic simulation. The importance and relevance of the comparisons is discussed. Carefully designed validation metrics for each comparison in the hierarchy are combined in a singlecomposite metric to assess the overall fidelity of the models. This work has allowed the possibility to quantitatively discriminate between simulations to best capture the essential features of interest, not only through comparisons with turbulent transport levels, but also through direct comparisons of the frequency and wavenumber spectra of the underlying turbulence.

6.1 Description of plasma conditions and linear stability

I will focus this study on a previously analyzed NSTX H-mode plasma discharge 141767 [212]. This discharge featured 2 MW of neutral beam injection (NBI) heating in the time span of interest, producing toroidal rotation levels with characteristic Mach number $M \approx 0.2$. This discharge featured relatively constant levels of line-integrated electron density ($\langle n_e \rangle \sim 6.10^{15}\text{cm}^{-2}$) and toroidal magnetic field ($B_t \sim 0.5$ T), with MHD activity shown to be quite low (more details about this discharge can be found in ref. [212, 214]). Figure 6-1.a) displays the plasma current I_p [MW] corresponding to this plasma discharge, where the flat-top phase is achieved after 0.3 s, settling at $I_p \sim 1.1$ MA. At $t \approx 0.4$ s a controlled current ramp-down takes place for about 50 ms, setting a lower plasma current in a new steady phase of $I_p \sim 0.9$ MA. Our validation study will focus on two distinct plasma conditions: before the current ramp-down at $t = 398$ ms will be the **strong ETG drive** condition (blue), corresponding to strong high-k turbulence levels; after the current ramp-down phase at $t = 565$ ms will be the **weak ETG drive** condition (green), corresponding to weak high-k fluctuation levels detected by the high-k scattering system [65].

Figure 6-1.b) shows the radial profiles of the background electron temperature T_e and density n_e corresponding to the strong and weak ETG drive conditions. High-k scattering data from 3 channels is available in the neighborhood of major radius $R \approx 135$ cm ($r/a \approx 0.7$) delimited by the gray shaded region, and will be the main region of interest in this work. The equilibrium electron density gradient displays a large change at the scattering region between the two conditions, changing by a factor of 4 between the two times ($a/L_n \equiv -a\nabla n/n \approx 1$ for the strong ETG case to $a/L_n \approx 4$ for the weak ETG case). As was reported in [212, 214], this big increase in the background electron density gradient was correlated with reduced levels of high-k fluctuation amplitude detected by the high-k scattering system, consistent with previous work [127, 130].

The high-k scattering system had 3 operational channels at each time of interest, each sensitive to turbulence wavenumbers $\vec{k}$ in the range $(k_x, k_z) \approx (1100\text{-}1900, 200\text{-}400)$ m^{-1}, or in normalized values $(k_x\rho_s, k_z\rho_s) \approx (7\text{-}13, 1.5\text{-}3)$ for the strong ETG condition. For the weak ETG condition, $(k_x, k_z) \approx (1500\text{-}2600, 150\text{-}300)$ m^{-1}, or equivalently

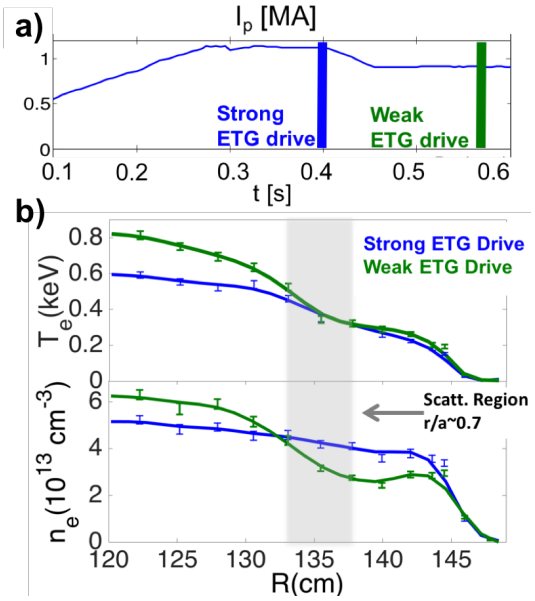

Figure 6-1: **a)** Plasma current time trace for NSTX shot 141767. The **Strong ETG drive time** (blue, t=398 ms) takes place during the flat-top phase right before the start of the controlled current ramp-down. The **Weak ETG drive time** (green, t=565ms) takes place after the current ramp-down during a different flat-top period. **b**) Radial profiles of electron temperature T_e and electron density n_e corresponding to the strong and weak ETG drive times. High-k scattering fluctuation data is available at the gray shaded region ($R \approx 135$ cm, $r/a \approx 0.7$).

$(k_x\rho_s, k_z\rho_s) \approx (10\text{-}18, 1\text{-}2)$ (the normalization by the ion sound gyro-radius $\rho_s \approx 0.7$ cm used TRANSP [105] local values of $T_e \sim 0.4$ keV and magnetic field $B_t \sim 0.5$ T). As in chapter 5 we denote k_x the wavenumber component along the major radius R, and k_z is component in the vertical direction. The wavenumber component in the toroidal direction k_φ was not used in this work due to the implementation of a 2D synthetic diagnostic. These wavenumber components are computed independently for each measurement channel of the diagnostic via ray tracing calculations, following the propagation of a single ray modeling the microwave beam propagation in the plasma. Synthetic turbulence spectra are computed by filtering GYRO-simulated turbulence fluctuations around the measurement wavenumbers by each diagnostic channel, as was shown in chapter 5.

Figure 6-2 shows the frequency and wavenumber power spectrum of high-k fluctuations detected by the high-k system for the strong and weak ETG conditions. The frequency spectrum in 6-2.a) is computed from the frequency analyzed density fluctuation signal of channel 1 (the highest k channel), and used to compute the spectral density $S(f)$. Both spectra exhibit a strong spectral peak at $f = 0$ owing to spurious reflections from

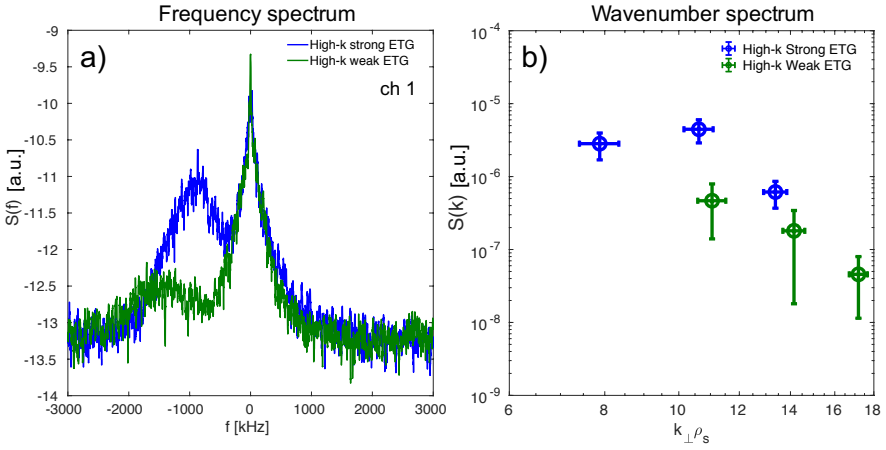

Figure 6-2: **a)** Spectral density $S(f)$, or equivalently the frequency power spectrum of electron-scale turbulence fluctuations detected by channel 1 of the high-k scattering system. **b)** Wavenumber spectrum of fluctuations indicative of the total spectral power $S(k)$ from each high-k diagnostic channel. Here $k_\perp$ is defined as the perpendicular component of $\vec{k}_+$ with respect to the background magnetic field. The strong ETG condition is shown in blue while the weak ETG condition is shown in green. Since the high-k diagnostic is not absolutely calibrated, spectra are shown in arbitrary units.

the incident microwave beam, resulting in a diagnostic artifact that pollutes the high-k signal. The turbulence spectral power feature is at negative frequency ($f \sim -1$ MHz), and is about an order of magnitude higher for the strong ETG condition with respect to the weak ETG condition (also noticeable from the wavenumber spectrum in 6-2). The changes in frequency fluctuation power between the strong and weak ETG are due to changes in the turbulence spectrum, but also due to a different wavenumber measurement range for channel 1, as can be seen in 6-2. The wavenumber spectrum is indicative of the total fluctuation power from each wavenumber detected by the high-k system, encoded in the wavenumber spectral density $S(k)$. In b) are plotted channels 1, 2 and 3, channel 1 corresponding to the highest-k value and channel 3 to the lowest-k. The reader will notice how channels 1, 2 and 3 of the high-k scattering system are sensitive to different wavenumbers at the strong and weak ETG conditions. The frequency and wavenumber spectra are plotted in arbitrary units due to lack of absolute calibration. More analysis details are given in chapter 5 and appendix A.

With respect to transport, experimental power balance estimates were computed via TRANSP calculations [105]. A total electron thermal power of $P_e \approx 1.48 \pm 0.33$ MW was obtained for the strong ETG condition, and $P_e \approx 1.02 \pm 0.23$ MW for the weak ETG

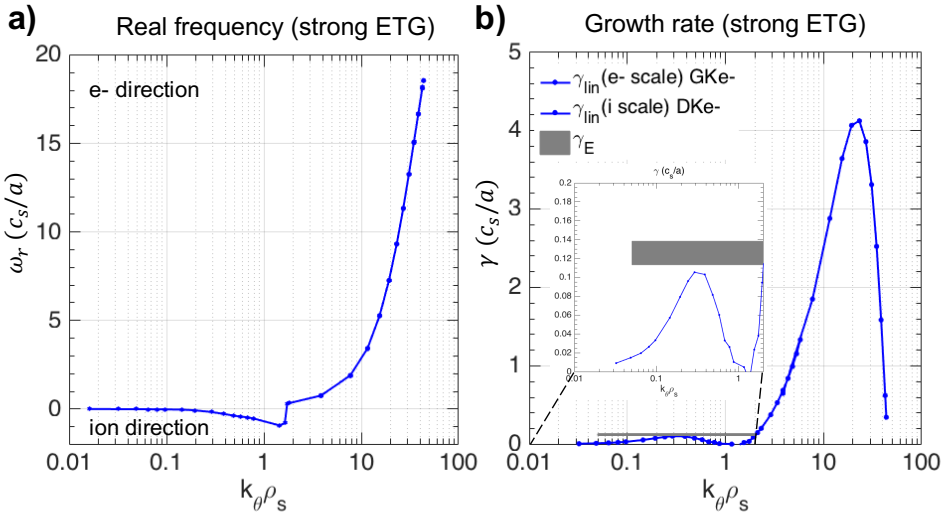

Figure 6-3: GYRO linear simulation output at strong ETG conditions. **a)**. Real frequency ω_r of instability propagates marginally in the ion direction at low-k ($k_\theta\rho_s \lesssim 1$), and electron directed for $k_\theta\rho_s \gtrsim 1$. **b)** Linear growth rate γ of instability. Zooming on the low-k part of the spectrum shows that the maximum linear growth rate is smaller than the $E \times B$ shearing rate, suggesting the ion-scale instability might be suppressed in this condition (Waltz' rule [184]).

condition (the $\pm$ sign denotes the 1-σ error bar computed via error propagation analysis). As was discussed in detail in [212, 214], the reduction of ETG fluctuations at the weak ETG time (figure 6-2) was correlated with decreased electron thermal power levels. For reference, ion thermal power $P_i \sim 0.5$-0.6 MW for both conditions, compatible with the neoclassical levels predicted by NEO [215] within uncertainty.

Linear stability analysis for the full multiscale spectrum $k_\theta\rho_s \in [0.1, 100]$ was performed with the gyrokinetic code GYRO [114] in order to understand the main instabilities present for each plasma condition. Experimental profiles taken from TRANSP output were used as input for the simulations performed at the scattering location ($r/a \sim 0.7$). Low-k modes were modeled by the drift-kinetic electron approximation, which was shown to agree with the fully gyrokinetic electron approximation up to wavenumber values $k_\theta\rho_s \sim 5$ (not shown), well beyond the expected applicability region and providing confidence in the computed linear growth rates.

The real frequency ω_r and linear growth rate γ for the strong ETG plasma condition are shown in figure 6-3.a) and b). At ion-scales, the dominant instability is a ballooning-parity mode propagating in the ion diamagnetic drift direction ($\omega_r < 0$) and exhibiting a peak linear growth rate at $k_\theta\rho_s \approx 0.3$ (possibly a mixed, hybrid mode: the mode exhibited

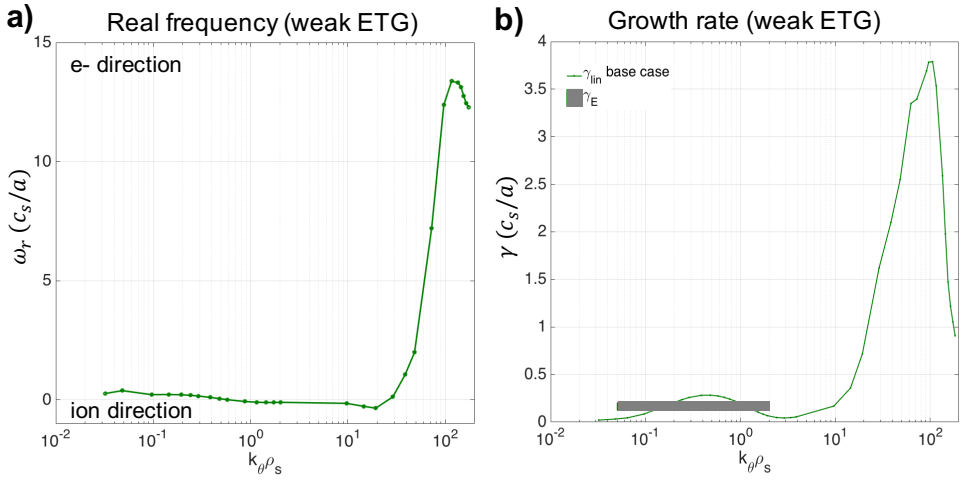

Figure 6-4: GYRO linear simulation output at weak ETG conditions for the base case (using experimental profile parameters as input). **a)**. Real frequency ω_r of instability propagates in the electron direction at low-k and electron-directed at high-k ($k_\theta\rho_s \gtrsim 10-30$). Note the ion directed mode for $1 \lesssim k_\theta\rho_s \lesssim 30$ transitions to the electron direction for $k_\theta\rho_s \gtrsim 30$. **b)** Linear growth rate γ of instability and the $E \times B$ shearing rate γ_E according to the Waltz definition [184]. Note how the linear growth rate at ion-scales is greater than γ_E for the most unstable modes, suggesting ion-scaled turbulence might not be fully suppressed in this condition.

mixed response to the ion temperature gradient, was stabilized by beta and collisions). A zoomed snapshot of the instability at low-k (Fig. 6-3.b) shows that the maximum linear growth rate is smaller than the local $E \times B$ shearing rate for all poloidal wavenumbers $k_\theta\rho_s < 1$, suggesting that the linear instability at ion-scales might be suppressed in this condition [184]. At electron-scales, the dominant linear instability is an electron directed ETG mode ($\omega_r > 0$), exhibiting much higher linear growth rates peaking at $k_\theta\rho_s \approx 20$. This linear gyrokinetic analysis suggests that the ETG mode is a potential candidate to (nonlinearly) drive experimentally relevant values of electron thermal transport.

Linear stability analysis for the weak ETG condition (Fig. 6-4) exhibits an electron directed, tearing parity microtearing mode at very low-k ($k_\theta\rho_s < 0.1$), transitioning to an electron directed trapped electron mode peaking at $k_\theta\rho_s \approx 0.4$-$0.5$, which was enhanced by electromagnetic effects (not shown). A range of wavenumbers exhibit linear growth rate values that surpass the local $E \times B$ shearing rate (gray band in figure 6-4.b)) suggesting the ion-scale instability might not be fully suppressed and could potentially drive significant electron heat flux. The dominant instability exhibits an ion directed mode for electron-scale wavenumbers in the range $1 \lesssim k_\theta\rho_s \lesssim 30$, rapidly transitioning to an elec-

tron directed ETG mode for $k_\theta \rho_s \gtrsim 30$. The ETG peak linear growth rate occurring at $k_\theta \rho_s \approx 100$ suggests these very small mode structures will probably not drive substantial amounts of electron heat flux. With respect transport, ion thermal power P_i lies very close to neoclassical levels, and as we will see, nonlinearly the low-k turbulence is stabilized by $E \times B$ shear at the weak ETG condition.

Previous transport predictions from nonlinear gyrokinetic simulation

Previous nonlinear GYRO simulations carried out for this discharged suggested that ETG could produce experimentally relevant electron thermal transport levels $P_e^{\text{sim}}/P_e^{exp} \sim 30\%$ for the strong ETG condition, but clearly underpredicting the experimental values. For the weak ETG condition, both ion and electron scale turbulence were predicted to be suppressed, producing negligible electron thermal transport. In the rest of this chapter we will test the simulation predictions within small sensitivity scans of the main turbulence drive terms in the inputs. If the uncertainty analysis performed cannot match all the experimental observations, then there must be a different transport mechanism other than ETG at play. To do so, we perform a systematic validation study of nonlinear gyrokinetics spanning ion and electron-scale turbulence by combining transport estimates along with direct comparisons of the frequency and wavenumber spectra from high-k turbulence. Using appropriate validation metrics, the comparisons performed in this work will guide the selection of the simulations that exhibit closest fidelity to the experimental constraints, implying the closest representation of reality.

6.2 Nonlinear gyrokinetic simulation setup

Three different types of nonlinear gyrokinetic simulations are discussed in this validation study: ion-scale gyrokinetic simulation spanning only ion-scale turbulence ($k_\theta \rho_s \lesssim 1$); electron-scale gyrokinetic simulation featuring a conventional domain resolving the ETG mode ($(L_r, L_\theta) = (4.5, 4)\rho_s$); electron-scale simulation with an unusually large simulation domain ($(L_r, L_\theta) = (20, 20.6)\rho_s$). The three simulation types will be used to compare turbulence fluxes with TRANSP power balance estimates, but only 'big-box' electron-scale simulation will prove satisfactory for direct high-k turbulence comparisons.

	$\mathrm{d}r$	$L_r[\rho_s]$	n_r	$\max(k_r\rho_s)$	$L_\theta[\rho_s]$	$\mathrm{d}k_\theta\rho_s$	$\max(k_\theta\rho_s)$	n_n	$T[a/c_s]$	$dt[a/c_s]$
ion-scale	$0.3\rho_s$	$70-80$	≈ 200	4	$70-75$	0.08	1.1	14	>200	$2.10^{-3}-10^{-3}$
electron-scale	$2\rho_e$	$6-8$	≈ 200	50.5	$4-5$	1.5	$65-85$	40	30	$10^{-3}-5.10^{-4}$
'big-box' electron-scale	$2.5\rho_e$	$20-25$	≈ 500	$30-40$	$20-22$	0.3	$65-88$	≈ 200	30	$10^{-3}-5.10^{-4}$

Table 6.1: Same as table 5.1, but this time including resolution parameters from ion-scale simulation.

Ion-scale simulations model electrons by the drift-kinetic equation, with deuterium ions and carbon impurity gyrokinetically. Standard and 'big-box' electron-scale simulations will model all 3 species gyrokinetically. As was mentioned in the previous chapter, both standard and 'big-box' electron-scale simulations model the same physics phenomena, essentially ETG-driven turbulence. However the different wavenumber resolution is purely an argument based on the numerics needed to resolve the scattering wavenumber from the high-k system.

6.3 Validation metrics

I present here the validation workflow performed in this study. The fidelity of each simulation is quantified via validation metrics for electron thermal power and turbulence spectra comparisons. Thermal power predictions from all simulation types will be compared to power balance calculations (TRANSP) in section 6.4, but only synthetic spectra from 'big-box' electron-scale simulation will be directly compared to the measured turbulence spectra by the high-k system (section 6.5), using a synthetic diagnostic for high-k scattering developed for this work. The methodology employed for the selection of models that best agree with the hierarchy comparisons presented will also be discussed.

In order to identify simulations that best satisfy the experimental constraints, I compare simulation and experiment on three levels in validation hierarchy. Electron thermal power comparisons are at the highest level, performed for all simulation types in section 6.4. Local profile values will be scanned around the most significant input drive terms: ∇T and ∇n are varied within 1-σ uncertainty, while q is varied by $10\ \%$ and $\hat{s}$ is varied by $20\ \%$ (constituting reasonable errors in the magnetic equilibrium). The specific drive term values are provided in next section. These local transport comparisons will select the 'big-box' electron-scale simulations that best match the electron thermal power (P_e

[MW]) within experimental uncertainty. For the strong ETG case, 5 'big-box' electron-scale simulations producing experimentally relevant electron thermal transport P_e will be used for further detailed comparisons of high-k spectra. For the weak ETG condition, 2 'big-box' electron-scale simulations are performed, but only one of them will be able to match the electron thermal power. Frequency spectra comparisons will be at the lowest level and shown in section 6.5, providing detailed information about the spectral peak $< f >$ and spectral width W_f. However, these will not prove useful for the purpose of model selection. Wavenumber spectra comparisons will be at the second level in the hierarchy, and will yield comparisons of the fluctuation level ratio and the k-spectrum shape. Wavenumber spectra comparisons will prove extremely useful for discriminating against turbulence models that best match the experimental constraints, and will be performed for the 5 'big-box' electron-scale simulations at the strong ETG and one flux-matching simulation at weak ETG.

I choose the following observables $\mathbf{X}$ for multi-level hierarchy comparisons of the 'big-box' electron-scale simulation models: electron thermal power $\mathbf{P_e}$, fluctuation level ratio $\mathbf{ratio}$ and wavenumber spectra shape $\mathbf{shape}$, defined as

$$
\begin{array}{ll}
\textbf{Electron thermal power} & \mathbf{X} = \mathbf{P_e} \\
 & \text{from TRANSP and nonlinear GYRO simulation} \\
\textbf{Fluctuation level ratio} & \mathbf{X} = \mathbf{ratio} = \log_{\mathbf{10}} \left(\dfrac{\langle \mathbf{S(k_i)} \rangle^{\mathbf{strong\ ETG}}}{\langle \mathbf{S(k_i)} \rangle^{\mathbf{weak\ ETG}}} \right) \\
 & \text{ratio of mean spectral densities} \\
k\textbf{-spectrum shape} & \mathbf{X} = \mathbf{shape} = \mathbf{S(k_i)} \\
 & \text{spectral density from each channel}
\end{array}
\tag{6.1}
$$

where $\langle \mathbf{S(k_i)} \rangle = \sum_i S(k_i)/3$ denotes the average fluctuation power over the different channels $\mathbf{i}$ computed using the spectral density $S(k)$ (respectively for the strong and weak ETG conditions in order to compute the ratio). The absence of absolute calibration of the high-k scattering diagnostic power motivates the use of the fluctuation level ratio between the strong and weak ETG conditions as a meaningful metric. The quantity $\frac{\langle \mathbf{S(k_i)} \rangle^{\mathbf{strong\ ETG}}}{\langle \mathbf{S(k_i)} \rangle^{\mathbf{weak\ ETG}}}$ was observed to vary by 2 orders of magnitude and motivated the choice of the function

$\log_{\mathbf{10}}$ as a metric measure. Each of the three observables ($\mathbf{P_e}$, $\mathbf{ratio}$ and $\mathbf{shape}$) use predictions from simulation $\mathbf{X}^{\text{sim}}$, and are directly compared to experiment $\mathbf{X}^{\text{exp}}$ via a validation metric of distance $\mathbf{d_X}$ that quantifies the goodness of agreement (following methodologies described in [101,103]). In order to have a bounded measure of agreement between 0 and 1, I compute the quantity $\mathbf{R_X}$ from $\mathbf{d_X}$. Both quantities are defined in past validation works [101, 103] as

$$\begin{aligned} \mathbf{d_X} &= \sqrt{\frac{(\mathbf{X^{exp}} - \mathbf{X^{sim}})^2}{\sigma(\mathbf{X^{exp}})^2 + \sigma(\mathbf{X^{sim}})^2}} \\ \mathbf{R_X} &= \frac{1 + \tanh((\mathbf{d_X} - d_0)/\lambda)}{2} \end{aligned} \tag{6.2}$$

where I employed characteristic values of $d_0 = 1.5, \lambda = 0.5$ [101, 103]. Using the bounded metric $\mathbf{R_X}$ from each of the three observables, a composite metric $\mathbf{M_1}$ can be constructed to quantify the overall fidelity of the experiment/model comparison. A value of 0 in $\mathbf{M_1}$ and $\mathbf{R_X}$ indicates perfect agreement, while 1 is indicative of complete disagreement. The $\mathbf{M_1}$ composite metric will prove useful for discerning and discriminating the different models that best agree with the experimental constraints, indicating the 'best' model representative of reality. A validation table summarizing and quantifying the comparisons of the 5 strong ETG and one weak ETG 'big-box' electron-scale simulations will be shown at the end of section 6.5 (table 6.5).

6.4 Local transport comparisons via gyrokinetic simulation

I present in this section electron thermal power predictions (P_e [MW]) from nonlinear gyrokinetic simulations using the GYRO code, separately resolving ion and electron-scale turbulence. Parametric scans were performed for the main turbulence drive mechanisms $(a/L_{Te}, a/L_{Te}, q, \hat{s})$, are $a/L_{Te} = -a\nabla T_e/T_e$ and $a/L_{ne} = -a\nabla n_e/n_e$ are the background electron temperature and density gradients respectively, q is the magnetic safety factor and $\hat{s}$ is the magnetic shear (I will note $a/L_{Te}, a/L_{ne}$ interchangeably by $\nabla T, \nabla n$ in the rest of this thesis).

6.4.1 Strong ETG drive conditions

It was discussed in section 6.1 that electron-scale gyrokinetic simulation using experimental profile values as input can only provide $\approx 30\%$ of the experimental electron thermal power estimate from TRANSP, where $P_e^{exp} \approx 1.48 \pm 0.33$ MW. Ion-scale simulation is shown to be suppressed by the large value of $E \times B$ shear, consistent with the linear simulation results of figure 6-3. This clear underprediction of P_e^{exp} leads us to perform parametric scans for the main turbulence drive mechanisms, both at electron and ion-scales: the background electron temperature gradient $a/L_{Te} \approx 3.36$ is the ETG turbulence drive mechanism, and a 1σ uncertainty corresponds to 25% of the background value. The electron density gradient a/L_{ne} is shown to be a stabilizing mechanism ([212]), and a 1σ uncertainty corresponds to 50% of the background value (note a/L_{ne} is small for this condition, ≈ 1). The uncertainties in the profile gradients were computed from uncertainties in the background electron density and temperature profiles followed by a Montecarlo analysis approach. The main sensitivity scans performed using 'big-box' electron-scale simulation are shown by table 6.2.

Figures 6-5.a) and b) show the electron thermal power P_e predictions by ion-scale (red), electron-scale (blue) and 'big-box' electron-scale simulation (magenta) when the experimental value of normalized equilibrium electron temperature gradient ∇T is scanned within experimental uncertainty. The experimental value, as computed by TRANSP, is shown in black. Figure 6-5.a) shows simulations run using the experimental value of the background electron density gradient ∇n as input. Figure 6-5.b) shows simulations that were run using a reduced value of the background density gradient within 1σ experimental uncertainty in the input, in order to maximize the turbulence drive.

Figures 6-5.a) and b) show that ion-scale simulation predicts negligible electron thermal power for all parametric scan values in ∇T and ∇n (red dots), consistent with turbulence suppression by $E \times B$ shear. However, electron-scale simulation can match P_e^{ext} in figure 6-5.b), using scaled values of ∇n and ∇T (blue dots). 'Big-box' electron-scale simulation provides very similar P_e predictions as electron-scale simulation when run using the same profile inputs, essentially matching P_e^{exp} when temperature and density gradients are scaled simultaneously (black dot in 6-5.b)). In order to test the sensitivity

	base	$\sigma(\nabla T, \nabla n)$	$\sigma(\nabla T), q, \hat{s}$	$\sigma(\nabla n), q, \hat{s}$	$\sigma(\nabla T, \nabla n), q, \hat{s}$
$\mathbf{a/L_{Te}}$	3.3626	4.2032	4.2032	3.3626	4.2032
$\mathbf{a/L_{ne}}$	1.0048	0.5024	1.0048	0.5024	0.5024
$\mathbf{q}$	3.7892	3.7892	3.4103	3.4103	3.4103
$\hat{\mathbf{s}}$	1.8047	1.8047	2.1656	2.1656	2.1656
$\mathbf{P_e^{sim}/P_e^{exp}}$	29%	70%	95%	91%	170%

Table 6.2: Table summarizing the sensitivity scans performed using 'big-box' electron-scale simulation for the strong ETG case, including the value of the drive terms scanned ($a/L_{Te}, a/L_{ne}, q, \hat{s}$) used in the input, as well as the predicted value of the electron thermal power with respect to the experimental level P_e^{sim}/P_e^{exp}.

of P_e to small changes in safety factor q and magnetic shear $\hat{s}$ (reasonable uncertainties in the magnetic equilibrium reconstruction), additional scans with reduced safety factor q by 10% and increased magnetic shear $\hat{s}$ by 20% were performed using 'big-box' electron-scale simulation: the purple square in 6-5.a) corresponds to a flux-matching 'big-box' electron-scale simulation with scaled (∇T) within 1-σ uncertainty ($a/L_{Te} = 3.7$) in addition to -10%q and +20%$\hat{s}$; the green diamond in 6-5.b) is also flux-matching, and uses scaled (∇n) within uncertainty (1-σ), -10%q and +20%$\hat{s}$; the dark green cross in 6-5.b) overpredicts P_e, and uses scaled ($\nabla T, \nabla n$) within uncertainty, -10%q and +20%$\hat{s}$ (table 6.2). These simulations highlight how ETG can be equally or even more sensitive to q and $\hat{s}$ than to the traditional $\eta_e = \nabla T/\nabla n$ dependence. More importantly, among the 5 'big-box' electron-scale simulations in figure 6-5, I emphasize that 2 of them clearly reproduce the experimental P_e value within error-bars, providing strong evidence pointing towards electron-scale turbulence as the main mechanism responsible for anomalous electron thermal transport in this condition. Negligible ion thermal power was predicted by all electron-scale and 'big-box' electron-scale scale simulations, consistent with the inference that ion thermal transport is neoclassical. In the next section, synthetic spectra comparisons will be performed for the 5 'big-box' electron-scale scale simulations of figures 6-5.a) and b).

6.4.2 Weak ETG drive conditions

As was discussed in section 6.1 the weak ETG condition is especially interesting from a validation perspective, since neither ion nor electron-scale gyrokinetic simulations pro-

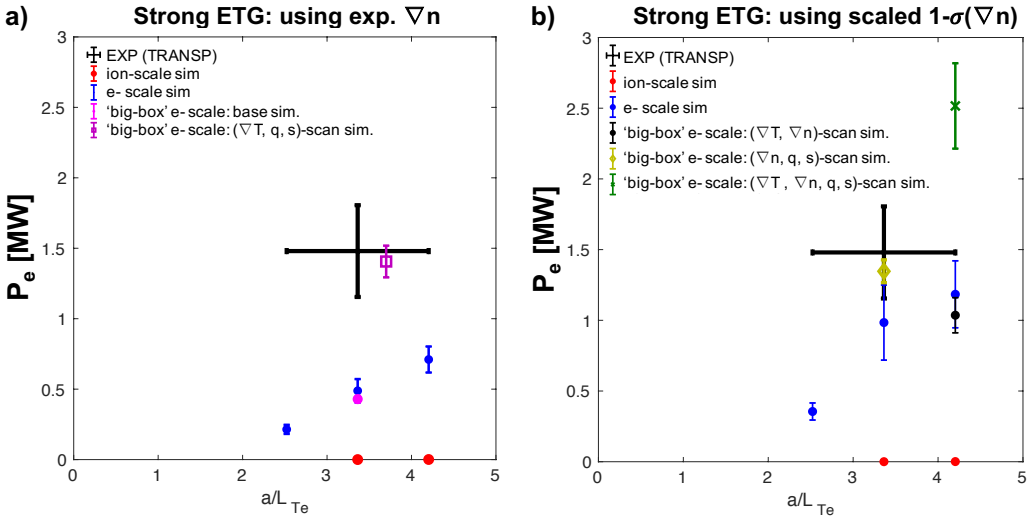

Figure 6-5: **a)** Total thermal transport budget from experiment (TRANSP, black) along with GYRO simulations that use experimental value of ∇n as input, corresponding to the strong ETG drive condition. The magenta dot corresponds to the 'big-box' electron-scale simulation run for base experimental parameters. The purple square corresponds to 'big-box' electron-scale simulation with scaled (∇T) within 1-σ uncertainty in addition to -10% q and $+20\%\hat{s}$. **b)** GYRO simulations have scaled ∇n by 1-σ to maximize turbulence drive $(-\sigma(\nabla n))$. Black dot corresponds to 'big-box' electron-scale scale simulation scanning $(\nabla T, \nabla n)$ within uncertainty. Green diamond scans (∇n) within uncertainty, -10% q and $+20\%\hat{s}$. Dark green cross scans $(\nabla T, \nabla n)$ within uncertainty, -10%q and $+20\%\hat{s}$. These simulations show that ion-scale turbulence is stabilized by $E \times B$ shear and electron scale turbulence can explain the experimental electron thermal transport levels within small variations in the input drive terms.

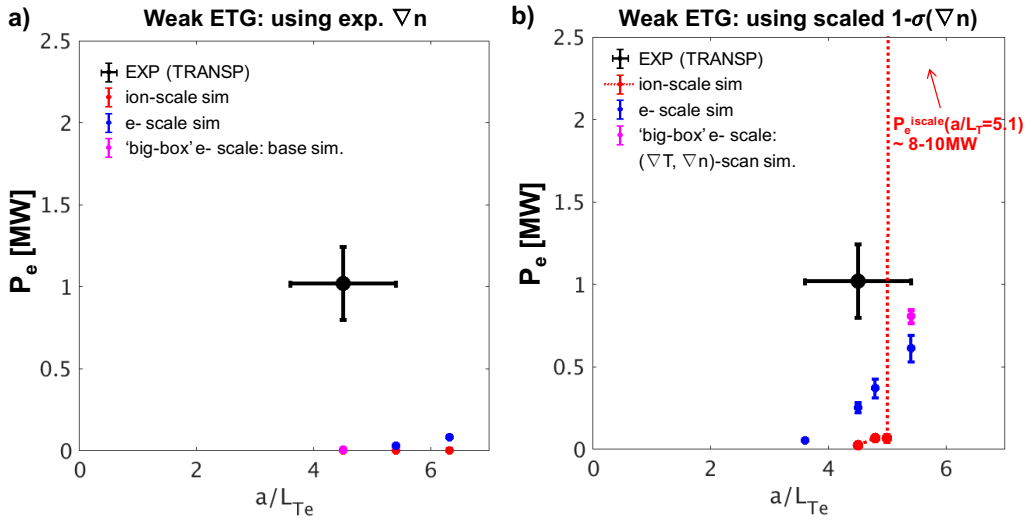

Figure 6-6: **a)** Total thermal transport budget from experiment (TRANSP, black) along with GYRO simulations that use the experimental value of ∇n as input, corresponding to the weak ETG drive condition. **b)** GYRO simulations with scaled ∇n by 1-σ to maximize turbulence drive ($-\sigma(\nabla n)$). Note the significant increase in stiffness predicted from electron-scale turbulence (blue) and especially ion-scale turbulence (red) when ∇n is scaled by 1-σ.

duce experimentally relevant values of electron thermal power when the simulation is run using the experimental profile values as input. As mentioned, the TRANSP power balance estimate for this conditions is $P_e^{exp} \approx 1.02 \pm 0.23$ MW.

Similar to the approach followed for the strong ETG condition, parametric scans varying electron temperature gradient input a/L_{Te} were performed within experimental uncertainty, using the experimental density gradient value in figure 6-6.a), and a fixed scaled value of density gradient within 1-σ uncertainty in figure 6-6.b). In red are ion-scale simulation predictions, blue are electron-scale simulation predictions, and in magenta are 'big-box' electron-scale simulation predictions. Note that here the 1-σ uncertainties are 20 % and 30 % of the background value for a/L_{Te} and a/L_{ne} respectively.

Figure 6-6.a) shows that negligible electron thermal transport is obtained when the background density gradient is set to the experimentally measured value, both from ion and electron-scale simulations. On the other hand, when a temperature gradient scan is performed in addition to a 1σ scaled value of the electron density gradient as in figure 6-6.b), a huge increment in the predicted P_e can be observed in the ion-scale simulations. For values of $a/L_{Te} < 5$, the turbulence state is shown to be dominated by large zonal flow amplitudes suppressing the ion-scale fluctuations and transport. For $a/L_{Te} > 5$ the

ion-scale simulations predict values of P_e up to factors of 10 larger than the experimental levels. In addition, the transition from a zonal flow dominated state for $a/L_{Te} < 5$ to a turbulent state dominated by large amplitude turbulent fluctuations happens abruptly near $a/L_{Te} \approx 5$, indicative of extremely large stiffness. In fact, ion-scale simulations run for values of $a/L_{Te} = 4.5, 4.8, 5$ display zonal flow dominated time phases producing negligible transport, followed by sudden turbulence bursts where lone largescale eddies produce instanteneous high levels of transport. These large-scale eddies are eventually damped by the strong zonal flows present, producing negligible time-averaged electron thermal power as shown in 6-6.b). This behavior is reminiscent of a Dimits shift-like turbulence regime very close to the nonlinear threshold and mediated by the large amplitude zonal flows [220], and more recently observed in conditions of subcritical ITG turbulence enabled by $E \times B$ flow shear [174]. However, for $a/L_{Te} > 5$, the turbulence drive from the background gradients is shown to be too strong for zonal flows to damp a highly unstable ion-scale mode. It is interesting to note that this highly unstable TEM branch is strongly sensitive to $\delta B_{||}$ fluctuations, exhibiting complete turbulence stabilization by when $\delta B_{||}$ fluctuations were not included in the simulation. Linear stability analysis showed the KBM β_e threshold was very close to the experimental β_e value (within $\sim 20\%$ for the base experimental parameters). Previous work [136] already reported on a hybrid TEM/KBM mode being capable of driving substantial experimental thermal transport which could possibly be linked to this highly unstable ion-scale turbulence regime.

Figure 6-7 shows the ion and electron thermal power from ion-scale simulation. The predicted ion thermal power is negligible for $a/L_{Te} < 5$ (similarly to the electron thermal power), but overpredicts the experimental TRANSP value by factors of $\sim$ 2-3 (magenta curve) for $a/L_{Te} > 5$. Since the TRANSP P_i is very close to the neoclassical NEO prediction, we conclude that ion-scale turbulence should produce negligible transport (P_e and P_i), and the TEM/KBM-stable regime ($a/L_{Te} < 5$) is the most experimentally relevant at the weak ETG condition.

Electron-scale turbulence is also shown to be very close to the nonlinear threshold in this plasma regime. As is shown by the blue dots in figure 6-6.b), a linear dependence of P_e with a/L_{Te} shows a clearly active ETG mode producing experimentally relevant P_e values that are close to matching the experimental TRANSP levels for the highest

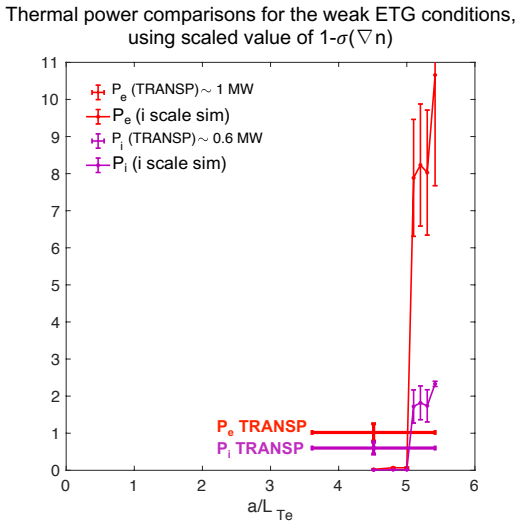

Figure 6-7: Total thermal power on the electron and ion channel (P_e and P_i respectively) as a function of driving mechanism a/L_{Te} for the weak ETG drive condition. The density gradient scale length value a/L_{ne} in the simulations presented in this figure has been scaled by 1-σ of the experimental uncertainty. Note the great increase in predicted P_e and P_i for $a/L_{Te} \sim 5$, displaying large stiffness from a highly unstable TEM branch.

temperature gradient scanned and exhibiting finite stiffness. A 'big-box' electron-scale simulation was run for this highest drive condition (magenta dot), matching P_e^{exp} and slightly overpredicting the electron-scale simulation value for the same scaled a/L_{Te} and a/L_{ne} values. This slight mismatch between electron and 'big-box' electron-scale simulation P_e predictions could be due to the inclusion of highly unstable ion-scale modes down to $k_\theta \rho_s \sim 0.3$ (as shown by ion-scale simulation in red). However those are not fully developed and have not reached a fully saturated state due to the of lack resolution (both temporal and spatial) in 'big-box' electron-scale simulation resolving ion-scale modes. 'Big-box' electron-scale simulation run for the base case is shown in figure 6-6.a), producing negligible P_e.

These results suggest that ETG rather than ion-scale TEM/KBM is responsible for electron thermal transport in these conditions. This is consistent with 'big-box' electron-scale simulations being able to match P_e^{exp} within experimental uncertainty in $(\nabla T, \nabla n)$, while the neoclassical ion-thermal transport constraint suggests that the TEM/KBM stable regime is the most experimentally relevant. To test whether electron-scale turbulent fluctuations predicted by GYRO are consistent with the turbulence spectra measurements from the high-k diagnostic, I set out to establish quantitative turbulence comparisons in

the next section.

6.5 Synthetic diagnostic comparisons of high-k fluctuation spectra

6.5.1 Frequency spectra comparisons

Following the procedure outlined in chapter 5 one can extract the frequency spectral peak $< f >$ and spectral width W_f and use them as validation metrics. Figures 6-8.a), b) and c) show frequency spectra comparisons for all channels of the strong and weak ETG case (blue and green respectively), using simulations that matched the electron thermal power. Note that the synthetic frequency spectra was computed implementing the full Doppler shift value (experimental ω_0). Experimental frequency spectra were computed within time windows of 546μs (≈ 120 a/c$_s$), and containing 8,192 time points. Due to the large simulation requirements, synthetic frequency spectra were computed in time windows of 15 a/c$_s$ for the strong ETG condition and 22 a/c$_s$ for the weak ETG condition, typically containing 1,500-2,200 time points. It was found that frequency spectra characteristics had little variation with time windows larger than ≈ 15 a/c$_s$ for these conditions. In order to reduce simulation noise, the synthetic frequency spectra was ensemble averaged using five time windows for the strong ETG case (five time windows of ~ 3 a/c$_s$), and seven time windows for the weak ETG case (seven time windows of ~ 3 a/c$_s$). The experimental f-spectra are normalized by the same constant (both the strong and weak ETG conditions), preserving the fluctuation level ratio (section 6.5 for details).

Good agreement in the frequency spectra is obtained both for the strong and weak ETG conditions and for all operating channels, as is shown in figure 6-8 and tables 6.3 and 6.4. Particularly good agreement is found in the spectral peak of fluctuations $< f >$, which lie in the range $< f >\sim$ 1-1.5 MHz, typically within 5% of the experimental spectral peak and much higher than the values obtained when no Doppler shift is applied (figure 6-9). Agreement is expected owing to the dominant Doppler-shift contribution to the spectral peak.

The spectral width W_f yields close agreement to experiment for the strong ETG con-

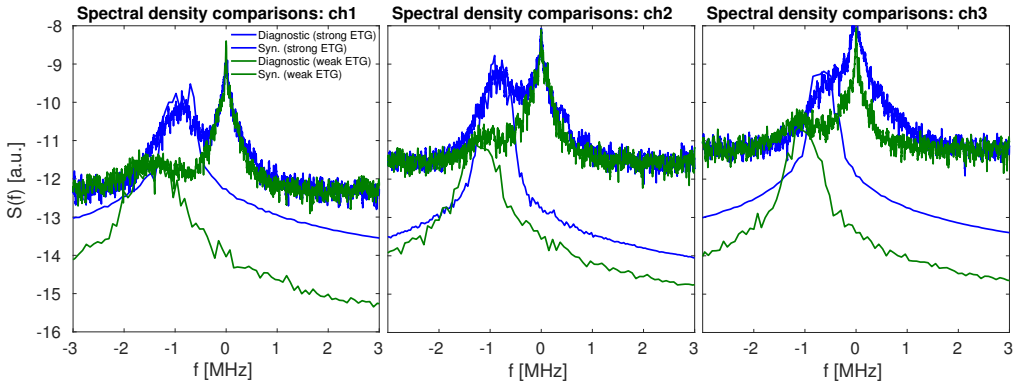

Figure 6-8: Frequency spectrum of high-k fluctuations from channels 1, 2 and 3 and synthetic frequency spectrum corresponding to flux-matched (P_e) simulations. Synthetic spectra includes Doppler shift. For the strong ETG case spectra are computed from the $\sigma(\nabla n), q, \hat{s}$-scan simulation (purple square in figure 6-5.a)), while the weak ETG spectra use the $\sigma(\nabla T, \nabla n)$-scan simulation (magenta dot in figure 6-6.b)). Experiment and simulation are plotted with the same color code, blue for the strong ETG condition and green for the weak ETG condition.

Frequency spectra comparisons (Strong ETG)						
	ch 1		**ch 2**		**ch 3**	
/[MHz]	$< f >$	W_f	$< f >$	W_f	$< f >$	W_f
Exp.	-0.91	0.21	-0.81	0.19	-0.62	0.19
Sim.	-0.97	0.18	-0.76	0.16	-0.65	0.14

Table 6.3: Frequency spectra comparisons for the strong ETG condition corresponding to the frequency spectra in figure 6-8 (blue curves). The spectral peak $< f >$ and spectral width W_f are compared between experimental high-k measurements and synthetic predictions, shown for the three operating channels of the high-k diagnostic (in [MHz]). Remarkable agreement is obtained in the spectral peak $< f >$ for all channels, a confirmation of the Doppler shift dependence of the synthetic signal and of the correct wavenumber sampled by the high-k diagnostic (recall the Doppler shift frequency f_D is proportional to the measurement k). Good agreement is also found for the spectral width in this condition, lying within $\sim 20\%$ of the experimentally detected value for all channels.

dition, within 20% of the experimental range (table 6.3), a value marginally within the experimental uncertainty value (the uncertainty in $< f >$ and W_f is estimated to be $\sim$ 15-20$\%$ computed by varying the prescribed frequency window size). However W_f tends to be slightly underpredicted for the weak ETG condition (up to 40-50%, table 6.4). This could be due to the reduced signal to noise ratio for the strong ETG condition, which could provide an unreliable measure of the experimental spectral width, or possibly due to the discreteness in the simulated turbulence producing a reduced spectral width prediction. Additionally, it could also be that the simulations presented here do not model an essential physics process that impacts the spectral width, such as, possibly, cross-scale interactions. In this work we were limited by computational resources and multiscale simulation was out of the scope.

Frequency spectra comparisons (Weak ETG)						
	ch 1		**ch 2**		**ch 3**	
/[MHz]	$< f >$	W_f	$< f >$	W_f	$< f >$	W_f
Exp.	-1.39	0.36	-1.21	0.34	-1.07	0.34
Sim.	-1.4	0.26	-1.23	0.22	-1.05	0.19

Table 6.4: Frequency spectra comparisons for the weak ETG condition corresponding to the frequency spectra in figure 6-8 (green curves). The spectral peak $< f >$ and spectral width W_f are compared between experimental high-k measurements and synthetic predictions, shown for the three operating channels of the high-k diagnostic (in [MHz]). The uncertainty in $< f >$ and W_f is estimated to be $\sim$ 20-25$\%$ computed by varying the prescribed frequency window size. Remarkable agreement is obtained in the spectral peak $< f >$ for all channels. However the spectral width tends to be slightly underpredicted by the synthetic diagnostic (up to 40-50%). This could be due to the reduced signal to noise ratio in this condition, possibly providing an unreliable measure of the spectral width. Alternatively it could be that the discreteness in the simulated turbulence or a missing physics process not being modeled are resulting in a reduced spectral width prediction.

It was mentioned in chapter 5 how the spectral peak cannot be used to discriminate between the different simulations, since it is dominated by Doppler shift. With respect to the spectral width of fluctuations W_f, the effect of Doppler shift is less pronounced but can still modify W_f by factors of up to ~ 2. Questioning whether the spectral width W_f could be a useful metric to discriminate against turbulent models, I compare the predicted values for W_f from the 7 'big-box' electron-scale simulations in the absence of Doppler shift (5 strong ETG and 2 weak ETG 'big-box' electron-scale simulations), $ie.$ I compare the predicted, intrinsic plasma frame value of the spectral width for different drive

terms. In figure 6-9 are plotted the frequency spectra from the 5 strong ETG 'big-box' e- scale simulations in a), and in b) for the weak ETG case, corresponding to channel 1. The spectral width W_f is shown to exhibit very similar values in the plasma frame for all 7 spectra, in the range $W_f \approx 150$-180 kHz. These values are within the 1-σ uncertainty range ~ 15-20%, determined via variations in the prescribed frequency band of analysis. Notice how W_f is insensitive to extremely different turbulence drive conditions, spanning up to 5 orders of magnitude in the total spectral power: from fully suppressed ETG in $b)$ (red curve) to highly unstable ETG in $a)$. I note how the same numerical resolution was employed for the strong and weak ETG simulations respectively, and the measurement wavenumber was very similar in both conditions ($k_\theta \rho_s \sim -5.4$ was unchanged, while k_r changed by $\sim 30\%$). This suggests that the spectral width is not a good discriminator of turbulence models with varying turbulence drive terms. The spectral width measured by the high-k system could then be strongly influenced by the specific characteristics of the measurement, and only weakly by the intrinsic plasma-frame turbulence conditions. In fact, the synthetic calculations presented in section 5.5.8 showed that the predicted spectral width can be very sensitive to the diagnostic resolution Δk in combination with Doppler shift when both values are large. This would mean that the high-k measurement can strongly prescribe the value of the measured spectral width. For the current experimental value of the wavenumber resolution and toroidal rotation frequency ω_0 we find that the lab-frame spectral width W_f lies within experimental uncertainty of the intrinsic plasma-frame value for the strong ETG case, but has a more important impact in the weak ETG case due to the enhanced toroidal rotation.

We can assess the influence of Doppler shift on W_f for the strong ETG condition by comparing the orange curve in figure 6-9.$a)$ (without Doppler shift) to channel 1 from table 6.3 (with Doppler shift), corresponding to the same simulation. This shows that Doppler shift does not have a substantial impact on W_f in this condition, varying from $W_f^{\omega_0=0} \sim 178.9$ kHz to $W_f \sim 182.5$ kHz. However, a similar analysis performed for channel 1 of the weak ETG condition (comparing green curve from figure 6-9.$b)$ to channel 1 in table 6.4) shows the spectral width varies from $W_f^{\omega_0=0} \sim 180.5$ to $W_f \sim 261.5$ kHz, lying clearly outside the uncertainty range. This change can now be exclusively attributed to Doppler shift: even though the measured wavenumber is unchanged between

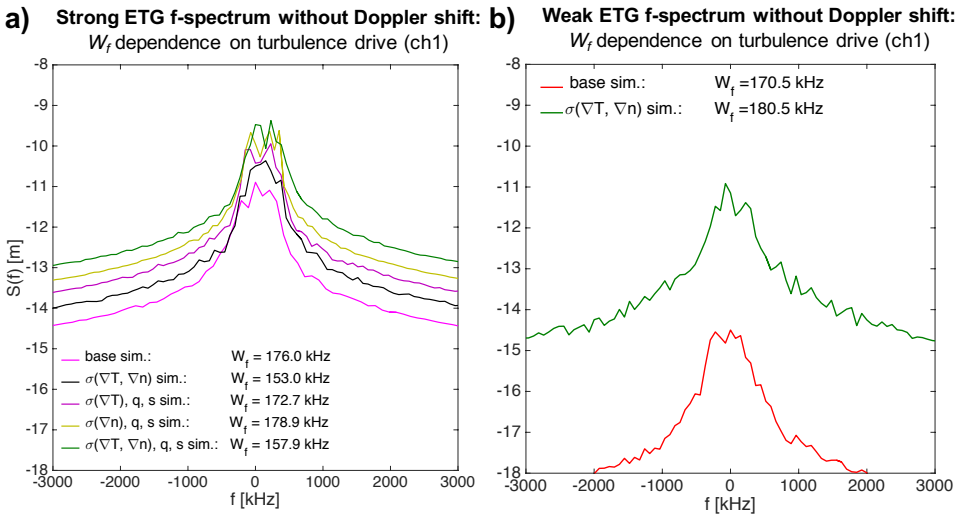

Figure 6-9: Synthetic frequency spectrum of high-k fluctuations from channel 1, respectively for 5 strong ETG 'big-box' electron-scale simulations in a) and 2 simulations for the weak ETG condition in b). The synthetic spectra was computed in the absence of Doppler shift ($\omega_0 = 0$), showing that the average plasma-frame propagation frequency of fluctuations $< f >_{\omega_0=0}$ is ~ 10 smaller than the experimentally measured value, suggesting the Doppler shift completely dominates the frequency spectrum. Surprisingly, the spectral width W_f exhibits very similar values for all 7 simulations, in spite of the fact that simulations span 5 orders of magnitude in spectral power. This suggests that the spectral width is not sensitive to the plasma turbulence conditions, but is mainly determined by the specific characteristics of the measurement (detected wavenumber $\vec{k}_+$ and diagnostic resolution Δk, implemented here via the synthetic diagnostic) and not by the intrinsic plasma-frame turbulence conditions. This figure shows how neither the spectral peak $< f >$ nor the spectral width W_f provide reliable metrics to discriminate against the different turbulent models with varying drive terms.

the strong and weak ETG conditions ($k_\theta \rho_s \sim -5.4$ for channel 1), the toroidal rotation frequency was $\sim 60\%$ higher for the weak ETG case, giving rise to a higher spectral peak $< f >$ and a widening of the spectral width W_f.

Together, the analysis performed on the synthetic spectra and the comparisons to experiment have shown that frequency spectra characteristics do not provide reliable validation metrics, as they are insensitive to the plasma frame turbulence conditions, and strongly affected by external factors such as Doppler shift (calculations shown in appendix 5.5.8 additionally show how the spectral width can be strongly prescribed by the high-k measurement). However, it is still highly valuable to perform experiment/model comparisons of the frequency spectrum. A successful validation activity should still be able to match the frequency spectra characteristics, independently of their ability to discriminate between models, and could be used as a test of the synthetic diagnostic. Overall, the frequency spectra comparisons are highly satisfactory, but suggest additional validation metrics are needed in order to be able to accurately discriminate between turbulence models.

6.5.2 Wavenumber spectra comparisons

Recall that the experimental turbulence power level from the high-k diagnostic is not absolutely calibrated and can only provide a relative fluctuation level. I settle to use the k-spectrum shape and the fluctuation level ratio between the strong and weak ETG conditions as validation metrics to perform the comparisons to experiment. As was outlined in section 6.4, I use the 5 available 'big-box' e- scale simulations for the strong ETG case, and only the flux-matching simulation for the weak ETG (magenta dot in figure 6-6.b)).

Figure 6-10 shows the 5 k-spectra shape comparisons for the strong ETG condition. Only in this figure, the synthetic k-spectrum is scaled in order to minimize the corresponding distance to the experimental spectrum given by the blue circles - this yields a visual comparison of the *shape*. The ETG drive is increased from a) to e). The predicted P_e is shown for each simulation. Close inspection of figure 6-10 highlights that simulations that underpredict the electron thermal power P_e are unable to match the shape of the spectrum: increasing the ETG drive from a) to b) does not improve the k-spectrum

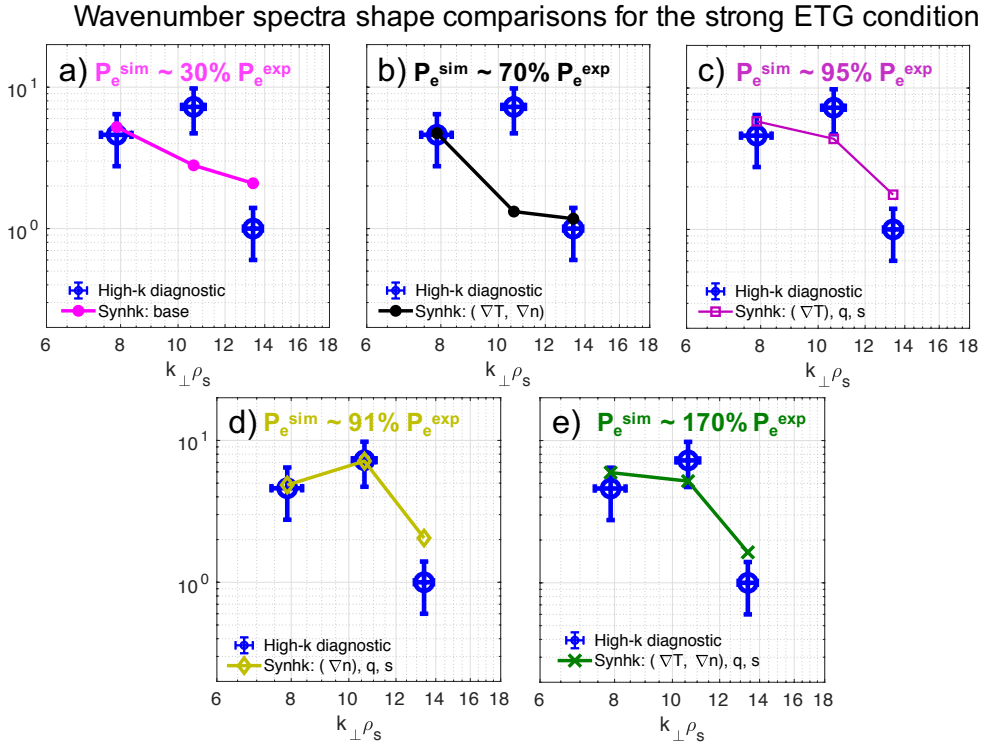

Figure 6-10: Wavenumber spectra shape comparisons for the strong ETG condition. Experimentally detected high-k fluctuations by the high-k system are shown by blue circles. Synthetic turbulence fluctuations correspond to the 5 'big-box' electron-scale-scale simulations in figures 6-5.a) and b). The total synthetic fluctuation power is scaled (only in this plot) to minimize distance with respect to experimental fluctuation levels, allowing accurate comparisons of the wavenumber spectra shape. **a)** 'big-box' electron-scale simulation run for experimental base values of electron temperature and density gradient. **b)** Scaled 'big-box' electron-scale simulation by temperature and density gradient within 1-σ uncertainty. **c)** Flux-matched 'big-box' electron-scale simulation run with scaled temperature gradient within 1-σ uncertainty and an additional -10% in safety factor q and $+20\%$ in magnetic shear $\hat{s}$. **d)** Flux-matched 'big-box' electron-scale simulation run with scaled density gradient within 1-σ uncertainty and an additional -10% in safety factor q and $+20\%$ in magnetic shear $\hat{s}$. **e)** Scaled 'big-box' electron-scale simulation by temperature and density gradient within 1-σ uncertainty and an additional -10% in safety factor q and $+20\%$ in magnetic shear $\hat{s}$.

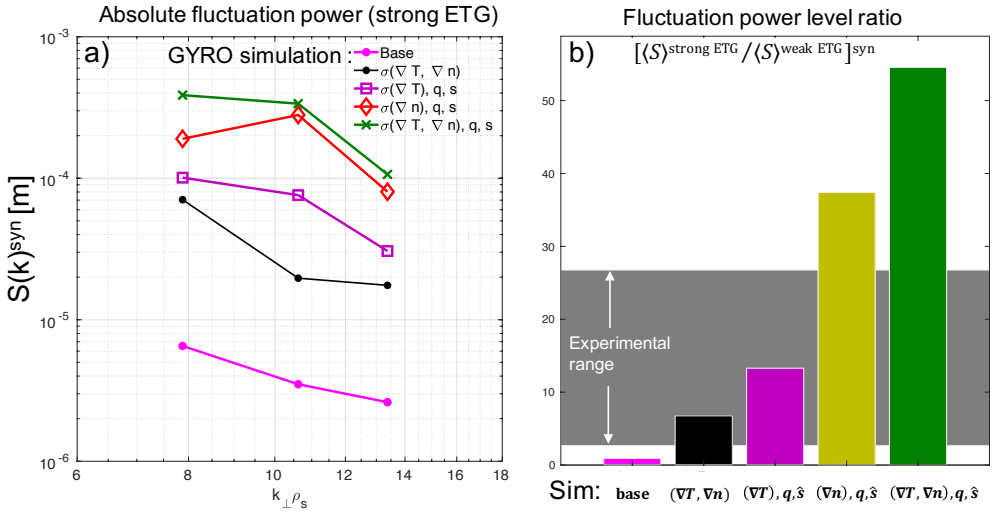

Figure 6-11: **a)** Absolute fluctuation power $S(k)^{\text{syn}}$ (wavenumber spectrum) from 'big-box' electron-scale-scale simulation carried for the strong ETG condition. Combinations of input drive terms correspond to the same simulations in figure 6-10 (here the synthetic k-spectrum has not been scaled but has absolute units). **b)** Synthetic fluctuation level ratio between strong ETG and weak ETG conditions. In computing the synthetic fluctuation level ratio $[\langle S\rangle^{\text{strong ETG}}/\langle S\rangle^{\text{weak ETG}}]^{\text{syn}}$, the strong ETG fluctuation power levels correspond to 'big-box' electron-scale simulations from a), while the weak ETG fluctuation power levels are computed from the same simulation for all comparisons in b), corresponding to the flux-matching weak ETG 'big-box' electron-scale simulation (magenta dot in figure 6-6). The gray band denotes the experimental fluctuation power level ratio between the strong and weak ETG conditions, with value of $\sim 14.7 \pm 80\%$. Simulations with scaled $(\nabla T, \nabla n)$ and $(\nabla T), q, \hat{s}$ lie within the 1-σ experimental range of the fluctuation level ratio.

shape, but worsens it. Importantly, simulations with scaled q and shear produce a much better agreement, 2 of them being able to match P_e (c) and $d)$). This suggests q and shear play a crucial role in determining the spectral shape in these conditions. Note how the scale in the y-axis is logarithmic, meaning the shape of the wavenumber spectrum is a very sensitive metric for comparisons. The spectral shape comparisons are quantified via a validation metric $\mathbf{d_{shape}}$ and shown in table 6.5.

The fluctuation level comparisons are shown in figure 6-11. 6-11.$a)$ shows the synthetic k-spectra from the 5 strong ETG simulations, this time plotted in absolute units (meters [m] due to normalization with respect to the toroidal length of the scattering volume, non-existent in the 2D implementation). I note how the spectral power at the measurement wavenumbers $\vec{k}_+$ is highly sensitive to the ETG drive, spanning about 2 orders of magnitude. This is highly desirable for a validation metric, allowing clear discrimina-

tion of the different turbulence models. Note however how the predicted P_e is much less sensitive to the drive terms (spanning only a factor of ~ 5). In figure 6-11.b) are shown the comparisons of the fluctuation level between the strong and weak ETG conditions. The average fluctuation power between the three channels is computed for each simulation in a). Then this average power is normalized by the average power from the flux-matching, weak ETG simulation (magenta dot in figure 6-6.b)). This yields a specific value of the fluctuation level ratio for each simulation in a). This ratio can be readily compared to the experimental fluctuation ratio, computed in the same manner. Figure 6-11.b) shows that two simulations clearly lie within the 1-σ experimental range: in black with scaled $(\nabla T, \nabla n)$ and in purple with scaled $(\nabla T), q, \hat{s}$. Notice how the latter was a flux-matching simulation, also producing reasonable agreement in the wavenumber spectrum shape (figure 6-10.c)). The high sensitivity of the ratio with varying drive terms motivated the use of a logarithmic metric. Note how simulations in purple and orange in 6-11.b) (scaled $(\nabla T), q, \hat{s}$ and $(\nabla n), q, \hat{s}$) were both clearly matching P_e and the spectral shape (figure 6-10), but they exhibit factors of 2-3 difference in fluctuation level: again a confirmation of the sensitivity and pertinence of the metric. Note additionally how the predicted P_e was higher for the purple case but the fluctuation level was lower than the orange case, consistent with the change in the shape of the wavenumber spectrum between the two cases. The fluctuation level ratio comparisons are also quantified via a validation metric $\mathbf{d_{ratio}}$, as shown in table 6.5.

6.5.3 Validation metrics to quantify overall simulation fidelity

Having identified three meaningful metrics to establish direct experiment/model comparisons (electron thermal power level $\mathbf{P_e}$, fluctuation level ratio $\mathbf{ratio}$ and wavenumber spectral shape $\mathbf{shape}$), I set out to quantify the overall fidelity of the different models. Each validation observable $\mathbf{X}$ is compared to experiment via a validation metric of distance $\mathbf{d_X}$, itself used to compute a normalized measure $\mathbf{R_X}$ between 0 and 1 for each comparison. Table 6.5 summarizes these most pertinent comparisons from sections 6.4 and 6.5. In this table, the simulations are shown with increasing ETG drive as in figure 6-10. Focusing on the third column, the bounded metric associated to electron thermal power

$\mathbf{R_{Pe}}$ shows a clear disagreement for the base case simulation as expected ($\mathbf{R_{Pe}} \approx 0.999$). As we increase ETG drive, the P_e comparisons improve and $\mathbf{R_{Pe}}$ decreases down to 0.006 for the simulation with scaled $\sigma(\nabla T), q, \hat{s}$. The comparison worsens again as we further increase ETG drive in the last row for scaled $\sigma(\nabla T, \nabla n), q, \hat{s}$, which predicted $\sim 170\%$ of the experimental P_e level. A similar analysis can be performed for the 5^{th} column of the fluctuation level ratio. With respect to the shape of the k-spectrum, the best agreement is found for the simulation with scaled $\sigma(\nabla n), q, \hat{s}$, as suggested by inspection of figure 6-10.

	Validation table						
	$\mathbf{P_e}$		**Fluct. level ratio**		k**-spec. shape**		**Composite metric**
Simulation	$\mathbf{d_{Pe}}$	$\mathbf{R_{Pe}}$	$\mathbf{d_{ratio}}$	$\mathbf{R_{ratio}}$	$\mathbf{d_{shape}}$	$\mathbf{R_{shape}}$	$\mathbf{M_1}$
Base	3.22	0.999	1.11	0.18	5.08	1	0.672
$\sigma(\nabla T, \nabla n)$	1.27	0.29	0.74	0.046	4.24	0.99	0.472
$\sigma(\nabla T), q, \hat{s}$	0.215	0.006	0.38	0.01	2.52	0.98	0.397
$\sigma(\nabla n), q, \hat{s}$	0.397	0.012	1.47	0.47	1.53	0.53	0.402
$\sigma(\nabla T, \nabla n), q, \hat{s}$	3.12	0.998	1.74	0.72	1.78	0.76	0.762

Table 6.5: Validation table with the most relevant metrics allowing accurate discrimination between models: the electron thermal power $\mathbf{P_e}$, the electron-scale fluctuation level ratio and the k-spectrum shape. Comparisons are only made for the 5 'big-box' electron-scale-scale simulations in the strong ETG case in figure 6-5. To compute the fluctuation level ratio between the strong and weak ETG conditions, I used the flux-matching 'big-box' electron-scale-scale simulation for the weak ETG case (magenta dot in figure 6-6). The parameters $\mathbf{d_X}$ denote a validation 'distance' for the comparison of each observable $\mathbf{X}$, while $\mathbf{R_X}$ denotes the corresponding bounded error metric between 0 and 1 and computed from $\mathbf{d_X}$. The composite metric $\mathbf{M_1}$ quantifies the overall model agreement, with 0 indicating perfect agreement and 1 indicating complete disagreement. Definitions for $\mathbf{d_X}$, $\mathbf{R_X}$ and $\mathbf{M_1}$ are taken from [101, 103].

A composite metric $\mathbf{M_1}$ combining the different metric results is used to quantify the overall fidelity of each model. $\mathbf{M_1}$ is defined in [103] as $\mathbf{M_1} = \frac{\sum_i h_i R_i}{h_i}$, where $h_i = 1$ for the k-spectra comparisons (shape and ratio) and $= 0.5$ for the P_e comparisons, while R_i are the metrics for all the three comparisons ($\mathbf{R_{Pe}}, \mathbf{R_{ratio}}, \mathbf{R_{shape}}$). This is shown in the last column of table 6.5, with 0 indicating agreement and 1 indicating disagreement. Counter-intuitively, the overall comparison is worse for the last simulation with scaled $\sigma(\nabla T, \nabla n), q, \hat{s}$ than for the base case, owing to the overprediction of P_e and especially to the overprediction of the fluctuation level ratio. The best overall agreement is found for simulations with scaled $\sigma(\nabla T), q, \hat{s}$ and $\sigma(\nabla n), q, \hat{s}$, yielding an approximate value

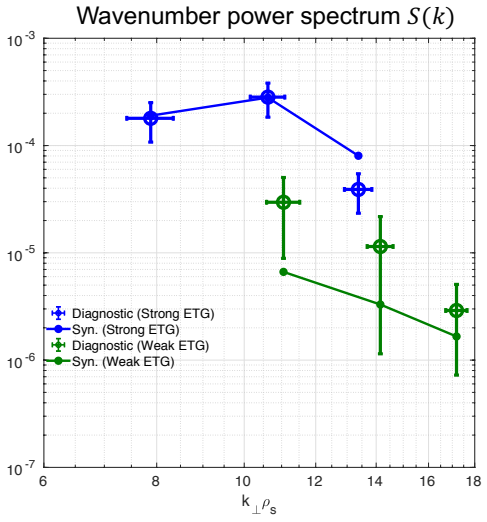

Figure 6-12: Wavenumber spectra comparisons between experimental spectra and synthetically generated spectra from flux-matched (P_e) simulations, both for the strong and weak ETG conditions. The strong ETG synthetic spectra are generated from the $\sigma(\nabla n), q, \hat{s}$-scan simulation that predicts $P_e^{sim} \approx 95\%\ P_e^{exp}$, and correspond to the frequency spectra in figure 6-8, also producing a best match in the validation metric comparisons (table 6.5). The experimental strong ETG k-spectrum is scaled in order to minimize the 'distance' with the synthetic k-spectra. The weak ETG experimental k-spectra are scaled by the same constant in order to preserve the fluctuation level ratio. The weak ETG simulation spectrum corresponds to a 'big-box' electron-scale simulation that matches P_e within experimental uncertainty ($P_e^{sim} \approx 80\%\ P_e^{exp}$). These results give strong evidence suggesting ETG fluctuations alone may be the main mechanism driving electron thermal transport in both the strong and weak ETG conditions.

of ~ 0.4. It is satisfactory that both simulations are able to match the experimental level of electron thermal power. The wavenumber power spectrum from experiment and simulation for one of the two best matched cases is shown in figure 6-12.

6.5.4 Discussion on the metrics employed

At first sight the use of the metrics $\mathbf{d_X}$ and $\mathbf{R_X}$ for observable $\mathbf{X}$ might appear arbitrary (equation 6.2). The choice of the parameters $d_0 = 1.5$ and $\lambda = 0.5$ also appear arbitrary. Here I try to bring some intuition behind these choices. The definitions of $\mathbf{d_X}$ and $\mathbf{R_X}$ are restated here for reference

$$\begin{aligned} \mathbf{d_X} &= \sqrt{\frac{(\mathbf{X^{exp}} - \mathbf{X^{sim}})^2}{\sigma(\mathbf{X^{exp}})^2 + \sigma(\mathbf{X^{sim}})^2}} \\ \mathbf{R_X} &= \frac{1 + \tanh((\mathbf{d_X} - d_0)/\lambda)}{2} \end{aligned} \tag{6.3}$$

The distance $\mathbf{d_X} \epsilon [0, \infty]$. It is normalized by the uncertainties σ. $\mathbf{d_X}$ approaches the value of 0 as the simulation and experiment differ by values less than the uncertainty. On the other hand, $\mathbf{d_X}$ approaches ∞ as the simulation and experiment differ by values well beyond the uncertainty. However if one wants to have a normalized metric ϵ $[0, 1]$, one option is to use the $\tanh$ function as with the $\mathbf{R_X}$ metric.

The $\tanh$ function has essentially a linear dependence for approximate values of $\mathbf{d_X}$ $\epsilon[d_0 - \lambda, d_0 + \lambda]$. The parameter d_0 is chosen in this thesis to be 1.5, while $\lambda = 0.5$, as suggested by previous works [101, 103]. The metric $\mathbf{R_X}$ takes the value of 0.5 when $\mathbf{d_X} = d_0$. $\mathbf{R_X} = 0.0025$ when $\mathbf{d_X} = 0$ (perfect agreement), while $\mathbf{R_X} \to 1$ for $\mathbf{d_X} \to \infty$. $\mathbf{R_X}$ has an approximative constant dependence (it 'saturates') for $\mathbf{d_X} < d_0 - \lambda$ and $\mathbf{d_X} > d_0 + \lambda$.

In order to gain intuition behind the meaning of each metric value, a simple example is discussed here. Call $\delta = |\mathbf{X^{exp}} - \mathbf{X^{sim}}|$, and assume the experimental and simulation uncertainties are equal $\sigma(\mathbf{X^{exp}}) = \sigma(\mathbf{X^{sim}}) = \sigma$. Then we have $\mathbf{d_X} = \delta/(\sqrt{2}\sigma)$. For $d_0 = 1.5$ and $\lambda = 0.5$, we have:

- When $\mathbf{d_X} = d_0 = 1.5$, then $\mathbf{R_X} = 0.5$ and $\delta \approx 2\sigma$. This means that the linear dependance of $\mathbf{R_X}$ is centered at $\mathbf{R_X} = 0.5$ and takes place when the experimental and simulation distance δ is approximately twice the values of the uncertainty σ. $\mathbf{R_X}$ is approximately linear for $\mathbf{d_X}$ $\epsilon[1, 2]$, where $\mathbf{R_x}$ approximatively takes the values $\mathbf{R_X}$ $\epsilon[0.1, 0.9]$. This can be called the region of 'linear dependence'.

- When $\mathbf{d_X} \gtrsim 2$, we have $\mathbf{R_X} \gtrsim 0.9$ and $\delta \gtrsim 3\sigma$. This means that when the distance between experiment and simulation δ is greater than three times the uncertainty value σ, the behavior of $\mathbf{R_X}$ is exponential towards the value of 1 as δ tends to infinity. This can be called the 'bad agreement region'.

- When $\mathbf{d_X} \lesssim 1$, we have $\mathbf{R_X} \lesssim 0.1$ and $\delta \lesssim 1.4\sigma$. This means that when the distance between experiment and simulation δ is less than 1.4 times the uncertainty value σ, the behavior of $\mathbf{R_X}$ is exponential towards the minimum value of $\mathbf{R_X} = 0.0025$ as δ tends to 0. This can be called the 'good agreement region'.

- When $\delta = \sigma$, then $\mathbf{d_X} \approx 0.7$ and $\mathbf{R_X} \approx 0.04$. This means that values of $\mathbf{d_X} \lesssim 0.7$

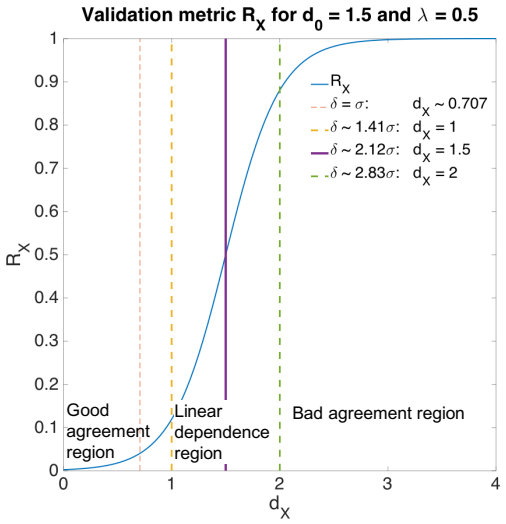

Figure 6-13: Metric $\mathbf{R_X}\ \epsilon\ [0,1]$ as a function of the validation distance $\mathbf{d_X}$ corresponding to the parameters $d_0 = 1.5$ and $\lambda = 0.5$. In this plot the experimental and simulation uncertainties are given the same value σ.

and $\mathbf{R_X} \lesssim 0.04$ correspond to distance between experiment and simulation δ less than the uncertainty σ.

The different regions of the metric $\mathbf{d_X}$ described here are shown in figure 6-13. With this intuition in mind, figures 6-14.a), b) and c) show the corresponding validation metric $\mathbf{R_X}$ as a function of $\mathbf{d_X}$ for the different comparisons between experiment and simulation used in this thesis: $\mathbf{R_{Pe}}, \mathbf{R_{ratio}}$ and $\mathbf{R_{shape}}$ respectively in a), b) and c). Note that in the discussion that follows we still maintain $d_0 = 1.5$ and $\lambda = 0.5$, however now experiment and simulation have different uncertainty values.

With respect to the $\mathbf{Pe}$ comparisons in figure 6-14.a), due to the reduced uncertainties in experiment and simulation (see figure 6-5), the 'base' and $\sigma(\nabla T, \nabla n), q, \hat{s}$ simulations exhibit bad agreement to experiment with $\mathbf{R_{Pe}} \approx 1$ due to under- and over-prediction of the experimental value respectively. On the other hand, the $\sigma(\nabla T), q, \hat{s}$ and $\sigma(\nabla n), q, \hat{s}$ exhibit close agreement to experiment with $\mathbf{R_{Pe}} \approx 0$. The simulation with scaled $\sigma(\nabla T, \nabla n)$ is shown to have modest agreement with experiment with a distance of $\mathbf{d_{Pe}} \approx 1$ in the linear region of variation of $\mathbf{R_{Pe}}$.

The fluctuation level ratio comparisons in figure 6-14.b) seem to be more evenly distributed in the linear region of $\mathbf{R_{ratio}}$ as well as in the region of good agreement close to $\mathbf{R_{ratio}} \approx 0$. This can be explained by the large uncertainty in experiment and simulation

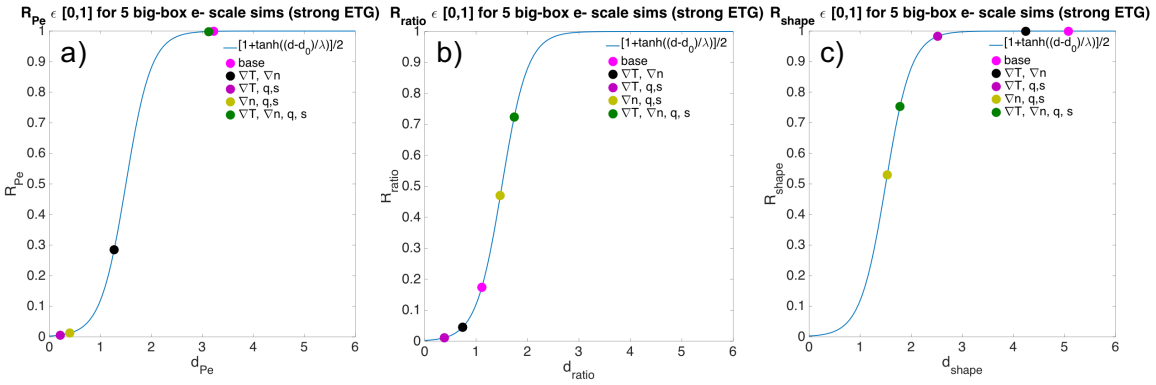

Figure 6-14: Validation metrics $R_{\text{Pe}}, R_{\text{ratio}}, R_{\text{shape}}\ \epsilon[0,1]$ as a function of the distance $d_{\text{Pe}}, d_{\text{ratio}}, d_{\text{shape}}$ for the five 'big-box' electron-scale simulations for the strong ETG of interest in this thesis.

of the fluctuation level ratio, which is close to 80% the experimental value as can be seen from figure 6-11.b). The large uncertainty brings the comparisons closer to the 'good agreement' region near $\mathbf{R_{ratio}} \approx 0$.

The comparisons of the shape of the density fluctuation wavenumber spectrum in figure 6-14.c) appear to be distributed towards the 'bad agreement' region where $\mathbf{R_{shape}} \gtrsim 0.9$, although simulations with scaled $\sigma(\nabla n), q, \hat{s}$ and $\sigma(\nabla T), q, \hat{s}$ are in the linear region of variation of $\mathbf{R_{shape}}$ and exhibit the best agreement, respectively with values $\mathbf{R_{shape}} \sim 0.53, 0.76$. This fact could not possibly have been perceived by visual inspection of figure 6-10, and tells us that, in spite of having large uncertainty values, it is extremely difficult to match the shape of the wavenumber spectrum. The cumulative agreement between experiment and simulation is generally the worst for this observable than for the electron thermal power $\mathbf{P_e}$ and fluctuation level ratio $\mathbf{ratio}$.

The discussion presented here tries to give a sense of intuition behind the numeric values of $\mathbf{d_X}$ and $\mathbf{R_X}$ from table 6.5. The definition of $\mathbf{d_X}$ presented here is close to the χ^2 metric defined in [100] as $\chi^2 = 1/N_{deg} \sum_i \left(\frac{\mathbf{X^{exp}} - \mathbf{X^{sim}}}{\sigma(\mathbf{X^{exp}}) + \sigma(\mathbf{X^{sim}})} \right)^2$, where sum is over the different realizations and N_{deg} are the degrees of freedom. The metric $\mathbf{R_X}$ could also be applied to this χ^2 metric, yielding very similar results as presented here. Although not necessary to assess the fidelity of each comparison, $\mathbf{R_X}$ provides a normalized metric between 0 and 1, where the meanings of 0, 1 and values in between are discussed and shown in figure 6-13.

With respect to the composite metric $\mathbf{M_1} = \frac{\sum_i h_i R_i}{h_i}$ used here, where here i is summing over the different observable comparisons. Note the value h_i takes into account the importance in the comparison according to the place of each comparison in the validation hierarchy. Although the value of h_i should be higher for lower levels in the hierarchy (frequency spectra or wavenumber spectra), the numerical values used here are arbitrary (we used $h_i = 0.5$ for $\mathbf{P_e}$ while $h_i = 1$ for $\mathbf{ratio}$ and $\mathbf{shape}$ as suggested in [100]). The different weights in the comparisons emphasize the more constraining aspect of the lower levels in the hierarchy, and also the difficulty towards obtaining agreement. Intuitively, this means that the wavenumber spectra comparisons are more model constraining than the power balance transport comparisons. Additional composite metrics could have been used, and are proposed in the literature [101, 103]. For example, one could have chosen to not give any special preference to the hierarchy comparisons, setting the value of $h_i = 1$ (metric $\mathbf{M_0}$), or one could additionally have normalized the comparisons by an exponential of the uncertainty normalized to the mean value, defined as $\mathbf{M_2} = \frac{\sum_i h_i S_i R_i}{h_i S_i}$, where $S_i = \exp(-\sigma(\mathbf{X^{exp}})/\mathbf{X^{exp}})$. The values of the different composite metrics for the five comparisons of this chapter are shown in table 6.6. A metric $\mathbf{M_3}$ could also be constructed taking additional account of the uncertainty in the simulation in an exponential factor similar to S_i. Overall very similar conclusions are taken from all three metrics $\mathbf{M_0}, \mathbf{M_1}, \mathbf{M_2}$: the best agreement is found for simulations with scaled $\sigma(\nabla T), q, \hat{s}$ and $\sigma(\nabla n), q, \hat{s}$, while the worst is for $\sigma(\nabla T, \nabla n), q, \hat{s}$ closely followed by the Base simulation.

Comparison of composite metrics $\mathbf{M_0}, \mathbf{M_1}, \mathbf{M_2}$			
Simulation	$\mathbf{M_0}$	$\mathbf{M_1}$	$\mathbf{M_2}$
Base	0.73	0.67	0.73
$\sigma(\nabla T, \nabla n)$	0.44	0.47	0.47
$\sigma(\nabla T), q, \hat{s}$	0.33	0.40	0.37
$\sigma(\nabla n), q, \hat{s}$	0.34	0.40	0.36
$\sigma(\nabla T, \nabla n), q, \hat{s}$	0.83	0.76	0.82

Table 6.6: Validation table comparing the five simulations of interest in this chapter using different definitions of validation metrics. $\mathbf{M_0} = \sum_i R_i/3$ where the sum is over the number of comparisons (=3). $\mathbf{M_1} = \sum_i h_i R_i/h_i$ with $h_i = 0.5$ for $\mathbf{P_e}$ and $h_i = 1$ for $\mathbf{ratio}$ and $\mathbf{shape}$. $\mathbf{M_2} = \sum_i h_i S_i R_i/h_i S_i$ where $S_i = \exp(-\sigma(\mathbf{X^{exp}})/\mathbf{X^{exp}})$. Overall very similar conclusions are taken from all three metrics: the best agreement is found for simulations with scaled $\sigma(\nabla T), q, \hat{s}$ and $\sigma(\nabla n), q, \hat{s}$, while the worst is for $\sigma(\nabla T, \nabla n), q, \hat{s}$ closely followed by the Base simulation.

6.6 Summary of findings

The extensive validation effort performed for this NSTX NBI heated H-mode plasma has tried to shed some light towards understanding the origins of electron thermal transport in the core gradient region of spherical tokamak H-modes, by combining direct comparisons at three different levels in the validation hierarchy: electron thermal power comparisons at the highest level, along with direct high-k turbulence comparisons of the k-spectrum (second level) and f-spectrum (lowest level), made possible via a synthetic diagnostic developed for this work.

Electron thermal transport for the strong ETG condition

Starting with the strong ETG condition, we found that ion-scale turbulence cannot be destabilized within experimental uncertainties in the main turbulence drives and all electron thermal power can be explained by the electron-scale turbulence. This was confirmed by electron thermal power comparisons in figure 6-5 showing 'big-box' electron-scale scale simulation can match the experimental thermal power level within small changes in background gradients. These results gave strong indications pointing to ETG-driven turbulence as the responsible heat loss mechanism, and were confirmed by direct k-spectra comparisons shown in figures 6-10 and 6-11, which showed that the 'big-box' e- scale simulation can simultaneously match the local transport and the high-k wavenumber-spectra constraints. Additionally, remarkable agreement in the spectral peak and spectral width was shown in figure 6-8 and table 6.3. Although the frequency spectrum cannot be used to discriminate between the different simulations, it should be able to reproduce the experimental frequency spectrum and could be used as a test to the simulation and synthetic diagnostic. This confirmed the veracity of the strong ETG simulation conditions that best reproduce the experimental constraints, indicating they are a reasonable representation of reality.

Electron thermal transport for the weak ETG condition

Concerning the weak ETG condition, figure 6-6 showed how ion-scale turbulence plays a negligible role on transport and lies very close to the nonlinear threshold, but can be destabilized within uncertainty in $\nabla T, \nabla n$ and predict up to a factor of 10 or higher

in the experimental electron thermal power. For this case it is useful to compare the ion thermal transport channel. The TRANSP estimate of the ion thermal power P_i is a factor of $\sim$ 2 smaller than electron thermal power P_e (figure 6-7) and lies very close to the neoclassical prediction from NEO. When ion-scale simulation is run for the conditions that overpredict P_e by a tenfold, it is also shown to overpredict P_i. Due to the neoclassical ion thermal transport constraint, I conclude the high ion-scale transport regime is not experimentally relevant. Electron-scale turbulence predicted by 'big-box' electron-scale simulation on the other hand is also shown to be very close to the nonlinear threshold of ETG, and able to produce transport levels that can match the experimental thermal transport levels when scaled within uncertainty in $\nabla T, \nabla n$ (magenta dots in figure 6-6). These results point to ETG, and not ion-scale turbulence, as responsible for anomalous electron thermal transport at the weak ETG condition.

In this context, it is worth pointing out previous work by G. Staebler *et al.* [213] and N. Howard *et al.* [74, 75] as part of the multiscale simulation efforts for some C-Mod L-mode discharges. These indicated that multi-scale effects were important when ion-scales were near-marginal and ETG was strongly drivenm which resembles the weak-ETG case. Additionally, [213] indicated the value of $(\gamma/k_\theta)_{ion}/(\gamma/k_\theta)_{ETG}$ is a proxy for testing the importance of multiscale interactions, where γ is the peak linear growth rate and k_θ is the corresponding wavenumber, respectively for the ion-scale and electron-scale spectrum (denoted by the subscripts ion and ETG). Staebler $et\ al.$ found that cross-scale interactions tend to be important for values of $(\gamma/k_\theta)_{ion}/(\gamma/k_\theta)_{ETG} < 1$. In the present conditions we find $(\gamma/k_\theta)_{ion}/(\gamma/k_\theta)_{ETG} \sim 1.9$ for the strong ETG case and $(\gamma/k_\theta)_{ion}/(\gamma/k_\theta)_{ETG} \sim 18$ for the weak ETG (figures 6-3 and 6-4). This would suggest that cross-scale interactions are not important, even less for the weak ETG condition. It may also be that this rule of thumb, which was implemented based on C-Mod L-mode plasmas, is not applicable for the present conditions and would need further revision for spherical tokamak conditions. The question remains open and only multiscale simulation would confirm whether cross-scale interactions are relevant in these conditions.

Chapter 7

Discussion, conclusions and future work

In this chapter the main contributions of this thesis to understanding electron thermal transport in spherical tokamaks are summarized. Relevance to the field of validation of core-transport models via gyrokinetic simulation is also discussed. Important approximations in the models employed in this thesis are addressed and ideas of future work that directly emanate from this thesis are presented.

7.1 Summary of the main contributions of this thesis

The extensive validation effort performed for this NSTX NBI heated H-mode plasma has tried to shed some light towards understanding the origins of electron thermal transport in the core gradient region of spherical tokamak H-modes. By using high fidelity nonlinear gyrokinetic simulations coupled with a synthetic diagnostic for high-k scattering, I have presented experiment-theory comparisons of electron thermal power P_e along with quantitative comparisons of electron-scale frequency and wavenumber spectra. The main contributions from this thesis can be categorized as those pertaining to **1)** the physics uncovered via the validation of gyrokinetic simulations in the core-gradient region of NSTX NBI-heated H-modes with quantitative comparisons with a synthetic diagnostic for high-k scattering, and **2)** the development of the synthetic diagnostic for high-k scattering.

7.1.1 Physics contributions

First simultaneous agreement between experiment and simulation of electron thermal transport, electron scale frequency spectra, wavenumber spectra shape and fluctuation level ratio between strongly driven and weakly driven ETG turbulence conditions. This is the strongest experimental evidence to date that ETG turbulence can dominate electron thermal transport in the outer-core of low-to-modest β NSTX NBI-heated H-modes.

To my knowledge, this is the first time a validation exercise has proven successful in reproducing the electron-scale frequency and wavenumber density fluctuation spectra in a spherical tokamak. Most importantly, the agreement between experiment and theory in the electron-scale turbulence characteristics is achieved simultaneously with agreement of electron thermal power. Ion thermal transport is explained by neoclassical theory. These simultaneous, multi-level comparisons in the hierarchy validate the local, nonlinear, electromagnetic, electron-scale simulations presented in this thesis, and result in the strongest experimental evidence to date supporting ETG-driven turbulence as the main contributor to anomalous electron thermal transport in the core-gradient region of low-to-modest β NSTX NBI-heated H-modes.

Isolation of the important role of safety factor and magnetic shear in determining the shape and peak of the high-k density fluctuation wavenumber spectrum.

The wavenumber spectra comparisons between the synthetic and experimental k-spectra have highlighted the critical role that the safety factor q and magnetic shear $\hat{s}$ play in constraining the shape of the wavenumber spectrum of ETG fluctuations. Only simulations that were run with scaled q and $\hat{s}$ were able to match the wavenumber spectra shape and the fluctuation level ratio between the strong and weak ETG conditions. These results were shown to be reproduced with the smaller-box standard e- scale simulations run with scaled q and $\hat{s}$, showing this to be a robust argument independent of the simulation type and exclusively pertaining to the underlying physical mechanisms of electron-scale turbulence.

Simulations that best match all experimental observables predict that the measured high-k turbulence is close to the streamer peak.

One of the important results of this thesis is that the original high-k scattering system is sensitive to fluctuations that are much closer to the spectral peak of fluctuations given by streamers than previously thought. Originally designed to be sensitive to small k_θ and high-k_r, accurate mapping of the detected $\vec{k}_+$ to the field-aligned wavenumber definitions has revealed that $\vec{k}_+$ has a much smaller k_r component than previously predicted (by a factor $\sim$ $\times$3-6), while k_θ remains relatively unchanged from previous predictions. The geometric effects impacting the wavenumber mapping are exaggerated at small aspect ratio, high Shafranov shift and strong flux-surface shaping of spherical tokamaks. In addition, the spectral density $S(k_r, k_\theta)$ is shown to exhibit a tilt in (k_r, k_θ) space (mainly due to the background $E \times B$ shearing rate γ_E), exhibiting a finite k_r that peaks at values $k_r\rho_s \sim 1-2$, which are very accessible by the high-k system. This hints at the possibility that the old high-k scattering system may in fact already have been sensitive to streamer fluctuations in other experimental conditions and high-k scattering geometry. This motivates careful analysis of additional NSTX plasma discharges in order to confirm this speculation. The synthetic diagnostic developed for this thesis will be essential to this study.

For the first time, multi-level hierarchy comparisons are performed in a systematic way in the context of the spherical tokamak.

Carefully designed validation metrics were successfully applied to 'big-box' electron-scale simulations in this thesis at three different hierarchy levels. In the absence of absolute calibration of the high-k scattering diagnostic, I introduced a validation metric assessing the **shape** of the wavenumber spectrum. In addition, I introduced a validation metric assessing the **ratio** of the fluctuation power between the strong and weak ETG conditions. These metrics proved highly useful, exhibiting great sensitivity to the input drive terms in the simulation models and yielding great discriminating power. Subsequently, these metrics were combined with thermal power comparisons to differentiate between simulations with varying turbulence drive conditions. A composite metric was then applied to assess the overall fidelity of the models analyzed. The outcome of this work is a model that best

describes all the available experimental observables, which indicates which model is the best representation of reality.

7.1.2 Synthetic diagnostic for high-k scattering

Equivalence real-space $vs.$ k-space implementation of synthetic diagnostic.

In this thesis I have derived and implemented two new, equivalent synthetic diagnostics for GYRO high-k scattering measurements, in real-space $vs.$ k-space. The implementation in real space is a new approach, and derived from first-principles scattering theory. The real-space implementation is naturally more general, and better suited for implementing in general geometries. The traditional synthetic diagnostic implementation in k-space from previous treatments [144, 208–211] is derived from the real-space formulation. The synthetic diagnostic method in k-space is also expanded here to include full 3D axisymmetric geometry. The tools to generate these synthetic spectra will be made available for other uses of GYRO and CGYRO specifically. Both the real space as well as the wavenumber space formulations are applicable for additional diagnostics based on coherent scattering such as Doppler backscattering, reflectometry as well as other high-k scattering diagnostics. Internal magnetic field fluctuation measurements by cross-polarization scattering could be similarly treated by many of the methods outlined here, however sampling internal magnetic field fluctuations and not electron density fluctuations.

Realization that a new type of simulation was required to quantitatively compare with the measured frequency spectra of the high-k density fluctuations.

An important contribution to this thesis is the careful design of electron-scale simulations featuring an unusually large simulation domain $(L_r, L_\theta) \approx (20, 20)\rho_s$. Traditional electron-scale simulations were shown to exhibit a grid in wavenumber space (k_r, k_θ) too coarse to accurately resolve the wavenumbers $\vec{k}_+$ measured by the high-k system. This resulted in inaccurate frequency spectra with respect to experimental spectra, attributed to the lack of wavenumber resolution in the simulation. These inaccuracies were resolved when using 'big-box' electron-scale simulation, showing agreement in the frequency spectra characteristics. The enhanced agreement was due to the improved

wavenumber resolution needed to resolve the measured wavenumbers by the high-k system, an argument purely based on numerics and not on the simulated physics. As far as I could tell, both 'big-box' and standard electron-scale simulations contain the same physics phenomena, ETG-driven turbulence.

Frequency spectrum of high-k scattering is not a critical constraint on the simulation models.

The direct frequency and wavenumber spectra comparisons performed as part of this study yielded a profound understanding of the high-k measurement at NSTX. Past validation studies [100] have indicated that "comparison of time series data provide some of the most fundamental validation tests". However, we have learned in this validation work that it is nearly hopeless to discern between simulations by direct comparisons of the frequency spectra. The spectral peak $< f >$ has shown to be dominated by Doppler shift, while the spectral width W_f is insensitive to the state of the turbulence. However, I want to emphasize that it is still highly valuable to perform experiment/model comparisons of the frequency spectrum. A successful validation activity must be able to match the frequency spectra characteristics as a first step.

Initial assessment of 3D effects for the original high-k scattering system at NSTX.

In this thesis I perform an initial assessment of the potential importance of 3D effects on the scattering signal for the old high-k scattering system. These show that the scattering matrices in 2D and 3D are almost unnoticeably different, suggesting that 3D effects have little effect on the scattering signal and a 2D implementation might be sufficient. This condition is not a general statement and might be different for additional scattering experiments, which will have to be analyzed case by case. Although only qualitative and preliminary, additional tests should be performed to compare the actual synthetic signal and total scattered power between the 2D and 3D implementations, not performed in this work.

7.2 Discussion on the approximations performed

Approximations in the synthetic diagnostic

There is no doubt that the synthetic high-k turbulence predictions presented here suffer from uncertainties and inaccuracies emanating from the approximations made in the synthetic model. One important approximation lies in the $2D$ implementation. This approximation is justified by the toroidal localization of the high-k system as detailed in [90, 91]. As is briefly discussed in appendix C, preliminary assessments have suggested that 3D effects are indeed expected to be negligible for the high-k scattering diagnostic, as long as the scattering condition $\vec{k} \cdot \vec{B}$ is satisfied. The inclusion of a finite toroidal extent in the scattering volume and the exploration of 3D effects on turbulence scattering measurements could be the object of a future publication.

An additional approximation in the synthetic diagnostic is based on a constant-k: the same turbulence wavenumber is sampled within the whole simulation domain. In fact, the measurement wavenumber provided by ray-tracing calculations is only representative of the central ray of the input microwave beam (which is the one that contributes the most to the synthetic signal). A slightly different wavenumber is sampled by the diagnostic at different radial, poloidal and toroidal locations within the scattering volume. To assess the impact of this constant-k approximation, additional ray tracing calculations were performed for non-central rays within the scattering volume. These have shown that the measurement-k can at most vary $\sim 20\%$ within the scattering volume. This would have a small impact on the synthetic frequency and k-spectra characteristics when compared to other factors such as the simulation wavenumber resolution or Doppler shift, especially since the non-central rays which are associated to a different sampled k are filtered down with respect to the central ray, and produce smaller power contributions to the synthetic signal. However, it is possible that taking into account the spatial variation of k within the scattering volume could recover the underpredictions observed in the frequency spectral width in tables 6.3, 6.4.

All simulations presented here are based on the local approximation, representing only one flux surface, and background profiles are linear in the simulation domain. However it can be seen in figure 6-1 that the scattering volume has a finite radial extent, meaning the

high-k measurement has contributions from turbulence fluctuations present at different flux surfaces and subject to different turbulence drive terms. However here once more I can argue that it is the central flux surface containing the scattering location that will have the biggest contribution to the high-k spectra while turbulence fluctuation contributions from other nearby flux surfaces are filtered down and will likely have negligible contributions to the high-k signal. As can be seen from figure 6-1, the background temperature and density gradients have small profile variations within the scattering volume, which are in fact captured via the sensitivity scans in the background temperature and density gradients presented here. Global gyrokinetic simulation including profile variation would be able to give a more definite answer to confirm this hypothesis, however this was out of the scope of this work.

Within the realm of these approximations, I have reasonable confidence in the synthetic calculations presented. Additionally, as part of this work, two synthetic diagnostics for high-k scattering were implemented: one based on filtering in real space and an additional based on filtering in wavenumber space. These two synthetic diagnostic implementations, which are analytically equivalent, also produce the same synthetic spectra within small percentage variations (figure 5-10). This agreement further strengthens the confidence in the results shown.

Comments on the nonlinear gyrokinetic simulation models implemented

A substantial effort has been made in this work to include as many relevant physics processes as was reasonably possible within our computational constraints and availability of physics models implemented in the simulations: resolving ion to electron-scales with fully electromagnetic fluctuations, 3 kinetic species, background parallel and toroidal flow shear, etc. However, there is no question that there are missing physics processes not being directly modeled within this work that could potentially impact our conclusions. I have already discussed the potential importance of cross-scale interactions between electron-scale and ion-scale turbulence as well as profile variation, neither of which are modeled in this work. Concerning profile variation, past work performed for the weak ETG condition showed that global gyrokinetic simulation by the GTS code [115] predicts negligible electron thermal transport from ion-scale turbulence, similarly to what is observed when

using the experimental profile values as input. Additionally, nonlinear GYRO simulations did not include a fast ion population due to the small fast-ion pressure $\sim 10\%$ (but could have been included by user choice). This is understandable because the fast ion pressure with respect to the electron pressure is small, on the order to 10%. Negligible impacts from fast ion population are expected.

It is worth saying a few words with respect to the collisional model and high collisionality conditions in these plasmas ($\nu_{ei} \sim 1$ c$_s/a$), as well as the implementation in GYRO. Electron collisions were included in these simulations via a pitch angle scattering collision operator. Energy diffusion is not modeled in the collision operator, which could be relevant in these high collisionality conditions. Improved collisional models such as implemented in CGYRO [190] could be needed. Ion-ion collisions have also not been modeled in the present work. Although ion-ion collisions generally play a negligible effect on the predicted transport levels, they may become important in near marginal conditions and high collisionalities such as we observe for the weak ETG condition, as was suggested by past work [217–219, 221, 222]. Recent work using the CGYRO code [222] simulating ITG turbulence for the GA standard case has shown how the residual zonal flow potential calculated using the advanced Sugama collision operator can vary by close to an order of magnitude at high levels of electron collisionality (similar to those used here) with respect to the simpler Lorentz model implemented in GYRO. In fact, work presented on appendix G on these NSTX H-mode plasma conditions suggests ion-ion collisions could play an important role in determining the saturation of the zonal flow amplitude in conditions very close to the nonlinear threshold. Ion-ion collisions are shown to produce an additional damping mechanism on the zonal flow, which is weakened in near marginal conditions. This results in an increase of the ion-scale turbulence level when very close to the nonlinear threshold ($a/L_{Te} \sim 5$ in figures 6-6, 6-7), but not for far from threshold conditions. Overall, including ion-ion collision was shown to bring the effective nonlinear threshold of ion-scale turbulence closer to the experimentally detected base profile values, while still predicting a factor of 10 higher than the experimental levels within experimental uncertainty in $\nabla T, \nabla n$. Ion-ion collisions were shown to have small impact on electron-scale turbulence simulation. Since negligible thermal transport can be expected on the ion channel (owing to the neoclassical P_i values), these simulations point

to the same result: ETG is the dominant mechanism, able to explain P_e for the weak ETG condition.

In order to test the impact that a further improved collisional model could have on our conclusions, linear simulations with the CGYRO code were performed for the base case weak ETG condition, for which GYRO predicted stable ion-scale turbulence. Preliminary linear CGYRO simulations showed that the linear growth rates lied within 25% of the GYRO predictions. Corresponding ion-scale nonlinear CGYRO simulation showed ion-scale turbulence was suppressed by strong $E \times B$ shear, an identical prediction to the one made by GYRO. These tests having been performed, I have confidence to assert that the conclusions that one can draw by using improved collisional models will remain strictly the same as the ones presented here: near threshold behavior of ion-scale turbulence in the TEM-stable regime, while electron-scale turbulence is the dominant heat loss mechanism and cross-scale interactions possibly important. I am greatly thankful to Dr. J. Candy for carrying out the corresponding CGYRO simulations.

7.3 Next steps

In addition to the contributions presented in this chapter, this thesis has highlighted and left open questions that motivate future work.

The validation study presented here has made extensive use of the high-k scattering fluctuation data to place strict constraints on the gyrokinetic simulation models, specifically on electron-scale simulation models. However, no specific experimental measurement of ion-scale turbulence or zonal flows are used in this study, leaving them fully unconstrained in this work. Additional fluctuation measurements would be needed to constrain ion-scale simulations. In fact, this work highlights the possibility that ion-scale fluctuations could have an important role to play, specifically for the weak ETG condition. Low-k fluctuation measurements, such as provided by beam emission spectroscopy (BES), as well as fluctuation scattering diagnostics sensitive to low-k and intermediate range wavenumbers like doppler back-scattering (DBS) and reflectometry would provide invaluable information to constrain our turbulence models at all relevant scales characteristic of microturbulence fluctuations. This would be highly relevant noting the

recent interest in pursuing multi-scale simulation in some C-Mod, DIII-D and AUG plasmas [72–76, 223].

Zonal flow fluctuation measurements could also provide critical constraints on the turbulence models, as has previously been shown via Doppler reflectometry measurements [226]. The zonal flow is a special actor contributing to the ultimate saturation amplitude of turbulence fluctuations in some regimes. Constraining the zonal flow amplitude could be especially important in the weak ETG condition predicting large zonal flow amplitudes by GYRO. Constraining the zonal flow amplitude in zonal-flow dominated $vs.$ turbulence dominated regimes could be a meaningful contribution to the understanding of the zonal flow / electron-scale / ion-scale turbulence paradigm. Constraining the zonal flow amplitude could additionally be critical test to the advanced collisional models recently developed in gyrokinetic codes such as CGYRO [222], valid in high collisionality regimes characteristic of spherical tokamaks as well as in the tokamak pedestal. Recent efforts have shown how advanced collision operators such as the Sugama operator [225] can produce residual-flow fluctuation potential exhibiting close to an order of magnitude difference with respect to the simpler Lorentz collision operator (GYRO) through the inclusion of ion-ion collisions in the Sugama model. Future work could combine multiscale simulation with turbulence fluctuation measurements and ion and electron scales as well as measurements of the zonal flow.

Additionally, measurements of internal magnetic field fluctuations via cross polarization spectroscopy (CPS) would prove extremely valuable to diagnose the microtearing and KBM modes destabilized at high-β. Both modes are expected to play an important role in future high performance tokamak plasmas in the inner core (KBM) as well as in the pedestal (KBM and MT). KBMs are also predicted to couple to Alfvén eigenmodes, as suggested by nonlinear gyrokinetic simulation of JET plasmas [227–229] as well as some initial scoping studies in high-performance NSTX plasmas [230]. Detailed understanding of the KBM mode could be gained both from first-principles gyrokinetic simulation and quantitative comparisons of magnetic field fluctuations to cross-polarization scattering measurements (CPS). The pedestal region would be a likely candidate to direct high-k scattering measurements to assess the role of ETG, as well as CPS measurements allowing assessment of the role of the MT and KBM mode in the pedestal. In MAST-U, electron-

scale turbulence studies and comparisons with DBS measurements should also be pursued in the future, both in the core-gradient region, as well as in the inner core and in the more unexplored pedestal region.

Several arguments presented here have pointed to multiscale simulation as a possible future avenue emanating from this work. To my knowledge no successful attempt has been made to carry out multiscale simulation of spherical tokamak plasma. Past work performed for C-Mod L-mode discharge showed how cross-scale coupling became important when ion-scale turbulence was near marginal - similarly to the weak ETG condition analyzed here. Operating at different parametric regimes, typically at higher β, increased shaping and higher toroidal rotation than standard tokamaks, multiscale simulation of spherical tokamak differs from current multiscale simulation efforts. Coupling multiscale simulation with fluctuation measurements and synthetic diagnostics would be critical towards determining the conditions required for multiscale simulation and the subsequent contributions to electron thermal transport in the ST. Additionally, owing to the large normalized value of the ion gyro-radius $\rho_\star$, it could be that global, multi-scale simulation including profile variation is required in an ST, representing even a greater computational challenge.

If the ultimate goal is to predict electron thermal transport and consequently the equilibrium plasma profiles of future high performance plasmas and fusion reactors, further emphasis should be placed on predictive transport simulations coupled with reduced transport models such as TGLF. This work has shown both the great value as well as cost of performing first-principles gyrokinetic simulations. Reduced transport models are, by nature, much less computationally intensive. Developing reduced transport models accurate to the high beta, high flow and low-aspect ratio ST regime should be a main research priority of future confinement studies in the ST. Additionally, a natural next step would be to couple TGLF to a synthetic high-k diagnostic, guiding the development of more sophisticated gyrokinetic simulations. Together, these efforts would drive the prediction and optimization of the performance of future fusion reactors.

Appendix A

Basics of coherent scattering theory for density fluctuation measurements

In this appendix we present a succinct derivation of the spectral power density $S(\vec{k}_+, \omega)$, directly related to the total scattered power. The formulas derived are relatively standard, but are presented here in the context of coherent scattering turbulence measurements with the idea of having a complete reference equations in one same place. The expression of the spectral density derived here is the starting point of the synthetic diagnostic implementation.

A.1 Scattered electric field from an ensemble of electrons

The basic principles behind scattering of electromagnetic waves by plasmas rely on the radiation field of accelerated electrons by a laser or microwave field. Plasma electrons are accelerated by the electric field of the incoming electromagnetic wave, and in turn radiate electromagnetic energy in the form of a radiation field. Ions, in turn, are also accelerated by the incoming electric field, but due to their heavier mass are only accelerated a factor of m_e/m_i with respect to the electron's acceleration and contribute only negligibly to the scattered electric field. We will only focus in these notes to the scattering contribution from electrons. In this paragraph we construct the expression of the radiation electric field from a plasma characterized by density fluctuations δn_e. We start by calculating the contribution from an individual electron. We note the scattered electric field at location $\vec{R}$

and time at observer t, produced by one electron j, as $\vec{E}_{s,j}(\vec{R},t)$

$$\vec{E}_{s,j}(\vec{R},t) = -\frac{e}{Rc}\hat{s}\times(\hat{s}\times\dot{\vec{\beta}}_j(t')) \tag{A.1}$$

In this expression, $\vec{R}$ is the vector from the origin to observer and $R = |\vec{R}|$ is the physical distance from the origin to the observer, e is the electron charge, c is the speed of light, $\hat{s}$ is the unit vector along the scattering direction to observer, and $\dot{\vec{\beta}}_j = \dot{\vec{v}}_j/c$ is the acceleration of electron j normalized by the speed of light. Electrons are accelerated by an electromagnetic field of pulsation ω_i which is much higher than any typical plasma frequency ($\omega_{pe}, \omega_{ce}, ...$), and wave-vector $\vec{k}_i$. Thus, on the time scale associated to the incident wave field, the plasma is stationary, and we can express the acceleration of electron j by

$$\dot{\vec{\beta}}_j = -\frac{e}{m_e c}\vec{E}_i(\vec{r_j}',t') \tag{A.2}$$

where $\vec{E}_i(\vec{r_j}',t')$ is the incident wave field at the location of electron j and m_e is the electron mass. The incident wave field $\vec{E}_i$ can in turn be written as

$$\vec{E}_i(\vec{r_j}',t') = \vec{E}_{i0}(\vec{r_j}')cos(\vec{k}_i.\vec{r_j}' - \omega_i t') \tag{A.3}$$

Here $\vec{r_j}'(t')$ refers to the location of the jth electron with respect to the origin, $\vec{r_j}(t')$ refers to distance between electron j and the observer ($cf.$ Fig. A-1); t corresponds to the time measured at the observer, and t' corresponds to a retarded time, or time measured at the particle position. The difference between t and t' is the time taken by the scattered light to propagate from electron j to the observer. Each electron j has a time associated with it, t' that can be related to t (time at the observer) by

$$t' = t - \frac{|\vec{r}_j|}{c} = t - \frac{|\vec{R}(t) - \vec{r_j}'(t')|}{c} \approx t - \frac{|\vec{R}| - \hat{s}\cdot\vec{r_j}'(t')}{c} \tag{A.4}$$

Plugging in expression A.2 into A.1, using expression A.3, we arrive at the expression of the scattered electric field from electron j

$$\vec{E}_{s,j}(\vec{R},t') = \frac{e^2}{Rmc^2}\hat{s}\times(\hat{s}\times\hat{E}_i(\vec{r_j'},t')) \tag{A.5}$$

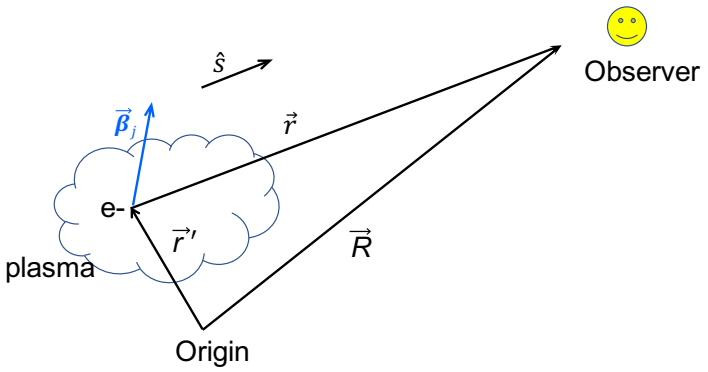

Figure A-1: Scattering geometry

Integrating over the whole region where electrons are accelerated by the wave field (the scattering volume), we arrive at the total electric field due to an electron density fluctuation $\delta n(\vec{r'}, t')$

$$\vec{E}_s(\vec{R}, t') = \frac{r_0}{R} Re \int_{V_s} d^3\vec{r'}\, \delta n(\vec{r'}, t')[\hat{s} \times (\hat{s} \times \vec{E}_{i0}(\vec{r'}))] e^{i(\vec{k_i}\cdot\vec{r'} - \omega_i t')} \tag{A.6}$$

where Re denotes the real part of the integral (δn is a real quantity), $r_0 = \frac{e^2}{m_e c^2}$ is the classical electron radius and V_s is the scattering volume.

In expression A.6, we note that the scattered electric field is a real quantity falling off with distance as $1/R$, consistent with a scattered power dependence as $1/R^2$. In addition, this expression shows that the scattered electric field has two basic components. One, a fast component, the electromagnetic wave produced by the incident microwave beam $e^{i(\vec{k_i}\cdot\vec{r'} - \omega_i t')}$. Two, a slow component, given by the fluctuation of the electron density $\delta n(\vec{r'}, t')$. The total scattered electric field is indeed a combination of two these two components. It is the slow component that provides the ultimate information we want to extract from a coherent scattering experiment.

We can write the incident electric field spatial envelope $\vec{E}_{i0}(\vec{r'})$ as $\vec{E}_{i0}(\vec{r'}) = \vec{E}_0 U(\vec{r'})$, where $\vec{E}_0$ contains the amplitude and unit of the incident electric field and U contains the spatial shape of the incident electric field into the plasma. $U(\vec{r'})$ essentially determines the shape of the scattering volume, dictated by the shape of the incident microwave beam, which is generally modeled to be Gaussian. We will refer to U as the filter of fluctuations in real space.

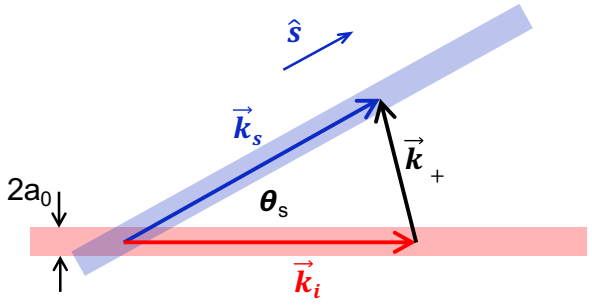

Figure A-2: Schematic of incident $\mathbf{k}_i$, scattered $\mathbf{k}_s$ and plasma wave-vector $\mathbf{k}_+$, corresponding to a conservation law of type $\mathbf{k}_+ = \mathbf{k}_s - \mathbf{k}_i$. The incident beam of radiation has a $1/e^2$ radius of a_0. The intersecting volume between the incident and the scattered beams is called the scattering volume V_s.

Consider a beam of incident electromagnetic waves with wave vector $\vec{k}_i$ and angular frequency ω_i into a plasma with electron density fluctuations $\delta n(\vec{r'}, t')$. As the electromagnetic waves propagate in the plasma, they are scattered in all directions. Consider a scattered direction of radiation given by $\hat{s}$, which defines a scattered 'beam' of radiation with wave number $\vec{k}_s$ and angular frequency ω_s. We are interested to know what is the power that is scattered from the plasma P_s with respect to the incident power of radiation P_i. The derivation of the scattered power from electron density fluctuations follows closely that presented in H.K. Park's thesis (ref. [216]), and outlined in section A.3 for reference.

We can further simplify equation A.6 to be

$$\vec{E}_s(\vec{R}, t') = \frac{r_0}{R} Re \int_{V_s} d^3\vec{r'}\, \delta n(\vec{r'}, t')[\hat{s} \times (\hat{s} \times \vec{E}_0)]U(\vec{r'})e^{i(\vec{k}_i \cdot \vec{r'} - \omega_i t')}$$

$$\approx \frac{r_0}{R}[\hat{s} \times (\hat{s} \times \vec{E}_0)]Re \int_{V_s} d^3\vec{r'}\, \delta n(\vec{r'}, t')U(\vec{r'})e^{i(\vec{k}_i \cdot \vec{r'} - \omega_i t')} \tag{A.7}$$

where we have taken $[\hat{s} \times (\hat{s} \times \vec{E}_0)]$ out of the integral sign, based on the far-field approximation: the extent of the scattering volume, over which the integration is carried out, is very small compared to the distance from the scattered volume to the detector ($cf.$ Fig. A-1). As a rough estimate, one can express this as $(V_s)^{1/3}/R << 1$.

From $\delta n(\vec{r'}, t')$ and $U(\vec{r'})$ we can define the following quantities:

$\vec{k}_+ = \vec{k}_s - \vec{k}_i$ Conservation law of wavenumber (momentum)

$\omega = \omega_s - \omega_i$ Conservation law of frequency (energy)

$\vec{k}_s = \frac{\omega_s}{c}\hat{s}$ Relation between $\vec{k}_s$ and ω_s

$t' = t - \frac{|\vec{R}|}{c} + \frac{\hat{s}\cdot\vec{r'}}{c}$ Relation between retarded time (at particle) t' and the time at observer t

$\delta n(\vec{k}, t') = \int d^3\vec{r'}\delta n(\vec{r'}, t')e^{-i\vec{k}\cdot\vec{r'}}$ Fourier transform in space of $\delta n_e(\vec{r'}, t')$

$\delta n(\vec{k}, \omega) = \int d^3\vec{r'}\int dt'\delta n(\vec{r'}, t')e^{i(\omega t' - \vec{k}\cdot\vec{r'})}$ Fourier transform in space and time of $\delta n_e(\vec{r'}, t')$

$I(\vec{k} - \vec{k}_+) = \int_{V_s} d^3\vec{r'}U(\vec{r'})e^{i(\vec{k}-\vec{k}_+)\cdot\vec{r'}}$ Filter in wavenumber space, or k-filter of fluctuations

$\delta n_{\mathrm{u}}(\vec{k}_+, t') = \frac{1}{(2\pi)^3}\int d^3\vec{k}\ \delta n(\vec{k}, t')I(\vec{k} - \vec{k}_+)$ Synthetic time signal of electron density fluctuations

$\delta n_{\mathrm{u}}(\vec{k}_+, \omega) = \frac{1}{(2\pi)^3}\int d^3\vec{k}\ \delta n(\vec{k}, \omega)I(\vec{k} - \vec{k}_+)$ Synthetic frequency signal of electron density fluctu

(A.8)

These definitions will be used in the following sections to express the scattered power from plasma turbulent fluctuations, as well as to define the spectral density $S(\vec{k}_+, \omega)$ in section A.3.

A.2 Computation of synthetic signal without the specification of geometry

We will see in this section how we can express the scattered electric field from electron density fluctuations $\delta n(\vec{r'}, t')$ as a function of the synthetic time signal of electron density fluctuations $\delta n_{\mathrm{u}}(\vec{k}_+, t')$. This latter quantity can be computed in two different ways: in

Fourier space, the traditional way in which we interpret scattered signals, and in real space, which contributes an alternate and equivalent way to interpret scattered signals. Both methods of computing synthetic signals have advantages and disadvantages, as will be discussed.

A.2.0.1 Traditional formulation: filtering in k-space

In section 6.1 we found that the scattered electric field can be expressed as:

$$\vec{E}_s(\vec{R},t') \approx \frac{r_0}{R}[\hat{s}\times(\hat{s}\times\vec{E}_0)]Re\int_{V_s} d^3\vec{r'}\;\delta n(\vec{r'},t')U(\vec{r'})e^{i(\vec{k_i}\cdot\vec{r'}-\omega_i t')} \tag{A.9}$$

We start by expressing $\delta n(\vec{r'},t')$ and $U(\vec{r'})$ in Fourier space, in terms of $\delta n(\vec{k},\omega)$ and $I(\vec{k}-\vec{k}_+)$.

$$\delta n(\vec{r'},t') = \frac{1}{(2\pi)^4}\int d\omega \int d^3\vec{k}\;\delta n(\vec{k},\omega)e^{-i(\omega t'-\vec{k}\cdot\vec{r'})} \tag{A.10}$$

Using the expression of the retarded time t', $\vec{k}_+ = \vec{k}_s - \vec{k}_i$, and $\omega = \omega_s - \omega_i$ we find

$$\vec{E}_s(\vec{R},t') \approx \tfrac{r_0}{R}[\hat{s}\times(\hat{s}\times\vec{E}_0)]Re\textstyle\int_{V_s} d^3\vec{r'}\;\delta n(\vec{r'},t')U(\vec{r'})e^{i(\vec{k_i}\cdot\vec{r'}-\omega_i t')}$$

$$\approx \tfrac{r_0}{R}[\hat{s}\times(\hat{s}\times\vec{E}_0)]Re\textstyle\int_{V_s} d^3\vec{r'}\Big(\frac{1}{(2\pi)^4}\int d\omega\int d^3\vec{k}\;\delta n(\vec{k},\omega)e^{-i(\omega t'-\vec{k}\cdot\vec{r'})}\Big)U(\vec{r'})\;e^{i(\vec{k_i}\cdot\vec{r'}-\omega_i t')}$$

$$\approx \tfrac{r_0}{R}[\hat{s}\times(\hat{s}\times\vec{E}_0)]Re\tfrac{1}{(2\pi)^4}\int d\omega\int d^3\vec{k}\;\delta n(\vec{k},\omega)e^{-i\omega_s(t-R/c)}\textstyle\int_{V_s} d^3\vec{r'}U(\vec{r'})e^{-i\frac{\hat{s}\cdot\vec{r'}}{c}\omega_s}e^{i(\vec{k}+\vec{k}_i)\cdot\vec{r'}} \tag{A.11}$$

Note that $\frac{\omega_s}{c}\hat{s} = \vec{k}_s$, and $e^{-i\omega_i(t-R/c)}$ is a global phase in the full expression, it can be taken outside the integral, thus

$$\vec{E}_s(\vec{R},t') \approx \frac{r_0}{R}[\hat{s}\times(\hat{s}\times\vec{E}_0)]Re\frac{1}{(2\pi)^4}\int d\omega\int d^3\vec{k}\;\delta n(\vec{k},\omega)e^{-i\omega_s(t-R/c)}\int d^3\vec{r'}U(\vec{r'})e^{i(\vec{k}-\vec{k}_+)\cdot\vec{r'}}$$

$$\approx \frac{r_0}{R}[\hat{s}\times(\hat{s}\times\vec{E}_0)]\frac{1}{(2\pi)^4}Re\left(e^{-i\omega_i(t-R/c)}\int d\omega\int d^3\vec{k}\;\delta n(\vec{k},\omega)I(\vec{k}-\vec{k}_+)e^{-i\omega(t-R/c)}\right)$$

$$\approx \frac{r_0}{R}[\hat{s}\times(\hat{s}\times\vec{E}_0)]\frac{1}{(2\pi)}Re\left(e^{-i\omega_i(t-R/c)}\int d\omega\;\delta n_{\mathrm{u}}(\vec{k}_+,\omega)e^{-i\omega(t-R/c)}\right)$$

(A.12)

In this expression, $I(\vec{k}-\vec{k}_+)$ is effectively the filter in wavenumber space applied to the fluctuation density spectrum $\delta n(\vec{k},\omega)$ ($cf.$ equation A.8). We can think of the synthetic signal as a sum over all turbulence wavenumber contributions around the detected wavenumber $\vec{k}_+$, with a filter $I(\vec{k}-\vec{k}_+)$ applied to the wavenumber spectrum of fluctuations. This is the traditional way in which we interpret scattered signals from scattering experiments. Knowing this we arrive to the final expression of the scattered electric field

$$\vec{E}_s(\vec{R},t) \approx \frac{r_0}{R}[\hat{s}\times(\hat{s}\times\vec{E}_0)]Re\left(e^{-i\omega_i(t-R/c)}\delta n_{\mathrm{u}}(\vec{k}_+,t-R/c)\right) \tag{A.13}$$

We read explicitly from this last expression two spectral contributions to the scattered electric field: a fast contribution, $e^{-i\omega_i(t-R/c)}$, and a slow contribution, $\delta n_{\mathrm{u}}(\vec{k}_+,t-R/c)$. The fast contribution comes from the radiation field of accelerated electrons by the incident electromagnetic field of the microwave beam at a fast frequency ω_i. As the microwave beam propagates in the plasma, electrons are accelerated at the frequency ω_i, which is precisely the frequency at which they radiate. In turn, the slow contribution $\delta n_{\mathrm{u}}(\vec{k}_+,t-R/c)$ originates from the electron density fluctuations in the plasma. Note that, as we expect, both contributions to the scattered electric field $\vec{E}_s(\vec{R},t)$ are taken at a retarded time $t-R/c$.

$|\vec{R}|/c$ is effectively the time it takes light to propagate from the scattered volume to the observer. Assuming that $|\vec{R}| \approx 1$ m, we have $R/c \approx 3\cdot 10^{-9}$ s. We want to compare this time with a typical turbulence time scale. Knowing that $c_s/a \approx 2\cdot 10^5 s^{-1}$, we conclude that it takes light $\approx 6\cdot 10^{-4} a/c_s$ to propagate to the observer, which is smaller than typical time scales of electron turbulence. From this we can conclude that

$\delta n_{\mathrm{u}}(\vec{k}_+, t-R/c) \approx \delta n_{\mathrm{u}}(\vec{k}_+, t)$. In practice, we will not make a distinction between $t-R/c$ and t.

A.2.0.2 Equivalent formulation: filtering in real space

In the previous section we saw how to express the scattered electric field $\vec{E}_s(\vec{R}, t)$ as a function of the synthetic time signal of electron density fluctuations $\delta n_{\mathrm{u}}(\vec{k}_+, t)$, itself expressed in terms of its Fourier components $\delta n(\vec{k}, \omega)$. In this section, we express this synthetic signal in terms of its real space components. We start once more from formula A.7, and we use the expression for the retarded time t', $\vec{k}_+ = \vec{k}_s - \vec{k}_i$, $\omega = \omega_s - \omega_i$, and $\delta n(\vec{r'}, \omega)$

$$
\begin{aligned}
&\vec{E}_s(\vec{R}, t') \approx \tfrac{r_0}{R}[\hat{s} \times (\hat{s} \times \vec{E}_0)] Re \int_{V_s} d^3\vec{r'}\, \delta n(\vec{r'}, t') U(\vec{r'}) e^{i(\vec{k}_i \cdot \vec{r'} - \omega_i t')} \\
&\approx \tfrac{r_0}{R}[\hat{s} \times (\hat{s} \times \vec{E}_0)] Re \int_{V_s} d^3\vec{r'} \left(\tfrac{1}{2\pi} \int d\omega\, \delta n(\vec{r'}, \omega) e^{-i\omega t'} \right) U(\vec{r'}) e^{i(\vec{k}_i \cdot \vec{r'} - \omega_i t')} \\
&\approx \tfrac{r_0}{R}[\hat{s} \times (\hat{s} \times \vec{E}_0)] Re \left\{ e^{-i\omega_i (t-R/c)} \int_{V_s} d^3\vec{r'}\, U(\vec{r'}) \tfrac{1}{2\pi} \int d\omega\, \delta n(\vec{r'}, \omega) e^{-i\omega(t-R/c)} e^{-i\omega_s \frac{\hat{s}\cdot\vec{r'}}{c}} e^{i\vec{k}_i \cdot \vec{r'}} \right\} \\
&\approx \tfrac{r_0}{R}[\hat{s} \times (\hat{s} \times \vec{E}_0)] Re \left\{ e^{-i\omega_i (t-R/c)} \tfrac{1}{2\pi} \int d\omega\, e^{-i\omega(t-R/c)} \left(\int_{V_s} d^3\vec{r'}\, U(\vec{r'}) \delta n(\vec{r'}, \omega) e^{-i\vec{k}_+ \cdot \vec{r'}} \right) \right\}
\end{aligned}
\tag{A.14}
$$

At this point, we note that the last integral under the parenthesis is simply the synthetic signal of fluctuations in frequency space $\delta n_{\mathrm{u}}(\vec{k}_+, \omega)$. One can easily show that

$$
\delta n_{\mathrm{u}}(\vec{k}_+, \omega) = \frac{1}{(2\pi)^3} \int d^3\vec{k}\, \delta n(\vec{k}, \omega) I(\vec{k} - \vec{k}_+) = \int_{V_s} d^3\vec{r'}\, \delta n(\vec{r'}, \omega) U(\vec{r'}) e^{-i\vec{k}_+ \cdot \vec{r'}} \tag{A.15}
$$

One can read from this expression that the synthetic signal of fluctuations $\delta n_{\mathrm{u}}(\vec{k}_+, \omega)$ is the integral over the scattering volume of the total electron density fluctuations $\delta n(\vec{r'}, \omega)$. It is only within the scattering volume, where the microwave beam is present, that we have contributions from electron density fluctuations. In addition, this expression can be

thought of as the Fourier component $\vec{k}_+$ of $\delta n(\vec{r'}, \omega)$, which is effectively the way we understand a scattering experiment, in terms of selection of a particular wavenumber, that we note here $\vec{k}_+$. However, note this time that we are interpreting the synthetic signal from analytical expressions in real space, and applying a filter in real space $U(\vec{r'})$. Moreover, note that A.15 is not quite the Fourier component $\vec{k}_+$ of the electron density fluctuations, due to the presence of the real space filter $U(\vec{r'})$. This means that the synthetic signal is not only composed by contributions from one lone wavenumber component $\vec{k}_+$, but from an array of wavenumbers that are close to $\vec{k}_+$, given by the spectral width of the filter $I(\vec{k} - \vec{k}_+)$. In fact, the spectral width of detected wavenumbers is encoded in $U(\vec{r'})$, indirectly through $I(\vec{k} - \vec{k}_+)$.

Expression A.15 is the nexus between two completely analogous ways of interpreting a synthetic scattering signal: a selection of wavenumbers in wavenumber space on one side, and an integration over the scattering volume on the other side. Note that the full information about the detected turbulence wavenumber $\vec{k}_+$ and the spectral width are preserved in computing $\delta n_{\mathrm{u}}(\vec{k}_+, \omega)$ in both ways. In the end, we find the expression for the scattered electric field

$$\begin{aligned} \vec{E}_s(\vec{R}, t) &\approx \tfrac{r_0}{R}[\hat{s} \times (\hat{s} \times \vec{E}_0)] Re \left\{ e^{-i\omega_i (t - R/c)} \tfrac{1}{2\pi} \int d\omega \, e^{-i\omega(t - R/c)} \delta n_{\mathrm{u}}(\vec{k}_+, \omega) \right\} \\ &\approx \tfrac{r_0}{R}[\hat{s} \times (\hat{s} \times \vec{E}_0)] Re \left(e^{-i\omega_i (t - R/c)} \delta n_{\mathrm{u}}(\vec{k}_+, t - R/c) \right) \end{aligned} \tag{A.16}$$

which is exactly the same expression as A.13.

A.3 Scattered power and spectral density

In this section we present the derivation of the full expression of the scattered power as a function of the incident power from the microwave beam. We start by considering the incident power from the incident electric field.

A.3.0.1 Incident power

As we explicited in formula A.3, the shape of the incident electric field is taken to be

$$\vec{E_i}(\vec{r'}, t') = \vec{E}_{i0}(\vec{r'})cos(\vec{k_i}.\vec{r'} - \omega_i t') = E_0 U(x', y')cos(k_i z' - \omega_i t')\ \hat{e} \tag{A.17}$$

where $\hat{e}$ is in the direction of the incident electric field ($cf.$ Fig. A-3). The scattered power is carried by the incident Poynting vector $\vec{\Pi}_i = \frac{c}{4\pi}\vec{E_i} \times \vec{B_i}$, which is effectively an incident power per unit surface. In turn, $\vec{B_i}$ can be computed from $\vec{E_i}$ by using Ampere's law $\vec{\nabla} \times \vec{E} = -\frac{1}{c}\frac{\partial \vec{B}}{\partial t}$. One finds

$$\vec{\Pi} = \frac{c}{4\pi}E_0^2 cos^2(k_i z' - \omega_i t')\ \hat{i} \tag{A.18}$$

where $\hat{i}$ is set by the propagation of the incident beam $\hat{i} = \vec{k_i}/k_i$, taken to be in the z' direction here ($cf.$ Fig. A-3). The x' and y' directions here are perpendicular to the incident beam. The time-averaged incident Poynting vector is $|\vec{\Pi}| = p_0 = \frac{c}{8\pi}E_0^2$.

Note this is simply the Poynting vector from a plane wave. We can treat the incident electric field as a plane wave under the assumption $k_i a_0 << 1$, where a_0 is determined by the extent of the incident microwave beam ($cf.$ Fig. A-3). In the scattering experiments presented here, $k_i = 2\pi/\lambda_i \approx 6 \cdot 10^3 \text{m}^{-1}$, and $a_0 \approx 3$ cm, thus $k_i a_0 \sim 100 - 200$, and this assumption is indeed well satisfied. This is in fact the diffraction approximation. We conclude that the incident microwave beam suffers negligible diffraction due to its finite extent. In practical terms, the shape of $U(\vec{r'})$ varies negligibly along the scattering volume. In the more general situation, one should consider the broadening of the perpendicular extent of the microwave beam as the beam propagates through the plasma, and one should have a spatially varying beam extent $a_0(z')$. In our case, we can assume to be fixed $a_0(z') = a_0 =$ const. within the scattering volume. This is well justified by the design of the high-k scattering diagnostic [65].

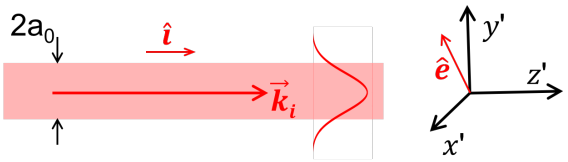

Figure A-3: Schematic of incident beam propagating in the $\hat{i}$ direction (z'). The x' and y' directions are perpendicular to the incident microwave beam. The incident beam of radiation has a $1/e^2$ radius of a_0.

A.3.0.2 Scattered power

We now turn to compute the expression of the scattered power P_s as a function of the electron density fluctuations. The detection of scattered power takes place at discrete points in time. Effectively, the detected scattered power at each discrete time point is the time-average over the time interval T, the sampling time: the time window between two consecutive time slices. We denote this time-average by $\langle . \rangle_T$. The expression of the scattered power is

$$p_s = \frac{c}{4\pi} \langle |\vec{E}_s(\vec{R}, t)|^2 \rangle_T \tag{A.19}$$

We note p_s the scattered power per unit surface, expressed in W/m^2, and P_s as the scattered power in W. Scattering measurements presented here were performed using 7.5 MS/s, and the corresponding sampling time is $T \approx 1.3 \cdot 10^{-7} s$. As we saw from formula A.13, the scattered electric field $\vec{E}_s(\vec{R}, t)$ has two differentiated time scales: a fast time scale associated to the incident microwave beam at $\omega_i = 2\pi \cdot 280$ GHz, and a slow time scale associated to the plasma electron turbulence fluctuations. We wish to know how T compares to these two time scales.

The fast time scale associated to ω_i is noted by t_w (wave time-scale), and $t_w = 2\pi/\omega_i \approx 3 \cdot 10^{-12}$ s. This time scale is indeed much faster than the sampling time T, and we expect the fast contribution $e^{-i\omega_i(t-R/c)}$ to $\vec{E}_s(\vec{R}, t)$ to be averaged out when integrated over T. On the other hand, we expect to capture the slow time-scale turbulence contribution to δn_u. The maximum detected turbulence frequency is given by the Nyquist frequency, here $\frac{1}{2T} \approx 4$ MHz. In comparison, the ion-cyclotron frequency $f_{ci} \approx 1/2\pi(eB/m_D)$ turns out to be also around 4 MHz at $B = 0.5\ T$. In practice, the

detected turbulence fluctuations in the scattering experiments presented here are smaller, on the order of $\approx$ 100 kHz$-$1 MHz. We conclude that we are able to capture the slow time-scales associated to electron scale turbulence using scattering experiments.

Turning back to the expression of the scattered power in equation A.19, at a given time slice we need to compute $\left\langle |\vec{E}_s(\vec{R},t)|^2 \right\rangle_T$. We have

$$|\vec{E}_s(\vec{R},t)|^2 = \vec{E}_s \cdot \vec{E}_s^* = \left(\frac{r_0}{R}\right)^2 |\hat{s}\times(\hat{s}\times\vec{E}_0)|^2 \left| \frac{\delta n_{\mathrm{u}}(\vec{k}_+,t_R)e^{-i\omega_i t_R} + \delta n_{\mathrm{u}}(\vec{k}_+,t_R)^* e^{i\omega_i t_R}}{2} \right|^2 \tag{A.20}$$

where we have noted the retarded time $t_R = t - R/c$. We now turn to carry out the time average of the scattered power over the sampling time T

$$\left\langle |\vec{E}_s(\vec{R},t)|^2 \right\rangle_T = \left(\frac{r_0}{R}\right)^2 |\hat{s}\times(\hat{s}\times\vec{E}_0)|^2 \frac{1}{T}\int_T dt \left\{ \frac{|\delta n_{\mathrm{u}}(\vec{k}_+,t_R)|^2}{2} + \frac{\delta n_{\mathrm{u}}(\vec{k}_+,t_R)^2 e^{-2i\omega_i t_R}}{4} + c.c. \right\} \tag{A.21}$$

where $c.c.$ denotes the complex conjugate of the latter term, having a $e^{-2i\omega_i t_R}$ dependence. In this situation, since $T >> t_w$, contributions from this last term to the integral average out to zero. Thus, at each time point of detection m ($cf.$ Fig. A-4), we have a discrete value of scattered power p_s given by

$$\begin{aligned} p_s(mT) &= \tfrac{c}{8\pi} E_0^2 \left(\tfrac{r_0}{R}\right)^2 |\hat{s}\times(\hat{s}\times\hat{e})|^2 \tfrac{1}{T} \textstyle\int_{(m-1/2)T}^{(m+1/2)T} dt |\delta n_{\mathrm{u}}(\vec{k}_+,t_R)|^2 \\ &= p_0 \left(\tfrac{r_0}{R}\right)^2 |\hat{s}\times(\hat{s}\times\hat{e})|^2 \left\langle |\delta n_{\mathrm{u}}(\vec{k}_+,t_R)|^2 \right\rangle_T \qquad [\mathrm{W/m^2}] \end{aligned} \tag{A.22}$$

where we have used the definition of the incident beam power p_0 and the unit vector along the scattered electric field $\hat{e}$ ($cf.$ Fig. A-3). From this formula, one can read that the detected scattered power p_s [W/m^2] at a discrete time point mT is given by the time average of the square amplitude of synthetic electron density fluctuation time signal $\delta n_{\mathrm{u}}(\vec{k}_+, t - R/c)$. The scattered power is factored by $(r_0/R)^2$, where r_0 is the classical electron radius and $R \sim 1$ m. This shows the small amplitude of the detected scattered power. The amplitude of the scattered power is also factored by a purely geometric term

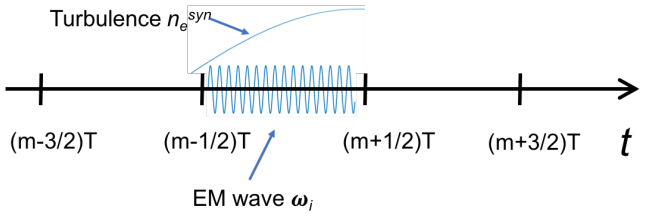

Figure A-4: Time axis showing schematic of time average during detection of scattered power from plasma density fluctuations. Fast time scales associated to EM wave propagation at ω_i are averaged out during detection, while slow time scales associated to plasma turbulence fluctuations δn_{u} are well preserved during measurement.

$|\hat{s} \times (\hat{s} \times \hat{e})|^2$ that depends on the direction of scattering ($cf.$ Fig. A-2).

A.3.0.3 Spectral density $S(\vec{k}_+, \omega)$

We now wish to express the total scattered power P_s (in [W]), as a function of the spectral density $S(\vec{k}_+, \omega)$. We define the spectral density $S(\vec{k}_+, \omega)$ as

$$S(\vec{k}_+, \omega) = \lim_{T\to\infty, V_s\to\infty} \frac{1}{TV_s} \left\langle \frac{|\delta n_{\mathrm{u}}(\vec{k}_+, \omega)|^2}{n_0} \right\rangle_T \tag{A.23}$$

and the total spectral density $S(\vec{k_+})$ as

$$S(\vec{k}_+) = \frac{1}{2\pi} \int d\omega S(\vec{k_+}, \omega) \tag{A.24}$$

Let's return to the expression of $\left\langle |\delta n_{\mathrm{u}}(\vec{k}_+, t_R)|^2 \right\rangle_T$. We have seen that at every discrete time point, we have

$$\left\langle |\delta n_{\mathrm{u}}(\vec{k}_+, t_R)|^2 \right\rangle_T = \frac{1}{T} \int_{-T/2}^{T/2} dt |\delta n_{\mathrm{u}}(\vec{k}_+, t_R)|^2 \tag{A.25}$$

by making use of Parseval's theorem, we have

$$\left\langle |\delta n_{\mathrm{u}}(\vec{k}_+, t_R)|^2 \right\rangle_T = \frac{1}{2\pi T} \int d\omega |\delta n_{\mathrm{u}}(\vec{k}_+, \omega)|^2 \tag{A.26}$$

In order to have this expression hold, we assumed $T >> \frac{1}{\omega' - \omega}$, where ω' and ω are frequencies of the fluctuating electrons within the scattering volume. This assumption means that we're filtering out all the fast electron motion associated to the incident elec-

tromagnetic wave frequency ω_i. To be more precise, in the limit $T \to \infty$, equation A.26 is exact. However, for a finite T, equation A.26 turns to be

$$\left\langle |\delta n_{\mathrm{u}}(\vec{k}_+, t_R)|^2 \right\rangle_T = \frac{1}{2\pi} \int d\omega \delta n_{\mathrm{u}}(\vec{k}_+, \omega) e^{-i\omega t_R} \frac{1}{2\pi} \int d\omega' \delta n_{\mathrm{u}}(\vec{k}_+, \omega')^* e^{i\omega' t_R} \operatorname{sinc} \frac{(\omega - \omega')T}{2} \tag{A.27}$$

which simplifies to A.26 in the limit $T >> \frac{1}{\omega' - \omega}$, as previously mentioned. In the end, we find

$$\frac{d^2 P_s}{d\omega dA_{det}}(mT) = \frac{dp_s}{d\omega}(mT) = \frac{P_0}{A_i} \frac{r_0^2}{R^2} |\hat{s} \times (\hat{s} \times \hat{e})|^2 \frac{n_0 V_s}{2\pi} S(\vec{k}_+, \omega) \tag{A.28}$$

Where dA_{det} is the detected beam area $A_{det} = R^2 d\Omega$ (Ω is the solid angle), P_0 is the incident beam power in W and A_i is the incident beam area $A_i = \pi a_0^2$.

The expression for the total scattered power is

$$\frac{d^2 P_s}{d\omega d\Omega} = \frac{P_0}{A_i} r_0^2 |\hat{s} \times (\hat{s} \times \hat{e})|^2 \frac{n_0 V_s}{2\pi} S(\vec{k}_+, \omega) \tag{A.29}$$

In terms of the total spectral density $S(\vec{k}_+)$ (integrated in frequency)

$$\frac{dP_s}{d\Omega} = \frac{P_0}{A_i} r_0^2 |\hat{s} \times (\hat{s} \times \hat{e})|^2 n_0 V_s \, S(\vec{k}_+) \tag{A.30}$$

A.3.0.4 Summary

We present here a summary of the formulas needed to achieve the final expression for the scattered power P_s

$$\delta n_{\mathrm{u}}(\vec{k}_+,t) = \int d^3\vec{r'} U(\vec{r'}) \delta n(\vec{r'},t) e^{-i\vec{k}_+\cdot\vec{r'}} = \frac{1}{(2\pi)^3}\int d^3\vec{k}\; I(\vec{k}-\vec{k}_+)\delta n(\vec{k},t)$$

$$\delta n_{\mathrm{u}}(\vec{k}_+,\omega) = \int dt\; \delta n_{\mathrm{u}}(\vec{k}_+,t) e^{i\omega t}$$

$$S(\vec{k}_+,\omega) = \frac{1}{TV_s}\left\langle \frac{|\delta n_{\mathrm{u}}(\vec{k}_+,\omega)|^2}{n_0} \right\rangle$$

$$S(\vec{k}_+) = \frac{1}{2\pi}\int d\omega S(\vec{k_+},\omega) \tag{A.31}$$

$$\frac{d^2P_s}{d\omega d\Omega} = \frac{P_0}{A_i} r_0^2 |\hat{s}\times(\hat{s}\times\hat{e})|^2 \frac{n_0 V_s}{2\pi} S(\vec{k}_+,\omega)$$

$$\frac{dP_s}{d\Omega} = \frac{P_0}{A_i} r_0^2 |\hat{s}\times(\hat{s}\times\hat{e})|^2 n_0 V_s\; S(\vec{k}_+)$$

Appendix B

Derivation of the wavenumber mapping to field-aligned geometry

In this section we present a derivation of the wavenumber mapping to field-aligned geometry. As a starting point, figure B-1 shows the reference geometry definitions in real space as well as in k-space that are used in this thesis.

In cylindrical coordinates (R, Z, φ), we define the wavenumber components (k_x, k_z, k_y) by

$$\begin{cases} k_x = -i\frac{\partial}{\partial R} & \text{along the major-radial direction} \\ k_z = -i\frac{\partial}{\partial Z} & \text{along the vertical direction} \\ k_y = -i\frac{1}{R}\frac{\partial}{\partial \varphi} & \text{along the toroidal direction} \end{cases} \tag{B.1}$$

Since we assume toroidal axisymmetry, we decide to pick our reference frame at a fixed toroidal angle $\varphi = 0$ as indicated in figure B-1. As was discussed in chapter 5, the geometric interpretation of $(k_x, k_y, k_z)_+$ and $(k_R, \varphi_k, k_Z)_+$ are shown in figure B-1.b). These wavenumber definitions are suitable for the present problem, since the wavenumber components $(k_{R+}, k_{Z+}, \varphi_{k+})$ do not vary in space. Additionally, note how the wavenumber components $(k_{R+}, k_{Z+}, \varphi_{k+})$ are cylindrical in k-space, but NOT in real space, ie. k_{R+} is the norm of $\vec{k}_+$ in the (x, y)-plane, namely $k_{R+} = \sqrt{k_{x+}^2 + k_{y+}^2}$, and does not generally correspond to the wavenumber component along the major radius direction.

Associated to the GYRO coordinates (r, θ, φ), and based on the GYRO/CGRYO decomposition of the fluctuating fields, GYRO defines the wavenumber components (k_r, k_θ,

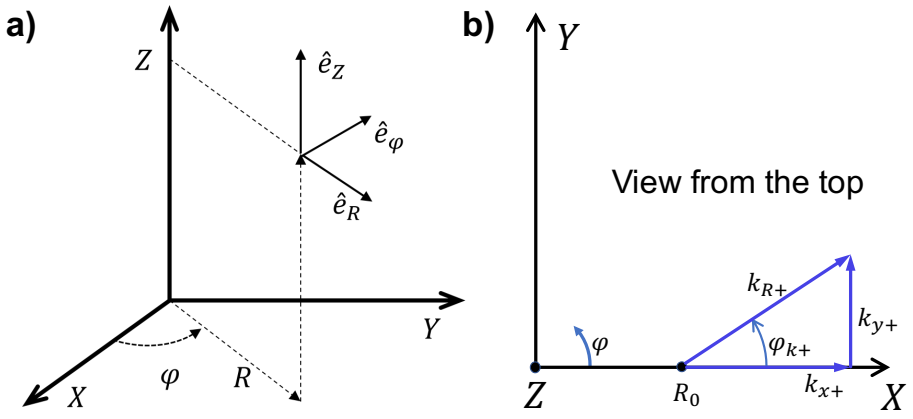

Figure B-1: **a)** Cylindrical coordinates (R, Z, φ) used to express density fluctuations amplitudes $\delta n(\vec{r}, t)$ for deployment of synthetic diagnostic in real space. **b)** Definitions of wavenumber $\vec{k}_+$ components in cartesian coordinates $(k_x, k_y, k_z)_+$ and in cylindrical coordinates $(k_R, k_Z, \varphi_k)_+$. Due to axisymmetry we assume a scattering location at $\varphi_0 = 0$.

k_φ) by

$$\begin{cases} k_r = \frac{2\pi p}{L} \\ k_\theta = \frac{nq}{r} \\ k_\varphi = -i\frac{1}{R}\frac{\partial}{\partial\varphi} \end{cases} \tag{B.2}$$

The radial wavenumber k_r is based on a Fourier decomposition of f in the radial coordinate. Note how $k_r \neq \frac{\partial}{\partial r}$, as we will soon see. The poloidal wavenumber k_θ is a flux surface quantity, independent of θ. The toroidal wavenumber k_φ has the same definition as in cylindrical coordinates, here $k_\varphi = -n/R$: thus note that $k_\varphi = k_y$, also consistent with figure B-1.b). With these definitions we now proceed to perform the wavenumber mapping from cylindrical coordinates (R, Z, φ) to GYRO coordinates (r, θ, φ). For a fixed toroidal mode number n and a fixed radial mode number p, we define the quantity $\mathrm{z}_{np}(r, \theta, \varphi, t) = \mathrm{f}_{np}(\theta, t)e^{-in(\varphi+\nu(r,\theta))}e^{i\frac{2\pi p}{L}r}$. With these definitions, we have

$$\begin{aligned} &\frac{\partial}{\partial r}\,\mathrm{z}_{np} = i\left(\frac{2\pi p}{L} - n\frac{\partial\nu}{\partial r}\right)\mathrm{z}_{np} \\ &\frac{1}{r}\frac{\partial}{\partial\theta}\,\mathrm{z}_{np} = \frac{1}{r}\left(\frac{\partial\log(\mathrm{f}_{np})}{\partial\theta} - in\frac{\partial\nu}{\partial\theta}\right)\mathrm{z}_{np} = -i\frac{n}{r}\frac{\partial\nu}{\partial\theta}\,\mathrm{z}_{np} \\ &\frac{1}{R}\frac{\partial}{\partial\varphi}\,\mathrm{z}_{np} = -i\frac{n}{R}\,\mathrm{z}_{np} \end{aligned} \tag{B.3}$$

the last equality simply showing the definition of $k_\varphi = k_y$. Note how $\partial\,\mathrm{f}_{np}/\partial\theta = 0$,

$\partial/\partial\theta$ only applies to the rapidly oscillating part of the fluctuations. We can make use of the chain rule relation to obtain

$$\begin{cases} \frac{\partial}{\partial r} = \frac{\partial R}{\partial r}\frac{\partial}{\partial R} + \frac{\partial Z}{\partial r}\frac{\partial}{\partial Z} + \frac{\partial \varphi}{\partial r}\frac{\partial}{\partial \varphi} = \frac{\partial R}{\partial r} ik_x + \frac{\partial Z}{\partial r} ik_z \\ \frac{\partial}{\partial \theta} = \frac{\partial R}{\partial \theta}\frac{\partial}{\partial R} + \frac{\partial Z}{\partial \theta}\frac{\partial}{\partial Z} + \frac{\partial \varphi}{\partial \theta}\frac{\partial}{\partial \varphi} = \frac{\partial R}{\partial \theta} ik_x + \frac{\partial Z}{\partial \theta} ik_z \end{cases} \tag{B.4}$$

combining B.3 and B.4, we have

$$\begin{cases} \frac{\partial}{\partial r}\,\mathrm{z}_{np} = i\left(k_r - n\frac{\partial \nu}{\partial r}\right)\mathrm{z}_{np} = i\left(\frac{\partial R}{\partial r}k_x + \frac{\partial Z}{\partial r}k_z\right)\mathrm{z}_{np} \\ \frac{1}{r}\frac{\partial}{\partial \theta}\,\mathrm{z}_{np} = -i\frac{n}{r}\frac{\partial \nu}{\partial \theta}\,\mathrm{z}_{np} = i\left(\frac{1}{r}\frac{\partial R}{\partial \theta}k_x + \frac{1}{r}\frac{\partial Z}{\partial \theta}k_z\right)\mathrm{z}_{np} \\ \frac{1}{R}\frac{\partial}{\partial \varphi}\,\mathrm{z}_{np} = -i\frac{n}{R}\,\mathrm{z}_{np} = i(k_y)\,\mathrm{z}_{np} \end{cases} \tag{B.5}$$

This relation being true for any arbitrary function z_{np}, we arrive to the GYRO wavenumber mapping relations, relating a measured wavenumber $\vec{k}_+$ with components $(k_x, k_y, k_z)_+$ (in the form typically issued by a ray-tracing code or equivalent) to the field-aligned components $(k_r, k_\theta, k_\varphi)_+$

$$\begin{cases} k_{r+} - \frac{r}{q}\frac{\partial \nu}{\partial r}k_{\theta+} = \frac{\partial R}{\partial r}k_{x+} + \frac{\partial Z}{\partial r}k_{z+} \\ -\frac{r}{q}\frac{\partial \nu}{\partial \theta}k_{\theta+} \quad = \frac{\partial R}{\partial \theta}k_{x+} + \frac{\partial Z}{\partial \theta}k_{z+} \\ k_{\varphi+} \qquad\qquad = k_{y+} \end{cases} \tag{B.6}$$

The reader will note how these three relations map only to two independent numbers: the toroidal mode number n and radial mode number p. Equation B.10 is thus overconstrained. It is also useful to define the mapping from $(k_x, k_y, k_z)_+$ to $(n^\theta_+, n^\varphi_+, p_+)$, which are in general not integers. This recovers formula 5.12 used in this thesis

$$\begin{cases} \frac{2\pi p_+}{L_r} - n^\theta_+\left.\frac{\partial \nu}{\partial r}\right|_0 = \left.\frac{\partial R}{\partial r}\right|_0 k_{x+} + \left.\frac{\partial Z}{\partial r}\right|_0 k_{z+} \\ -\left.\frac{n^\theta_+}{r_0}\frac{\partial \nu}{\partial \theta}\right|_0 \quad = \left.\frac{1}{r_0}\frac{\partial R}{\partial \theta}\right|_0 k_{x+} + \left.\frac{1}{r_0}\frac{\partial Z}{\partial \theta}\right|_0 k_{z+} \\ -\frac{n^\varphi_+}{R_0} \qquad\qquad = k_{y+} \end{cases} \tag{B.7}$$

Using these relations, given wavenumber components in cylindrical coordinates $(k_x, k_y, k_z)_+$, we can map them to the field-aligned wavenumber definitions $(k_r, k_\theta, k_\varphi)_+$ using B.10,

or equivalently to the mode number components $(n_+^\theta, n_+^\varphi, p_+)$ using B.7. Note how n_+^θ denotes a toroidal mode number mapped from a vertical component k_{z+}, while n_+^φ is a toroidal mode number mapped from a toroidal component k_{y+}. The in principle need not be equal to each other. However, as we will see in the next appendix, the condition for successful scattering $\vec{k} \cdot \vec{B} \approx 0$ is equivalent to $n_+^\theta \approx n_+^\varphi$.

These relations are the general wavenumber-mapping in full 3D geometry. In order to gain some intuition into B.10 and B.7, we present some approximations and limiting cases next.

Unshifted $s-\alpha$ geometry. In this situation we have $R(r,\theta) = R_0 + r\cos(\theta)$, $Z(r,\theta) = Z_0 + r\sin(\theta)$ and $\nu = -q\theta$, where R_0 and Z_0 are constants independent of r, thus

$$\begin{cases} k_{r+} + \hat{s}\theta\, k_{\theta+} = \cos(\theta)k_{x+} + \sin(\theta)k_{z+} \\ k_{\theta+} \qquad\qquad\quad = -\sin(\theta)k_{x+} + \cos(\theta)k_{z+} \\ k_{\varphi+} \qquad\qquad\quad = k_{y+} \end{cases} \tag{B.8}$$

These relations already show how fixed k_{x+}, k_{z+} values map to different $k_{r+}, k_{\theta+}$ depending on the poloidal location θ. Magnetic shear $\hat{s}$ also contributes importantly as one moves away from the outboard midplane. At the outboard midplane, this simplifies to $k_{r+} = k_{x+}, k_{\theta+} = k_{z+}$.

Shifted $s-\alpha$ geometry. In this situation the flux-surface values R_0 and Z_0 depend on r, thus

$$\begin{cases} k_{r+} + \hat{s}\theta\, k_{\theta+} = (\dfrac{dR_0}{dr} + \cos\theta)k_{x+} + (\dfrac{dZ_0}{dr} + \sin\theta)k_{z+} \\ k_{\theta+} \qquad\qquad\quad = -\sin(\theta)k_{x+} + \cos(\theta)k_{z+} \\ k_{\varphi+} \qquad\qquad\quad = k_{y+} \end{cases} \tag{B.9}$$

This time the term $\Delta = \frac{dR_0}{dr}$ related to the Shafranov shift is introduced, and the term $\frac{dZ_0}{dr}$ relating to the up-down asymmetry is also introduced. Unless specific up-down asymmetric configurations are used, the term $dZ_0/dr = 0$ in the tokamak core. At the outboard midplane, one thus finds $k_{r+} = (1 + \frac{dR_0}{dr})k_{x+}$, $k_{\theta+} = k_{z+}$. The Shafranov shift Δ is usually a negative quantity < 0. This relation shows how, for a fixed k_{x+},

Shafranov shift Δ produces a smaller k_{r+} with respect to the previous unshifted case. This can be understood by the compression of the flux-surfaces at the outboard midplane, which reduces the radial box-size at the outboard midplane and results in a smaller k_{r+} (thus longer wavelength) is that geometry frame. The opposite situation takes place at the inboard midplane $\theta = \pi$, where one finds a larger k_{r+} in the shifted flux-surface case with respect to the previous unshifted case, since flux-surface are now expanded outwards.

Shifted, elongated geometry. Now, in addition to shifted flux-surfaces from Shafranov shift, the flux surface are elongated. This corresponds to $R(r,\theta) = R_0(r) + r\cos(\theta)$, $Z(r,\theta) = Z_0 + r\kappa\sin(\theta)$, but this time ν has to be solved numerically. We have

$$\begin{cases} k_{r+} - \dfrac{r}{q}\dfrac{\partial\nu}{\partial r}k_{\theta+} = (\dfrac{dR_0}{dr} + \cos\theta)k_{x+} + (\dfrac{dZ_0}{dr} + \kappa\sin\theta)k_{z+} \\ -\dfrac{r}{q}\dfrac{\partial\nu}{\partial\theta}k_{\theta+} \quad = -r\sin(\theta)k_{x+} + r\kappa\cos\theta k_{z+} \\ k_{\varphi+} \quad = k_{y+} \end{cases} \tag{B.10}$$

which at the outboard midplane simplifies to $k_{r+} - \frac{r}{q}\frac{\partial\nu}{\partial r}k_{\theta+} = (1+\frac{dR_0}{dr})k_{x+}$, $-\frac{r}{q}\frac{\partial\nu}{\partial\theta}k_{\theta+} = r\kappa k_{z+}$.

These relations already show how fixed k_{x+}, k_{z+} values map to different $k_{r+}, k_{\theta+}$ depending on the poloidal location θ. Magnetic shear $\hat{s}$ also contributes importantly as one moves away from the outboard midplane. At the outboard midplane, this simplifies to $k_{r+} = k_{x+}, k_{\theta+} = k_{z+}$. Here note how a fixed k_{z+} value maps to larger $k_{\theta+}$ in the presence of elongation κ with respect to the non-elongated case. This can be explained via the flux-surface stretching at the outboard midplane due to κ. With finite elongation, the poloidal domain size is increased, thus a fixed wavelength in real space maps to a smaller wavelength in flux-surface geometry, thus a higher $k_{\theta+}$.

This last case of shifted, elongated geometry is yields very good agreement with the general mapping used in this thesis, specially for outboard midplane conditions. The effect of triangularity is shown to be negligible at the outboard midplane. The effect of squareness was not considered in this work, nor the case of updown asymmetric configurations.

Appendix C

Derivation of the scattering signal & comments on toroidal effects

In this appendix we show the derivation of the computation of the synthetic signal of density fluctuations $\delta n_{\mathrm{u}}(\vec{k}_+, t)$ in realistic flux-surface geometry. Written in cylindrical coordinates (R, Z, φ), the scattering signal expression (equation 5.5) is repeated here once more for reference

$$\delta n_{\mathrm{u}}(\vec{k}_+, t) = \int_{V_s} d^3\vec{r'}\, \delta n(\vec{r'}, t) U(\vec{r'}) e^{-i\vec{k}_+ \cdot \vec{r'}} = \int d\varphi R dR dZ \delta n(R, Z, \varphi, t) U(R\text{-}R_0, Z\text{-}Z_0, \varphi\text{-}\varphi_0) e^{-i\vec{k}_+ \cdot \vec{r}} \tag{C.1}$$

where $\vec{k}_+$ is the measurement wavenumber in a particular scattering experiment, assumed constant in time and space in this thesis. The scattering volume shape U is centered around (R_0, Z_0, φ_0), and has spatial extent $\sim (\Delta R, \Delta Z, \Delta\varphi)$. We place ourselves at the outboard midplane, thus assume $Z_0 \approx 0$ (but not exactly 0). Due to axissimetry, we choose a coordinate system in which we set the toroidal angle of scattering to $\varphi_0 = 0$. The quantities $\Delta R, \Delta Z, \Delta\varphi$ are much smaller than minor radius a but much greater than the corresponding wavelengths associated to $\vec{k}_+$. As we saw in chapter 5, the product $\vec{k}_+ \cdot \vec{r}$ needs to be computed in cylindrical coordinates. As an intermediate step, define the wavenumber components in cartesian coordinates $\vec{k}_+ = (k_x, k_y, k_z)_+$ as shown in figure B-1. In these coordinates, write the product $\vec{k}_+ \cdot \vec{r}$ as

$$\vec{k}_+ \cdot \vec{r} = Rk_{R+}\cos(\varphi\text{-}\varphi_{k+}) + Zk_{Z+}$$

where

$$\begin{aligned} k_{x+} &= k_{R+}\cos(\varphi_{k+}) \\ k_{y+} &= k_{R+}\sin(\varphi_{k+}) \\ k_{z+} &= k_{Z+} \end{aligned} \tag{C.2}$$

The cylindrical wavenumber components $(k_{R+}, k_{Z+}, \varphi_{k+})$ are appropriate since they do not vary in space. In fact, $(k_{R+}, k_{Z+}, \varphi_{k+})$ are cylindrical in k-space, but NOT in real space, ie k_{R+} is the norm of $\vec{k}_+$ in the (x, y)-plane, namely $k_{R+} = \sqrt{k_{x+}^2 + k_{y+}^2}$, and does not generally correspond to the wavenumber component along the major radius direction. For a given scattering wave-vector $\vec{k}_+$, we wish to know what are the 'mapped' toroidal and radial mode numbers n_+ and p_+ in GYRO that correspond to the measurement wavenumber $\vec{k}_+ = (k_x, k_y, k_z)_+$. The wavenumber mapping is repeated here once more for reference

$$\begin{cases} \dfrac{2\pi p_+}{L_r} - n_+^\theta \dfrac{\partial \nu}{\partial r}\bigg|_0 = \dfrac{\partial R}{\partial r}\bigg|_0 k_{x+} + \dfrac{\partial Z}{\partial r}\bigg|_0 k_{z+} \\ -\dfrac{n_+^\theta}{r_0}\dfrac{\partial \nu}{\partial \theta}\bigg|_0 = \dfrac{1}{r_0}\dfrac{\partial R}{\partial \theta}\bigg|_0 k_{x+} + \dfrac{1}{r_0}\dfrac{\partial Z}{\partial \theta}\bigg|_0 k_{z+} \\ -\dfrac{n_+^\varphi}{R_0} = k_{y+} \end{cases} \tag{C.3}$$

Recall all quantities computed here are local, given by the subscript 0. With these definitions in mind, we wish to compute the scattering signal δn_{u} from equation C.1. We start from expanding the real density field δn as a sum of toroidal and radial mode numbers n and p. In GYRO and CGYRO, we have $\delta n(r, \theta, \varphi, t) = \sum_{np} \delta n_{np}(\theta, t) e^{-in(\varphi+\nu)} e^{i2\pi p/L_r}$ (ignore here Doppler shift $\overline{\omega}_0$). Plugging into equation C.1, we find

$$\begin{aligned} &\delta n_{\mathrm{u}}(\vec{k}_+, t) \approx \sum_{n,p} U_{np}\delta n_{np}(\theta_0, t) \\ &\text{where } U_{np} \text{ is defined by} \\ &U_{np} = \int d^3\vec{r} U(\vec{r}) e^{\text{-}in\alpha} e^{i2\pi pr/L_r} e^{\text{-}i\vec{k}_+\cdot\vec{r}} \end{aligned} \tag{C.4}$$

and have assumed slowly varying $\delta n_{np}(\theta_0, t)$ in θ. At the outboard midplane it is reasonable to assume a scattering volume envelope to be separable in (R, Z, φ), such as

$U(R, Z, \varphi) \approx \Psi_R(R\text{-}R_0)\Psi_Z(Z\text{-}Z_0)\Psi_\varphi(\varphi)$. Now the scattering signal δn_{u} can be written as separate integrals over R, Z, and φ as

$$\begin{aligned} \delta n_{\mathrm{u}} &= \int dRdZ e^{-iZk_{z+}} \Psi_R \Psi_Z \sum_n e^{-in\nu} \delta n_n(r, \theta, t) I_{n^\varphi} \\ &\text{where} \\ I_{n^\varphi} &= R \int d\varphi \Psi_\varphi e^{-in\varphi} e^{-iRk_{R+}\cos(\varphi - \varphi_{k+})} \end{aligned} \tag{C.5}$$

where we used expression C.2 for $\vec{k}_+ \cdot \vec{r}$. Since we assume a localized measurement in φ, the $\cos$ term in the exponent can be expanded about $\varphi \approx 0$, leading to

$$\begin{aligned} \cos(\varphi - \varphi_{k+}) &\approx (1 - \varphi^2/2)\cos(\varphi_{k+}) + \varphi \sin(\varphi_{k+}) \\ &\text{thus} \\ Rk_{R+}\cos(\varphi - \varphi_{k+}) &\approx Rk_{x+}(1 - \varphi^2/2) + Rk_{y+}\varphi \end{aligned} \tag{C.6}$$

where we used equation the k_{x+}, k_{y+} definitions in equation C.2. Using this expansion, the integral I_{n^φ} can then be written as

$$\begin{aligned} I_{n^\varphi} &\approx e^{-iRk_{x+}} \Psi_{n^\varphi}(n\text{-}n_+^\varphi) \\ &\text{where} \\ \Psi_{n^\varphi}(n\text{-}n_+^\varphi) &\approx R_0 \int d\varphi \Psi_\varphi e^{i(\varphi^2/2)Rk_{x+}} e^{-i\varphi(n - n_+^\varphi)} \end{aligned} \tag{C.7}$$

We assumed $R \approx R_0$ in Ψ_n^φ due to the slow spatial dependence on (r, θ), and we made use of the wavenumber mapping C.3. The expression for Ψ_{n^φ} is nothing but a Gaussian integral, which is relatively standard to compute, and leads to

$$\begin{aligned} \Psi_{n^\varphi}(n\text{-}n_+^\varphi) &\approx R_0 \left(\frac{4\pi}{(\Delta n_\varphi)^2} \right)^{1/2} e^{-(n\text{-}n_+^\varphi)^2/(\Delta n_\varphi)^2} \\ &\text{with} \\ (\Delta n_\varphi)^2 &= 4/\Delta\varphi^2\text{-}2iR_0k_{x+} \end{aligned} \tag{C.8}$$

Here the toroidal mode number resolution Δn_φ is complex in nature, and depends on the relative ratio between the toroidal extent of the scattering volume $\Delta\varphi$ and the x component of the sampled wavenumber $R_0 k_{x+}$. The ratio between these two quantities

is dependent on the specific scattering experiment and geometry, thus would have to be analyzed case by case. Now the scattering signal δn_{u} can be written as

$$\delta n_{\mathrm{u}} = \int dRdZe^{-iZk_{z+}}e^{-iRk_{x+}}\Psi_R\Psi_Z\sum_n e^{-in\nu}\delta n_n(r,\theta,t)\Psi_{n^\varphi}(n-n_+^\varphi) \tag{C.9}$$

The complex exponential part in δn_{u} can also be expanded about $(r,\theta) \approx (r_0,\theta_0)$, leading to

$$Rk_{x+} + Zk_{z+} + n\nu \approx [\text{phase}] - r[k_r^{\mathrm{loc}} - k_{r+}^{\mathrm{loc}}] - r_0\theta[k_\theta^{\mathrm{loc}} - k_{\theta+}^{\mathrm{loc}}] + n\left[\nu_0 - r_0\frac{\partial\nu}{\partial r}\Big|_0 - \theta_0\frac{\partial\nu}{\partial\theta}\Big|_0\right] \tag{C.10}$$

where we have introduced $k_\theta^{\mathrm{loc}} = -\frac{n}{r}\frac{\partial\nu}{\partial\theta}$ and $k_r^{\mathrm{loc}} = k_r - n\frac{\partial\nu}{\partial r}$ only for easiness of notation in C.10. As was shown in chapter 5, we can also expand (R,Z) about (r_0,θ_0) in the expressions for Ψ_R, Ψ_Z, leading to

$$\begin{aligned}
&U(R,Z,\varphi) \approx \Psi_r(r\text{-}r_0)\Psi_\theta(\theta\text{-}\theta_0)\Psi_\varphi(\varphi)\\
&\text{with}\\
&\Psi_r(r\text{-}r_0) = \exp[\text{-}(r\text{-}r_0)^2/\Delta r^2]\\
&\Psi_\theta(\theta\text{-}\theta_0) = \exp[\text{-}(\theta\text{-}\theta_0)^2/\Delta\theta^2]\\
&\Psi_\varphi(\varphi) = \exp[\text{-}\varphi^2/\Delta\varphi^2]
\end{aligned} \tag{C.11}$$

where $\Delta r = |\nabla r|_0\Delta R$ and $\Delta\theta = \Delta Z/(r_0\kappa)$. Next we can write the Jacobian J_r from $(R,Z,\varphi) \to (r,\theta,\varphi)$ as approximately $J_r(r,\theta) \approx R_0 r_0\kappa/|\nabla r|_0$. Putting equations C.8, C.9, C.10 and C.11 together, we can now write the scattering matrix U_{np} being composed of

$$
\begin{aligned}
U_{np} \quad & = e^{-in\nu_0} e^{ir_0 k_r} \Psi_{n^\varphi}(n\text{-}n_+^\varphi)\Psi_{n^\theta}(n\text{-}n_+^\theta)\Psi_p(p\text{-}p_+) \\
\text{with} & \\
\Psi_{n^\varphi}(n\text{-}n_+^\varphi) & \approx R_0 \left(\frac{4\pi}{(\Delta n^\varphi)^2}\right)^{1/2} e^{-(n\text{-}n_+^\varphi)^2/(\Delta n^\varphi)^2} \qquad \text{3D} \\
& \approx R_0 \Delta\varphi \qquad \text{2D} \\
\Psi_{n^\theta}(n\text{-}n_+^\theta) & \approx \sqrt{\pi}(\Delta Z) e^{-(n\text{-}n_+^\theta)^2/(\Delta n^\theta)^2} \\
\Psi_p(p\text{-}p_+) & \approx \sqrt{\pi}(\Delta R) e^{-(k_r\text{-}k_{r+})^2/\Delta k_r^2} \qquad \text{Global simulation} \\
& \approx \frac{L_r}{|\nabla r|_0} \,\mathrm{sinc}[(k_r\text{-}k_{r+})L_r/2] \qquad \text{Local simulation}
\end{aligned}
\tag{C.12}
$$

Equation C.12 gives the general expression of the scattering matrix U_{np} in 3D and 2D, at the outboard midplane and assuming axisymmetry. The scattering signal can be computed similarly as before via $\delta n_{\mathrm{u}}(\vec{k}_+, t) = \sum_{n,p} U_{np} \delta n_{np}(\theta_0, t)$.

Recall $k_r = \frac{2\pi p}{L_r}$ and $k_{r+} = \frac{2\pi p_+}{L_r}$. The different radial mode number filter Ψ_p in a local $vs.$ global simulation stems from the fact that local simulation has the same profiles along the full radial domain. Thus, for all intents and purposes one can choose a radial filter in real space $\Psi_r = 1$, resulting in the sinc function, where L_r is the radial extent of the simulation. The toroidal, poloidal and radial mode number resolutions are

$$
\begin{aligned}
(\Delta n^\varphi)^2 &= 4/\Delta\varphi^2\text{-}2iR_0 k_{x+} \\
\Delta n^\theta &= \frac{2}{\Delta\theta \frac{\partial\nu}{\partial\theta}|_0} \\
\Delta k_r &= \frac{2}{\Delta r} = \frac{2|\nabla r|_0}{\Delta R}
\end{aligned}
\tag{C.13}
$$

With respect to the toroidal filter, in the 2D approximation $\Delta\varphi \to 0$, or equivalently $\Psi_\varphi = \delta(\varphi/\Delta\varphi)$ a delta function, and the toroidal mode number filter Ψ_{n^φ} is simply constant. Taking into account the toroidal variation of the scattering volume leads to a combination of 2 toroidal mode number filters. The toroidal filter in real space Ψ_φ gives rise to a toroidal mode number filter Ψ_{n^φ} about n_+^φ. The poloidal filter in real space (Ψ_Z or Ψ_θ) gives rise to a toroidal mode number filter $\Psi_{n_+^\theta}$ about n_+^θ. However, recall how n_+^φ and n_+^θ are a priori independent, since they are separately computed from $(k_x, k_z)_+$ and

k_{y+} respectively. The question remains whether n_+^θ and n_+^φ have actually similar values. For the simple s-α geometry at the outboard midplane, one finds

$$\begin{cases} n_+^\theta = \left. \dfrac{\frac{\partial R}{\partial r}k_{x+} + \frac{\partial Z}{\partial r}k_{z+}}{-\frac{\partial \nu}{\partial \theta}} \right|_0 \rightarrow \dfrac{r_0}{q_0}k_{z+} \\ n_+^\varphi = -R_0 k_{y+} \end{cases} \tag{C.14}$$

Setting the condition $n_+^\varphi \approx n_+^\theta$ needed for achieving finite amplitude scattering signal, one recovers the condition $\vec{k}_+ \cdot \vec{B} \approx 0$, ie. fluctuations are aligned with $\vec{B}$. This information is directly encoded in the ballooning expansion along the field lines via the definition of ν, and recovered here in the context of the computation of the scattering signal.

Consequences of the 3D implementation for the old high-k scattering system in NSTX

The question arises whether toroidal effects are indeed important for the old high-k scattering system at NSTX. This could be an important question for this thesis since we have assumed a 2D implementation of the synthetic diagnostic. In this thesis we have set $\Psi_{n^\varphi} \approx R_0\Delta\varphi$, consistent with equation C.12. In fact, our synthetic diagnostic is scaled by $R_0\Delta\varphi$.

How do toroidal effects modify the scattering signal of the old high-k scattering system? As is suggested by equation C.12, the most important dependence on toroidal mode number n from the scattering matrix U_{np} comes from the filters $\Psi_{n^\varphi}(n - n_+^\varphi)$ and $\Psi_{n^\theta}(n - n_+^\theta)$. In particular, we wish to understand how $\Psi_{n^\varphi}(n - n_+^\varphi)$ and $\Psi_{n^\theta}(n - n_+^\theta)$ compare to each other for different values of the toroidal scattering volume length $R_0\Delta\varphi$. This is an unknown quantity so far, although good estimates could be found following the procedures outlined in [90, 91]. Figure C-1 summarizes the preliminary analysis performed to assess the importance of 3D effects and toroidal scattering length $R_0\Delta\varphi$ on the filters. These tests were performed for scattering wave-vector components corresponding to channel 1 of the scattering system an using realistic NSTX geometry from the strong ETG condition. The values of the vertical extent of the scattering volume $\Delta Z = 0.03$ m, consistent with the old high-k scattering system.

In C-1.a) is shown the toroidal mode number filter Ψ_{n^φ} for varying values of the toroidal scattering length $R_0\Delta\varphi\ \epsilon\ [0.001 - 0.6]$ m. Small values of $R_0\Delta\varphi \lesssim 0.05$ m

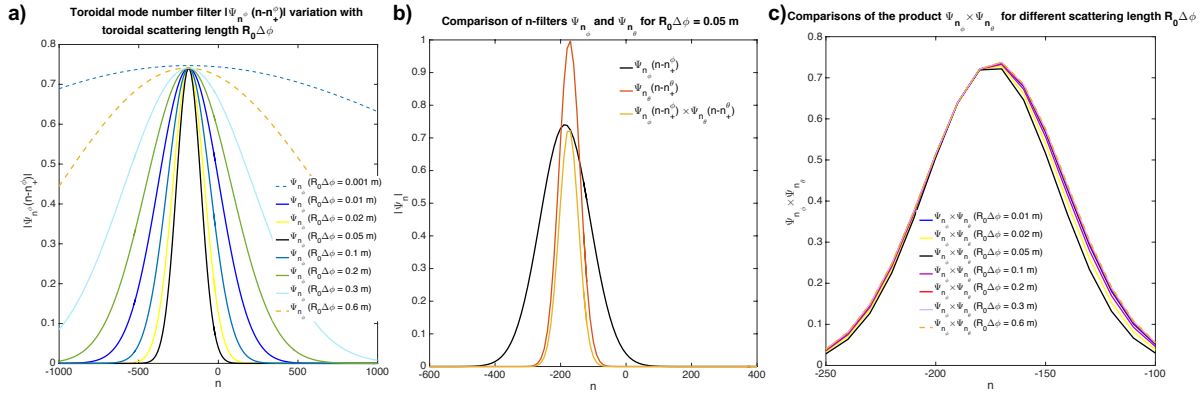

Figure C-1: **a)** Shape of toroidal mode number filter Ψ_{n^φ} for different toroidal length values $R_0\Delta\varphi$ of the scattering volume. **b)** Comparison of toroidal mode number filters Ψ_{n^φ} and Ψ_{n^θ}. **c)** Comparison of the total effect of a varying toroidal length of the scattering volume $R_0\Delta\varphi$ on the total product toroidal mode number dependence of the scattering matrix U_{np}, given by the product $\Psi_{n^\varphi} \times \Psi_{n^\theta}$.

correspond to highly toroidally localized measurements. The toroidal mode number resolution $(\Delta n^\varphi)^2 \approx 4/\Delta\varphi^2$ (equation C.13) dominated by the $4/\Delta\varphi^2$ contribution, and decreases with increasing $R_0\Delta\varphi$ from $R_0\Delta\varphi = 0.001$ m to $R_0\Delta\varphi = 0.05$ m. In this situation Ψ_{n^φ} is a real quantity. As the toroidal scattering length $R_0\Delta\varphi$ further increases for $R_0\Delta\varphi \gtrsim 0.05$ m, we are in the opposite situation and $(\Delta n^\varphi)^2 \approx -2iR_0k_{x+}$ is now a complex quantity. In this situation, an increasing scattering length for values larger than 0.05 m has the opposite effect of widening the resulting toroidal mode number width Δn^φ, increasing from $R_0\Delta\varphi = 0.05$ m to $R_0\Delta\varphi = 0.6$ m. Note how the narrowest width in this scan was found for a value of $R_0\Delta\varphi = 0.05$ m. We now wish to compare these filters to the toroidal mode number filter Ψ_{n^θ}.

Figure C-1.b) shows an actual comparison of the toroidal mode number filters Ψ_{n^φ} (black) and Ψ_{n^θ} (red), defined in equation C.12, and corresponding to the narrowest toroidal width found in a) for $R_0\Delta\varphi = 0.05$ m. The toroidal mode number filter Ψ_{n^φ} is shown to be wider than the filter Ψ_{n^θ}, even in this 'worst-case' scenario in which Δn^φ was narrowest. This suggests than one can assume Ψ_{n^φ} to be constant in the regime of variation of Ψ_{n^θ}. In orange is shown the overall product $\Psi_{n^\varphi} \times \Psi_{n^\theta}$. Comparing $\Psi_{n^\varphi} \times \Psi_{n^\theta}$ (orange) and Ψ_{n^θ} (black), the main impact of Ψ_{n^φ} is a scaling factor. However the overall width of the filter seems not to be much affected by the inclusion of Ψ_{n^φ}.

Figure C-1.c) shows the overall product $\Psi_{n^\varphi} \times \Psi_{n^\theta}$ for all the corresponding values

$R_0\Delta\varphi$ performed in a). As can be seen, varying $R_0\Delta\varphi$ is shown to have little influence on the overall toroidal mode number filter $\Psi_{n^\varphi} \times \Psi_{n^\theta}$. This can be understood from figure C-1.b), since the filter Ψ_{n^φ} is shown to be wider than Ψ_{n^θ} for essentially all values of $R_0\Delta\varphi$, thus being well approximated by a constant, resulting in an excellent approximation $\Psi_{n^\varphi} \times \Psi_{n^\theta} \approx \text{const.}\Psi_{n^\theta}$ which recovers the 2D implementation of the synthetic diagnostic presented in this thesis.

Although only a qualitative assessment, we have not implemented a 3D synthetic diagnostic and cannot as of the time of the writing of this thesis compare actual frequency power spectra from 2D and 3D synthetic diagnostics. However this preliminary assessment on the wavenumber filters suggests that the effect of the toroidal extent of the scattering volume is expected to be negligible for the old high-k scattering system, and the 2D approximation is shown to hold to a high degree of accuracy. A more detailed analysis comparing the actual frequency spectra from 2D and 3D synthetic diagnostics, as well as additional assessments to the one presented here for other coherent scattering experiments might be the object of a future publication.

Appendix D

List of Matlab routines used in this thesis

D.1 Main Matlab routines used in this thesis

The routines used in the course of this work were mostly written in Matlab. Some of the routines used were written by myself, although I would like to show my gratitude especially to W. Guttenfelder and Y. Ren for having put their personal routines available to me. The routines presented here are used to access and plot NSTX data, perform ray tracing calculations, prepare and analyze input and output files for using GYRO, for using TRANSP and routines concerning the synthetic diagnostic implementation. The routines are located in my personal directory `/p/gyro/jruizrui/matlab/myroutines`.

The following routines were used to access NSTX and TRANSP data and for experimental analysis:

- `get_shot_charact.m` Get general characteristics of the plasma dicharge (see details in the acutual routine).
- `get_mirnov.m` Get signal from Mirnov coils.
- `get_bfield.m` Get components of magnetic field B.
- `get_efit.m` Get data from EFIT equilibrium reconstruction.
- `get_lrdfit.m` Get data from LRDFIT equilibrium reconstruction.

- `get_s.m` Get magnetic shear $\hat{s}$ and other equilibrium reconstruction parameters.
- `get_mpts.m` Get MPTS data.
- `get_chers.m` Get CHERS data.
- `get_transp.m` Get TRANSP data.
- `plot_chi_transp.m` Produce plots from TRANSP data.
- `mean_freq_dop.m` Perform Doppler shift frequency subtraction.
- `get_hkdata.m` Get data from high-k fluctuation data.
- `get_kspec_more_nofit.m` Get wavenumber spectrum of fluctuations from high-k diagnostic.
- `k_spectrum_t.m` Obtain wavenumber spectrum of high-k fluctuations.
- `plot_highk_spec.m` Construct and plot high-k fluctuation spectrogram.
- `analysis_routine_3.m` Analyze correlations between equilibrium quantities and high-k data.
- `get_sigmagrad.m` Obtain experimental uncertainties profile gradient values ($\partial n_e/\partial r$, etc.), $E \times B$ shearing rate γ_E and thermal power uncertainties from power balance P_i, P_e (TRANSP).

The ray-tracing routines used in this thesis are the following:

- `call_raytracing.m` main routine that calls ray_tracing_nstx.m.
- `ray_tracing_nstx.m` (function) inputs: (shot, time, lxang, lzang, cmxang, ew_win, ew_xang,ew_yang,varargin). outputs: matlab structure (rt) with information from probe beam (pb), scattered beam (sb), and other relevant information.
- `ray_tracing_2010.m` Equivalent routine to ray_tracing_nstx.m.

- `get_raytracing_sca_rz.m` routine able make plots of the propagation trajectories of the incident and scattered beams, calculation of the minimum distance between the rays etc.

The following routines are used to create input files for GYRO and also to plot and analyze GYRO output. I am greatly thankful to Dr. Walter Guttenfelder at PPPL for providing most of the original routines used for GYRO analysis.

- `make_gacode_radial_resolution_scan.m` Create linear GYRO input file. Can also submit GYRO input file to the PPPL cluster.

- `plot_gyro_linear_scan_ga_juan.m` Routine used to analyze the output of the linear GYRO simulations. This routine can be used to generate linear growth rate spectra.

- `plot_gyro_gbflux_ga.m` Routine used to analyze the turbulent fluxes and turbulence amplitude of GYRO nonlinear simulations. This routine can plot the time traces of the turbulent heat fluxes, the poloidal wavenumber spectra of the heat fluxes, the radial profile of the heat fluxes, and zonal flow $vs.$ turbulence amplitudes.

- `plot_gyro_kxkyspec_ga_juan.m` Routine used to analyze the GYRO output file `out.gyro.kxkyspec`, containing the flux-surface averaged value of the electrostatic potential. With this routine one can plot the 2D (k_r, k_θ) spectrum of the flux-surface averaged potential, as well as the 1D spectra.

- `plot_gyro_outgyrokxkyspec_momentu.m` Similar to `plot_gyro_kxkyspec_g` but can plot the 2D (k_r, k_θ) spectrum of the flux-surface averaged potential, as well as the 1D spectra at specific poloidal locations and for different fields ex. $\delta n_e, \delta A_{||}, \delta B_{||}$, etc., making use of the large output files `out.gyro.moment_n`, `out.gyro.moment_u`, etc.

- `make_n_RZ_time_interp_2_juan.m` Routine able to plot GYRO fluctuation fields in 2D and 3D in real space (R, Z, φ), such as $\delta n_e(R, Z, \varphi, t)$ etc.

The following are the main routines used for the synthetic diagnostic to generate frequency and wavenumber spectra from high-k wavenumbers.

- `synhk_k_r_parfor.m` Main routine used for the generation of synthetic spectra from high-k fluctuations. Using a series of other routines reading GYRO outputs which are embedded, the main purpose of this routine is to analyze the GYRO output file `out.gyro.moment_n` and process it to generate turbulent frequency spectra by filtering in real-space as well as in wavenumber space.

D.2 Figures generated in this thesis

Here I outline the routines used in this thesis to generate the main content figures presented in this thesis. Some of the figures are used mainly for indicative purposes and are not generated by this thesis, but are taken from other sources (specially in the beginning chapters). Those are clearly cited and sourced in the main text and not described here.

D.2.1 Chapter 1

- **Figure 2-4** was generated using the Matlab routine `make_n_RZ_time_interp_2_juan.m`, using output from an electron-scale simulation in which the input value of the $E \times B$ shearing rate γ_E was set to 0, simply for the purpose of display in this figure. The simulation output files can be found in my PPPL directory at `/p/gyro/jruizrui/gacode/gyro/s`

D.2.2 Chapter 4

- **Figure 4-1** was generated using the Matlab routine `get_raytracing_sca_rz.m`, found in `/p/gyro/jruizrui/matlab/myroutines`. This routine is able to plot ray trajectories in 2D and in 3D. The trajectories correspond to NSTX shot 141767.

- **Figure 4-2** was generated using the Matlab routine `plot_highk_spec.m` in a). b) was generated as 'snapshots' of a) at specific time slices.

- **Figure 4-3** was generated using the Matlab routine `get_sigmagrad.m`, which uses data from profiles, TRANSP and LRDFIT to generate profile uncertainties using a Monte-Carlo approach.

- **Figure 4-4** was generated using the routine `plot_gyro_linear_scan_ga_juan.m`.

- **Figure 4-5** was generated using the routine `plot_gyro_gbflux_ga.m` using the output from example ion-scale, electron-scale and 'big-box' electron-scale simulation, showing a visual comparison of the three simulation types performed in this thesis.

- **Figure 4-7** was generated using the routine `plot_gyro_gbflux_ga.m` applied to an example of electron-scale simulation.

D.2.3 Chapter 5

Most figures pertaining example spectra from standard and 'bib-box' electron-scale simulation in this section use simulation output from the following directories:

dir1: `/p/gyro/jruizrui/gacode/gyro/sim/Walter_141767_ETG /cori_rep_juan/edison_escale/engaging/t398_alne_alte_scans /t398e_kt65_exp_t75`.
dir2: `/p/gyro/jruizrui/gacode/gyro/sim/Walter_141767_ETG /cori_rep_juan/edison_synhksim_tests/t398/2018_runs /t398h_exp_kt65_nomp4_r1_exp_t22`.

- **Figure 5-3** was generated using the partial subroutine `get_r_filter.m` built in in the main Matlab routine `synhk_k_r_parfor.m`, run several times for different poloidal locations.

- **Figure 5-4** was generated using the partial subroutines `get_krkth_grid` and `get_krkth_exp.m` built in in the main Matlab routine `synhk_k_r_parfor.m`. $a)$ and $b)$ were generated using output respectively from standard and 'big-box' electron-scale simulation, found in **dir1** and **dir2**.

- **Figure 5-5** was generated using partial subroutine `get_k_filter.m` built in in the main Matlab routine `synhk_k_r_parfor.m`. Red and blue curves were generated using output respectively from standard and 'big-box' electron-scale simulation, found in **dir1** and **dir2**.

- **Figure 5-6** was generated using the main Matlab routine `synhk_k_r_parfor.m`, applied respectively to output from standard and 'big-box' electron-scale simulation, found in **dir1** and **dir2**. The Matlab variable `plot_rz_fluct` must be set to `0` in the beginning of the routine script in order for these figures to be plotted by Matlab.

- **Figures 5-7** and **5-8** was generated using the main Matlab routine `plot_gyro_kxkyspec_ga_juan.m`, applied respectively to output from standard and 'big-box' electron-scale simulation, found in **dir1** and **dir2**.

- **Figure 5-9** was generated using the main Matlab routine `synhk_k_r_parfor.m` using output respectively from standard and 'big-box' electron-scale simulation, found in **dir1** and **dir2**.

- **Figure 5-10** was generated using the main Matlab routine `synhk_k_r_parfor.m` using output from 'big-box' electron-scale simulation found in **dir2**, and using the real and k-space filter implementations built in `synhk_k_r_parfor.m`.

- **Figure 5-11** was generated using the main Matlab routine `synhk_k_r_parfor.m` using output from 'big-box' electron-scale simulation found in **dir2**. Simulation output is the same for both curves, but Doppler shift was applied only in one of them. Doppler-shift can be introduced in the synthetic spectra via the Matlab variables `doppler_flag = 1` and `M = ...` at the beginning of the main Matlab script.

- **Figure 5-12** was generated using the main Matlab routine `synhk_k_r_parfor.m` using output from 'big-box' electron-scale simulation found in **dir2**. Simulation output is the same for all curves, but Doppler shift was only applied when indicated in the figure.

- **Figure 5-13** was generated using the main Matlab routine `synhk_k_r_parfor.m` using output from 'big-box' electron-scale simulation found in **dir2**. Simulation output is the same for all curves, but the vertical wavenumber resolution of the diagnostic Δk_Z was varied as indicated in the figure. The Matlab variable `dkZ_exp` can be used to determine the value of Δk_Z in the beginning of the Matlab script.

D.2.4 Chapter 6

- **Figure 6-1** was generated using the Matlab routines `get_lrdfit.m` for I_p and `get_mpts.m` for the n_e and T_e profiles.

- **Figure 6-2** was generated using the Matlab routines `plot_hkspec_times.m` for the frequency spectrum and `plot_kspec_times.m` for the wavenumber spectrum.

- **Figures 6-3** and **6-4** were generated using the Matlab routines `plot_gyro_linear_scan_ga_juan.m`, respectively to the strong and weak ETG conditions, found in `/p/gyro/jruizrui/gacode/gyro/sim /Walter_141767_ETG/cori_rep_juan/t398_exp/linruns/ra71` and `/p/gyro/jruizrui/gacode/gyro/sim/Walter_141767_ETG/cori_rep_juan /t565_exp/linruns/ra68/allk_exp_lowk_dke_hk_gke_merge` respectively for the strong and weak ETG conditions.

- **Figures 6-5** and **6-6** were generated using output from several nonlinear GYRO simulations, using routine `t565_total_qeqi_balance.m`.

- **Figure 6-9** is generated by use of Matlab routine `synhk_k_r_parfor.m` applied to 5 'big-box' electron-scale simulations for the strong ETG condition, found in `/p/gyro/jruizrui/gacode/gyro/sim/Walter_141767_ETG /cori_rep_juan/edison_synhksim_tests/t398/2018_runs` and `/p/gyro/jruizrui/gacode/gyro/sim/Walter_141767_ETG /cori_rep_juan/edison_synhksim_tests/t398/2019_runs`. The two simulations for the weak ETG conditions are found in `/p/gyro/jruizrui`

/gacode/gyro/sim/Walter_141767_ETG/cori_rep_juan
/edison_synhksim_tests/t565/reducedbox_dec17.

- **Figure 6-8** was generated by use of Matlab routine `plot_hkspec_times.m` applied to 'big-box' electron scale simulations, found respectively in the same directories as those noted by figure 6-9.

- **Figures 6-10, 6-11** and **6-12** were generated using Matlab routine `plot_hkspec_times.m` applied to 'big-box' e- scale simulations found in `/p/gyro/jruizrui/gacode/gyro/sim/Walter_141767_ETG/cori_rep_juan /edison_synhksim_tests/t398/2019_runs` for the strong ETG case.

- **Figure 6-7** was generated using Matlab routine `t565_total_qeqi_balance.m`.

Appendix E

Experimental plasma parameters input in GYRO

Parameter	Strong ETG value	Weak ETG value
r/a	0.70839	0.67864
$R_0(r)/a$	1.5227	1.5922
$\Delta = dR_0(r)/dr$	-0.30412	-0.355
κ	2.1127	1.9792
$s_\kappa = rd\ln(\kappa)/dr$	0.153963	0.190789
δ	0.248295	0.167812
$s_\delta = rd\delta/dr$	0.323972	0.323851
q	3.7892	3.0723
$\hat{s}$	1.8047	2.3464
$\rho^\star$	0.00328	0.00382
$M = R\omega_0/c_s$	0.16	0.21
$\gamma_E = -r/qd\omega_0/dr$	0.1258	0.1646
$\gamma_p = -R_0 d\omega/dr$	1.0362	1.1558
ν_{ei}	1.379113	1.0310
Z_{eff}	1.9504	1.8425
n_D/n_e	0.78503	0.80371
n_C/n_e	0.035828	0.032715
T_D/T_e	1.1352	1.3964
T_C/T_e	1.1352	1.3964
a/L_{nD}	1.4973	4.0319
a/L_{nC}	-0.8769	4.0801
a/L_{ne}	1.0048	4.0576
a/L_{TD}	2.9599	3.0929
a/L_{TC}	2.9599	3.0929
a/L_{Te}	3.3626	4.5128
β_e	0.002736	0.002956
λ_D/a	0.0000371	0.0000417
$\mu = (M_D/m_e)^{1/2}$	60	60
$n_e\ [10^{19}/m^3]$	4.2714	3.4282
T_e [keV]	0.39060	0.40116
B_{unit}	1.44613	1.26986
$a\ [m]$	0.6012	0.5960
$c_s/a\ [10^5/s]$	2.2749	2.3252

Table E.1: Plasma parameters input in GYRO simulations presented in this work.

Appendix F

Electron-scale and 'big-box' electron scale nonlinear simulation resolution tests.

The nonlinear simulation transport predictions presented with the GYRO code have been extensively tested for convergence of the numerical solution. All numerical simulations were fully electromagnetic including $(\delta\phi, A_{||}, B_{||})$ field fluctuations, electron collisions ($\nu_{ei} \sim 1$), parallel flow and flow shear $(M, \gamma_E, \gamma_p) \sim (0.20.3, \sim 0.10.2, \sim 1)$, and simulating 3 kinetic species (all species gyrokinetic for electron and hybrid simulations, and using drift-kinetic electrons for ion-scale simulations). Ion-ion collisions ν_{ii} were not included in this study ($cf.$ chapter 7 for additional details). All nonlinear simulations carried out as part of this work had the same poloidal resolution of 14 poloidal grid points ($\times 2$ signs of parallel velocity), 12 energies and 12 pitch-angles (6 passing + 6 trapped), which were tested for numerical convergence (although not shown here). The choice of numerical grids was consistent to previous convergence and accuracy tests for the GYRO code simulating micro-instabilities in the core of NSTX [136]. In this section are shown resolution and convergence tests carried out for electron and hybrid scale simulations for the strong ETG condition. Numerical convergence is shown in the radial box-size (L_r) and poloidal box-size domains (L_θ, inversely proportional to the poloidal wavenumber grid step $\Delta k_\theta \rho_s$), in radial resolution for varying radial grid steps ($\Delta r/\rho_e$) and in the

maximum resolved poloidal wavenumber $\max(k_\theta \rho_s)$.

Similar resolution and convergence tests were carried out for the weak ETG condition (not shown here). For this condition, it is worth separating the discussion on numerical convergence between the TEM-stable regime (figure 6-6.a), and 6-6.b) for $a/L_{Te} < 5$) and the TEM-unstable regime (figure 6-6.b) for $a/L_{Te} > 5$). In the TEM-unstable regime, a slight disagreement between standard and hybrid simulation is obtained in the heat transport predictions (for varying box-sizes (L_r, L_θ)), lying slightly outside the numerical standard deviation in predicted thermal transport ($cf.$ the rightmost blue and magenta dots from figure 6-6.b)). These slight disagreements might be related to the highly unstable ion-scale modes present due to a strongly driven TEM, since some of those ion-scale modes were shown to play a small but non-negligible role in the larger box hybrid-scale simulation for the weak ETG condition. We cannot at this point ensure numerical box-size convergence for the electron and hybrid scale simulations presented for the weak ETG condition in the TEM-unstable regime. However, we have argued in this article how the TEM-unstable regime itself is not a good approximation of reality, since it cannot comply with the electron and ion thermal transport constraints (figure 6-7 for $a/L_{Te} > 5$), making the absence of absolute numerical convergence in the TEM-unstable regime a less relevant result. However, excellent numerical convergence is achieved between electron and hybrid scale simulation in the TEM-stable regime. In fact, figure 6-6.a) shows identical heat transport predictions between electron and hybrid simulation (overlaid blue and magenta dot in figure 6-6.a)). In addition, good convergence was shown in radial resolution $\Delta r/\rho_e \sim 3$ and maximum resolved poloidal wavenumber $\max(k_\theta \rho_s) \sim 87$ for the weak ETG condition, both in the TEM-stable and TEM-unstable regimes.

Preliminary convergency tests were also carried out for ion-scale nonlinear simulations (specifically for the TEM-unstable branch in the weak ETG condition, which predicted $\sim \times 10$ the experimental electron thermal power level). These resolution tests for the ion-scale simulations confirmed the presence of the highly unstable TEM branch in the weak ETG condition, and predicted similar heat transport levels lying within the numerical standard deviation, both in the TEM-stable and unstable regimes.

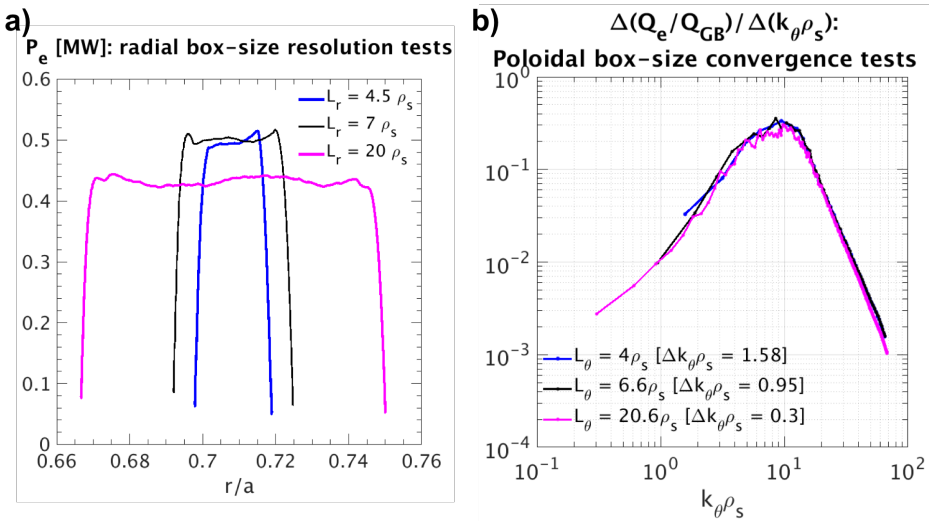

Figure F-1: Radial and poloidal box-size convergence tests carried out for three different radial and poloidal box-size domains, corresponding to electron and hybrid simulations for the strong ETG condition (experimental profile parameters were used as input). **a)** Radial box-size convergence tests: electron thermal power P_e is plotted versus normalized minor radius r/a for standard electron-scale simulations ($L_r = 4.5, 7\rho_s$) and hybrid scale simulation ($L_r = 20\rho_s$). Similar electron thermal power is predicted for simulations with $L_r = 4.5\rho_s$ and $7\rho_s$, and a slight decrease of $\sim 10-15\%$ is observed when the radial box size is increased to $L_r = 20\rho_s$. Although this small decrease might be related to the impact of ion-scale modes associated to the larger box-size, or the shorter simulation time in the larger box-size due to limited computational resources ($T \sim 20$ a/c$_s$), we note however that this small difference lies well inside the simulation standard deviation, indicating convergence in radial box-size (note the error bars in the nearby blue and magenta dots of figure 6-5.a) corresponding to the black and red curves in this plot). The GYRO buffer regions are not included in the calculation of the radial box-size. **b)** Poloidal box-size convergence tests: the fractional electron heat flux ΔQ_e per poloidal wavenumber increment $\Delta k_\theta \rho_s$ is plotted versus normalized poloidal wavenumber $k_\theta \rho_s$ for standard electron-scale simulations ($L_\theta = 4, 6.6\rho_s$) and hybrid scale simulation ($L_\theta = 20.6\rho_s$). A larger box-size is inversely proportional to the poloidal wavenumber increment $\Delta k_\theta \rho_s$. All simulations resolve up to $k_\theta \rho_s^{max} \sim 65$. A very similar k_θ spectrum is obtained for all simulations, in addition to similar predicted electron thermal power ($10-15\%$ agreement lying within the numerical standard deviation). We conclude convergence in poloidal box-size. The blue and magenta curves correspond to the nearby blue and magenta simulation points in figure 6-5.a). The hybrid scale simulation with the larger box-size consumed over $1M$ CPU h for completion NERSC's Edison supercomputer.

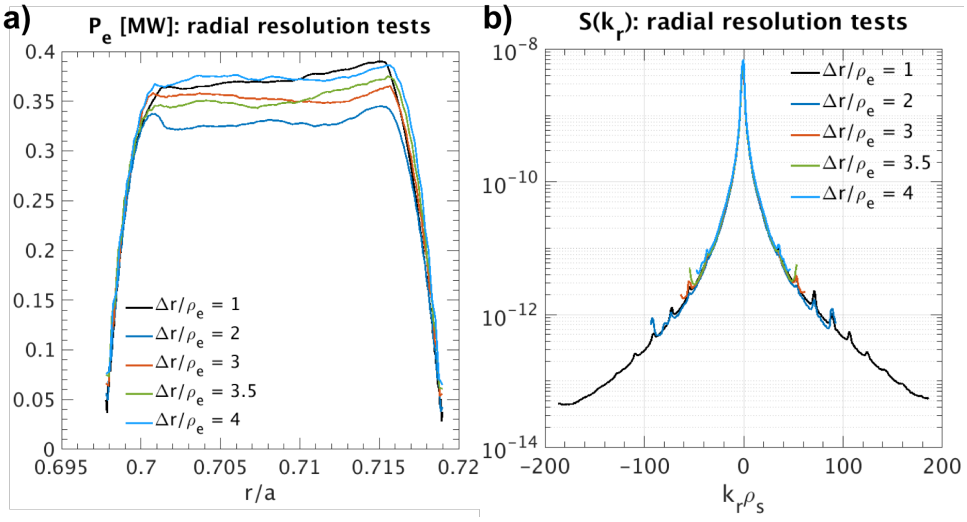

Figure F-2: Radial resolution tests for 5 different radial grid steps $\Delta r/\rho_e$ of electron scale simulations for the strong ETG condition (experimental profile parameters were used as input). **a)** P_e[MW] is shown over the full radial domain, showing very close P_e agreement between all simulation predictions. **b)** Radial wavenumber power spectrum associated to potential fluctuations $|\delta\phi|^2$. The field $\delta\phi$ exhibits the largest amplitude among all electromagnetic field components $(\delta\phi, \delta A_{||}, \delta B_{||})$, and is responsible for the dominant contribution to electron heat transport P_e by some $\sim$ 2 orders of magnitude over contributions from shear $\delta A_{||}$ and compressional perturbations $\delta B_{||}$. All simulation resolution scans presented here are carried out on standard electron scale simulations with box-sizes $(L_r, L_\theta) = (4.5, 4)\rho_s$.

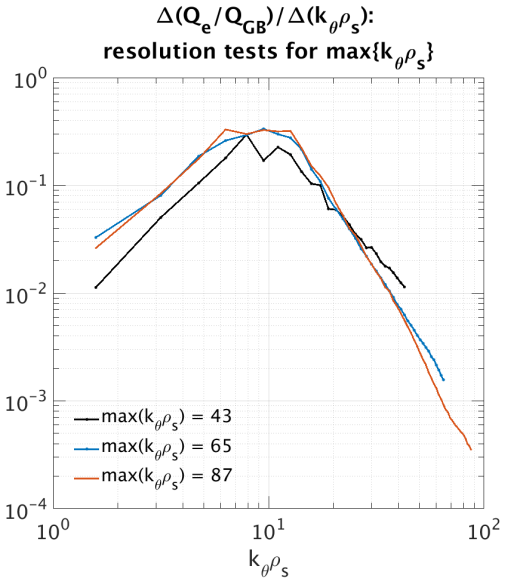

Figure F-3: Poloidal resolution tests for 3 different values of the maximum $k_\theta \rho_s$ resolved in electron scale simulations for the strong ETG condition (experimental profile parameters were used as input). Simulation resolving a maximum $\max(k_\theta \rho_s) = 43$ exhibits reduced total electron thermal power (up to 30% reduction) and noticeably different spectral slope at high-k with respect to simulations with $\max(k_\theta \rho_s) = 65, 87$. Note however how negligible differences can be observed between simulations resolving $\max(k_\theta \rho_s) = 65$ $vs.$ $\max(k_\theta \rho_s) = 87$. This last point gives us confidence that simulation is converged for $\max(k_\theta \rho_s) = 65$. Consequently hybrid scale simulations for the strong ETG case will resolve a maximum poloidal wavenumber of 65.

Appendix G

Effect of ion-ion collisions on low-k turbulence at the weak ETG condition

Although all the available experimental evidence showed in this thesis has pointed to ETG-driven turbulence as the main contributor to electron thermal transport both at the strong and weak ETG conditions, the state and the role that ion-scale turbulence might play at the weak ETG conditions is still not fully understood, and requires more careful analysis. Ion-scale simulation suggests ion-scale turbulence is nonlinearly suppressed by large zonal flow amplitudes, in a state reminiscent of a Dimits' shift regime [220], and possibly linked to the recently observed subcritical fluctuations [174]. However, a strong TEM/KBM branch is destabilized within experimental uncertainty, leading up to 10 times the experimental value of electron thermal power.

We present here a series of ion-scale nonlinear gyrokinetic simulations carried out for the weak ETG condition, with the goal of studying the effect of ion-ion collisions. Ion-ion collisions have been known to act as a damping mechanism on the zonal flow for at least two decades [217–219]. In GYRO ion-ion collisions are not a standard numerical flag, since they are supposed to be negligible for finite turbulence amplitudes dominated by turbulence interactions with the zonal flow. In those situations commonly encountered in the tokamak core, ion-ion collisions play a negligible role in damping the zonal flow.

However, ion-ion collisions can become important in conditions where the turbulence is very close to the nonlinear threshold. This effect can be exaggerated at high collisionality values $\nu_{ei} \sim 1$ c_s/a. These are precisely the conditions found for the weak ETG

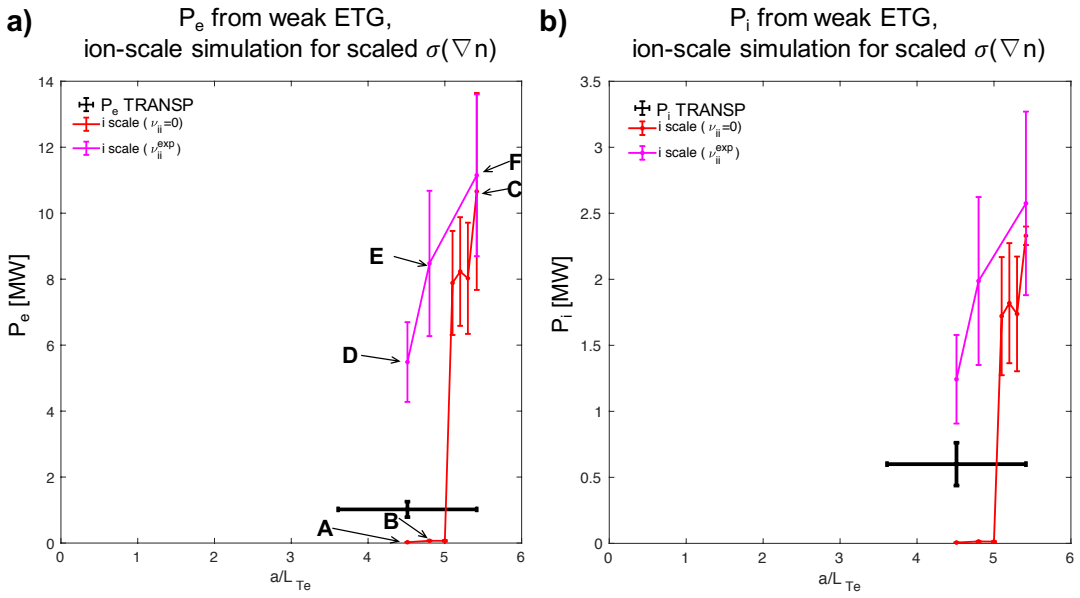

Figure G-1: **a)** Electron thermal power from ion-scale simulation run with scaled density gradient value within 1σ uncertainty, for different values of electron temperature gradient a/L_{Te}. In red is shown simulation output when the value of ion-ion collision frequency ν_{ii} was set to 0. In magenta is shown simulation output when the value of ion-ion collision frequency was set to the experimental value $\nu_{ii} = \nu_{ii}^{exp}$ was set to 0. **b**) Same as a) but showing the ion thermal power P_i instead of the electron thermal power P_e.

case analyzed in this thesis, and motivate this preliminary analysis on the effect of ion-ion collisions on ion-scale turbulence.

Figure G-1 shows the total, saturated values of the electron and ion thermal power P_e, P_i [MW], for different values of the driving parameter a/L_{Te}. All simulations were run using a constant, scaled value of a/L_{ne} within 1-σ uncertainty. In red are shown simulations that are already presented in this thesis (figures 6-6, 6-7). These we recall were run without the inclusion of ion-ion collisions, as all the rest of simulations performed in this thesis. Looking at the red curve, ion-scale simulation predicted negligible P_e and P_i for $a/L_{Te} < 5$ values, but a highly unstable TEM/KBM branch for $a/L_{Te} > 5$. The letters **A**, **B** and **C** denote simulations run with input values of $a/L_{Te} = 4.5, 4.8, 5.4$ respectively. The magenta curves are the result of three simulations that were restarted from **A**, **B** and **C** by including ion-ion collisions on the zonal flow $n = 0$ (via the GYRO flag `KILL_COLL_FLAG`). The saturated values of P_e and P_i from such simulations are shown by the letters **D**, **E** and **F**. It can be clearly seen from figure G-1 that ion-ion collisions have a very substantial effect on the turbulence saturated state for **A** and **B**, leading to the highly

unstable turbulence regimes **D** and **E**. However, note how **C** and **F** predict essentially the same transport. These results suggest that ion-ion collisions are mostly important in close to threshold conditions (close to marginality as in **A** and **B**), but not far from threshold (as in **C**).

The role of ion-ion collisions on **A**, **B** and **C** are more clearly shown in figures G-2.a), b) and c). These show time traces of the electromagnetic field fluctuation amplitudes $(\phi, A_{||}, B_{||})$ for the turbulence $(\sum n > 0)$ and zonal flow $(n = 0)$, corresponding to simulations **A**, **B**, **C**, **D**, **E** and **F** in figure G-1. Simulations in G-2.a), b) and c) are run with the same value of electron density gradient (scaled by 1-σ) but different electron temperature gradients as input. All three simulations in G-2 are divided in three time phases. In the first time phase, simulations are started with a zero value of $E \times B$ shearing rate γ_E and zero value of ion-ion collision frequency $\nu_{ii,ZF} = 0$. In this phase, turbulence fluctuations follow the linear exponential growth phase for the first 50-100 a/c$_s$. After the linear growth phase, fluctuations saturate at high amplitudes without the suppressing effect of γ_E. In the second phase of the simulations, the experimental value of $E \times B$ shear is included, and corresponds to phases **A**, **B** and **C** respectively in figures 7.3.a), b) and c). In this phase, the finite n turbulence fluctuations are suppressed by the effect of γ_E. In G-2.a) and b), the state is dominated by strong potential fluctuations of the zonal flow ($\phi n = 0$, black dashed line) and the turbulence is shown to be fully suppressed. Negligible transport is predicted in this time phase, as can also be seen from **A** and **B** in figure G-1. In G-2.c) the state is dominated by strong finite-n, turbulence fluctuations, producing high values of transport (corresponding to **C** in figure G-1). The third phase of the simulations, the experimental value of the ion-ion collision frequency is included in the simulations, and preserving the previous parameters constant (γ_E, etc.). These are phases **D**, **E** and **F** respectively. In figures G-2.a) and b), the large value of the zonal flow amplitude is shown to be strongly damped by the inclusion of finite ν_{ii}. This has the effect of destabilizing finite-n perturbations, since now the weaker zonal flows are not able to efficiently suppress turbulence. In **D** and **E** finite-n perturbations are shown to saturate at very high amplitudes. As can be seen from figure G-1, phases **D** and **E** produce some 6-8 MW of electron thermal power, clearly overpredicting the experimental value of $P_e^{exp} \sim 1$ MW. In figure G-2.c), turbulence was already shown to be strongly driven in

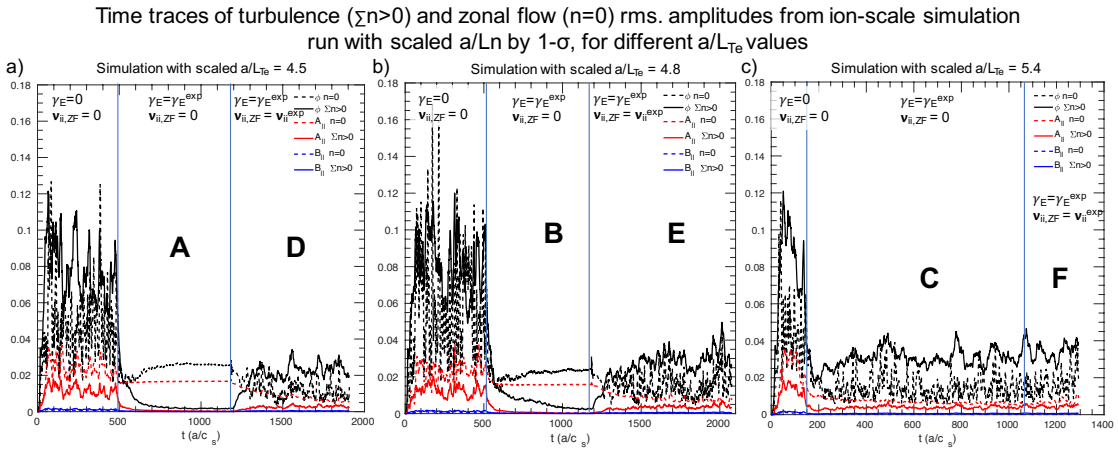

Figure G-2: Time traces of the electromagnetic field r.m.s. fluctuation amplitudes $(\phi, A_{||}, B_{||})$ for the turbulence $(\sum n > 0)$ and zonal flow $(n = 0)$, corresponding to simulations **A**, **B**, **C**, **D**, **E** and **F** in figure G-1. All simulations were run with a scaled value of a/L_{ne} within 1-σ uncertainty. **a)** Simulation was run using $a/L_{Te} = 4.5$. **b)** Simulation was run using $a/L_{Te} = 4.8$. **c)** Simulation was using $a/L_{Te} = 5.4$.

phase **C**, and the inclusion of ion-ion collisions in **F** is shown to have a negligible effect on the dynamics of the zonal flow, barely affecting the saturated levels and transport. In summary, figures 7.3 and 7.3 suggest that ion-ion collisions can have a very important effect on the turbulence amplitudes of the outer-core of NSTX H-modes via the damping of zonal flows in close to marginal conditions and at high values of collisionality $\nu_{ei} \sim 1$ c_s/a. However, the effect is shown to be negligible in far from threshold conditions exhibiting finite amplitude turbulence fluctuations.

Figures G-3.a) and b) show time traces of electromagnetic field fluctuations amplitudes $(\phi, A_{||}, B_{||})$, similar to figure G-2, but this time carried out for the nominal, experimental profile values (in particular, experimental a/L_{ne} and a/L_{Te}). As in G-2, simulations are started with a zero value of $E \times B$ shearing rate ($\gamma_E = 0$). In 7.3.a)the ion-ion collision frequency is initially set to 0 ($\nu_{ii,ZF} = 0$); in G-3.b), the ion-ion collision frequency is set to the experimental value ($\nu_{ii,ZF} = \nu_{ii}^{exp}$). In the second phase, the experimental value of γ_E is included, suppressing the finite-n modes. However, in the absence of ion-ion collisions in a), the zonal flows are not saturated, but exhibit n=0 potential perturbations that have a linear dependence in time ($|\phi_{n=0}|^2 \propto t$). This behavior is not observed in the presence of ion-ion collisions in b) (after t $\gtrsim$ 120 a/c_s), showing the undamped zonal flow amplitudes in a) are linked to the absence of ion-ion collisional

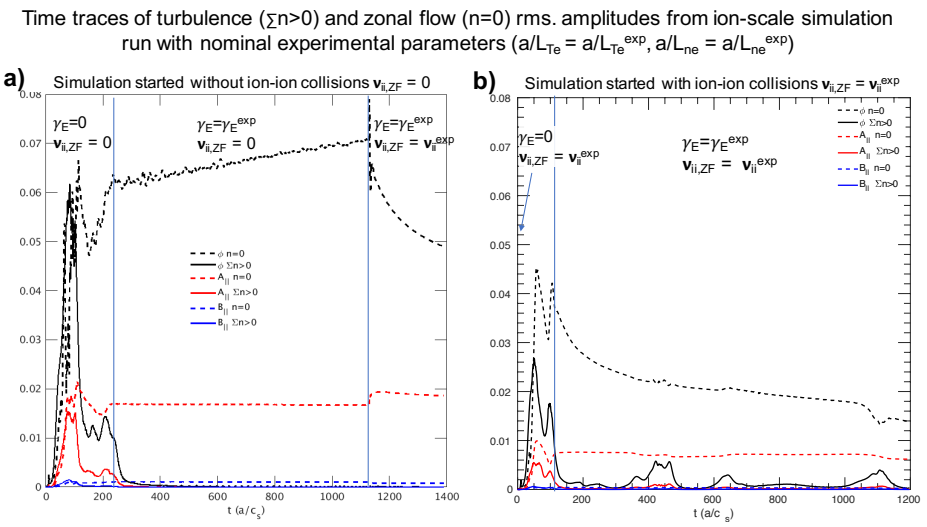

Figure G-3: Time traces of electromagnetic field r.m.s. fluctuation amplitudes $(\phi, A_{||}, B_{||})$, similar to figure G-2, but this time carried out for the nominal, experimental profile values (in particular, experimental a/L_{ne} and a/L_{Te}). **a)** The simulation is started at $t = 0$ a/c$_s$ using ion-ion collision frequency set to 0 ($\nu_{ii,ZF} = 0$). **b)** The simulation is started at $t = 0$ a/c$_s$ using ion-ion collision frequency set to the experimental value ($\nu_{ii,ZF} = \nu_{ii}^{exp}$).

damping on the zonal flows. In $b)$ one can observe sudden bursts of finite-n perturbations at $t \approx 400, 600, 1100$ a/c$_s$ (bold black line). These are in fact lone, large-scale eddies occupying most of the simulation domain and producing non-negligible levels of instantaneous transport, however they are eventually damped by the strong zonal flows present, producing negligible time-averaged transport levels. The observation of lone, large-scale eddies occupying most of the simulation domain is reminiscent of the subcritical transition to ITG turbulence observed in MAST [174].

The behavior of undamped, linear dependence of the zonal flow observed in G-3.$a)$ was highlighted in seminal work by Rosenbluth and Hinton [217, 218], and seems to be similar to the behavior observed in the outer core of this NSTX H-mode. A last time phase is included in figure G-3.$a)$ by including ion-ion collisions (after $t \approx 1130$ a/c$_s$). In this regime, the main effect of finite ν_{ii} shown to be on the zonal flow amplitude, exhibiting a nearly exponential decay. This behavior was also observed in [217, 218]. However the simulation in $a)$ was not run for long enough in order to observe the final saturated state of the zonal flow.

In this appendix we have shown that ion-ion collisions can have an important effect on zonal flows and ion-scale turbulence fluctuations in close to threshold conditions, but

not in far from threshold conditions. However, there are some important caveats worth pointing out in this analysis. Analysis performed here used the 'simple' Lorentz collision operator, only modeling pitch-angle scattering collisions and no energy-diffusion. The high collisionality of these plasmas ($\nu_{ei} \approx 1\ \mathrm{c}_s/a$) suggests the Lorentz model might not be valid in these regimes, and advanced collisional models such as implemented in CGYRO [190] might be needed. In fact, E. Belli and J. Candy have recently used the CGYRO code with the advanced Sugama collision operator to simulate ITG turbulence for the GA standard case [222]. This work has shown how the residual zonal flow potential calculated using the advanced Sugama collision operator can vary by close to an order of magnitude at high levels of electron collisionality (similar to those used here) with respect to the simpler Lorentz model implemented in GYRO. The results presented in this appendix motivates further work to understand the role of ion-ion collisions on the zonal flow, and the possible implications for the turbulence saturated levels, and possible implications for cross-scale coupling interactions, in realistic plasma conditions for spherical tokamak.

Appendix H

Linear effect of β on ion-scale modes

The linear effect of β on the ion-scale instability is shown to be different between the strong and weak ETG conditions. This might be especially significant for the weak ETG condition, since the experimental value of β is shown to be very close to the instability threshold of the KBM instability.

Figures H-1.a) and b) show the real frequency ω_r and linear growth rate γ from β scans for carried out for a particular wavenumber at ion-scales ($k_\theta \rho_s = 0.48$) for the strong ETG condition. At low β, an ion-directed, ballooning parity instability is shown to be the fastest growing mode, possibly identified to a trapped electron mode (noted TEM). The linear growth rate in b) is shown to be weaker than the background $E \times B$ shearing rate. At increasing value of β_e, the linear growth rate is shown to decrease with β_e up to values of $\beta_e \approx 0.25\%$, in which the dominant instability is shown to be an electron-directed, tearing parity microtearing mode (MT). The experimental β_e value is shown to sit right at the critical beta for the transition between the TEM and MT mode. For beta values $> 0.25\%$, the linear growth rate exhibits a weak, destabilizing dependence with β_e, characteristic of the MIT mode. However, the MT linear growth rate is very close to the background $E \times B$ shearing rate. For even greater β_e values, the MT mode becomes subdominant to an ion-directed kinetic ballooning mode, exhibiting high growth rate values that clearly surpass the $E \times B$ shearing rate value. This β_e scan clearly shows 3 different instabilities can co-exist for experimentally relevant NSTX plasma parameters. However, we point out that the TEM and MT modes are the most experimentally relevant for the present case, which are predicted to be suppressed by strong $E \times B$ shear in this

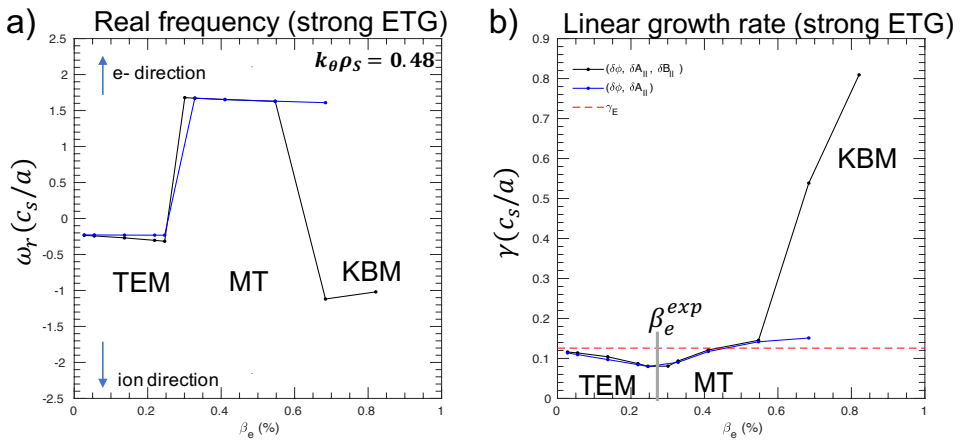

Figure H-1: **a)** Real frequency from a linear beta scan for $k_\theta \rho_s = 0.48$ for the strong ETG condition. **b**) Corresponding linear growth rate from a linear beta scan for $k_\theta \rho_s = 0.48$.

condition. Note β_e here uses the B_{unit} convention in GYRO, and the uncertainty of β_e is on the order of 10%. The beta scans presented also preserved the value of beta-prime β' fixed. The α_{MHD} value is shown to be ≈ 0.5 in this condition, suggesting the KBM may not be experimentally relevant in this condition as suggested by previous work [136].

The black curve in 7.3 shows linear scans computed included the full electromagnetic field perturbations $(\delta\phi, \delta A_{||}, \delta B_{||})$. In blue linear scans only included $(\delta\phi, \delta A_{||})$ perturbations. The TEM and MT modes are shown to be unaffected by the inclusion of $\delta B_{||}$ perturbations, however the KBM is shown to be stabilized without $\delta B_{||}$ perturbations.

Figure H-2 shows the corresponding β scan for the weak ETG condition. In this case, an electron-directed, ballooning parity TEM mode is most unstable at low beta. The growth rate is shown to be higher than the background $E \times B$ shearing rate. When full perturbations of the electromagnetic field are included (black line), the TEM mode transitions to an ion-directed, ballooning parity KBM mode at $\beta_e \approx 0.35$, with linear growth rates greatly exceeding the background $E \times B$ shearing rate. The transition from TEM to KBM happens within 20% of the experimental β_e value. This suggests the KBM might have an important role to play at the weak ETG condition. We only $(\delta\phi, \delta A_{||})$ perturbations were included in the simulation, the KBM is stabilized and the TEM transitions to an electron-directed, tearing parity MT mode, that ultimately transitions to the KBM for $\beta_e \approx 0.9$ (greatly exceeding the experimental β_e). It is worth pointing out how the TEM at low beta is shown to be stabilized when $\delta B_{||}$ perturbations were not included in the

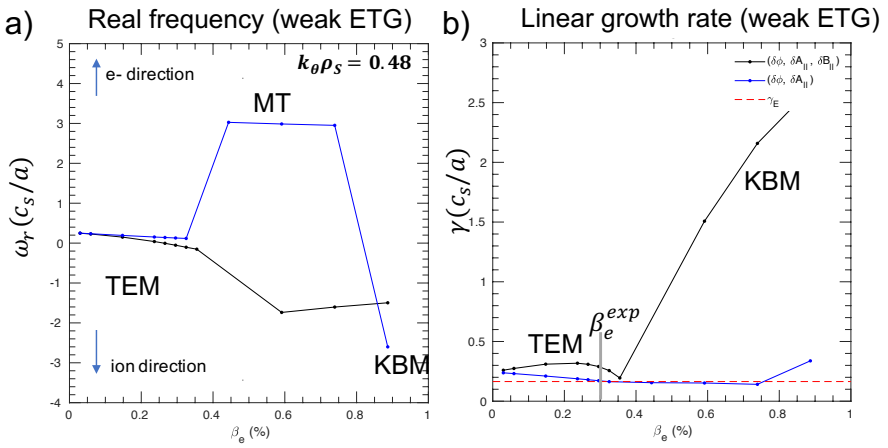

Figure H-2: **a)** Real frequency from a linear beta scan for $k_\theta \rho_s = 0.48$ for the weak ETG condition. **b**) Corresponding linear growth rate from a linear beta scan for $k_\theta \rho_s = 0.48$.

simulation. The uncertainty value of β_e is about 10%, showing the transition to KBM is outside uncertainty. The α_{MHD} value is shown to be ≈ 0.7-0.8 in this condition, suggesting KBM may be experimentally relevant as suggested by previous work [136].

Although very preliminary, these linear beta scans for ion-scale modes have shown how the KBM might be experimentally relevant at the weak ETG condition, but not at the strong ETG condition which was shown to be dominated by ETG. The relevance of the KBM at the weak ETG condition is relevant for future high performance ST scenarios at lower collisionality and high beta, in which the KBM is predicted to be unstable. These results motivate further linear and especially nonlinear analysis of this and other ST plasmas exhibiting unstable KBMs, which would guide the prediction and optimization of future ST scenarios.

Appendix I

Deployment of the synthetic diagnostic for Cyclone Base Case turbulence simulations

In this appendix I apply both synthetic diagnostic techniques (real space vs. k-space) to a well studied plasma benchmarking exercise: the Cyclone Base Case (noted CBC hereinafter). The motivations for this exercise are:

- 1. Test the validity and equivalence of the two synthetic diagnostic implementations (real space vs. k-space) in a simplified 2D geometry.
- 2. Understand the box size limitations in the synthetic diagnostic.

Equivalence between both synthetic diagnostic methods (real space vs. k-space) is analytically exact. However, different numerical errors under certain simulation conditions may arise during a numerical implementation, giving rise to disagreements in the calculated spectra. On the wavenumber filtering method, one needs to have a simulation setup that allows to accurately resolve the experimental wavenumbers (blue curves in figures 5-5.a) and b) are examples of well resolved wavenumbers). On the real space filtering, one needs to have a simulation setup that captures the scattering location and the full width of the incident microwave beam. In this section, we want to test how the wavenumber resolution and the spatial extent of the microwave beam affect the scattered signal. The

simplified geometry of the CBC has the property that $k_r = k_x$ and $k_\theta = k_z$, which will greatly simplify the wavenumber implementation. Understanding the box size limitations of the synthetic diagnostic is crucial to the implementation of the synthetic diagnostic, specially if aiming quantitative comparisons with experiment. One challenge faced by previous synthetic diagnostics for high-k scattering at NSTX [144] was the necessity of having a big enough simulation domain to cover the whole microwave beam extent, and at the same time resolving the small electron scale turbulence. Those two constrains amount for very expensive, 'big-box' electron scale simulations. With this motivation in mind, we wish to understand the consequences of having simulation domains that are smaller than the scattering volume on the power amplitude of fluctuations.

In this exercise, we move away from any experimental consideration, and focus on a numerical test of the synthetic diagnostic. The simulated plasma fluctuations are GYRO output from the CBC [231]. In this numerical test, there is no 'experimental' wavenumber nor 'scattering location' from a experimental plasma discharge. An arbitrary wavenumber is probed ($k_{r_+}\rho_s = 0.27, k_{\theta_+}\rho_s = 0.42$), and an arbitrary scattering location of ($R_0 = 3.28$ m, $Z_0 = 0.05$ m). In subsection I.0.1 is presented the numerical setup parameters of the GYRO nonlinear gyrokinetic simulation (based on the CBC) used to apply the synthetic diagnostic. In subsection I.0.2, the synthetic diagnostic is applied to a single simulation condition, using three distinct circular microwave filter widths ($a_0 = 5$ cm, $a_0 = 10$ cm, $a_0 = 20$ cm), in the 2D approximation. The real space filter shape is given by $U(R, Z) = \exp[-(R - R_0)^2/\Delta R^2] \exp[-(Z - Z_0)^2/\Delta Z^2]$. The resolution is $\Delta R = \Delta Z = a_0$ (circular beam section, Fig. I-1). In subsection I.0.3, the synthetic diagnostic is applied to the same numerical simulation, but this time varying the radial and vertical extent of the microwave filter independently, (ΔR, $\Delta Z = 2.5, 5, 10, 20, 40$ cm), in the 2D approximation. By making a scan on ΔR and ΔZ, we move will move away from a circular cross section filter, and we wish to understand what are its consequences on the fluctuation power. Looking further ahead, in views of obtaining quantitative comparisons with experiment, this section will help us understand if and how one will be able to extrapolate the value of the fluctuation power by using simulation domains that are smaller than the radial extent of the filters in real space U.

I.0.1 Simulation setup

The cyclone base case is a well diagnosed numerical plasma setup [231], for which we adapt the numerical simulation parameters to apply a synthetic diagnostic. Numerical simulations using the GYRO code are flux-tube simulations that resolve only ion scale turbulence, use 2 kinetic species with drift-kinetic electrons, electrostatic fluctuations, flux tube geometry with periodic boundary conditions and linear profiles, circular, non-shifted flux-surface geometry, and doppler shift given by a Mach number $M = 0.1$.

Numerical simulation parameters are summarized in the table below:

Numerical resolution parameters	
$\mathrm{d}k_r\rho_s = 0.049$	$\mathrm{d}k_\theta\rho_s = 0.049$
$k_r\rho_s^{max} = 3.14$	$k_\theta\rho_s^{max} = 3.093$
$L_r/\rho_s = 128$	$L_y/\rho_s = 128$
$\mathrm{d}n = 8$	$B_m = 4.94$
$\mathrm{d}x/\rho_s = 0.5$	$L_r/a = 0.28$
$n_r = 256$	$n_n = 64$

B_m denotes box-multiplier, an internal GYRO definition. Beware not to confuse $\mathrm{d}k_r\rho_s$ and $\mathrm{d}k_\theta\rho_s$ (numerical resolution of simulation in k-space, determined by GYRO simulation input parameters n_r, B_m, n_n) with $\Delta k_r\rho_s$ and $\Delta k_\theta\rho_s$ (wavenumber resolution of the synthetic diagnostic, determined by ΔR and ΔZ). L_r/ρ_s and L_y/ρ_s are the radial and poloidal box sizes respectively, dn is the toroidal number step, n_r is the number of radial grid-points and n_n is the number of toroidal mode numbers. A numerical simulation with the mentioned simulation parameters was run in the Dawson cluster at the Princeton Plasma Physics Laboratory (PPPL).

I.0.2 Numerical implementation of the synthetic diagnostic to circular filters with variable beam width a_0

The deployment of the synthetic diagnostic was done a posteriori, using three distinct beam widths, as can be seen on Figure I-1, showing the poloidal cross sections of the density fluctuation amplitude. The black dot marks the selected scattering location ($R_0 =$

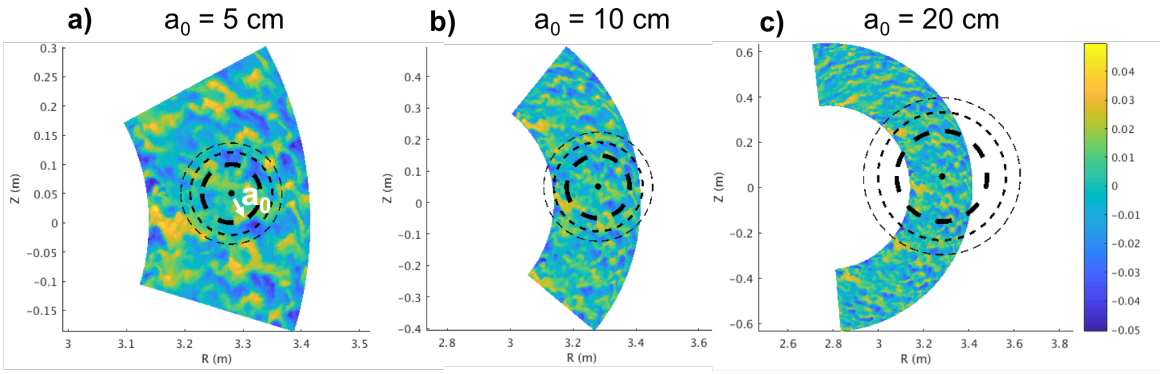

Figure I-1: Density fluctuation amplitude plotted in real space for the same numerical simulation, using three distinct beam widths. **a)** $a_0 = 5$ cm, beam width fits fully within the simulation domain. **b)** $a_0 = 10$ cm, beam width up to $1/e^2$ amplitude fits within the simulation domain. **c)** $a_0 = 20$ cm, beam width has significant portion outside the simulation domain. We are interested in applying a synthetic diagnostic to the last case to understand validity of using future synthetic diagnostics with reduced simulation domain, in views of saving computing time by reducing simulation domain.

3.28 m, $Z_0 = 0.05$ m). The circles marked by the dashed lines denote the $1/e, 1/e^2$ and $1/e^3$ amplitude of the real space filter U ($1/e$ amplitude radius is equal to a_0).

By transforming the filters in real space to wavenumber space, Figure I-2 shows how a different beam radius a_0 affects the wavenumber resolution of the synthetic diagnostic, for the same exact numerical simulation output. Note here how the filters in k_r and k_θ remain circular. A radius of $a_0 = 5$ cm equates to a well resolved filter in wavenumber space. However, resolution of the filter in wavenumber space decreases as we move towards wider beam widths ($a_0 = 10, 20$ cm.). A wide beam width a_0 corresponds to a spectrally narrow region in wavenumber space, and a thin beam width equates to a spectrally wide region in wavenumber space ($cf.$ Figure I-3). Physically, as one moves towards higher and higher beam widths a_0, the incoming radiation becomes a plane wave (spatially delocalized), and the wavenumber matching relation $\vec{k} = \vec{k}_s - \vec{k}_i$ becomes exact (wavenumber resolution becomes 0!). On the contrary, as one moves to narrower beam widths, radiation becomes more spatially localized, but loses spectral localization in wavenumber space. This argument is similar to Heisenberg's principle in quantum mechanics, stemming from a Fourier relation between k-space (momentum) and real space (position). In our case, a Gaussian filter provides the following relation between the real-space resolution and the wavenumber-space resolution: $\Delta k_R = 2/\Delta R$, $\Delta k_Z = 2/\Delta Z$.

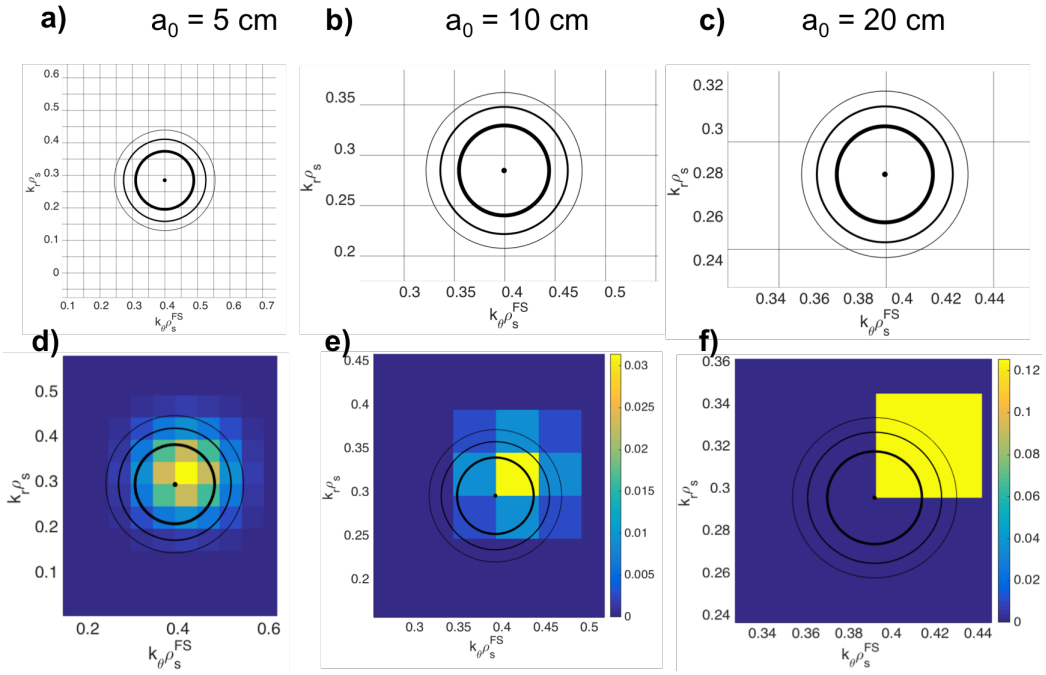

Figure I-2: **a), b), c)** show the wavenumber simulation grid along with the $1/e, 1/e^2$ and $1/e^3$ wavenumber filter amplitudes for $a_0 = 5, 10$ and 20 cm. **d), e), f)** show the wavenumber filters plotted along with the $1/e, 1/e^2$ and $1/e^3$ wavenumber filter amplitudes for $a_0 = 5, 10$ and 20 cm. Note how the $1/e$ amplitude shape of the wavenumber filters in (k_r, k_θ) preserves the circular nature of the filter in real space (Fig. I-1), due to the simplified circular, non-shifted flux surface geometry of the CBC.

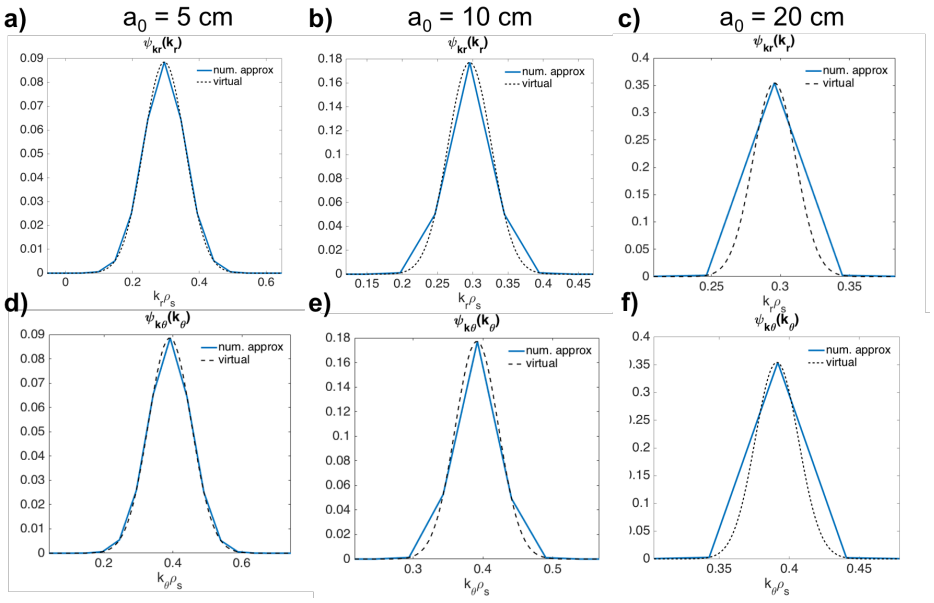

Figure I-3: 1D filters in wavenumber space. **a)**, **b)**, **c)** show the k_r-filter Ψ_{k_r} corresponding to the beam widths $a_0 = 5, 10, 20$ cm. **d)**, **e)**, **f)** show the k_θ-filter Ψ_{k_θ} for beam widths $a_0 = 5, 10, 20$ cm. Note how the radial and poloidal wavenumber filters lose resolution for wider beam widths a_0. The $a_0 = 20$ cm case (**c**, **f**), although laking spectral resolution, will be proven good enough to obtain a quantitative comparison with the synthetic diagnostic.

In this numerical test we have placed ourselves in simulation conditions that allow us to separate the 2D wavenumber filter in Figure I-2 into a product of radial and poloidal wavenumber filters, namely the scattering matrix U_{np} can be written as $U_{np} = \Psi_{kr}(k_r)\Psi_{k\theta}(k_\theta)$ (recall $k_r = 2\pi p/L_r$ while $k_\theta = nq/r$). On the set of Figures I-3 are shown the radial and poloidal wavenumber filters for the different beam widths under study. The case where $a_0 = 5$ cm is the best resolved in wavenumber space, and resolution decreases as one moves to higher a_0. The case where $a_0 = 5$ cm fully overlaps the microwave beam inside the simulation domain, which is not the case for $a_0 = 10, 20$ cm ($cf.$ Fig. I-1).

Application of synthetic diagnostic

Even though we have placed ourselves in a numerical test case, the CBC, we wish in this section to make the link between a numerical implementation of the synthetic diagnostic, and experimentally relevant quantities such as the spectral density $S(\vec{k}, \omega)$.

Following the wavenumber mapping (equation 5.12), Figures I-4 and I-5 show the wavenumber measurement region of the synthetic diagnostic CBC test. The wavenumber mapping allows us to spectrally locate the detected wavenumber $(k_r, k_\theta)_+$ by the synthetic

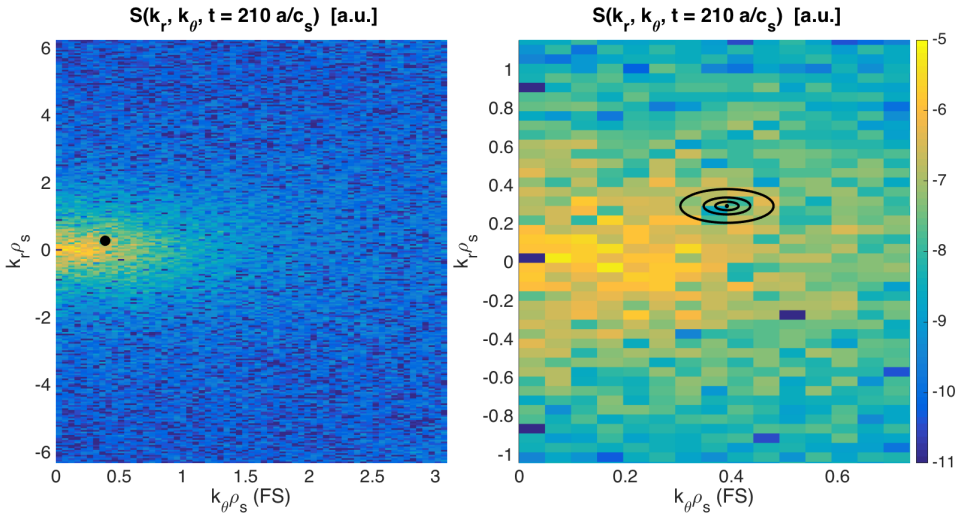

(a) Probed scattering wavenumber $(k_r, k_\theta)_+$ in simulated spectral density $S(k_r, k_\theta, t_0)$.

(b) Zoom in $S(k_r, k_\theta, t_0)$, along with $1/e$ amplitude of filters for $a_0 = 5, 10, 20$ cm.

Figure I-4: Spectral measurement range in the GYRO (k_r, k_θ) space. Probed wavenumber $(k_r, k_\theta)_+$ lies close to the spectral peak of ion-scale fluctuations in k-space (electron scale turbulence was not simulated in this case).

diagnostic in the GYRO (k_r, k_θ) plane of the spectral density $S(k_r, k_\theta, t_0)$, for a particular time in the discharge $t_0 = 210$ a/c$_s$. Note how the probed wavenumber is close to the spectral peak of fluctuations at ion-scales (Fig. I-4 and I-5). In a real life experiment, mapping $(k_r, k_\theta)_+$ would provide extremely useful information allowing to understand the measurement capabilities of our scattering diagnostic. In this particular example, a probed wavenumber having wavenumber components $k_{r_+}\rho_s = 0.27$ and $k_{\theta_+}\rho_s = 0.42$ is selected. Figure I-4b zooms in the (k_r, k_θ)-wavenumber measurement region of Figure I-4a. The ellipses in Figure I-4b are in fact circles (note axes are not square) showing the $1/e$ amplitude of the wavenumber filters $a_0 = 5, 10$ and 20 cm (cf. Figure I-2). The wavenumber measurement region can also be shown in k_θ. Figures I-5a and I-5b show the spectral density $S(k_\theta, t_0)$, where an integral has been performed along the k_r component ($S(k_\theta, t_0) = \sum_{k_r} S(k_r, k_\theta, t_0)$). Note how, in k_θ space, the probed wavenumber is close to the top of the slope in the k_θ-inertial range.

We now turn to compare the synthetic power spectra by applying the synthetic diagnostic to the three beam width conditions. The top three figures on Figure I-6 show the power on the density fluctuations frequency spectra $dP_s(\omega)/d\omega$, with respect to $\omega/(c_s/a)$.

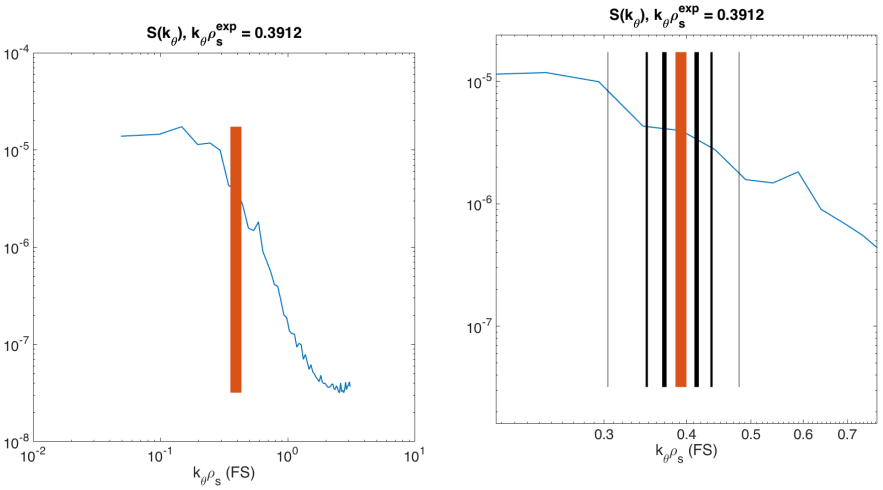

(a) Probed poloidal scattering wavenumber component $k_{\theta+}$ (red) in the simulated spectral density $S(k_\theta, t_0)$ (blue).

(b) Zoom in $S(k_\theta, t_0)$ about $k_{\theta+}$. Black lines show the k_θ-resolution (1/e amplitude) corresponding to the filters $a_0 = 5, 10, 20$ cm. Outer black lines - $a_0 = 5$ cm, inner black lines - $a_0 = 20$ cm.

Figure I-5: Spectral measurement range in k_θ. The spectral density in k_θ is obtained by integration (sum) of $S(k_r, k_\theta, t_0)$ along the k_r component $S(k_\theta, t_0) = \sum_{k_r} S(k_r, k_\theta, t_0)$.

As was shown in the previous section, Figure I-6 is obtained by: 1. filtering in real space and in wavenumber space (equation 5.4) the density fluctuation amplitude $\delta n(r, \theta, \varphi, t)$ and $\delta n_{np}(\theta, t)$ respectively; 2. Once a filtered synthetic signal $\delta n_{\mathrm{u}}(\vec{k}_+, t)$ is obtained, we compute the scattered power in frequency space, that is proportional to the spectral density evaluated at $\vec{k}_+$, $S(\vec{k}_+, \omega)$ (appendix A).

From Figure I-6, good agreement is found between the two filtering methods (k-filtering in red, real space filtering in blue) for the case where $a_0 = 5$ cm, with respect to the amplitude, frequency peak, spectral width and even with respect to the background 'noise' levels. This result indeed validates the application of both synthetic diagnostic methods in a simple GYRO simulation setting. With respect to the beam width of $a_0 = 10$ cm, quite good agreement is still observed in the synthetic frequency spectra, perhaps surprisingly if we take into consideration that the beam does not fully fit within the simulation domain (Fig. I-1). The simulation domain for this case fit the $1/e^2$ beam radius, however not the $1/e^3$ beam radius. With respect to the beam width $a_0 = 20$ cm, good qualitative agreement is observed between both synthetic diagnostic methods: the frequency peak and spectral width are matched, however the amplitude and background levels are a factor of $\times 2 - 3$ higher in the wavenumber filter method. Taking a closer

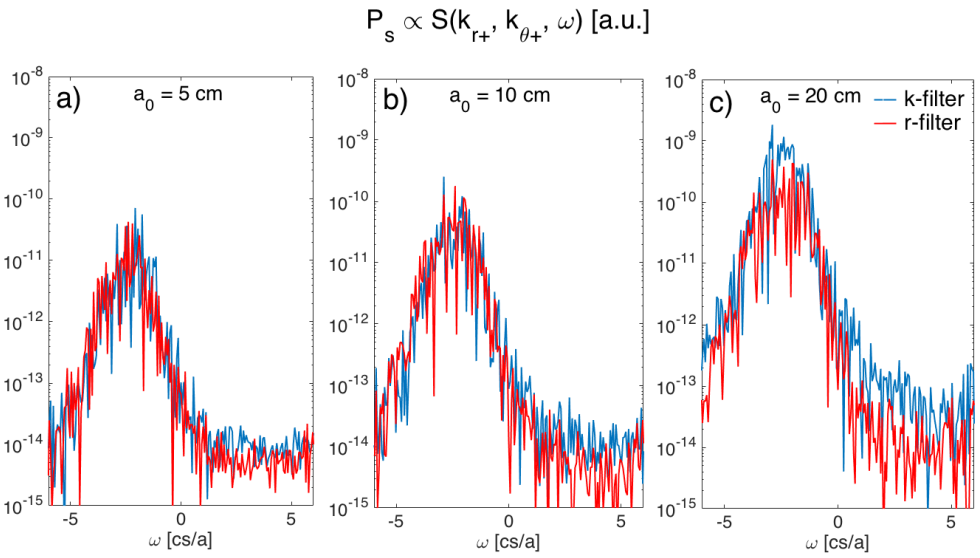

Figure I-6: Synthetic power spectra applying both synthetic diagnostic methods to Cyclone Base Case, for different circular beam width parameters $a_0 = 5, 10, 20$ cm. The total fluctuation power from the real and wavenumber space filter lies within 15% for cases $a_0 = 5, 10$ cm. The case $a_0 = 20$ cm shows a factor of 3 discrepancy in total fluctuation power between the real space and wavenumber filters. This last case shows a circular beam that is bigger than the simulation domain.

look at Figure I-1 one can have an intuition on why the fluctuation amplitude might be higher in the k-space filtering method: in the case where $a_0 = 20$ cm, the beam is essentially $\times 2 - 3$ times as big as the simulation domain. When applying a real space filter, one is equivalently integrating over zeroes, where fluctuation data is simply non-existent, thus effectively decreasing the fluctuation amplitude. Note however how the wavenumber filters for this case (Fig. I-3), although they do not capture the details of the Gaussian profile, they do quite a good job capturing the amplitude (area under the blue curves in Fig. I-3.c) and I-3.f) is close to the Gaussian area under the curve). In the next section we will see how the wavenumber filter resolution influences the total fluctuation power.

I.0.3 Synthetic diagnostic with non-circular microwave beam widths

As was mentioned in the introduction of this section, typical synthetic diagnostics of coherent scattering systems suffer from domain size limitations of numerical simulations of electron scale turbulence. The width of the scattering beam a_0 is generally much larger than the radial extent of a standard electron scale simulation (the situation is often similar to that depicted in Figure I-1.**c**)). Following our intuition, this should result in an under-

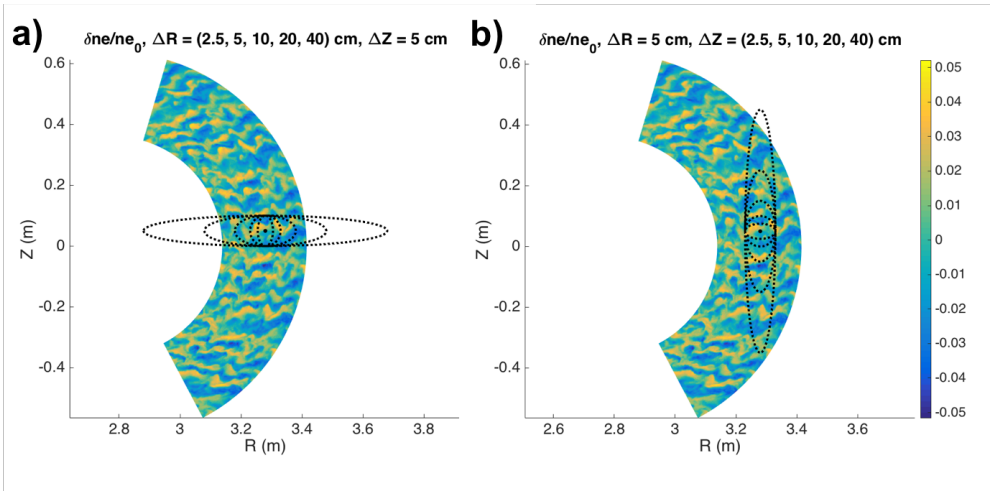

Figure I-7: Poloidal cross section of the density fluctuation amplitude $\delta n/n_0$, plotted along with the $1/e$ amplitude shape of the real space filters. **a)** shows a scan in the radial dimension of the beam $\Delta R = \{2.5, 5, 10, 20, 40\}$ cm), keeping the vertical dimension fixed to $\Delta Z = 5$ cm. **b)** shows a scan in the vertical dimension $\Delta Z = \{2.5, 5, 10, 20, 40\}$ cm, keeping $\Delta R = 5$ cm fixed.

prediction of the synthetic fluctuation power with respect to experiment, since the filtering region from simulation would be reduced by the domain size limitation. In this section we wish to understand how to extract a value for the total fluctuation power (that can be directly compared with experiment) in conditions where the microwave beam extent is larger than the simulation domain size.

We stick to the same initial shape of the real space filter $U(R, Z) = \exp[-(R - R_0)^2/\Delta R^2] \exp[-(Z - Z_0)^2/\Delta Z^2]$. This time we vary the radial extent ΔR and the vertical extent ΔZ independently, breaking the circular nature of the filter (poloidal cross section will become elliptical). We start by varying $\Delta R = 2.5, 5, 10, 20, 40$ cm while maintaining fixed $\Delta Z = 5$ cm. This situation is depicted in Figure I-7.**a)**, which shows a poloidal cross section of the density fluctuation amplitude $\delta n/n_0$, along with the $1/e$ amplitude of the real space filter shapes corresponding to different values of ΔR. Note how the poloidal cross section of our real space filter U becomes elliptically elongated in the horizontal direction. Cases $\Delta R = 20, 40$ cm go well beyond the radial extent of the simulation. In Figure I-7.**b)** we show the alternate exercise for ΔZ. This time $\Delta R = 5$ cm is kept fixed, and ΔZ is varied from $\Delta Z = 2.5, 5, 10, 20, 40$ cm. The poloidal cross section is elliptically elongated vertically, and essentially all beam widths fit within the simulation domain.

Figures I-8 and I-9 show the wavenumber filters Ψ_{k_r} and Ψ_{k_θ} corresponding to these to setup conditions. Note how ΔR values from 2.5 to 10 cm correctly resolve the radial wavenumber filter Ψ_{k_r}. However, $\Delta R = 20, 40$ are not able to resolve it correctly (Fig. I-8), consistent with the real space filter U overflowing the radial extent of the simulation ($cf.$ Fig. I-7.**a**)). The radial extent of the simulation sets a constraint on the radial wavenumber resolution. If we call $L_r = 2\pi/dk_r$ the radial extent of the simulation (dk_r is the radial wavenumber resolution of the simulation), L_r is essentially the radial length of the longest perturbation that is simulated. The constraint for achieving good resolution of the radial wavenumber filter is $\Delta k_r > dk_r$, and may simply be written in terms of length scales as $\Delta R < L_r$. We see here how, in order to have a well resolved radial filter in wavenumber space, one needs to have a beam extent ΔR that is smaller than the simulation box size L_r.

With respect to the poloidal resolution, Figure I-9 shows the poloidal wavenumber filters Ψ_{k_θ} associated to the different vertical extent of the beam ($\Delta Z = 2.5, 5, 10, 20, 40$ cm). We see once more in this situation how the cases $\Delta Z = 20, 40$ cm do not correctly resolve the poloidal wavenumber filter. One can define the poloidal extent of the simulation L_θ, heuristically as $L_\theta = 2\pi/dk_\theta$ (dk_θ is the poloidal wavenumber resolution of the simulation), associated with the longest perturbation in the poloidal direction that is simulated. The constraint $\Delta k_\theta > dk_\theta$ can be written as $\Delta Z < L_\theta$. Note how, even though poloidally all cases 'fit' within the simulation domain (Fig. I-7), we are not able to correctly resolve wavenumber filters associated with $\Delta Z = 20, 40$ cm, since only perturbations having a poloidal length up to L_θ are being actually resolved numerically. This will have implications on the value of the total fluctuation power.

With this setup in mind, we proceed to apply the synthetic diagnostics in real space and in wavenumber space. As was shown in the previous section, one can construct the frequency spectrum of fluctuations, associated to the spectral density $S(k_{r+}, k_{\theta+}, \omega)$ (as in Fig. I-6). In addition, one can equally define the integrated spectral density $S(\vec{k}_+)$ as an integral of $S(\vec{k}_+, \omega)$ (Appendix A). In Figure I-10 we show the wavenumber spectral density $S(k_{r+}, k_{\theta+})$ (directly proportional to the total fluctuation power P_{tot}) corresponding to the different synthetic diagnostic conditions of ΔR and ΔZ. Intuitively, a wider beam width (ΔR or ΔZ) should result in an increase in P_{tot}, since there will be an in-

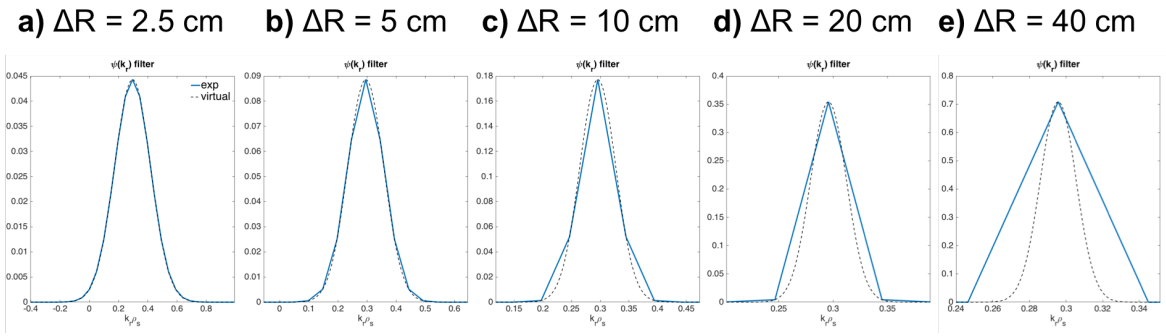

Figure I-8: Radial wavenumber filters Ψ_{k_r} corresponding to the different radial extent of the scattering volume $\Delta R = 2.5, 5, 10, 20, 40$ cm), for a fixed $\Delta Z = 5$ cm, as depicted in Figure I-7.**a**). Note how the resolution is best at lowest value of dR (corresponding to highest value of Δk_r), and decreases as ΔR increases. Recall the relation $\Delta k_r = 2/\Delta R$ applicable to circular non-shifted flux-surface geometry.

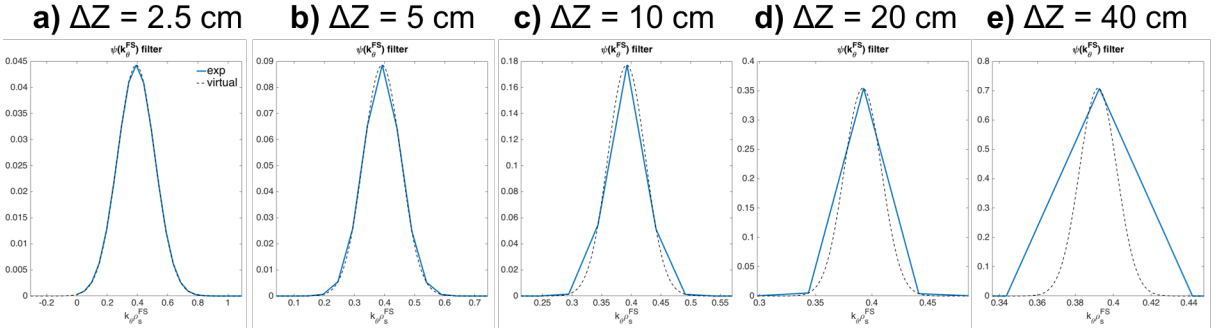

Figure I-9: Poloidal wavenumber filters Ψ_{k_θ} corresponding to the different radial extent of the scattering volume $\Delta Z = 2.5, 5, 10, 20, 40$ cm), for a fixed $\Delta R = 5$ cm, as depicted in Figure I-7.**b**). Note how the resolution is best at lowest value of dZ (corresponding to highest value of Δk_θ), and decreases as ΔZ increases. Recall the relation $\Delta k_\theta = 2/\Delta Z$ applicable to circular non-shifted flux-surface geometry.

creased collection area of fluctuations (a volume in case we were 3D-filtering). We want to answer how the beam width dimensions relate to an increase in P_{tot}.

From Figures I-10.**a)** one can see how P_{tot} from the real space (red) and wavenumber space filters (blue) essentially agree with each other for $\Delta R \leq 10$ cm (within 20%, see thick blue and red lines). Recall that $\Delta R \leq 10$ cm corresponds to beam dimensions fully fit within the simulation domain. The blue discontinuous line represents a quadratic fit $\propto (\Delta R)^2$ of P_{tot} for the wavenumber filter. Note that a quadratic relationship is naturally what one would expect, since a wider beam will translate to a larger collection area of fluctuations. More quantitatively, we also have $P_{tot} \sim |\delta n_{\mathrm{u}}|^2 \sim |\Psi_{k_r}|^2 \sim (\Delta R)^2$ (eqs. 5.17). However the power from the real space filter for $\Delta R = 20, 40$ cm underestimates this quadratic fit for P_{tot} (red line). One can convince himself of the reason by having a closer look at Fig. I-7. Cases $\Delta R = 20, 40$ cm have a filter that exceeds the simulation domain, and effectively one is carrying volume integral over 0-values of the fluctuation amplitude δn, Fig. I-7.**a)**. This will lower P_{tot} with respect to the expected quadratic dependence with $(\Delta R)^2$. However, one could take into account the area (volume in 3D) that the filter is exceeding the simulation domain, and scale the total fluctuation power in Fig. I-10.**a)** by that quantity. Performing such a correction leads to a value of P_{tot} from the real space filter that is consistently within 15% of the k-filter value, as is shown by the red squares in Fig. I-10.**a)**. This suggests that, for conditions where the real space filter exceeds the simulation domain, the total power computed by the real space filtering method can be scaled by the missing integration area of the filter to provide a quantitative value for the total power P_{tot}. As was the case in subsection I.0.2 (and Fig. I-6), the frequency peak of the frequency spectrum and frequency spectral width computed with the real and k-space formulations are in good quantitative agreement with each other (not shown here).

With respect to the vertical dimension scan (ΔZ), Fig. I-10.**b)** shows how P_{tot} computed using the wavenumber filter (blue line) follows a quadratic dependence with $\propto (\Delta Z)^2$. Once more, this can be explained by a simple scaling $P_{tot} \sim |\delta n_{\mathrm{u}}|^2 \sim |\Psi_{k_\theta}|^2 \sim (\Delta Z)^2$. We also observe how the real space filter (red line) underestimates P_{tot} for $\Delta Z = 20, 40$ cm. However, the underestimation in this case is not as pronounced as in the ΔR scan in Fig. I-10.**a)**, since for these cases the filter in real space better overlaps

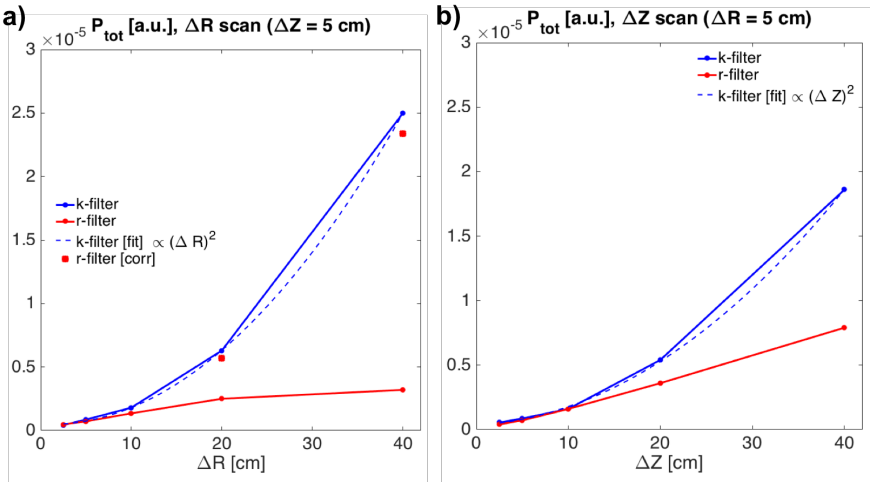

Figure I-10: Total synthetic fluctuation power resulting from application of both synthetic diagnostic methods (real space vs. k-space) to the Cyclone Base Case. **a)** shows the result of a scan in the radial dimension ΔR, showing a quadratic dependency of P_{tot} with ΔR. **b)** shows the result of a scan in the vertical dimension ΔZ. The dashed lines show a quadratic fit $P_{tot} \propto (\Delta R)^2, (\Delta Z)^2$. For values $\Delta R, \Delta Z = 20, 40$ cm, the real space filter ceases to follow the quadratic dependence since it exceeds the simulation domain. For these cases, we rescale P_{tot} by the total beam area missing in the simulation domain (red squares) brings it to agreement with respect to the k-space filter.

with the simulation domain, as is shown in Fig. I-7.**b)**.

It is important to mention that the simulations presented in this section are flux-tube. For these conditions, the background profiles are linear throughout the simulation radial domain, and the simulated turbulence is statistically similar throughout the radial domain. For this reason, we have proceeded to perform scans on the beam size dimensions $\Delta R, \Delta Z$, since we expect to have a self-similar frequency spectrum, independent of the beam size dimensions, and scaled solely by the value of $\Delta R, \Delta Z$ (this is well shown in Fig. I-10). Note that such a scan in $\Delta R, \Delta Z$ would not be legitimate in the case of global simulations, since in this case the background profiles would be different along the radial domain, thus giving rise to statistically different turbulent spectra.

In this section we have applied the synthetic diagnostic implementations in real and k-space to simulation output from the Cyclone Base Case. In subsection I.0.2 we learned how the filter resolution in wavenumber space is tightly linked to the radial and vertical dimensions ($\Delta R, \Delta Z$) of the real space filter (in 2D), as can be seen from Figs. I-2 and I-3. Real space filters whose dimensions are fully within the simulation domain give rise to

well resolved filters in k-space (e.g. $a_0 = 5$ cm in subsection I.0.2), and k-space resolution decreases as the beam a_0 increases. On the contrary, in conditions where the beam extent exceeds the simulation domain, this will result in a poorly resolved wavenumber filter, as was shown for the case where $a_0 = 20$ cm ($cf.$ figures I-1, I-2, I-3). We also learned in subsection I.0.2 how a circular simulation domain that captures the $1/e^2$ amplitude is sufficient to have quantitative agreement and have hope for quantitative comparisons with experimental fluctuation spectra, as is shown in Fig. I-6. A simulation domain capturing the $1/e^3$ amplitude beam radius would be preferable, but not necessary. Under these conditions, both synthetic diagnostic methods are shown to quantitatively agree. When the beam size a_0 is bigger than the simulation domain, the total fluctuation power ceases to agree quantitatively, although the spectra preserve the same features, such as the frequency peak and the frequency width of the frequency spectrum. These results can help us interpret the differences between standard and 'big-box' electron scale simulations of this thesis, however in that case we varied the numerical simulation while keeping the same resolution in the synthetic diagnostic, while here we keep the same simulation while we vary the resolutions $\Delta R, \Delta Z$. Additionally, in this appendix we employ a Gaussian filter in the radial and poloidal dimensions Ψ_{k_r} and Ψ_{k_θ} respectively, however in the rest of this thesis we have used Gaussian filter only in the poloidal dimension, while the filter in the radial dimension was given by a sinc function (equation 5.17).

In subsection I.0.3 we learned how the radial and vertical dimensions independently affect the total fluctuation power P_{tot} computed by the synthetic diagnostic. We observe a quadratic dependence of P_{tot} with ΔR and ΔZ, as is shown in Fig. I-10. Filtering in real space follows this quadratic dependence when the beam dimensions lie within the simulation domain ($\Delta R < L_r$ and $\Delta Z < L_\theta$). Under these conditions, the real and k-space implementations are shown to be quantitatively equivalent. However, as the filters in real space exceed the simulation domain ($\Delta R, \Delta Z = 20, 40$ cm) the power computed by the real space filter ceases to follow the quadratic scaling $\propto (\Delta R)^2, (\Delta Z)^2$. Further analysis taking into account the total area of the real space filter (that exceeds the simulation domain, $cf.$ Fig. I-7) brings the real space filter predictions for P_{tot} back in agreement within 10% of the k-space filter predictions.

Bibliography

[1] A. M. Bradshaw et al., Fusion Engineering and Design **86**, 2770 (2010).

[2] H. S. Bosch and G. M. Hale, Nucl. Fusion **32**, 611 (1992).

[3] J D Lawson, 1957 Proc. Phys. Soc. B **70** 6.

[4] `http://www.ideen2020.de/`, Max Planck Institute for Plasma Physics.

[5] `https://nstx-u.pppl.gov/`, NSTX 5 Year Plan for FY2009-2013, ch. 1, p. 4.

[6] J. P. Freidberg, *Plasma Physics and Fusion Energy*, Cambridge University Press, 2007.

[7] G. Rewoldt, *et al*, Phys. Plasmas **3**, 1667 (1996).

[8] S. M. Kaye *et al*, Nucl. Fusion **47**, (2007) 499.

[9] S. M. Kaye *et al*, Nucl. Fusion **49**, (2009) 045010.

[10] S. M. Kaye *et al*, Nucl. Fusion **49**, (2009) 045010.

[11] S. M. Kaye, R. E. Bell, D. Gates, B. P. LeBlanc, F. M. Levinton, J. E. Menard, D. Mueller, G. Rewoldt, S. A. Sabbagh, W. Wang, and H. Yuh, Phys. Rev. Lett **98** 175002 (2007).

[12] Kaye S., Gerhardt S., Guttenfelder W., Maingi R., Bell R., Diallo A., LeBlanc B. and Podesta M., Nucl. Fusion **53**, (2013) 063005.

[13] M. Valovič, R. Akers, M. de Bock, J. McCone, L. Garzotti, C. Michael, G. Naylor, A. Patel, C.M. Roach, R. Scannell, M. Turnyanskiy, M. Wisse, W. Guttenfelder, J. Candy and the MAST team, Nucl. Fusion **51** (2011) 073045.

[14] ITER Physics Basis, Nucl. Fusion **39**, 2178 (1999).

[15] S. M. Kaye, *et al.*, Fusion Technol. **36** (1999) 16.

[16] M. Ono, *et al.*, Nucl. Fusion **40** (2000) 557.

[17] `https://www.pppl.gov/`.

[18] Darke A. et al 1994 MAST: a Mega Amp Spherical Tokamak Proc. 18th Symp. on Fusion Technology (Karlsruhe, Germany, 22-26 August) vol **1** ed K. Herschbach et al (Amsterdam: The Netherlands) pp 799-802.

[19] A. Sykes, *et al.*, Nucl. Fusion **39** 1271 (1999).

[20] `https://www.tokamakenergy.co.uk/`.

[21] Y.-K.M. Peng, *et al.*, Fusion Sci. Technol. **56** 957 (1986).

[22] T. Brown, J. Menard, P. Titus, A. Zolfaghari, L. El-Guebaly, and L. Mynsberge, "Progess in developping the STFNSF configuration." These proceedings. [25th Symposium on Fusion Engineering (SOFE), San Francisco, June 10-14, 2013].

[23] J.E. Menard *et al.*, Nucl. Fusion **56** 106023 (2016).

[24] J.E. Menard *et al.*, Nuc. Fusion **52**, 083015 (2012).

[25] `http://www.ccfe.ac.uk/assets/documents/other/MAST-U_RP_v4.0.pdf`.

[26] G. Taylor, J. C. Hosea, C. E. Kessel, B. P. LeBlanc, D. Mueller, C. K. Phillips, E. J. Valeo, J. R. Wilson, P. M. Ryan, P. T. Bonoli, J. C. Wright, and R. W. Harvey, Phys. Plasmas **19**, 042501 (2012).

[27] P. K. Browning, *et al.*, Phys. Rev. Lett. **68** 1722 (1992).

[28] J. R. Wilson, *et al*., Phys. Plasmas **10**, 1733 (2003).

[29] G. Taylor, P. T. Bonoli, D. L. Green, R. W. Harvey, J. C. Hosea, E. F. Jaeger, B. P. LeBlanc, R. Maingi, C. K. Phillips, P. M. Ryan, E. J. Valeo, J. R. Wilson, J. C. Wright, and the NSTX Team, AIP Conference Proceedings **1406**, 325 (2011).

[30] F. L. Hinton and R. D. Hazeltine, Rev. Mod. Phys. **48**, 239 (1976).

[31] P. Helander and D. Sigmar, *Collisional Transport in Magnetized Plasmas*, Cambridge Monographs on Plasma Physics, Cambridge University Press, 2002.

[32] M. C. Zarnstoff *et al*., Phys. Rev. Lett. **60**, 1306 (1988).

[33] M. C. Zarnstorff and S. C. Prager, Phys. Rev. Let. **53**, 454 (1984).

[34] M. C. Zarnstorff and S. C. Prager, Phys. Fluids **29**, 298 (1986).

[35] M. C. Zarnstorff et al., Phys. Plasmas **4**, 1097 (1997).

[36] C Bourdelle., Plasma Phys. Control. Fusion **47**(5A), A317-A326 (2005).

[37] G. T. Hoang *et al*, Phys. Rev. Lett. **87** 125001 (2001).

[38] G. T. Hoang *et al*, Phys. Plasmas **10**, 405 (2003).

[39] W. Horton *et al*, Phys. Plasmas **11**, 2600 (2004).

[40] J. C. Hillesheim *et al*., Phys. Rev. Lett. **110** 045003 (2013).

[41] W. Horton., *Turbulent Transport in Magnetized Plasmas*, World Scientific, London 2012.

[42] A. J. Wootton *et al*., Phys. Fluids B **12**, 2879 (1990).

[43] W. Horton, Rev. Mod. Phys. **71**, 735 (1999).

[44] J. Weiland, *Collective Modes in Inhomogeneous Plasmas: Kinetic and Advanced Fluid Theory*, Series in Plasma Physics. Taylor and Francis, 2000.

[45] F. Chen. *Introduction to Plasma Physics and Controlled Fusion*, Springer, 1984.

[46] B. Coppi, M. N. Rosenbluth, and R. Z. Sagdeev, Physics. Fluids **10(3)** 582- 587 (1967).

[47] M. Porkolab and G. S. Kino, Phys. Rev. Lett., **15**, 752-755 (1965).

[48] M. Porkolab, Nucl. Fusion **8**(1), 29 (1968).

[49] W. Horton *et al*., Phys. Fluids **24**, 1077 (1981).

[50] B.B. Kadomtsev and O.P. Pogutse, Nuclear Fusion **11**(1), 67 (1971).

[51] W. Horton, B. G. Hong, and W. M. Tang, Phys. Fluids **31**(10), 2971-2983, 1988.

[52] J. Y. Kim, W. Horton, and J. Q. Dong, Phys. Fluids B: Plasma Physics **5**, 4030 (1993).

[53] J. Candy, Phys. Plasmas **12**, 072307 (2005).

[54] E. A. Belli, J. Candy, Phys. Plasmas **17**, 112314 (2010).

[55] J. Citrin *et al.*, Plasma Phys. Control. Fusion **57** (2015) 014032.

[56] J. Garcia *et al.*, Nucl. Fusion **55**, 053007 (2015).

[57] K. H. Burrell, Phys. Plasmas **4**, 1499 (1997).

[58] J. E. Kinsey *et al*., Phys. Plasmas **14**, 102306 (2007).

[59] W. Guttenfelder, *et al*., Phys. Plasmas **19**, 056119 (2012).

[60] W. Guttenfelder, *et al*., Nucl.Fusion **53**, 093022 (2013).

[61] NSTX Upgrade Five Year Plan for FY2014-2018, nstx-u.pppl.gov.

[62] D. Stutman *et al*., Phys. Rev. Lett. **102**, 115002 (2009).

[63] N. N. Gorelenkov *et al*., Nucl. Fusion **50**, 084012 (2009).

[64] Y. Ren, E. Belova, N. Gorelenkov, W. Guttenfelder, S. M. Kaye, E. Mazzucato, J. L. Peterson, D. R. Smith, D. Stutman, K. Tritz, W. X. Wang, H. Yuh, C. W. Domier and B. P. LeBlanc, Nucl. Fusion **57**, (2017) 072002.

[65] D. R. Smith *et al*., Rev. Sci. Instrum., **79**, 123501 (2008).

[66] J. W. Connor and O. P. Pogutse, Plasma Phys. Control. Fusion **43**, 155?175 (2001).

[67] W. Dorland, F. Jenko, M. Kotschenreuther, and B.N. Rogers, Phys. Rev. Lett. **85** 5579 (2000).

[68] F. Jenko, W. Dorland, M. Kotschenreuther, and B.N. Rogers, Phys. Plasmas **7** 1904 (2000).

[69] F. Jenko and W. Dorland, Phys. Rev. Lett. **89**, 225001 (2002).

[70] F. Jenko *et al*, Phys. Plasmas **8**, 4096 (2001).

[71] W. M. nevins *et al*., Phys. Plasmas **13**, 122306 (2006).

[72] N. T. Howard, A. E. White, M. Greenwald, C. Holland, and J. Candy, Phys. Plasmas 21, 032308 (2014).

[73] N. T. Howard, C. Holland, A. E. White, M. Greenwald, and J. Candy, Phys. Plasmas 21, 112510 (2014).

[74] N.T. Howard, C. Holland, A.E. White, M. Greenwald and J. Candy, Nucl. Fusion **56** (2016) 014004.

[75] N. T. Howard, C. Holland, A. E. White, M. Greenwald, J. Candy, and A. J. Creely, Phys. Plasmas **23**, 056109 (2016).

[76] S. Maeyama, Y. Idomura, T.-H. Watanabe, M. Nakata, M. Yagi, N. Miyato, A. Ishizawa, and M. Nunami, Phys. Rev. Lett. **114**, 255002 (2015).

[77] C. Holland *et al.*, Nucl. Fusion **57**, 066043 (2017).

[78] W. Guttenfelder and J. Candy, Phys. Plasmas **18**, 022506 (2011).

[79] G J Colyer, A. A. Schekochihin, F. I. Parra, C. M. Roach, M. A. Barnes, Y-c Ghim and W. Dorland, Plasma Phys. Control. Fusion **59** 055002 (2017).

[80] H. Sugama and W. Horton, Phys. Plasmas **5**, 2560 (1998).

[81] J. Candy, R. E. Waltz, and W. Dorland, Phys. Plasmas **11**, L25 (2004).

[82] B. F. McMillan *et al.*, Phys. Rev. Lett. **105** 155001 (2010).

[83] J. C. Hillesheim *et al.*, Rev. Sci. Instrum., **80**, 083507 (2009).

[84] L. Schmitz *et al.*, Rev. Sci. Instrum., **79**, 10F113 (2008).

[85] J.C. Hillesheim *et al.*, Nucl. Fusion **55** (2015) 073024.

[86] P. Hannequin *et al.*, Rev. Sci. Instrum., **75**, 3881 (2004).

[87] C. Zhou *et al.*, Rev. Sci. Instrum., **84**, 103511 (2013).

[88] T. Tokuzawa *et al.*, Rev. Sci. Instrum., **83**, 10E322 (2012).

[89] D. R. Smith, *Investigation of electron gyroscale fluctuations in the National Spherical Torus Experiment*, Ph.D. dissertation, Princeton University (2009).

[90] E. Mazzucato, Phys. Plasmas **10**, 753 (2003).

[91] E. Mazzucato, Plasma Phys. Control. Fusion **48**, 1749 (2006).

[92] P. J. Catto, W. M. Tang, and D. E. Baldwin, Plasma Physics **23** (7), 639 (1981).

[93] E. A. Frieman and Liu Chen, Phys. Fluids **25**(3), 502-508 (1982).

[94] G.G. Howes *et al.*, The Astrophysical Journal **651**, 590-614 (2006).

[95] A. J.Brizard and T. S. Hahm, Rev. Mod. Phys. **79**, 421 (2007).

[96] X. Garbet, Y. Idomura, L. Villard, and T.H. Watanabe, Nucl. Fusion, **50**(4), 043002 (2010).

[97] I. A. Abel *et al.*, Rep. Prog. Phys. **76** 116201 (2013).

[98] Candy J. and Waltz R.E. 2003 *J. Comput. Phys*. **186** 545.

[99] P. W. Terry *et al.*, Phys. Plasmas **15**, 062503 (2008).

[100] M. Greenwald, Phys. Plasmas **17**, 058101 (2010).

[101] P. Ricci *et al*., Phys. Plasmas **18**, 032109 (2011).

[102] P. Ricci *et al*., Phys. Plasmas **22**, 055704 (2015).

[103] C. Holland, Phys. Plasmas **23**, 060901 (2016).

[104] ITER physics basis editors and expert groups, Nucl. Fusion **39**, 2137 (1999).

[105] R. J. Hawryluk, *Physics of Plasma Close to Thermonuclear Conditions*, (Pergamon, New York, 1981).

[106] M. H. Redi M *et al*., 2003 *Proc. 30th EPS Conf. on Controlled Fusion and Plasma Physics (St Petersburg)* vol 27A (ECA) P-4.94

[107] M. H. Redi M *et al*., 2004 *Proc. 31st EPS Conf. on Controlled Fusion and Plasma Physics (London)* vol 28G (ECA) P2-162.

[108] M. H. Redi M *et al*., 2005 *Proc. 32nd EPS Conf. on Controlled Fusion and Plasma Physics (Tarragona)* vol 29C (ECA) P5-041.

[109] C. Bourdelle, Phys. Plasmas **10**, 2881 (2003).

[110] W. Horton *et al*., Nucl. Fusion, **45**, 976 (2005).

[111] D. Stutman, Phys. Plasmas **13**, 092511 (2006).

[112] F. M. Levinton, Phys. Plasmas **14**, 056119 (2007).

[113] M. Kotschenreuther *et al*, Comp. Phys. Commun. **88** 128 (1995).

[114] J. Candy and R.E. Waltz, Phys. Rev. Lett. **91**, 045001 (2003).

[115] W. X. Wang *et al*., Phys. Plasmas **13**, 092505 (2006).

[116] K. L. Wong *et al*., Phys. Rev. Lett. **99**, 135003 (2007).

[117] K. L. Wong *et al*., Phys. Plasmas **15**, 056108 (2008).

[118] J. F. Drake *et al*., Phys. Rev. Lett. **44**, 994 (1980).

[119] A. B. Rechester and M. N. Rosenbluth., Phys. Rev. Lett. **40**, 38 (1978).

[120] D. R. Smith *et al*., Rev. Sci. Instrum., **75**, 3840 (2004).

[121] E. Mazzucato *et al*., Phys. Rev. Lett. **101**, 075001 (2008).

[122] E. Mazzucato *et al*., Nucl. Fusion, **49**, 055001 (2009).

[123] D. R. Smith *et al*., Phys. Rev. Lett. **102**, 225005 (2009).

[124] D. R. Smith *et al*., Phys. Plasmas **16**, 112507 (2009).

[125] H. Y. Yuh *et al*, Phys. Plasmas **16**, 056120 (2009).

[126] H. Y. Yuh *et al*, Phys. Rev. Lett. **106**, 055003 (2011).

[127] Y. Ren *et al*, Phys. Rev. Lett. **106**, 165005 (2011).

[128] W. Guttenfelder, J. Candy, Phys. Plasmas **18**, 022506 (2011).

[129] J. L. Peterson *et al*., Phys. Plasmas **19**, 056120 (2012).

[130] Y. Ren *et al*., Phys. Plasmas **19**, 056125 (2012).

[131] Y. Ren *et al*., Nucl. Fusion, **53**, 083007 (2013).

[132] Y. Ren *et al*., Phys. Plasmas **22**, 110701 (2015).

[133] W. Guttenfelder *et al*., Phys. Rev. Lett. **106**, 155004 (2011).

[134] W. Guttenfelder *et al*., Phys. Plasmas **19**, 022506 (2012).

[135] W. Guttenfelder *et al*., Phys. Plasmas **19**, 056119 (2012).

[136] W. Guttenfelder *et al*., Nucl. Fusion **53**, (2013) 093022.

[137] D. R. Smith *et al*., Plasma Phys. Control. Fusion **53**, 035013 (2011).

[138] S. M. Kaye *et al*., Phys. Plasmas **19**, 082510 (2014).

[139] D. Stutman *et al*., Phys. Rev. Lett. **102**, 115002 (2009).

[140] N. N. Gorelenkov *et al*., Nucl. Fusion **50**, (2010) 084012.

[141] E. V. Belova *et al*., Phys. Rev. Lett. **115**, 015001 (2015).

[142] R. V. Bravenec and W. M. Nevins, Rev. Sci. Instrum., **77**, 015101 (2006).

[143] M. W. Shafer *et al*., Rev. Sci. Instrum., **77**, 10F110 (2006).

[144] F. M. Poli *et al*., Phys. Plasmas **17**, 112514 (2010).

[145] R. J. Akers *et al*., Plasma Phys. Control. Fusion **45**, A175 (2003).

[146] D. J. Applegate *et al*., Phys. Plasmas **11**, 5085 (2004).

[147] H. R. Wilson *et al*., Nucl. Fusion **44**, (2004) 917.

[148] M. Kotschenreuther *et al*., Nucl. Fusion **40**, (2000) 677.

[149] C. M. Roach *et al*., Plasma Phys. Control. Fusion **47**, B323 (2005).

[150] N. Joiner *et al*., Plasma Phys. Control. Fusion **48**, 685 (2006).

[151] D. J. Applegate *et al*., Plasma Phys. Control. Fusion **49**, 1113 (2007).

[152] R. J. Akers *et al*., Transport studies in the MAST spherical tokamak, *Proc. 22nd IAEA Fusion Energy Conf. (Geneva, Switzerland)* EX2-2.

[153] C. M. Roach *et al*., Plasma Phys. Control. Fusion **51**, 124020 (2009).

[154] H. P. Furth, J. Killeen and M. N. Rosenbluth, Phys. Fluids **6**, 469 (1963).

[155] P. J. Catto and M. N. Rosenbluth, Phys. Fluids **16**, 1719 (1973).

[156] S. Saarelma *et al*., Plasma Phys. Control. Fusion **54**, 085012 (2012).

[157] S. Joillet *et al*., Comp. Phys. Comm. **177**, 409 (2008).

[158] A. Bottino, Phys. Plasmas **14**, 010701 (2007).

[159] A. R. Field *et al*., Rev. Sci. Instrum., **83**, 013508 (2012).

[160] Y.-c. Ghim *et al*., Rev. Sci. Instrum., **81**, 10D713 (2010).

[161] G. McKee *et al*., Rev. Sci. Instrum., **70**, 913 (1999).

[162] Y.-c. Ghim *et al*., Plasma Phys. Control. Fusion **54**, 095012 (2012).

[163] Y.-c. Ghim *et al.*, Phys. Rev. Lett. **110**, 145002 (2013).

[164] P. Goldreich and Sridhar, Astrophys. J. **438**, 763 (1995).

[165] M. Barnes *et al.*, Phys. Rev. Lett. **107**, 115003 (2011).

[166] P. H. Diamond *et al.*, Plasma Phys. Control. Fusion **47**, R35 (2005).

[167] Y.-c. Ghim *et al.*, Nucl. Fusion **54**, (2014) 042003.

[168] A. R. Field *et al.*, Plasma Phys. Control. Fusion **56**, 025012 (2014).

[169] A. R. Field *et al.*, Rev. Sci. Instrum., **83**, 013508 (2012).

[170] A. Bottino *et al.*, Plasma Phys. Control. Fusion **53**, 124027 (2011).

[171] M. J. Fox *et al.*, Plasma Phys. Control. Fusion **59**, 034002 (2017).

[172] M. J. Fox *et al.*, Plasma Phys. Control. Fusion **59**, 044008 (2017).

[173] F. van Wyk *et al.*, Plasma Phys. Control. Fusion **59**, 114003 (2017).

[174] F. van Wyk *et al.*, J. Plasma Phys. **82**, 905820609 (2016).

[175] T. L. Rhodes *et al.*, 58th Annual Meeting of the APS Division of Plasma Physics, **61** 18, `http://meetings.aps.org/link/BAPS.2016.DPP.NP10.21`, (2016).

[176] J. C. Hillesheim *et al.*, Cross-Polarization Doppler Backscattering Measurements and Microtearing at the Top of the MAST H-mode Pedestal, *Proc. 25th IAEA Fusion Energy Conf. (St. Petersburg, Russian Federation)* EX/P4-35.

[177] J. C. Hillesheim *et al.*, Nucl. Fusion **55**, (2015) 073024.

[178] J. C. Hillesheim *et al.*, Plasma Phys. Control. Fusion **58**, 014020 (2016).

[179] J. W. Connor *et al.*, Phys. Rev. Lett. **40**, 6 (1978).

[180] `https://transp.pppl.gov/`.

[181] `http://w3.pppl.gov/transp/`.

[182] J. P. H. E. Ongena *et al*, *Proceedings of the Tenth Carolus Magnus Summer School on Plasma and Fusion Energy Physics*, Fusion Science and Technology **61** 2T 180-189 (2012).

[183] J. M. Schachter, *Local Transport Analysis for the Alcator C-Mod Tokamak*, Ph.D. dissertation, Massachusetts Institute of Technology (1997), url-http://hdl.handle.net/1721.1/9590.

[184] R. E. Waltz and R. L. Miller, Phys. Plasmas **6**, 4265 (1999).

[185] R. E. Waltz, R. L. Dewar, and X. Garbet, Phys. Plasmas **5**, 1784 (1998).

[186] `http://nstxops.pppl.gov:2461/?shotyear=&shotnumber=141767&runid=&rundate=&runby=`.

[187] I. H. Hutchinson, *Principles of Plasma Diagnostics* (Cambridge University Press, Cambridge, UK, 2002), 2nd ed.

[188] `http://gafusion.github.io/doc/`.

[189] J. Candy and E. Belli, *GYRO Technical Guide*, General Atomics, P.O. Box 85608, San Diego, CA 92186-5608, USA.

[190] J. Candy, E. A. Belli and R. V. Bravenec, 2016 *J. Comput. Phys*. **324** 93.

[191] `https://www.nersc.gov/`.

[192] `https://github.com/jcwright77/engaging_cluster_howto`.

[193] `https://markchil.github.io/3_Papers_Talks.html`.

[194] T. Kondoh *et al*., Rev. Sci. Instrum. **72**, 1143 (2001).

[195] M. Stejner *et al*., Plasma Phys. Control. Fusion **57** 062001 (2015).

[196] R. L. Miller *et al*, Phys. Plasmas **5** 973 (1998).

[197] R. Barchfeld *et al*., Rev. Sci. Instrum. **89**, 10C114 (2018).

[198] E. Holzhauer and J. H. Massig, 1978 Plasma Phys. **20** 867.

[199] R. E. Slusher and C. M. Surko, **23**, 472 (1980).

[200] D. Grésillon *et al*. **1982** Phys. Scr. 459 (1982).

[201] P. Devynck *et al*., Plasma Phys. Control. Fusion **35** 63 (1993).

[202] P. Hennequin *et al*., Rev. Sci. Instrum. **75** 3881 (2004).

[203] G. Conway *et al*., Plasma Phys. Control. Fusion **46** 951 (2004).

[204] J. C. Hillesheim *et al*., Rev. Sci. Instrum. **80** 083507 (2009).

[205] T. Happel *et al*., Rev. Sci. Instrum. **80** 073502 (2009).

[206] T. Tokuzawa *et al*., Rev. Sci. Instrum. **83** 10E322 (2012).

[207] C. Zhou *et al*., Rev. Sci. Instrum. **83** 103511 (2013).

[208] J. C. Hillesheim *et al*., Rev. Sci. Instrum., **83**, 10E331 (2012).

[209] J. C. Hillesheim, PhD. Dissertation, UCLA (2012).

[210] C. Holland *et al*, Nucl. Fusion **52**, (2012) 063028.

[211] D. R. Ernst *et al*, Phys. Plasmas **23**, 056112 (2016).

[212] J. Ruiz Ruiz, Y. Ren, W. Guttenfelder, A. E. White, S. M. Kaye, B. P. Leblanc, E. Mazzucato, K. C. Lee, C. W. Domier, D. R. Smith, and H. Yuh, Phys. Plasmas **22**, 122501 (2015).

[213] G. M. Staebler, J. Candy, N. T. Howard, and C. Holland, Phys. Plasmas **23**,062518 (2016).

[214] J. Ruiz-Ruiz, *Stabilization of Electron-Scale Turbulence by Electron Density Gradient in NSTX*, M.S. dissertation, Massachusetts Institute of Technology (2015).

[215] E. A. Belli and J. Candy, Plasma Phys. Control. Fusion **50** 095010 (2008).

[216] H. K. Park, *Tokamak Plasma Wave Studies via Multi-Channel Far Infrared Laser Scattering*, PhD dissertation, University of California, Los Angeles (1984).

[217] M. N. Rosenbluth and F. L. Hinton, Phys. Rev. Lett. **80**, 724 (1998).

[218] F. L. Hinton and M. N. Rosenbluth, Plasma Phys. Control. Fusion **41**, A653 (1999).

[219] Z. Lin, T. S. Hahm, W. W. Lee, W. M. Tang, and P. H. Diamond, Phys. Rev. Lett. **83**, 3645 (1999).

[220] A. M. Dimits *et al*., Physics of Plasmas **7**, 969 (2000).

[221] D. R. Mikkelsen and W. Dorland, Phys. Rev. Lett. **101**, 135003 (2008).

[222] E. A. Belli and J. Candy, Plasma Phys. Control. Fusion **59** 045005 (2017).

[223] C. Holland *et al.*, Nucl. Fusion **57**, (2017) 066043.

[224] A.J. Creely, A.E. White, E.M. Edlund, N.T. Howard and A.E. Hubbard, Nucl. Fusion **56**, 036003 (2016).

[225] H. Sugama, T.-H. Watanabe, and M. Nunami, Phys. Plasmas **16**, 112503 (2009).

[226] G. Conway *et al.*, Plasma Phys. Control. Fusion **47** 1165 (2005).

[227] J. Citrin *et al*., Phys. Rev. Lett. **111**, 155001 (2013).

[228] Plasma Phys. Control. Fusion **57** 014032 (2015).

[229] Plasma Phys. Control. Fusion **55** 053007 (2015).

[230] W. Guttenfelder, private communication.

[231] http://gs2.sourceforge.net/PMP/itg.html

99